The University Of Sheffield.

Graphite Immobilisation in Glass Composite Materials

Mohd Zul Hilmi Mayzan

A thesis submitted in partial fulfilment of the requirements for the degree of Doctor of Philosophy

Immobilisation Science Laboratory
Department of Materials Science and Engineering
The University of Sheffield

September 2015

Abstract

Irradiated graphite is a problematic nuclear waste stream and currently raises significant concern worldwide in identifying its long-term disposal route. This thesis describes the use of glass materials for the immobilisation of irradiated graphite prepared by microwave, conventional and sparks plasma sintering methods. Several potential glass compositions namely iron phosphate, aluminoborosilicate, calcium aluminosilicate, alkali borosilicate and obsidian were considered for the immobilisation of various loadings of graphite simulating irradiated graphite. The properties of the samples produced using different processing methods are compared selectively. An investigation of microwave processing using an iron phosphate glass composition revealed that full reaction of the raw materials and formation of a glass melt occurs with consequent removal of porosity at 8 minutes microwave processing. When graphite is present, iron phosphate crystalline phases are formed with much higher levels of residual porosity of up to 43 % than in the samples prepared using conventional sintering under argon. It is found that graphite reacts with the microwave field when in powder form but this reaction is minimised when the graphite is incorporated into a pellet, and that the graphite also impedes sintering of the glass. Mössbauer spectroscopy indicates that reduction of iron occurs with concomitant graphite oxidation. The production of graphite-glass samples using various powdered glass compositions by conventional sintering method still resulted in high porosity with an average of 6-17 % for graphite loadings of 20-25 wt%. Due to the use of pre-made glasses and controlled sintering parameters, the loss of graphite from the total mass is reduced compared to the microwaved samples; the average mass loss is < 0.8 %. The complication of iron oxidation and reduction is present in all the iron containing base glasses considered and this increases the total porosity of the graphite-glass samples. It is concluded that the presence of iron in the raw materials or base glasses as an encapsulation media for the immobilisation of the irradiated graphite waste is not advisable. The production of glass and graphite-glass samples based calcium aluminosilicate composition by spark plasma sintering method is found highly suitable for the immobilisation of irradiated graphite wastes. The advantages of the method includes short processing time *i.e.* < 40 minutes, improved sintering transport mechanisms, limited graphite oxidation, low porosity (1-4 %) and acceptable tensile strength (2-7 MPa). The most promising samples prepared using spark plasma sintering method were loaded with 30-50 wt% graphite.

Acknowledgements

I would like to express my heartfelt thanks to my supervisors, Prof. Russell J. Hand and Dr. Martin C. Stennett for their guidance, expertise and patience. Without their support and advice, the completion of this thesis would not have been possible. Many thanks to Prof. Neil C. Hyatt, Dr. Claire Corkhill and Dr. Hajime Kinoshita for their comments and suggestions to the research work, specifically for a challenging 2nd year group presentation. Prof WE (Bill) Lee is thanked for an insightful discussion and enjoyable viva.

I must thank all of the technical staff and students who have helped me to gather all the results for this thesis. Particularly, I would like to thank Ian P. Watts, Dr. Lisa Hollands and Dr. Sheng Heng Tan for helping with glass melting and sintering; Bev C. Lane and Ben G. Palmer for working late so the thermal analysis and density measurements could be completed out of hours; Dr. Nik Reeves-Mclaren for teaching me how to operate the XRDs and Raman spectroscopy; Dr. Peter Korgul and Dr. Le Ma for providing an excellent assistance during SEM observation; Michael Bell for helping with sample polishing and optical microscope observation; Dr. Jesus A. Gonzalez Rodriquez for taking time out of his busy schedules to teach me optical profilometer operation and Dean Haylock for an unlimited supply of crucibles and helping with tensile strength measurements. Special thanks to all ISL group members especially Mehul A. Chavda, Silvia Madeddu, James E. Vigor, Sebastian Lawson and Seddon Atkinson for keeping me entertained and spending time to listen to my writing issues.

I am grateful to the Ministry of Education Malaysia and the Universiti Tun Hussein Onn Malaysia for giving me an opportunity to further study in the University of Sheffield and for their generous financial support.

Most of all I would like to thank my parents for everything.

Published Work

Paper

Mayzan M Z H, Stennett M C, Hyatt N C and Hand R J 2014 Graphite immobilisation in iron phosphate glass composite materials produced by microwave and conventional sintering routes *J. Nucl. Mater.* **454** 343–51

Conferences

Mayzan M Z H, Stennett M C and Hand R J Glass Composite prepared by microwave heating for encapsulation of irradiated graphite waste *Society of Glass Tecnology - Living Glass Conference, 5-7th September 2012, University of Cambridge* (Oral presentation)

Mayzan M Z H, Stennett M C and Hand R J 2013 Microwave processing of glass composites for irradiated graphite waste immobilisation *23rd International Congress on Glass, 1-5th July 2013, Praha, Czech Republic* (Oral presentation)

Contents

Abstract ii

Acknowledgements iii

Published Work iv

1. Introduction 1

2. Literature Review and Theory 3

2.1. History, Current and Future Usage of Nuclear Technology 3

2.2. Commercial Nuclear Power Reactor 5

2.2.1. Main Components 7

2.3. Nuclear Wastes 10

2.3.1. High Level Waste 10

2.3.2. Intermediate Level Waste 11

2.3.3. Low Level Waste 12

2.4. Irradiated Graphite 13

2.4.1. Structure and Properties of Graphite 13

2.4.2. Production of Nuclear Graphite 16

2.4.3. Waste Origin and Volume 20

2.4.4. Radiation Effects on Graphite 21

2.4.5. Disposal Options and Challenge for the Waste Immobilisation 26

2.5. Processing Routes for the Immobilisation of Irradiated Graphite 28

2.5.1. Glass Materials 29

2.5.2. Microwave Processing 32

2.5.3. Cold Press Sintering Processing 33

2.5.4. Spark Plasma Sintering Processing 35

2.6. Summary 37

3. Materials and Experimental Methods 39

3.1. Introduction 39

3.2. Irradiated Graphite Waste Simulant 39
3.3. Microwave Processing 39
3.3.1. Experimental Setup 40
3.3.2. Sample Preparation 41
3.4. Conventional Processing 42
3.4.1. Batch Preparation 43
3.4.2. Glass Melting 43
3.4.3. Preparation of Powdered Glasses 45
3.4.4. Cold Press Sintering 46
3.5. Spark Plasma Sintering Processing 47
3.6. Particle Size Analysis 49
3.7. Thermogravimetric Analysis 51
3.8. Differential Thermal Analysis 51
3.9. Dilatometry 51
3.10. Chemical Analysis 52
3.11. Volume Shrinkage 53
3.12. Assessing Mass Loss 54
3.13. Density 54
3.14. Porosity 55
3.15. X-ray Diffraction 56
3.16. Fourier Transform Infrared Spectroscopy 57
3.17. Microscopy 59
3.18. Raman Spectroscopy 62
3.19. Mössbauer Spectroscopy 63
3.20. Indirect Tensile Testing – Brazilian Method 65

4. Results and Discussion I: Graphite Immobilisation in Iron Phosphate Glass Composite Materials Prepared using Microwave and Conventional Processing 67
4.1. Introduction 67
4.2. Characterisation of Graphite 67

4.2.1. Particle Size and Density 67
4.2.2. Effect of Heating under Air and Argon 68
4.2.3. XRD 69
4.2.4. FTIR 70
4.2.5. Microstructure and EDS Analysis 71
4.3. Characterisation of Iron Phosphate Base Glasses 75
4.3.1. Chemical and Physical Properties 75
4.3.2. XRD 76
4.3.3. FTIR 77
4.4. Characterisation of Iron Phosphate Glass Composites 78
4.4.1. Physical Properties 78
4.4.2. XRD 81
4.4.3. FTIR 82
4.4.4. Microstructure and EDS Analysis 83
4.5. Mössbauer Spectroscopy Analysis 88
4.6. Discussion 91
4.7. Summary 94

5. Results and Discussion II: The Production of Various Graphite-Glass Composites by CPS Method for the Immobilisation of Irradiated Graphite Waste 96
5.1. Introduction 96
5.2. Characterisation of Base Glasses 96
5.2.1. Chemical Composition and Physical Properties 97
5.2.2. XRD 99
5.2.3. FTIR Spectroscopy 100
5.2.4. Raman Spectroscopy 103
5.3. The Effects of Sintering Temperature on Graphite-glass Composites 107
5.3.1. Volume Shrinkage 108
5.3.2. Mass Loss 109
5.3.3. Density and Porosity 110

5.3.4. XRD 113
5.3.5. Optical Microscopy and Optical Profilometry 118
5.3.6. SEM and EDS 120
5.3.7. Mössbauer Spectroscopy 128
5.4. The Effects of Waste Loading on Graphite-glass Composites 130
5.4.1. Volume Shrinkage 131
5.4.2. Mass Loss 132
5.4.3. Density and Porosity 134
5.4.4. Indirect Tensile Testing 136
5.5. Discussion 137
5.6. Summary 142

6. Results and Discussion III: The Immobilisation of Simulant Irradiated Graphite in Calcium Aluminosilicate Glass Composites Using Spark Plasma Sintering 144
6.1. Introduction 144
6.2. Sintering Profile of SPS 144
6.3. Sintered CAS Glass Prepared using CPS and SPS Methods 146
6.3.1. Density and Porosity 146
6.3.2. XRD 147
6.3.3. Optical Microscopy 148
6.3.4. SEM and EDS 149
6.4. The Effect of Sintering Temperatures on CAS30G Composites 151
6.4.1. Density and Porosity 152
6.4.2. XRD 154
6.5. The Effect of Sintering Dwell Time on CAS30G Composites 155
6.5.1. Density and Porosity 155
6.5.2. XRD 157
6.6. Microstructural Analysis of CAS30G Composites 158
6.6.1. Optical Microscopy and Optical Profilometry 158
6.6.2. SEM and EDS 161

6.7. The Effect of Waste Loading on CAS Glass Composites 163
6.7.1. Density and Porosity 164
6.7.2. Indirect Tensile Testing 166
6.8. Discussion 167
6.9. Summary 171

7. Conclusions and Suggestions for Further Work 172
7.1. Introduction 172
7.2. Contamination of Graphite simulants in Graphite-glass Wasteforms 172
7.3. Graphite Immobilisation using Microwave Processing 173
7.4. Graphite Immobilisation in Various Glass Compositions by CPS 174
7.5. Graphite Immobilisation in CAS Glass Composites using SPS 176
7.6. Future Work and Recommendations 176

References 178
Appendix 194
A1 Density of Distilled Water at Various Temperatures 194

1. Introduction

The maintaining, decommissioning and dismantling of certain types of nuclear power plants used to generate electricity are mainly responsible for the production of problematic irradiated graphite wastes. Currently, the conditioning and disposal plan for the irradiated graphite waste remains unclear in all waste producing countries (*i.e.* UK, Russia, US, France). The major concern related to the irradiated graphite is the huge volume of the waste, which accounted worldwide about 260 000 tonnes and the present of long-lived radionuclides *i.e.* ^{3}H, ^{14}C, ^{16}Cl. Historically relative little attention has been given to identifying a disposal strategy for irradiated graphite waste. The irradiated graphite waste now urgently requires disposal management solutions and this triggered interest in studying immobilisation methods that may be suitable for the production of irradiated graphite wasteform based glass materials.

A survey of the literature reveals several potential immobilisation methods that may suitable for the production of graphite glass composite wasteforms. This leads to the novel aim of the thesis; to investigate the potential of glass materials as a host for the production of irradiated graphite wasteforms prepared using unconventional and conventional processing methods. The aim can be divided into three primary research objectives as follow:

i. To assess the potential of microwave processing method for the production of graphite wasteforms using iron phosphate glass.
ii. To explore and assess the potential of conventional sintering in the production of graphite wasteforms prepared using various glass systems as a host.
iii. To investigate the potential of spark plasma sintering method for the production of graphite wasteforms using calcium aluminosilicate glass.

In order to achieve the mentioned aim and objectives, the thesis is structured and organised into six further chapters including literature review and theory, materials and experimental methods, result and discussion I, result and discussion II, result and discussion III and finally conclusion and suggestions for further work. Chapter 2 provides the background of nuclear power reactors as a source of radioactive wastes and particular focus is given to irradiated graphite waste; the

structure, properties, waste origin and problems arising from the irradiated graphite waste are reviewed. Attention is also given to recognise the suitability and materials processing techniques of microwave, conventional sintering and spark plasma sintering for the production of graphite-glass wasteforms.

Chapter 3 presents a description of graphite simulant and details about immobilisation methods used and processing methods employed throughout the preparation of graphite-glass composite wasteforms. All the basic principles of the instruments and the materials characterisation techniques conducted on the produced samples are explained in detail. This includes a variety of analytical techniques used such as particle size analysis, thermogravimetric analysis, differential thermal analysis, dilatometry, chemical analysis, volume shrinkage, assessing mass loss, density, porosity, X-ray diffraction, fourier transform infrared spectroscopy, microscopy, Raman spectroscopy, Mössbauer spectroscopy and indirect tensile testing – Brazilian method.

Results and discussion are split into three chapters and structured accordingly to each of the research objectives. Chapter 4 gives the characterisation results of graphite simulant, iron phosphate glass and composite wasteforms prepared using microwave as well as a comparison of potential microwave samples with samples produced using conventional sintering. Findings from Chapter 4 lead to the development of Chapter 5, which discussed the use of various glass compositions as a host to encapsulate graphite simulant. The iron phosphate glass composition is used as a baseline in comparing with the results obtained using other glass compositions namely alumino-borosilicate, calcium aluminosilicate, modified alkali borosilicate and obsidian. Based on Chapter 4 and 5, Chapter 6 was developed and specifically focuses on the production of low porosity graphite-glass wasteforms using calcium aluminosilicate glass. The obtained data were compared with the sample produced using conventional sintering.

The key findings from the results and discussion chapters are summarised in Chapter 7. In this chapter, future works and recommendations are also presented as guidelines to identifying an ideal wasteform for the immobilisation of irradiated graphite waste.

2. Literature Review and Theory

2.1. History, Current and Future Usage of Nuclear Technology

In 1932, James Chadwick discovered the neutron (Chadwick 1932). The next year Enrico Fermi found a much greater variety of artificial radionuclides was formed when using neutrons instead of protons as a source for bombarding the atoms. The history of nuclear fission started at the end of 1938, when Otto Hahn and Fritz Strassmann attempted to create transuranic elements by bombarding uranium with neutrons. They expecting heavy elements, however, the product produced from the experiment were lighter elements including ^{141}Ba and others which were about half the mass of uranium. This result was interpreted by Lise Meitner and Otto Frisch working under Neil Bohr (Meitner and Frisch 1939); they suggested that the neutron was captured by nucleus and causing severe vibration leading to the nucleus splitting into two roughly equal parts which termed fission (essentially the fission of ^{235}U had occurred). In 1939, Otto Frisch successfully confirmed that the fission of ^{235}U yielded numerous amount of energy, ~200 MeV (Frisch 1939) and realised the potential of a fission chain reaction. This was the first experiment confirming the theory of Albert Einstein, which explained the equivalence between mass and energy, $E = mc^2$ (Einstein 1905).

Motivated from the neutron-induced fission, and thus potentiality of fission chain reaction to generate huge amounts of energy in a short time period, Enrico Fermi and co-worker developed the first man-made nuclear reactor (Chicago pile 1, originally known as 'atomic piles') with self sustaining nuclear fission chain reaction on 2 Dec 1942. The reactor utilised natural abundance of U, was graphite moderated, and controlled by a removable Cd neutron absorber; in order to achieve criticality (balance of neutrons for sustaining nuclear fission chain reaction), the crude reactor used 6 tonnes of uranium metal, 50 tonnes of uranium oxide and ~400 tonnes of graphite (Greenwood and Earnshaw 1997). It is unfortunate that the first nuclear reactor was purposely aimed to build nuclear weapons as part of Manhattan Project, evidenced in Trinity test explosion (16th July 1945) and controversial dropping of two atomic bombs to end World War II with Japan (6,9th August 1945). Nevertheless, it is evidence that graphite has been used in nuclear technology from the earliest days.

The new era of nuclear reactors used for generating electricity began in the 1950s and they have been improved ever since. The first nuclear reactor to generate electricity was built in a small scale by Argonne National laboratory, Idaho, USA in 1951. The reactor was called Experimental Breeder Reactor (EBR-1) and successfully powered four 100 W light bulbs. At present, more than 400 nuclear reactors are being used to generate electricity and the reference data of operated reactors connected to the grid at the end of 2013 is listed in Table 2-1. Note that the graphite is continuously used as moderator in current operated gas-cooled and light water graphite reactors.

Table 2-1: Nuclear power reactors in commercial operation, 31 Dec 2013 (IAEA 2014b).

Reactor type	Main countries	Number	GWe	Fuel	Coolant	Moderator
Pressurised Water Reactor (PWR)	US, Fance, Japan, Russia, China	273	253	Enriched UO_2	Water	Water
Boiling Water Reactor (BWR)	US, Japan, Sweeden	81	76	Enriched UO_2	Water	Water
Pressurised Heavy Water Reactor 'CANDU' (PHWR)	Canada	48	24	Natural UO_2	Heavy Water	Heavy Water
Gas-cooled Reactor (AGR, Magnox)	UK	15	8	Natural U metal, enriched UO_2	CO_2	Graphite
Light Water Graphite Reactor (RBMK, EGP)	Russia	15	10.2	Enriched UO_2	Water	Graphite
Fast Neutron Reactor (FBR)	Russia	2	0.6	PuO_2 and UO_2	Liquid Sodium	None
Total		434	~372			

The electricity supply from nuclear reactors worldwide is estimated to be about 11.3 % in 2013; the other types of energy sources generating electricity are estimated to contribute about 68.5,

17.8, and 2.4 % for thermal (solids, liquids, gasses, biomass and waste), hydro and renewable (geothermal, wind, solar, tide) energy respectively (IAEA 2014a). The use of nuclear power reactors to generate electricity is gaining attention as it makes significant contribution to the mitigation of green-house gas emissions *e.g.* in 2009, it was claimed that the nuclear power reactors reduced by about 10 % of CO_2 emission from the world energy consumption (Adamantiades and Kessides 2009, Menyah and Wolde-Rufael 2010). Furthermore the use of a small amount of fuel, improved design of reactor and reliable energy source making the nuclear reactors favourable technology among the others in terms of generating electricity.

It is clear that the global plan is to reduce the CO_2 emissions, minimise the green-house gases and consequently decrease the amount of manmade global warming. This means that the use of coal thermal power plan will be further reduced and to meet the demand for electricity consumption that keeps increasing (global energy demand is estimated to increase by ~37 % by 2040), the use of nuclear, hydro and renewable energy is being increased (IEA 2014b). It is also evidence in the past (from 1973-2012) that the total global electricity demand is increased from 9.4 to 18.1 % (IEA 2014a). As a result, more nuclear reactors are being built and are planned to be built in the future. In 2013 alone, 77 nuclear reactors were under construction and 48 of those reactors were located in Asia (IAEA 2013). This is the highest number of reactors being constructed since 1989 and the figure is more likely to increase in the future, which may account for ~17 % of the global electricity production in 2050 (OECD *et al* 2015). Furthermore generation IV nuclear reactors (expected to arrive in ~2030) such as prismatic and pebble bed designed High Temperature Gas-cooled Reactor (HTGR) also utilise graphite as a reactor core and fuel matrix – tristructural-isotropic (TRISO) fuel and fuel pebble (OECD Nuclear Energy Agency 2014). Thus one can predict that more irradiated graphite will be produced in the future.

2.2. Commercial Nuclear Power Reactor

Commercial nuclear power reactors generate electricity by converting thermal energy from nuclear fission reactions (heat generated from kinetic energy of fission products, absorption of gamma rays and radioactive decay from fission products) to mechanical energy. In principle, the process usually initiated by transferring heat to coolant and then water to produce high pressure

steam of which used to rotate the multiple blades in the turbine. The turbine is designed to minimise the energy lost and capable to condense the steam back into water so that the cycle could operate continuously. The kinetic energy created from the rotation of blades in the turbine is converted into electrical energy by a generator. Essentially, all the nuclear power reactors utilise similar concepts to generate electricity and schematics of the most popular commercial reactors to date is shown in Figure 2-1. Note that the turbine and generator parts of the reactors are not shown in the figure.

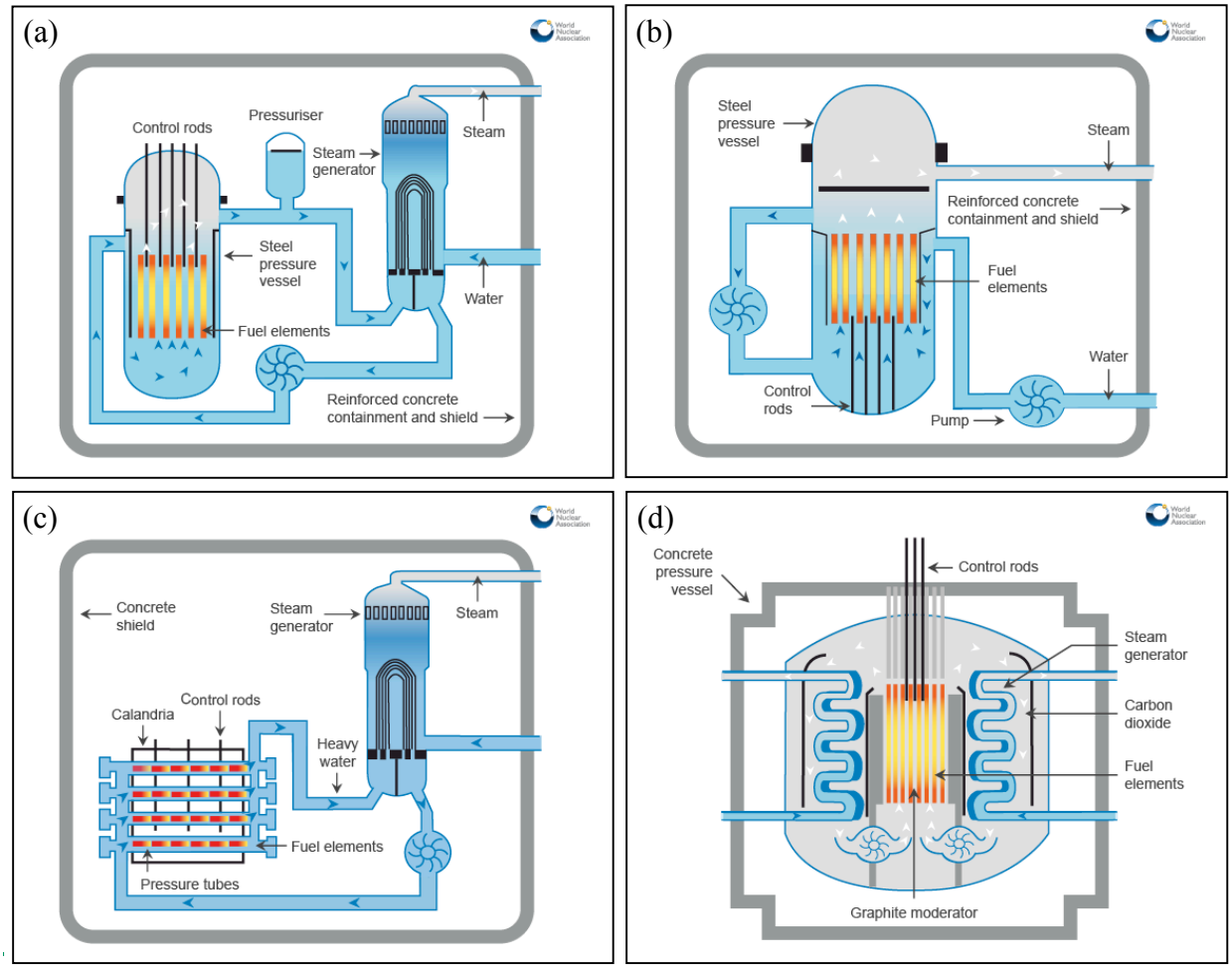

Figure 2-1: Schematic of currently used nuclear reactors, (a) PWR, (b) BWR, (c) PHWR/Candu and (d) AGR (taken from WNA 2015).

2.2.1. Main Components

The nuclear power reactors currently used for generating electricity can be categorised into 2 types: fast and thermal (slow) reactors. Unlike the explosion of nuclear weapons, nuclear power reactors are meant to control the nuclear fission activity and sustain the nuclear chain reaction as well as maintaining the production of electricity in a long term condition; the expectation of lifespan is ~30-40 years. As evidenced in Table 2-1, the use of fast reactors (FBR) is less favourable compared to the thermal reactors (PWR, BWR, PHWR, AGR, Magnox, RBMK, EGP). The reason behind this is solely because fast reactors are difficult to build and very expensive to operate, although fast reactors are capable of generating ~60 times energy than thermal reactors. In spite of both reactors are technically different, most of the reactors components are largely similar and can be simplified as follows (Duderstadt and Hamilton 1976, Wilson 1996, IAEA 2007, Stacey 2007, Lewis 2008):

Fuel (fissile element) – The main difference between both fast and thermal reactors are the types of fuels. A fast reactor usually employs enriched ^{239}Pu or enriched ^{235}U (require about 20-30% of fissile nuclei) core surrounded with ^{238}U (fissionable/fertile element) blanket. This type of reactor generates more fuel than it consumes; this occurs because ^{238}U has high probability to capture a fast neutron from the fission of ^{239}Pu or ^{235}U, neutrons induced by fission are then captured by ^{238}U and consequently breed ^{239}Pu as well as releasing two β-decays (Cochran *et al* 2010). The new generated ^{239}Pu radionuclides can later be utilised as new fuel in future reactors. In contrast, thermal reactor mainly uses natural uranium (contained ~0.7 ^{235}U) or enriched ^{235}U (up to 5 % of ^{235}U) fuel. Generally the fuel is fabricated into pellets, being vertically arranged/stacked in a cladding tube (*i.e.* zircaloy, stainless steel, Mg alloy) called fuel rod and numerous fuels rod form the fuel assembly that specifically designed to be lifted into and out of the reactor core. To start the nuclear fission reaction, a neutron is captured by a fissile nucleus and the reactions occurring from ^{235}U or ^{239}Pu are given in Equation 2-1 and 2-2 respectively. Note that Equation 2-1 and 2-2 are the fissions caused by the thermal neutron without considering the energy from neutrinos.

$$^{235}\mathrm{U} + \text{neutron} \rightarrow \text{fission fragments} + 2.4\,\text{neutrons (average)} + 192.9\ \text{MeV} \qquad [2\text{-}1]$$

$$^{239}\text{Pu} + \text{neutron} \rightarrow \text{fission fragments} + 2.9\,\text{neutrons (average)} + 198.5\ \text{MeV} \quad [2\text{-}2]$$

Moderator – In a fast nuclear reactor, the use of moderator is not necessary because the reactor utilises fast neutrons to cause fission in their fuel. Due to the low probability of fission versus neutron capture, the highly enriched fissile fuel is used to sustain the chain reaction. However, in the thermal reactors, the fast neutrons (resulting from fission) must be slowed by the moderator; as fast neutrons (kinetic energy ≥ 1 MeV) are most likely to be captured by ^{238}U, which is non-fissile. Only the thermal neutrons (kinetic energy < 1 eV) have a high cross-section (probability) to efficiently maintain and sustain the fission reaction of ^{235}U. Theoretically, the neutrons are slowed by collisions with nuclei of about similar mass and these materials are not neutron absorbers. The common moderators used to date are ordinary water and purified graphite as well as the most excellent one but expensive heavy water. For gas-cooled nuclear power reactors *i.e.* AGR and Magnox, purified graphite is the most suitable material and widely used as a moderator. In fact the voluminous irradiated graphite waste largely originates from moderator part of nuclear power plant.

Control Rod – The purpose of control rod is to maintain the rate of fission chain reaction, so that the nuclear power reactor achieves criticality and operates at a steady power level. To control the rate of fission reaction, neutron-absorbing materials whose nuclei absorb neutrons without undergoing any addition reaction, such as B, Cd or Hf are used for the production of control rods. The control rods are being inserted or withdrawn from the reactor core to control the number of the neutrons; absorbing more neutrons means that less neutrons are available for nuclear fission, thus inserting the control rod deeper into the reactor core will reduce the power output of the nuclear reactor and vice versa. The control rod is also used to halt the nuclear power reactor by absorbing all the neutrons to stop the fission reactions.

Coolant – Nuclear reactor coolant circulating around the reactor core and is primarily used to remove and transfer the heat energy from the core to generate steam. The coolant must be mobile in nature, hence only satisfied by liquid or gas materials. In fast reactors, the use of moderator type coolants (water, heavy water) is not possible as water can moderate the fast neutron. In addition, the more compact core of fast reactor produces high temperature that cause severe

cooling problems, thus a more efficient coolant such as liquid Na or Pb is used. In thermal reactors, ordinary water, heavy water (water usually pressurised to maintain at liquid phase) or CO_2 gas are commonly used as a coolant. All the thermal reactors except BWR type separate the cooling system from the water that will be boiled to produce high pressure steam.

Pressure Vessel or Protective vessel – Fast reactors do not utilised pressurised coolant, thus the protective vessel is used as containment for its coolant and reactor core. In the thermal reactors, a steel pressure vessel (PWR, BWR, AGR, Magnox) or pressure tubes (PHWR) is used to hold the circulated pressurised coolant as well as acting as containment for the moderator, control rods (except PHWR) and reactor core (see Figure 2-1). The pressure vessel/tube or protective vessel also worked as the first layer of shielding; preventing most of the radiation and radionuclides from leaching out to the biological environment. In some cases, a reflector is installed inside the vessel or surrounding the core to reflect the scattered neutrons back to the reactor core (Duderstadt and Hamilton 1976); this increases the efficiency of the fission of the fuel and at the same time protects the vessel from neutron induced damage which decreases the lifespan of the vessel. Characteristically, the reflector possesses similar properties to the moderator and sometimes similar materials serve a dual purpose in the nuclear power reactor. The most common material used as a reflector is graphite.

Steam Generator – This component is specifically designed as a heat exchanger, which converts water into steam. The steam generator is constructed separately in fast and thermal reactors. Only BWR (thermal reactor) boils the water in a pressurised vessel and directly uses steam generated in-situ by this process.

Containment and Shielding – The purpose of containment and shielding is to protect the atmosphere and biological environment from contamination by radionuclides and radiation as well as acting as a safety system if any malfunctions of the components occur inside the reactors. Nuclear reactors are a source of intense radiation and contain radioactively contaminated components/systems, the whole reactor apart from the turbine (excluding BWRs) must be isolated and shielded from the biological system. A BWR usually needs a complete containment and shielding due to the whole components including the turbine containing radioactive

materials. Typically, a metre thick reinforced concrete or steel/lead structure is used as containment and shielding in current commercial reactors.

Turbine and Generator – The turbine and generator are the key components to generate electricity from the nuclear energy and these components are being installed in all types of commercial nuclear reactors. In practice, the high pressure steam turns the turbine and the generator converts the produced mechanical energy to electrical energy by using an electromagnetic field. The produced electrical energy is then manipulated by the transformers, connected to the grid and supplied to the consumers.

2.3. Nuclear Wastes

Nuclear power reactors are a mature technology and have been proven safe while generating reasonably clean electrical energy. The drawback of using nuclear power reactor is the fact that the nuclear reactor creates significant amount of radioactive waste from the fission process. The decay process of the waste emitting α, β and γ radiation can take up to millions of years. This is problematic as within this time period the nuclear wastes must be isolated from biosphere; the migration of the radioactive materials to the biosphere causes adverse effects and is highly hazardous to all biological systems/organisms. Therefore the nuclear waste must be treated with an appropriate fashion, stored in properly engineered storage facility and must not impose undue burden for future generations (IAEA 2011). The classification of the nuclear waste depends on the waste management policy of each waste producing country, typically taking account of the radiation levels, decay activity and disposal issues. In this study, the classification of the waste, characterisation and the waste disposal management will be based on the current UK regulations and policies. The radioactive wastes in the UK are divided into three categories and the details are as follows:

2.3.1. High Level Waste

High Level Waste (HLW) is defined as waste "in which the temperature may rise significantly as a result of their radioactivity, so that this factor has to be taken into account in designing storage

or disposal facilities" (Her Majesty's Stationery Office 1995). Within the UK, HLW mainly existed in liquid form and is a by-product from the reprocessing of spent nuclear fuel; the process is carried out at Sellafield and will continue until 2018 (NDA and DECC 2013). Due to the heat generated and very high radiation levels, the HLW liquid requires continuous engineered cooling and substantial shielding. In order to increase the efficiency of the nuclear fuel cycle, the spent nuclear fuel reprocessing is aimed at recovering/extracting the (re-)usable uranium and plutonium. The extracted uranium and plutonium are later being recycled for the production of new fuel called mixed oxide (MOX) fuel. For immobilisation, the HLW liquid is calcined to become solid, mixed with alkali borosilicate glass frit and is converted into homogeneous glass by a vitrification process, poured into a stainless steel canister after which a lid is welded onto it (~150 litre capacity) and stored in an engineered air-cooled facility at Sellafield for at least 50 years to allow the reduction of radioactivity by natural decay processes; the current plan for final disposal of the HLW canisters is long term disposal in a geological disposal facility (Ojovan and Lee 2005, CoRWM 2006, Defra *et al* 2008, NDA 2009, DECC 2014).

2.3.2. Intermediate Level Waste

Intermediate Level Waste (ILW) is defined as waste "with radioactivity levels exceeding the upper boundaries for low level wastes, but which do not require heating to be taken into account in the design of storage or disposal facilities" (Her Majesty's Stationery Office 1995). The ILW may contain very long half live radionuclides, in particular, alpha emitting radionuclides and can require significant shielding during disposal process and storage (CoRWM 2006). Essentially, ILW comprises a wider range of materials than HLW and the major constituents of the waste include fuel cladding, irradiated graphite (see Section 2-4), contaminated reactor components and sludge from the treatment of radioactive liquid effluents. Typical treatment for ILW is cement encapsulation, packaged in 500 litre or higher volume containers manufactured from stainless steel, iron or concrete and temporarily stored in interim ILW storage at Berkeley, Bradwell, Hinkley Point A and Sizewell A; the final disposal plan of the ILW will be similar to the HLW namely in a geological disposal facility but not located in similar vault (Ojovan and Lee 2005, Lee *et al* 2013, Magnox and NDA 2013, DECC 2014).

2.3.3. Low Level Waste

Low Level Waste (LLW) is defined as "radioactive waste having a radioactive content not exceeding 4 GBq per tonne of alpha or 12 GBq per tonne of beta/gamma activity"; a sub-category of LLW is Very Low Level Waste (VLLW), which is split into two groups according to the specific disposal method as follows (Defra *et al* 2007):

- Low volume VLLW (dustbin loads) – Defined as "radioactive waste which can be safely disposed of in an unspecified destination with municipal, commercial or industry waste (dustbin disposal), each 0.1 m^3 of waste containing less than 400 kBq of total activity or single item containing less than 40 kBq of total activity". With respect to VLLW that contains ^{14}C and ^{3}H, the activity limits from both radionuclides is 4000 and 400 kBq in each 0.1 m^3 and for any single item respectively. No controls on disposal are needed when removing these wastes from premises to a disposal site.
- High volume VLLW (bulk disposals) – Defined as "radioactive waste with maximum concentration of 4 MBq per tonne of total activity which can be disposed of to specified landfill sites". The concentration limit for waste containing ^{3}H is 40 MBq per tonne. Controls on disposal specified by the environmental regulators are required when removing these wastes from premises to a disposal site.

In general, LLW and VLLW are materials that are lightly contaminated with radionuclides or materials that have been used in environment where radioactive materials are present. The volume of the wastes commonly arises from soil, metal components, building rubble, plastic, paper, protective clothing and laboratory equipment (Lee *et al* 2013). Since 1995, the LLW has been compacted in steel drums, stacked into larger containers, cement grouted and finally stored/disposed in an engineered concrete vault near Drigg, Cumbria (NDA 2010, 2011). The VLLW is either incinerated or undergoes controlled landfill disposal according to the aforementioned waste classification.

2.4. Irradiated Graphite

Irradiated graphite is a problematic waste resulting from the long term exposure of nuclear grade graphite or purified graphite to neutrons and mainly originates from gas-cooled nuclear power reactors. Currently, all the irradiated graphite waste producing countries have raised significant concerns about the management and disposal routes for the irradiated graphite waste. It is also worth mentioning that at present, there is no ideal solution for the final disposal of irradiated graphite (IAEA 2006, 2010). In addition, the complexity of irradiated graphite waste usually makes the handling (dismantling during decommissioning), transportation and waste packages challenging. Although the literature on the immobilisation of irradiated graphite waste is limited at the time being, in this section, it is intended to discuss the available literature about nuclear graphite, which includes the structure and properties of graphite, production of nuclear graphite, waste origin and volume, radiation effects on graphite and finally challenges for its waste immobilisation and disposal.

2.4.1. Structure and Properties of Graphite

Graphite is a crystalline allotrope of carbon that is made up from stacks of parallel aromatic or graphene layers. Each sp^2 hybridised carbon atom in the graphene layer plane is bonded with three other similar carbon atoms to form a series of continuous hexagons in a network (infinite two-dimensional molecule). There are 2 types of bonds present in the graphene layer; (i) sigma bond (covalent) between each carbon atom in the hexagon structure, the bond length is 0.141 nm and it has a high strength of 524 kJ/mole; (ii) π-bond (van der Waals) from the hybridised fourth valence electron located perpendicular to the graphene layer plane paired with another delocalised electron from the adjacent graphene layer plane, the spacing between the graphene layer plane is 0.335 nm (twice the van der Waals radius of carbon) and it has a low strength of 7 kJ/mole (Kelly 1981, Pierson 1993, Burchell 1999). The weak van der Waals bonds explains the soft characteristic of graphite which in general easily shears (cleaves) when force is applied. In nature, there are two known structures of graphite formed by different graphene staking sequences; -ABABAB- stacking for hexagonal graphite and -ABCABCABC- stacking for rhombohedral graphite (see Figure 2-2 and 2-3).

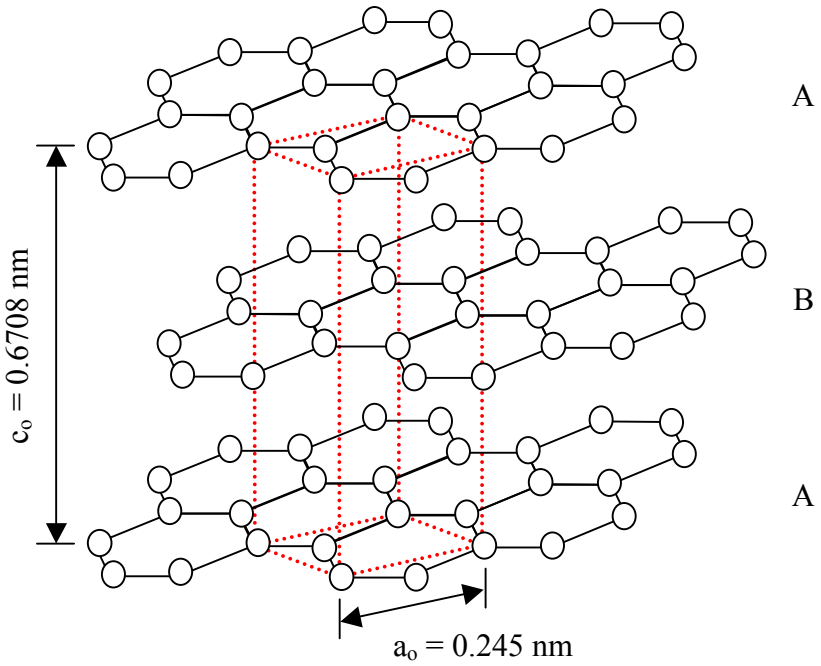

Figure 2-2: Hexagonal unit cell of graphite, space group: $D_{6h}^{4} - P6_3/mmc$ (Pierson 1993).

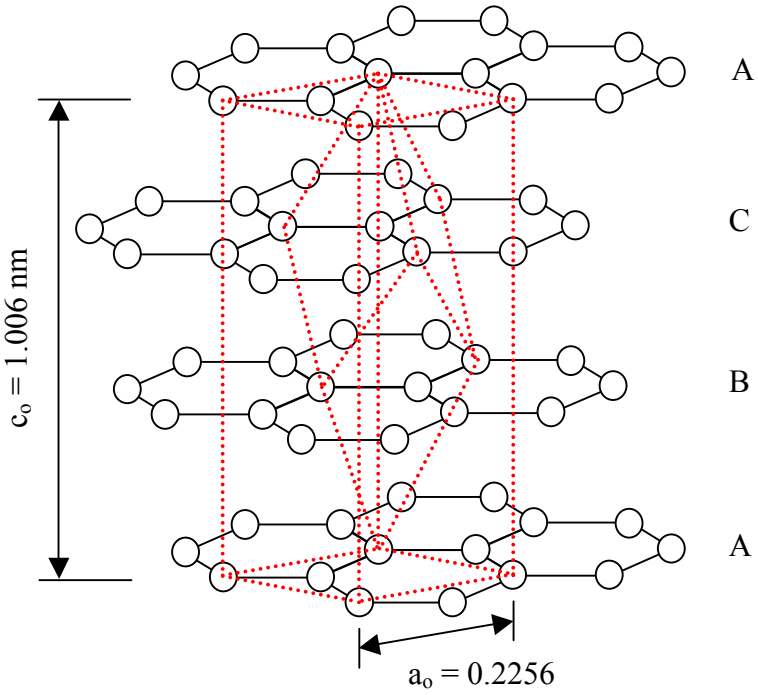

Figure 2-3: Rhombohedral unit cell of graphite, space group: $D_{3d}^{5} - R\bar{3}m$ (Reynolds 1968).

The hexagonal (alpha) structure of the graphite is thermodynamically stable and it is the commonest structure. In contrast, the rhombohedral (beta) graphite structure is thermodynamically unstable and the form is best known as an extended stacking fault of hexagonal graphite. The rhombohedral graphite is never found in the pure form and always exists in combination with hexagonal graphite. Normally natural and synthetic graphites contain a proportion of rhombohedrally structured material of which the amount found is typically less than 40 % (Pierson 1993, IAEA 2000). It is worthy of note that the content of rhombohedral graphite can be increased by grinding (shear deformation) and can also revert progressively to hexagonal graphite by heat treatment above 1300°C (Pierson 1993, IUPAC 1997).

As mentioned previously, graphite is used in the nuclear industry due to its capability to reduce the kinetic energy of fission neutrons by collisions (moderator in Section 2.2.1) and it has a low neutron cross-section *i.e.* the value is around 3.5-3.8 mb for pure nuclear graphite (Nightingale 1963). In addition, the properties of graphite such as being strong enough for structural components (produced by extrusion or vibration moulding or isostatic pressing), having good machinability, being stable and certified as one of the most inert materials make it highly attractive as well as suitable for many nuclear applications. The detailed properties of graphite can be seen in Tables 2-2 and 2-3; note that all the properties are based on the ideal graphite structure in powder form.

Table 2-2: Physical properties of graphite (Kelly 1981, Pierson 1993, Burchell 1999).

Property	Description
Colour	Black
Lattice parameters	See Figure 2-2
Atomic volume	5.315 cm^3/mol
Theoretical density (300 K, 1 atm)	2.26 g/cm^3
Melting point (estimated)	4450 K

Table 2-3: Thermal, electrical, mechanical and chemical properties of graphite (Kelly 1981, Pierson 1993, Burchell 1999).

Property	Description
Thermal	
Specific heat (at 25°C)	0.690-0.719 kJ/kg·K
Average thermal conductivity (at 25°C)	*ab* directions = 398 W/m·K, *c* direction = 2.2 W/m·K
Electrical	
Resistivity	*ab* directions = 2.5-5.0 × 10^{-6} ohm.m, *c* direction = 3000 × 10^{-6} ohm.m
Mechanical	
Bulk Modulus	286 GPa
Young's modulus	*ab* directions = 1020 GPa, *c* direction = 36.3 GPa
Chemical	
Low chemical resistance on these elements	Liquefied – air, F_2, He, H_2, methane, N_2, O_2. Oxidising – Begins in air at 350-400°C – F_2, N_2O_4, O_2 above 150°C – Steam above 300°C

2.4.2. Production of Nuclear Graphite

Nuclear power reactors utilised highly purified synthetic polycrystalline graphite and the processing steps for the production of this material are shown in Figure 2-4. Basically, nuclear graphite is produced using a carbonaceous filler and carbonised binder by thermal, mechanical and chemical treatments. Special attention is given to producing a high degree of crystallinity, low porosity and high purity of the end product. The filler material can be petroleum coke, metallurgical coke, anthracite or lampblack, however, petroleum coke is the most common raw material used as it is cheap (considering tonnage quantities required) and can achieve a higher degree of crystallinity compared to the other mentioned materials. For the carbonised binder, coal-tar pitch (by-product of metallurgical coke production) is the material of choice as it has all the required properties such as being a good thermoplastic material, having high carbon content (~93 %), high specific gravity (1.3 g/cm^3) as well as being relatively inexpensive from the tonnage quantity point of view.

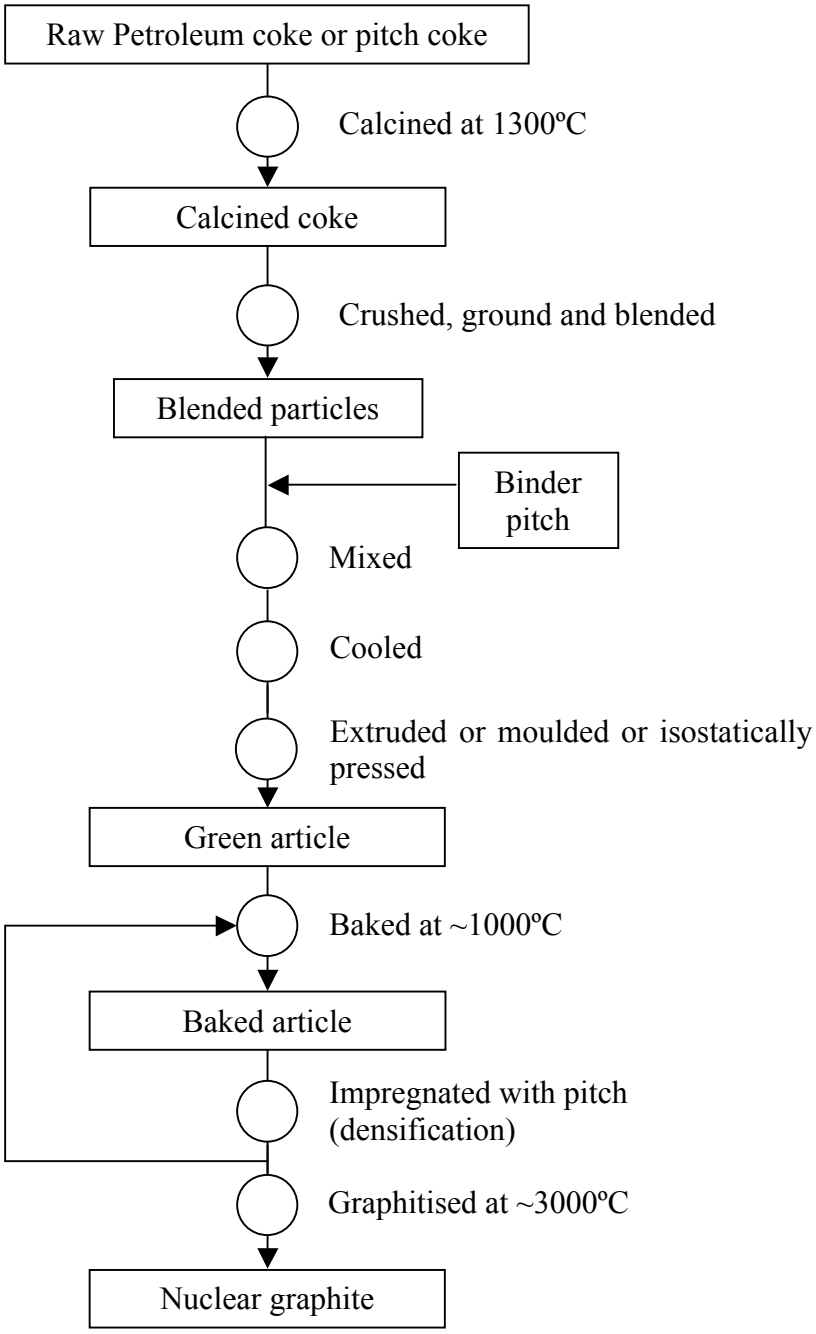

Figure 2-4: Flow diagram showing the manufacturing process of nuclear graphite (Nightingale 1963, Pierson 1993, Burchell 1999, Windes *et al* 2007).

In the production of nuclear graphite, calcined petroleum coke is mixed with coal-tar pitch and sometimes additives are added *i.e.* furnace blacks, fine coke particles (< 10 μm) or extrusion oil which are added accordingly to the forming technique used, for example extrusion, vibration

moulding or cold isostatic pressing. The amounts of petroleum coke and coal-tar pitch are usually about 70 wt % and 30 wt % respectively. The produced green articles are baked at ~1000°C (carbonisation) and impregnated with petroleum pitch several times (2-6) to increase strength and density of the bulk materials (Burchell 1999). The pre-treated bulk material is then graphitised at ~3000°C to form hexagonal graphite that closely matches the ideal hexagonal graphite structure. During graphitisation, chemical purification is carried out using cleaning agents (*i.e.* chlorine, fluorine, sodium fluoride, magnesium fluoride) and essentially heat treated in a halogen atmosphere. It is well known that halogen gases are capable of penetrating the pore structure of graphite, reacts with the impurities (neutron absorbing elements *i.e.* aluminium, boron, calcium, iron, silicon, vanadium, titanium) and vaporises as volatile halide salts. In the past (~1960), both chlorine and Freon gases were used to purify the graphite and in order to remove the residual chlorine from the graphite pore structures, the system was flushed with nitrogen or inert gas (Nightingale 1963). There is no clear information on any other gases used to flush the system, however the use of nitrogen is questionable as nitrogen will increase the production of ^{14}C (see Section 2.4.4). It should be stressed that the residual impurities from the graphite and purification process also lead to the creation of problematic radionuclides. Due to the different raw materials, manufacturing and purification processes used, the properties of nuclear graphite are in general not similar as shown in Table 2-4; see also Table 2-5 for the chemical impurities detected in AGR and Magnox nuclear graphite.

Table 2-4: Characteristics of nuclear graphite (Lim *et al* 2008, Béghein *et al* 2012).

Parameter	Grade of nuclear graphite		
	IG-11	NBG-17	NBG-18
Raw material	Petroleum coke	Pitch coke	Pitch coke
Forming technique	Isostatic pressing	Vibration moulding	Vibration moulding
Bulk density (g/cm^3)	1.77	1.89	1.85
Impurity (ppm)	Ash = < 20 B = 1.4 Si = 0.7 Ti = 0.6 V = 0.23 Na, Al, K, Ca, Cr, Mn, Fe, Cu, Ni = < 0.1	Ash = 180 B = 0.9 Cl = < 10 U = < 0.13 Th = < 0.05	Ash = 180 B = 0.9 Cl = < 10 U = < 0.13 Th = < 0.05

Table 2-5: Impurities detected in Magnox and AGR nuclear graphite (White *et al* 1984).

Element	Magnox (ppm)	AGR (ppm)
B	0.1	0.5
N	10	10
Na	1.0	4.0
Mg	0.1	0.4
Al	1.0	4.0
Si	35	35
S	50	60
Cl	2.0	4.0
Ca	35	25
Ti	3	0.7
V	12	0.4
Cr	0.35	0.4
Mn	0.04	0.25
Fe	10	28
Co	0.02	0.70
Ni	1.0	6.0
Zn	0.13	1.0
Sr	0.4	0.4
Mo	0.1	2.5
Sn	0.05	1.0
Ba	1.5	0.5
W	0.12	0.15
Pb	0.12	0.8
Li, Be, Ag, Cd, In, Sm, Eu, Gd, Dy, Bi	< 0.1	< 0.1

The microstructure of Magnox and AGR nuclear graphite is illustrated in Figure 2-5. Essentially, the microstructure of nuclear grade graphite is largely dependent on the characteristic of filler material and forming process used in the production stage. Pile grade A (PGA) graphite utilised in Magnox nuclear reactors is produced using filler particles derived from the petroleum industry and formed using an extrusion technique. This type of filler particles tends to have an elongated, needle-like shape that preferentially aligns with the extrusion axis (Figure 2-5a). As the crystallites within the filler particles were also preferentially aligned, the bulk PGA graphite had anisotropic material properties. Gilsocarbon (GIL), on the other hand, is the type of nuclear grade graphite used in AGR nuclear reactors. The GIL graphite is manufactured using Gilsonite,

(naturally occurs in USA asphalt mine) as a filler material and formed by moulding technique. The coke prepared from Gilsonite produced spherical, onion-like grains, which had no preferential alignment to the forming process (Figure 2-5b). Thus the crystallites within the particles tended to align circumferentially leading to the production of bulk material with near isotropic behaviour.

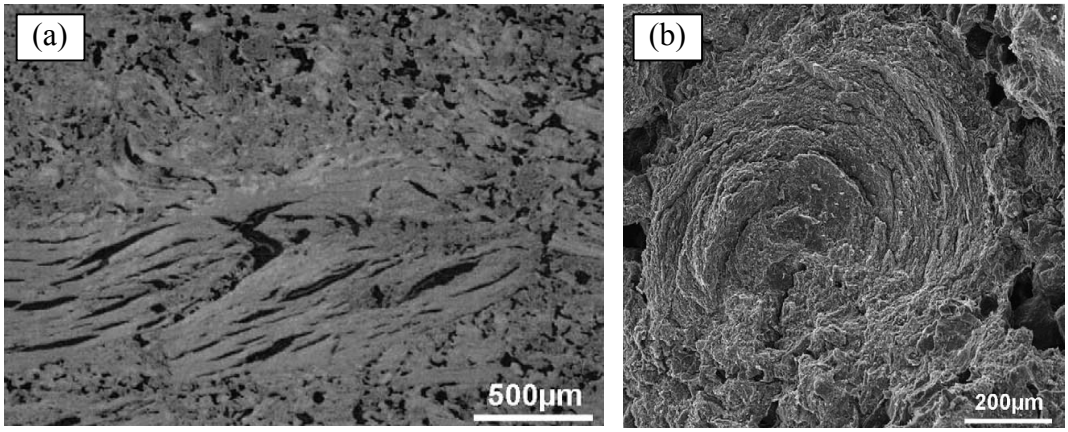

Figure 2-5: Optical micrographs of nuclear grade graphite, (a) PGA graphite used in Magnox nuclear reactors, (b) GIL graphite used in AGR nuclear reactors (Hall *et al* 2006).

2.4.3. Waste Origin and Volume

As mentioned above nuclear graphite has been widely used in the past for the construction of various components in certain types of nuclear power reactors, for *e.g.* gas-cooled reactors and light water graphite reactors. The decommissioning and dismantling of these types of nuclear reactors consequently leads to irradiated graphite waste. This waste mostly originates from the moderator and reflector components as well as other minor applications such as fuel-channel sleeve, thermal column, fuel matrix and control rod materials (Nightingale 1963, IAEA 2006, 2010). At present, the huge volume of irradiated graphite waste has drawn significant attention and concern in all nuclear member countries. Approximately 260 000 tonnes of irradiated graphite waste requires an appropriate disposal decision and the volume identified in each waste producing country can be viewed in Figure 2-6. As can be seen in the pie chart, it is obvious that

the UK is the major contributor of irradiated graphite waste, followed by Russia, US, France and other minor contributors. This reflects the design of nuclear power reactors which utilise significant amounts of nuclear graphite. The main types of nuclear power reactors that are responsible for such volumes of irradiated graphite waste are as follows: UK – advanced gas-cooled reactor (AGR), magnesium alloy graphite moderated gas-cooled uranium oxide reactor (Magnox), Russia – "reaktor bolshoy moshchnosti kanalniy" reactor (RBMK), US – high-temperature gas-cooled reactor (HTGR), light water graphite reactor (LWGR), France – "uranium naturel graphite gaz" reactor (UNGG).

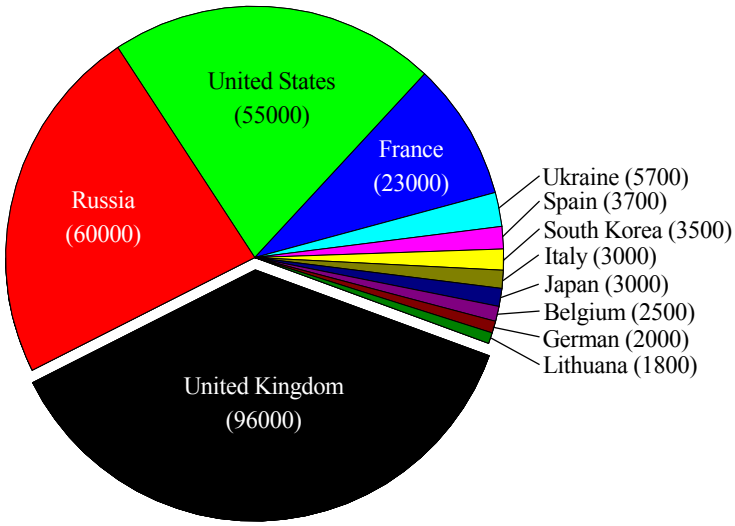

Figure 2-6: Estimated volume of irradiated graphite (IAEA 2006, 2010, Fachinger 2012), numbers are in tonnes.

2.4.4. Radiation Effects on Graphite

The effects of radiation on nuclear graphite are important in order to understand the properties of irradiated graphite waste; the knowledge will help to outline an ideal waste management strategy for its long term disposal. However the effects of radiation on nuclear graphite, be it the alteration of physical or chemical properties greatly depend on the initial properties and the treatments in the nuclear reactor. This is complicated as several nuclear graphite grades were

used for different applications resulting in different irradiation behaviours (Burchell *et al* 1992, Goodwin *et al* 2014). To simplify, the effects of radiation on nuclear graphite are explained in rather general terms by considering the effect of fast and slow neutrons which may occur in all grades of nuclear graphite.

Effects of fast neutrons – The use of nuclear graphite is purposely to reduce the kinetic energy of and/or reflect fast neutrons by elastic collisions. This elastic collision phenomenon results in structural alterations reducing the physical and mechanical properties of the original nuclear graphite (Kelly and Burchell 1994, Banhart 1999, Burchell and Snead 2007, Telling and Heggie 2007). For example, when a fast neutron (energetic particle) collides with an equilibrium graphite atom, the graphite atom will displace and create a cascade of displacements; a single neutron collides with multiple carbon atoms. The displaced carbon atoms recoil through the graphite lattice, displacing other carbon atoms and creating vacant lattice sites. Additionally, if the collisions happen in close proximity, clusters of point defects may occur (Telling and Heggie 2007). The displaced carbon atoms easily diffuse between the graphite layers and a proportion of these displaced carbon atoms will recombine immediately with the lattice vacancies (extremely dependent on the neutron flux and radiation temperature). This consequently creates a new graphite plane in so called dislocation loops or interstitial agglomerates (see Figure 2-7).

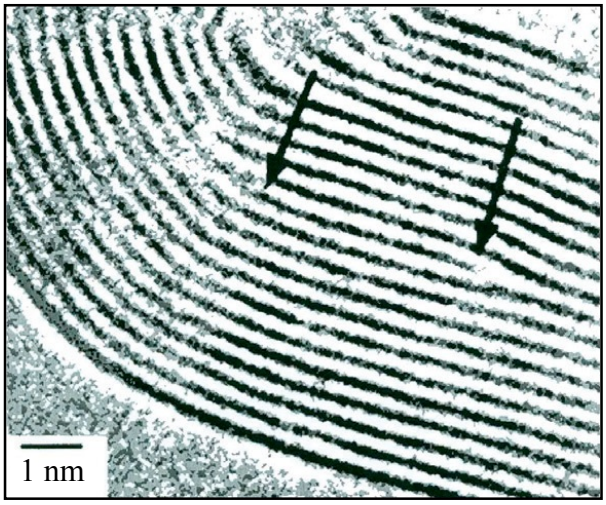

Figure 2-7: A dislocation loop between the graphitic nanoparticle basal planes (taken from Banhart 1999).

The interstitial clusters are less mobile than the vacancies and on further irradiation can be destroyed by fast neutron and/or carbon knock on atoms (irradiation annealing). The adjacent lattice vacancies in the same graphite layer may collapse towards the graphite layer and potentially form sinks for other vacancies, hence no longer able to recombine with and annihilate interstitials (Burchell 2012). It should be noted that this classical dislocation theory considers a simple situation that works on perfect parallel basal planes whereas in practice the graphite structure is far more complicated. As a result, more research needs to be carried out to understand the radiation damage in nuclear graphite *i.e.* taking account the displaced carbon atoms bridging to adjacent graphite planes and buckling as well as shearing effect of the graphite layers (Heggie *et al* 2011). Nevertheless, it has been shown that the displacement process altered the structure of original nuclear graphite leading to lower strength, making the graphite brittle with increased porosity and changed dimensions (swelling) and thus complicating the dismantling and handling during decommissioning process.

Another complicated phenomena occurring as a result of the displacement of carbon atoms by neutrons is the potential release of Wigner energy. Poor understanding of the effect of Wigner energy led to the Windscale pile 1 accident on 10th October 1957. Essentially, Wigner energy is the excess energy stored due to the presence of interstitial carbon atoms in non-ideal positions. This energy could be released when an interstitial carbon atom and a lattice vacancy recombine, or interplanar bonds are broken. The increase of stored Wigner energy only occurs with low temperature graphite radiation, < 250°C (IAEA 2000, 2006). This energy can be released violently as heat when the irradiated graphite is heated/annealed at 50°C above its initial irradiation temperature. Studies have demonstrated that the temperature rise during the release of Wigner energy could be as high as 1400°C (Rappeneau *et al* 1966). The effect of Wigner energy in nuclear reactors that are operated above 300°C is negligible as the stored energy is released slowly during operation (Burchell 2012). Due to the potential release of a huge amount of energy leading to a fire hazard, care must be taken when dealing with irradiated graphite that originated from low temperature (< 250°C) nuclear reactors.

Effects of slow neutrons – The creation of problematic radionuclides in irradiated graphite wastes results from slow neutron activation of carbon atoms and various impurities that are

present in both nuclear graphite and nuclear reactors. The main radioactive isotopes that usually are of concern in irradiated graphite are ^{3}H, ^{14}C and ^{36}Cl (Brown *et al* 1999, IAEA 2004, Podruzhina 2004, Pichon *et al* 2008). The characteristic and activation reactions of these radioisotopes by impurities, which induce neutron capture cross-section are shown in Table 2-6.

Table 2-6: Characteristic and activation reactions of ^{3}H, ^{14}C and ^{36}Cl. Thermal neutron cross section data (Mughabghab *et al* 1981, Haynes 2014).

Radionuclide (half-life)	Activation reaction	Origin (natural abundance %)	Thermal neutron cross section (barn)
^{3}H (12.3 years)	$^{235}U(n,f)^{3}H$	Fission reaction of fuel (0.7204)	586
	$^{6}Li(n,\alpha)^{3}H$	Li impurity in graphite (7.59)	940
	$^{3}He(n,p)^{3}H$	He coolant (0.000134)	5330
	$^{10}B(n,2\alpha)^{3}H$	Control rod (19.9)	3840
^{14}C (5670 years)	$^{14}N(n,p)^{14}C$	Air in graphite (99.636)	1.93
	$^{13}C(n,\gamma)^{14}C$	Graphite, coolant, fuel (1.07)	0.0014
	$^{17}O(n,\alpha)^{14}C$	Air in graphite, coolant, fuel (0.038)	0.257
^{36}Cl (308000 years)	$^{35}Cl(n,\gamma)^{36}Cl$	Cl impurity in graphite – purification process (75.76)	43.7

Other minor contamination from graphite impurities, nuclear reactor components (impurities in coolant, metallic elements) and fission products may also be present in irradiated graphite, *e.g.* ^{60}Co, ^{55}Fe, ^{63}Ni (IAEA 2010). However this is very dependent on the origin of the nuclear graphite and the treatments given in the nuclear reactors. It should also be highlighted here that no two irradiated graphite wastes have identical (some may be similar) chemical properties or radionuclide species (see example in Table 2-7). These complexities are due to the different raw materials used to manufacture nuclear graphite, the range of chemicals used in the purification process and the various applications of nuclear graphite leading to different contamination. The presence of various radioactive isotopes in the irradiated graphite is a significant challenge in the nuclear industry, especially for the dismantling of nuclear reactors and the prevention of the radionuclides leaching out to the biosphere. Furthermore, these processes may require some

radiation shielding to protect the operators from being irradiated by the harmful radionuclides. The dismantling process must be carefully considered and aim at not accidently releasing the radionuclides to the environment. The irradiated graphite waste should be treated properly and the disposal options as well as the challenges for the immobilisation of irradiated graphite waste are summarised in Section 2.4.5.

Table 2-7: Radionuclide inventory of various irradiated graphite wastes.

Nuclide	German, AVR (Fachinger *et al* 2008, Vulpius *et al* 2013)		Spain, UNGG (Márquez *et al* 2011)		France, UNGG (Guiroy 1995)	UK, gas-cooled (White *et al* 1984)
			Vandellós I		Marcoule G3	Magnox
	Reflector (Bq/g)	Fuel matrix (Bq/g)	Fuel sleeve (Bq/g)	Moderator (Bq/g)	Moderator (Bq/g)	Moderator (Bq/g)
^{3}H	8.84×10^{5}	3.2×10^{5}	8.93×10^{4}	2.75×10^{5}	2.9×10^{5}	5.37×10^{4}
^{14}C	9.50×10^{4}	5.7×10^{3}	1.35×10^{4}	5.62×10^{4}	2.4×10^{5}	3.81×10^{4}
^{36}Cl	-	-	-	-	1.4×10^{3}	9.5×10^{2}
^{60}Co	2.70×10^{4}	1.9×10^{2}	4.00×10^{4}	1.34×10^{4}	3.0×10^{3}	4.25×10^{4}
^{90}Sr	-	9.5×10^{3}	-	-	-	-
^{137}Cs	1.94×10^{3}	1.2×10^{4}	3.79×10^{2}	-	6.6×10^{1}	-
^{133}Ba	-	4.9×10^{1}	-	-	6.3×10^{1}	2.51×10^{2}
^{152}Eu	-	2.0×10^{2}	-	-	-	9.85×10^{1}
^{154}Eu	5.60×10^{2}	1.7×10^{2}	4.35×10^{2}	-	3.1×10^{2}	2.33×10^{3}
^{155}Eu	-		-	-	8.5×10^{1}	7.17×10^{2}
^{55}Fe	-	-	2.70×10^{4}	9.15×10^{3}	-	6.72×10^{3}
^{59}Ni	-	-	6.25×10^{2}	-	-	4.16×10^{1}
^{63}Ni	-	-	5.88×10^{4}	8.77×10^{3}	4.1×10^{3}	5.82×10^{3}
^{241}Pu	-	-	6.82×10^{2}	6.89×10^{2}	-	-
^{93m}Nb	-	-	-	-	-	2.46×10^{-1}
^{10}Be	-	-	-	-	-	3.18×10^{1}
^{41}Ca	-	-	-	-	-	3.27×10^{2}
^{54}Mn	-	-	-	-	-	1.21×10^{-1}
^{65}Zn	-	-	-	-	-	9.40×10^{-2}
^{93}Mo	-	-	-	-	-	3.81×10^{-1}
^{94}Nb	-	-	-	-	-	4.48×10^{-5}
^{99}Tc	-	-	-	-	-	7.61×10^{-2}
^{108m}Ag	-	-	-	-	-	1.03×10^{1}
^{113m}Cd	-	-	-	-	-	4.48
^{121m}Sn	-	-	-	-	-	2.01×10^{1}

2.4.5. Disposal Options and Challenge for the Waste Immobilisation

Due to the presence of long-lived radionuclides (^{3}H, ^{14}C, ^{36}Cl) and complicated contamination, irradiated graphite is classified as ILW in the UK and recognised as long-lived LLW in France (IAEA 2010). Historically, several methods have been considered for the disposal of irradiated graphite waste. These include land dumping (on surface), supervised interim storage (see Section 2.3.2), sea dumping (White *et al* 1984), incineration (Guiroy 1995) and in a geological disposal facility. In the UK, on surface disposal, sea dumping and incineration of the irradiated waste is strictly forbidden (Wickham *et al* 1999). This is solely due to the concern of releasing the long-lived radionuclides namely ^{3}H, ^{14}C and ^{36}Cl to the biosphere. This trio of radionuclides are highly biocompatible elements which readily and rather easily react with water and/or organic species. For example, the organic ^{14}C can transform to $^{14}CO_2$ and $^{14}CH_4$ through microbial degradation reactions (Yim and Caron 2006). The produced contamination ^{14}C gases consequently will deplete the radionuclide inventory of the irradiated graphite via the groundwater pathway. The ^{3}H (T) and ^{36}Cl species can potentially react with water (sea water, vapour or groundwater) according to the reactions shown in Equations 2-3 and 2-4 respectively. Thus on surface and sea dumping disposal are not an option as these methods pose risk to the biosphere; radionuclide contaminated food chains are highly hazardous to biological organisms hence strictly unacceptable.

$$HT + H_2O \xrightarrow{RT} HTO + H_2 \qquad [2\text{-}3]$$

$$^{36}Cl_2 + H_2O \xrightarrow{RT} H^{36}ClO + H^{36}Cl \qquad [2\text{-}4]$$

France and Russia are the leading countries that have suggested the incineration method for the disposal of irradiated graphite waste; pilot plants have been built and preliminary studies on the release of radionuclides especially ^{14}C, looking at the advantages and disadvantages of this method have been undertaken (Guiroy 1995, Dubourg 1998, Girke *et al* 2012, Rublevskiy 2012). Essentially, when the irradiated graphite waste is incinerated, the ^{14}C will be released via formation of $^{14}CO_2$ and ^{14}CO through the oxidation processes given in Equations 2-5 and 2-6. It is known that the incineration of irradiated graphite at a rate of 600 tonne/year over 50 years

operation of an incinerator will only increase the natural source of ^{14}C by 0.5 % (Dubourg 1998). Although the release of ^{14}C is low and negligible to the current natural radiation inventory, the emission of CO_2 and CO is an issue. The nuclear power reactors are being used to reduce CO_2 and CO emissions. Incinerating the irradiated waste will rule out the aim of using nuclear power reactor regardless the potential release of other radionuclides (see Table 2-7). One may think that the chemical separation of radionuclides can be carried out before the incineration process, however chemical separation is in general expensive and also complicated due to various radionuclides being present. Another issue with the incineration method is the incinerator plant itself; the components in the plant will consequently be classified as radioactive waste, thus other options to dispose irradiated graphite might be better and should be considered.

$$^{14}C + O_2 \xrightarrow{\Delta H = -394.5\, kJ/mol} {}^{14}CO_2 \qquad [2\text{-}5]$$

$$2\,^{14}C + O_2 \xrightarrow{\Delta H = -110.5\, kJ/mol} 2\,^{14}CO \qquad [2\text{-}6]$$

As mentioned in Section 2.3, most of the ILW produced in the UK is stored in supervised interim storage and the favourable final disposal route is in the geological disposal facility. However, the process for developing the geological disposal facility is slow and currently still at the initial stage of identifying suitable location and raising public awareness as well as enhancing cooperation for the implementation (DECC 2013, 2014). In the geological disposal facility, the waste package will be disposed deep underground (~1000 m) by utilising the multibarrier systems of which aiming to limit the ground water penetration (Figure 2-8).

It is worth noting that at present there is no immobilisation route for irradiated graphite; Figure 2-8 shows the common treatment for the ILW in the UK in which the waste is encapsulated by cement and contained in a stainless steel container. In case of packaging the irradiated graphite wasteform, there is an issue with the stainless steel containment; graphite can act as a noble metal and has the possibility to increase the galvanic corrosion rate of the stainless steel (Fachinger 2012). Although there is a possibility of water penetration, the multiple barriers namely host rock, clay buffer, containment (stainless steel) and irradiated graphite wasteform should lower the rate of water diffusion. Ideally the water should not come into contact with the

wasteform until completing the decay process. The most significant current discussions regarding the disposal of irradiated graphite waste relate to the choice of materials for incorporation or encapsulation of the waste for long-term disposal in geological disposal facility. This is important as the material used is the last chemical barrier to prevent the radionuclides from leaching out to the biosphere. This is reviewed in the next section.

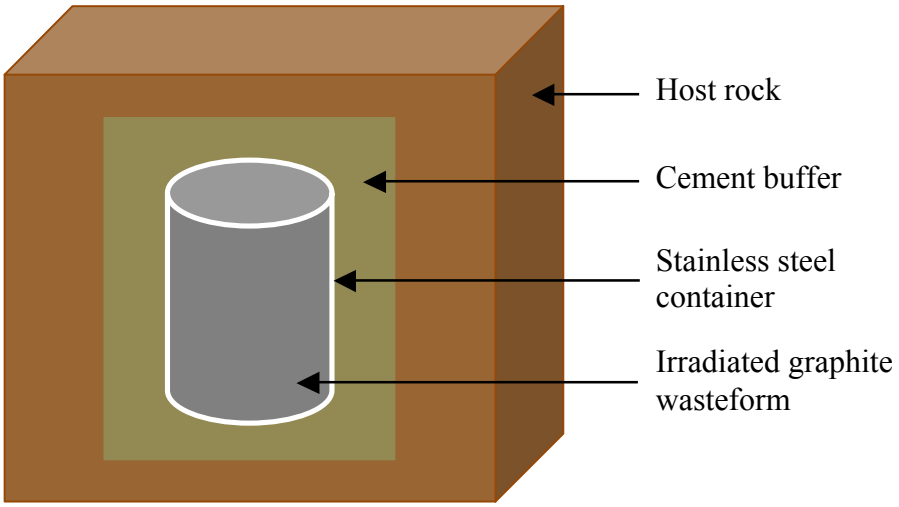

Figure 2-8: Cross-section of irradiated graphite wasteform in geological disposal facility (DECC 2014).

2.5. Processing Routes for the Immobilisation of Irradiated Graphite

Identifying a suitable immobilisation route for irradiated graphite waste is an important challenge for the nuclear industry. For this purpose, the material used and the production process must be appropriate to solve the issues of irradiated graphite waste (Section 2.4) and efficient in overall processing cost.

One suggested route is cement encapsulation, however poor wetting of graphite by the cement pastes and density driven stratification are problematic. Yim and Caron (Yim and Caron 2006) suggested using calcite ($CaCO_3$) to incorporate the ^{14}C followed by cement encapsulation. Other studies have claimed that almost complete incorporation of ^{14}C in the aqueous solutions in

cementitious material can be expected due to the precipitation of calcite within the pores of the cement (Hietanfn *et al* 1984, Bayliss *et al* 1987, Serne *et al* 1992). Therefore, cement can be an effective long-term chemical barrier for the immobilisation of ^{14}C. However cementation involves a volume increase leading to significant additional storage and disposal volume requirements. Hence if cementation is used to immobilise 260 000 tonnes irradiated graphite waste in a geological disposal facility, it will ridiculously increase the cost of waste management.

Ceramics such as SiC and TiC are recognised as materials that have good mechanical properties and are thermally as well as chemically stable. Karlina *et al* (2005) showed that ^{14}C in irradiated graphite can be transformed to TiC by undertaking the so called self-sustaining exothermic reaction at average temperature of 2300 ± 50K (Equation 2-7).

$$3^{14}C + 4Al + 3TiO_2 \longrightarrow 3Ti^{14}C + 2Al_2O_3 \qquad [2\text{-}7]$$

However, the temperatures used in the reaction or in general to produce all ceramics are high and this is an issue for irradiated graphite waste; as graphite is vulnerable to oxidation at high temperature (see Table 2-3), thus releasing problematic radionuclides. Other evidence of graphite oxidation at temperature <1000°C is given by Schweitzer and Singer (1965), Lim *et al* (2008), Dunzik-Gougar and Smith (2014) and Huang *et al* (2014).

2.5.1. Glass Materials

Glasses are well known materials for the immobilisation of HLW. For example, borosilicate glasses are used in France and the UK for the immobilisation of HLW. Specifically, $5.3Li_2O$-$11.1Na_2O$-$21.9B_2O_3$-$61.7SiO_2$ (wt%) borosilicate glass commonly called 'MW' glass is utilised in the vitrification of HLW at Sellafield, UK (Donald 2010). Since the development of the vitrification method in ~1960s, a number of borosilicate glasses for the immobilisation of HLW have been developed and information regarding their processing characteristics, corrosion behaviour, mechanical performance, thermal stability as well as radiation stability is widely available (Donald *et al* 1997, Plodinec 2000, Yang *et al* 2006, Ojovan and Lee 2005, Ojovan 2011).

Essentially, glass is defined as any material produced by any processing techniques that have an amorphous structure, while completely lacking in long range order of periodic atomic arrangement and exhibiting a region of glass transformation behaviour (Shelby 2005). The glass transformation behaviour considering the enthalpy and temperature parameters is presented in Figure 2-9. Basically, most liquids (melts) on cooling below the melting temperature will crystallise resulting in a long range periodic atomic structure; the enthalpy decreases abruptly on crystallisation and continues decrease due to the heat capacity of the crystal. However, if the melt is not crystallised, a supercooled liquid is obtained and the enthalpy decreases slowly due to the discontinuous structure rearrangement. Further cooling the melt increases the viscosity until at some point the viscosity becomes so great that the atoms cannot rearrange to the equilibrium liquid structure; the enthalpy deviates from the equilibrium line. As the melt cools, the viscosity will further increase and at this point the structure of the melts is fixed as a frozen solid and is called a glass.

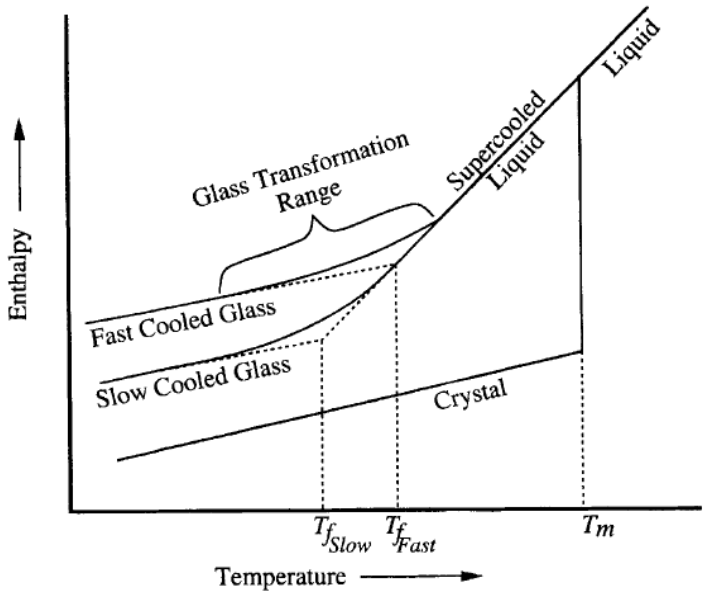

Figure 2-9: The enthalpy versus temperature diagram for a glass forming melt (taken from Shelby 2005).

There are three classes of components for oxide glasses: namely network formers (*i.e.* Si, B, Ge), modifiers (*i.e.* Ca, Pb, Li, K) and intermediates (*i.e.* Ti, Al, Zn, Mg). Basically, glass is made up

from the combination of at least one glass former elements with or without glass modifier and/or glass intermediate elements. For the case of MW glass, according to the Zachariasen-Warren structural model, the network formers polyhedra ($[SiØ_4]$, $[BØ_3]$, $[BØ_4]^-$, $[SiO_3O]^-$) will corner share oxygens (bridging oxygen shown as Ø) to create a random network structure and network modifiers (Li and Na) will occupy interstices within the random network as well as charge balancing singly-bonded oxygen atoms (non-bridging oxygens). It is worthy of note that the use of glass in nuclear industry is due to this material being capable of incorporating a wide range of chemical elements in its structure as modifier network and/or chemically bonded with the former network (glass former and intermediate elements).

For the immobilisation of irradiated graphite, the vitrification or glass melting process used for HLW seems irrelevant and due to graphite oxidation at low temperatures in air *i.e.* below 1000°C. However, the glass encapsulation method is of interest as this particular method offers significant advantages to immobilise low solubility nuclear waste (Ojovan and Lee 2005) and might be suitable to encapsulate inert materials, in this case, irradiated graphite waste. Generally, the glass encapsulation method involves mixing the powdered glass with waste, pressing the mixture at a certain pressure and heat treating at a temperature lower than the melting temperature of the glass. The main advantage of using the glass encapsulation technique is as follows:

- The heating process can be carried out using a variety of techniques such as conventional furnace, microwave, hot pressing and spark plasma sintering (considered heating techniques in this study is discussed in the following sections).
- The oxidation of irradiated graphite can be controlled by introducing heating in inert atmosphere *i.e.* argon, vacuum.
- The final volume of the wasteform is generally lower than with cement encapsulation.
- The physical and mechanical properties of the final wasteform could be altered as needed by optimising the processing parameters *i.e.* glass composition, particle size, pressing pressure and sintering temperature.

2.5.2. Microwave Processing

Microwave or dielectric heating for the synthesis of materials is gaining attention because it offers several potential advantages such as being fast, clean and more economical compared to conventional heating (Rao *et al* 1999, Thostenson and Chou 1999). Microwaves are electromagnetic radiation, with wavelengths lying in the frequency range 0.3 to 300 GHz. However, for microwave heating purposes, only narrow frequency windows centred at 900 MHz and 2.45 GHz are permitted. To utilise direct microwave heating in the production of glasses and composites, it is essential for the composition to include components that can couple to the microwave field. By considering the interaction with electromagnetic radiation, materials can be divided into three categories: microwave reflectors (typically bulk metals and alloys), transmitters (*e.g.* fused quartz and zircon) and absorbers (mainly transition metals). In the production of glasses using a microwave oven, it is crucial that the glass batch contains one (or more) microwave absorbing material(s) as (a) major constituent(s) of the batch to take up energy from the microwave field and heat up very rapidly (Kharissova *et al* 2010, Stennett *et al* 2011). The evidence of rapid heating and temperature detected on various elements, minerals and compound using microwaves is listed in Table 2-8. Other literature that discussed the potential materials, which could be heated very rapidly using microwave radiation can be found elsewhere (Vidhyanathan *et al* 1994, Mcgill *et al* 1995, Meredith 1998).

Essentially, the absorbers heat up rapidly starting from the molecular levels and the interaction usually can be explained based on two main effects; polar molecules and dielectric solids with charged particles (Menéndez *et al* 2010, Kim *et al* 2014).

- Polar molecules – The alternating electric field of the electromagnetic radiation forces both permanent and induced dipoles to rotate and this causes friction and creates heat energy by dipolar polarization. For *e.g.* water and polar fluids.
- Dielectric solids with charged particles – The charged particle such as π-electrons in graphite material are only free to move in a delimited region and these electrons cannot couple to the change of the electric field phase. Due to this, heat is generated according to the Maxwell-Wagner effect either by interfacial or Maxwell-Wagner polarisation.

Additionally, the interaction of microwave with charged particles also generates electric conduction by obtaining the external kinetic energy from the electric field; the collisions with neighbouring atoms produce heat and the heating process known as Joule heating.

A survey of the literature on the production of glasses using microwave heating indicated the potential of using iron phosphate glass compositions (Almeida *et al* 2007, Stennett and Hyatt 2009, Wang *et al* 2009). It is known that the addition of iron improves the chemical durability of phosphate glasses and iron phosphates have been suggested for use in the immobilisation of nuclear wastes (Huang *et al* 2004, Sengupta 2012). It is hypothesised that the rapid heating using microwave synthesis should minimise the oxidation of the graphite when heating in air.

Table 2-8: Microwave active elements, minerals and compounds heated using ordinary domestic microwave operating at 1 KW, 2.45 Ghz (Rao *et al* 1999).

Element/mineral/compound	Exposure time (min)	Temperature detected (K)
C (amorphous, <1 μm)	1	1556
C (graphite, 200 mesh)	6	1053
C (graphite, < 1 μm)	1.75	1346
Co	3	970
Fe	7	1041
Mo	4	933
W	6.25	963
Zn	3	854
TiB_2	7	1116
Co_2O_3	3	1563
CuO	6.25	1285
Fe_3O_4 (magnetite)	2.75	1531
MnO_2	6	1560
V_2O_5	11	987
WO_3	6	1543

2.5.3. Cold Press Sintering Processing

The use of cold press sintering processing in this research is inspired from previous work (Abdelouas *et al* 2006, McGann and Ojovan 2011, Heath *et al* 2013), which attempted to

encapsulate graphite powder and tristructural-isotropic (TRISO) fuel using glass materials. Basically TRISO fuel is the new generation micro-fuel particle (diameter < 1 mm) for generation IV nuclear power reactors. A TRISO fuel particle is designed based on a multi-layer concept in which the outer layer consists of pyrolytic carbon (essentially similar to graphite); this will raise comparable issues to irradiated graphite waste.

Graphite-glass composites prepared by cold press sintering have shown some potential for the encapsulation of irradiated graphite waste (McGann and Ojovan 2011). These authors examined three different base glass compositions and, of the ones studied, they found that soda-lime-silica based glass compositions appeared to be the most promising. However conventional sintering involves heating the waste for relatively long times and it is necessary to use an inert atmosphere to prevent excessive oxidation of the graphite. Furthermore, the porosity of the graphite-glass composites obtained was relatively high, between 7 and 55 %. In this work, it is therefore of interest to further investigate the potential of cold press sintering using other glass composition as well as to optimise the sintering parameters such as temperature and waste loading limit of the graphite.

The encapsulation of TRISO fuel using powdered glass materials have been shown to be promising and this sheds some light on the potential encapsulation of irradiated graphite waste. For example, various glass compositions such as French borosilicate (R7T7) and soda-lime silica glasses have been tested and the cold press sintering method used seen as advantageous (Abdelouas *et al* 2006, Heath *et al* 2013) with low processing temperatures compared to the initial glass melting, good mechanical properties, minimal oxidation of the pyrolitic carbon and overall good chemical durability of the wasteform. However, from their study, several issues regarding the use of glass materials and the cold press sintering methods have been highlighted as follows: (a) the waste loading of the TRISO fuel is low ~10 %. This is acceptable for HLW but in the case of the irradiated graphite, the waste loading must be higher, otherwise it will be cost inefficient. (b) The wetting problem between glass materials. This can be argued whether there is genuine wetting issue or this is solely due to the different thermal expansion of the TRISO particle itself (note that the green mixtures have been pressed in order to help densification); as sintering take place the TRISO fuel will expand and shrink faster than the glass

materials, when cooling the increasing viscosity of the glass limits the viscous flow, leaving space between the glass and TRISO particle. In addition, both expansion and shrinkage behaviour of the TRISO fuel during sintering will lead to the cracking of the glass matrix.

2.5.4. Spark Plasma Sintering Processing

Using hot pressing to sinter mixtures of powdered glass with irradiated graphite simulant and/or natural graphite results in better physical properties of the graphite wasteform (*i.e.* low porosity < 5 %, good mechanical properties) as well as maximising the waste loading; more than 50 wt % of waste was successfully incorporated (Fachinger *et al* 2012, Hrovat *et al* 2013). This led to the idea of using spark plasma sintering (also referred as field assisted sintering or pulsed electric current sintering) which potentially leads to similar results but a faster sintering process (Saheb *et al* 2012). This is due to more efficient heating by combination of thermal heating from the graphite mould and the reaction of the pulsed direct current with the green sample (see Figure 2-10). Indeed spark plasma sintering is similar to hot pressing sintering but the way of heating is different.

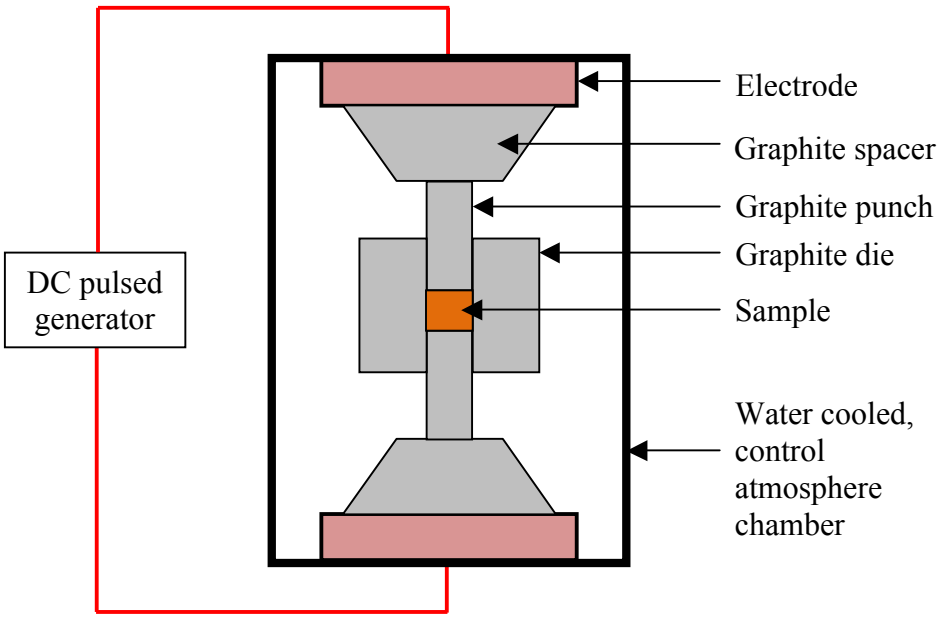

Figure 2-10: Basic schematic diagram of spark plasma sintering.

Basically, spark plasma sintering relies on the conductive graphite mould to produce heat. The heat is produced by the collision of the atoms, which is similar to Joule heating phenomenon occurred in the microwave processing (see Section 2.5.2). Currently, the mechanism of heating in spark plasma sintering method is not fully understood and more work needs to be carried out, especially to study the interaction of pulsed direct current with various types of materials. The sintering mechanism is often complicated as thermal, pulsed electric field (mainly used for conductive material and when materials produce a liquid phase) and external pressure take part simultaneously during sintering. In the literature, it is common to explain the interaction of pulsed electric current based on insulator (glass) and conductive (metal) materials. In the case of insulator materials, the heat is transferred from the graphite mould towards the sample by conduction and for conductive materials, heat conduction from the mould and pulsed electric effects may occur; if the sample is highly conductive (lower resistivity than graphite) the electric current will tend to flow directly through the sample rather than the surrounding graphite mould. It should be noted that when any material starts to become liquid, both heating from graphite mould and pulsed electric current will affect the heating process. The interaction of pulsed electric current is complicated as many mechanisms potentially occur depending on the electrical properties of the materials. A typical mechanism discussed in the literature are pulsed electric diffusion effect and the schematic is shown in Figure 2-11 (Tokita 1999, Saheb *et al* 2012, Suárez *et al* 2013). Recent publications also suggest several possible interactions between pulsed electric current and microstructure of the materials; (a) percolation effects of the current in the initially porous powder bed, (b) Peltier effect at the interface between the green body and punches, (c) electrochemical interaction and the interfaces and (d) electromigration (Guillon *et al* 2014).

A survey of material processing using spark plasma sintering revealed production of several glassy materials namely silicate (Zhang *et al* 2012) and silicon oxycarbide (Mazo *et al* 2012, Tamayo *et al* 2014) glasses. These studies highlighted that the processing time is fast (a matter of minutes), the sintering process enhances densification over grain growth, the density of the produced product is close to the theoretical density (> 98 %) and also limits the crystallisation of glass. Hence, it is seen that spark plasma sintering method is promising for immobilising irradiated graphite waste. Furthermore, it is also of interest to study the effects of glass material

and graphite-glass compositions using this method; the literature on mechanism of sintering for glassy materials based spark plasma sintering or simply the usage of this method in nuclear immobilisation is limited.

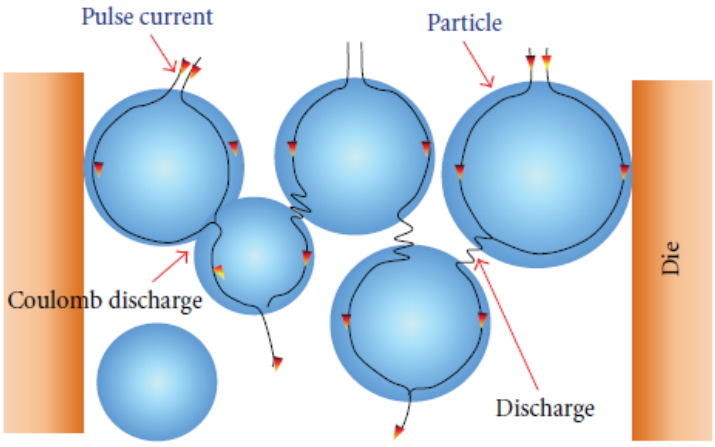

Figure 2-11: Pulsed current flow through powder particles, coulomb discharge also referred to joule heat (taken from Saheb *et al* 2012).

2.6. Summary

It has been explained in some detail that irradiated graphite waste is problematic and requires attention worldwide for appropriate final disposal. The complications of irradiated graphite waste are as follows:

- Huge volume of the waste, 260 000 tonnes.
- Various contaminations of radionuclides and inconsistency of the radionuclides in each type of irradiated graphite waste. The most problematic radionuclides are long-lived ^{3}H, ^{14}C and ^{36}Cl, which are highly reactive in environment and biocompatibility.
- Low mechanical and physical properties of irradiated graphite.
- Wigner energy

Irradiated graphite waste made waste immobilisation challenging due to:

- Graphite being one of the most inert materials; chemical bonding with other materials is limited.
- Vulnerability to oxidation at temperatures above ~350°C.
- Thermal treatment used in the production of nuclear wasteforms is generally time consuming and typically undertaken at high temperatures.

Therefore, in this study, the potential use of microwave, cold press sintering and spark plasma sintering processing for the immobilisation of graphite simulant in glass system is investigated.

3. Materials and Experimental Methods

3.1. Introduction

In this chapter, the irradiated graphite waste simulant and three processing methods used for preparing glasses and/or glass graphite composites; namely microwave processing, conventional processing and spark plasma sintering are explained in detail. The sample preparation and the basic principle for each characterisation techniques employed throughout the research are briefly summarised.

3.2. Irradiated Graphite Waste Simulant

Non-active industrial grade graphite flake was used as an irradiated graphite waste simulant in this work. The graphite flake was obtained from China via Prof Shaowei Zhang (now at University of Exeter) and used directly without any physical and chemical treatment. Two graphite batches were utilised in different sample processing methods; the first batch in the microwave processing and the second batch in the conventional and spark plasma sintering processing. Because the graphite flake is soft and can shear easily between the graphene planes (due to the weak van der Waals bonding, refer Section 2.4.1), all the sample preparation associated with graphite were carefully conducted in order to minimise the graphite loss *i.e.* avoiding graphite smearing while grinding and polishing.

3.3. Microwave Processing

Microwave processing of the samples was undertaken using a domestic microwave oven (DMO) with nominal power output of 800 W, operated at a frequency of 2.45 GHz. Two similar DMOs were used in this work, manufactured by DēLonghi, model EM821AAN-X2 and IGENIX, model IG2080. The rotating glass table was removed from the DMO to allow constant positioning of the samples throughout the experiments. Any modifications that would lead to breaking the Faraday cage of the DMO were avoided.

3.3.1. Experimental Setup

At the beginning of the work, the hot-spot of the DMO was investigated by observing the rate of water vaporisation during operation of the microwave. In all cases, 5 mullite crucibles were filled with 5 ml distilled water and placed in the microwave cavity. The crucibles were then heated at full power for 5 min. The experiments were repeated several times with the crucibles at different locations and heights. The position with the highest water vaporisation rate was identified as the best position for absorption of the maximum microwave energy. The examples of the experiments are shown in Figure 3-1.

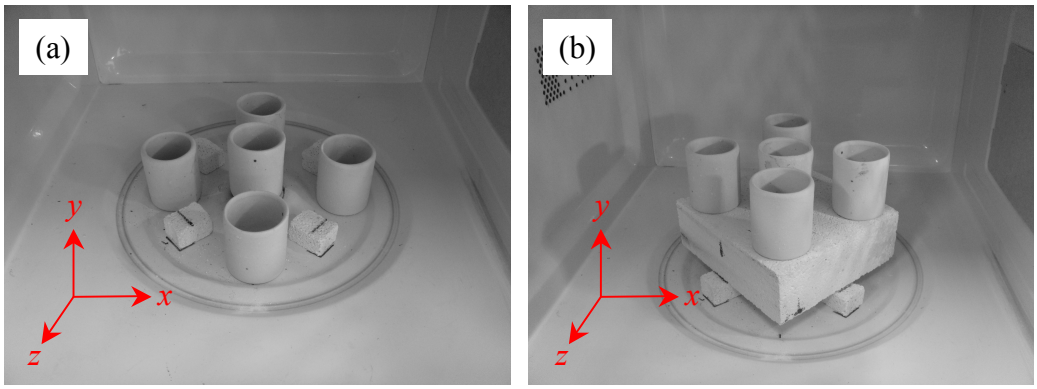

Figure 3-1: Position of the crucibles for optimum radiation spot experiment, (a) varying *x* and *z* axis, (b) varying *y* axis.

It was found that the best spot for optimum microwave radiation was at the horizontal centre and 5.4 cm above the base of microwave cavity. Although two different models of DMO were used in this work, results indicated that the optimum sample position in both microwaves was similar. Based on this finding, the alumina block has been designed to isolate the crucible and mounted on the alumina spacers to achieve the mentioned position. Any spaces between the crucible and the alumina block were filled with sintered alumina powder to minimise the heat losses during microwave heating the samples. A schematic diagram of the inside of the DMO is presented in Figure 3-2. Due to the potential toxic gases released when the decomposition of the raw materials takes place, all the DMO experiments, apart from the experiment in an inert atmosphere, were carried out in a fume cupboard.

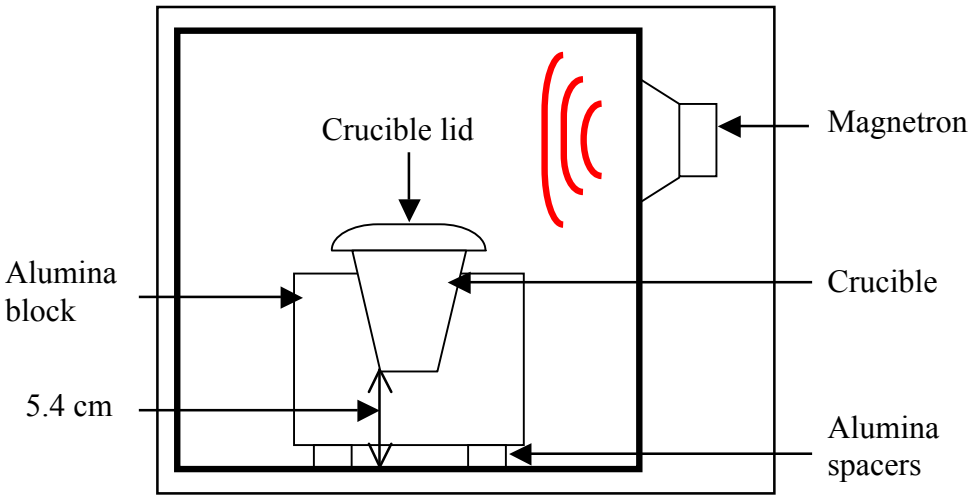

Figure 3-2: Schematic diagram of the experimental setup inside the DMO.

3.3.2. Sample Preparation

Many glass compositions were selected to be melted using microwave method. However, only the iron phosphate composition was successfully melted and showed some potential to immobilise graphite. Thus, iron phosphate glasses and their potential to encapsulate graphite have been studied using microwave processing method. The intention was to produce iron phosphate glass with a nominal composition of $40Fe_2O_3 – 60P_2O_5$ (mol%), here after known as IP, whilst varying the processing times and the amount of graphite added. Iron phosphate glasses and iron phosphate graphite glasses were prepared from laboratory grade magnetite (Fe_3O_4 – 97% pure, Alfa Aesar) and sodium dihydrogen phosphate ($NH_4H_2PO_4$ – 98% pure, Alfa Aesar) and, where relevant, graphite flake. In this processing method, graphite was combined directly into the batch of iron phosphate raw materials. The designation of the batch compositions are given in Table 3-1.

In all cases, batches necessary to produce 3 g samples were weighed using a high accuracy balance (±0.0001 g), mixed and manually ground in an agate mortar with a pestle for approximately 5 minutes to ensure homogeneity of the samples. 2 g of the batches were then inserted into a 13 mm diameter pellet mould and uniaxially compacted using a SPECAC press with a load of 3 tons and held for ~60 s. At the end of the compaction period the pressure was

released slowly. To avoid any unwanted chemical reaction with the raw materials, the batches were pressed without binder. The samples were placed in either vitreous silica (glass production) or mullite (graphite-glass sample production) crucibles with vitreous silica lids for microwave heating. The crucible containing the pellet was fitted inside the recessed alumina block in the DMO cavity (see Figure 3-2). The pellet was then irradiated at maximum power up to 20 minutes either in air or argon. For processing under flowing argon, the DMO was placed in a glovebox and a positive argon pressure was maintained while microwaving the samples. After microwave melting/sintering, the alumina block was removed from the microwave cavity. The crucible was taken out and cooled on a mullite plate to room temperature (RT) to maximise the cooling rate. The samples were kept dry for further characterisation.

Table 3-1: Designation for microwave processing samples, G – Graphite.

Designation	Batch composition (wt%)	
	Iron phosphate glass	Graphite loading
IP	100	0
IP20G	80	20
IP30G	70	30
IP38G	68	38

3.4. Conventional Processing

The glass compositions under consideration for the conventional processing method were aluminoborosilicate (ABS), calcium aluminosilicate (CAS), alkali borosilicate (G11), IP and obsidian (OB). The IP glass was also investigated here in order to compare the results with the one that was prepared using microwave processing. The natural obsidian glass originated from Monte Pilato, which is located on the northern tip of the Aeolian island of Lipari, Italy (last erupted in 729 AD). Obsidian glasses have shown good chemical durability as they have survived in the natural environment for millions of years (Ericson *et al* 1975, Vogel *et al* 2006, Morgan *et al* 2009). Furthermore by using natural glass, the sample processing steps could be minimised, hence lowering the processing cost.

3.4.1. Batch Preparation

The chemical compositions, precursors used, purity and its origin for in-house made glasses are listed in Table 3-2. In all cases, the necessary chemicals for a specific glass composition were weighed using a calibrated balance to an accuracy of ± 0.01 g. For safety reasons, the weighing procedures were carefully carried out in the fume cupboard. The batches were mixed using a spatula and transferred into polythene sample bags. The polythene bags together with the batches were then shaken for 5 min to ensure homogenisation of the chemicals. The homogeneous mixtures were stored and kept dry prior to melting.

Table 3-2: Nominal chemical compositions of batched glasses.

Oxide	ABS (mol%)	CAS (mol%)	G11 (mol%)	IP (mol%)	Precursor	Purity (%)	Supplier/Origin
Al_2O_3	5.29	7.17	2.59	-	$Al(OH)_3$	>99	Fisher Scientific
B_2O_3	7.48	-	9.24	-	H_3BO_3	≥99.5	Fisher Scientific
CaO	3.02	51.40	-	-	$CaCO_3$	98+	Fisher Scientific
Fe_2O_3	-	-	4.96	60.00	Fe_3O4	97	Alfa Aesar
Li_2O	-	-	9.69	-	$LiCO_3$	99+	Fisher Scientific
MgO	1.56	-	-	-	H_2MgO_2	>99	Sigma Aldrich
Na_2O	7.48	-	15.57	-	Na_2CO_3	99.5	Fisher Scientific
P_2O_5	-	-	-	40.00	$NH_4H_2PO_4$	98	Alfa Aesar
SiO_2	75.17	41.43	57.95	-	SiO_2	98	Tilcon/Loch Aline
Total	100.00	100.00	100.00	100.00			

3.4.2. Glass Melting

The different furnaces, crucibles, melting and annealing conditions for the conventional melting route are detailed in Table 3-3. Due to the high melting temperature required for the ABS glass, the batched composition was melted using a gas furnace. 150 g of glass batch was added to 4 separate crucibles and pre-heated overnight at 1000°C (2°C/min heating rate) in a Lenton box furnace. Whilst pre-heating the batches, the gas furnace was turned on and ramped to 1450°C. The pre-heated crucibles and batch were transferred into the gas furnace and the temperature of

the furnace was increased regularly until the melting temperature was achieved. An optical pyrometer was used to ensure the melting temperature was reached and remained consistent throughout the melting regime.

Table 3-3: Melting and annealing conditions for the laboratory made glasses.

Glass	Furnace	Crucible	Melting conditions	Annealing conditions
ABS	Gas	Alumina	3 h dwell at 1600˚C	1 h dwell at 700, 1°C/min to RT
CAS	Electric	Platinum	3 h dwell at 1450˚C	1 h dwell at 780, 1°C/min to RT
G11	Electric	Mullite	5 h dwell at 1100˚C	1 h dwell at 450, 1°C/min to RT
IP	Electric	Mullite	3 h dwell at 1150˚C	1 h dwell at 450, 1°C/min to RT

The CAS, G11 and IP glass batched compositions were melted in an ELITE electric top loading box furnace with Kanthal SiC furnace elements. The temperature of the furnace was regulated by an ELITE, TLCF1514-3216+2116 controller. For all of these glass compositions, batches required to produce 300 g of glass were melted using similar melting procedures. The procedures involved transferring approximately 100 g of the batched composition using a stainless steel scoop to a preheated crucible at 1000°C and placing the crucible into the furnace at the chosen melting temperature. After 15 min, volume reduction of the initial fill allowed more batch to be added. The crucible was taken out using iron tongs and the crucible was refilled with the batch for a second time. The crucible was then placed back into the furnace. This process was repeated until the entire batch had been added into the crucible. The melts were given 1 h batch free time before a stirrer (constructed of a similar material to the crucible) was inserted to a depth of approximately 1 cm from the base of the crucible. The stirrer was rotated at 60 rpm for the reminder of the melting time.

After completion of the melting schedule, about 50 % of the melts either prepared using the gas or electric furnace were cast into a pre-heated stainless steel mould and the rest were rapidly quenched into water to obtained glass frits (see Figure 3-3). Residual stresses in the cast glasses were removed by annealing process and the resulted glass blocks were stored for

characterisation. The glass frits were dried overnight at 90°C in a steel container with a lid; the lid was placed on top of the container with a small gap to accelerate the water vaporisation. The lid was used due to the glass frits spontaneously cracking during drying process (the effect of thermal shock).

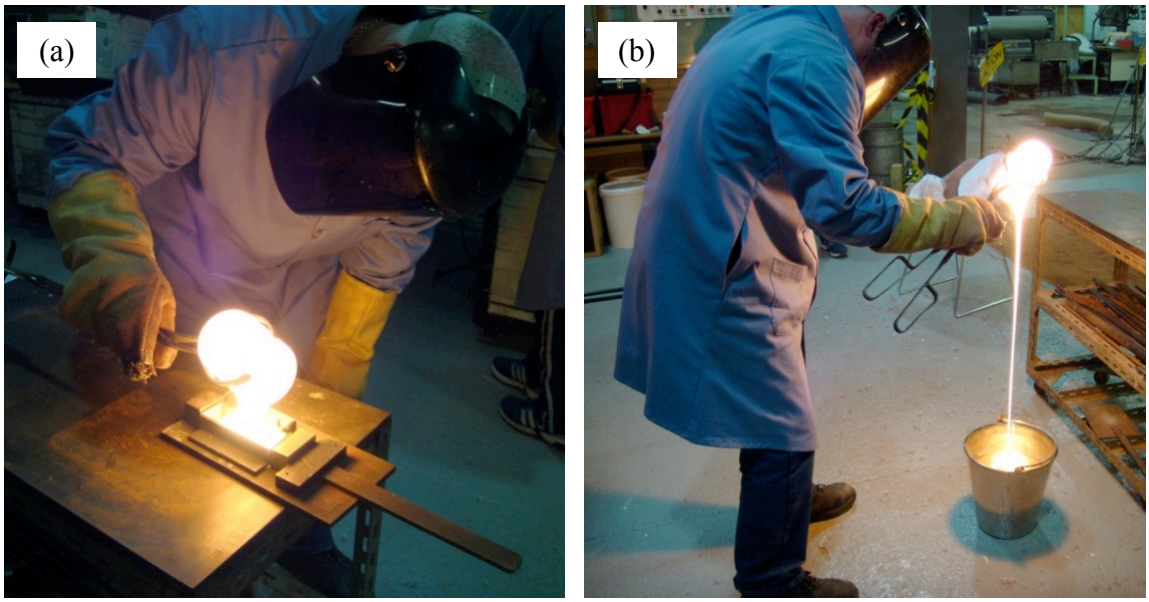

Figure 3-3: Pouring the glass melt: (a) into a pre-heated mould, (b) rapid quenching into water.

3.4.3. Preparation of Powdered Glasses

All the dried glass frits including obsidian (ABS, CAS, G11, IP and natural OB glasses) were crushed individually using a stainless steel percussion mortar. The resultant mixtures of glass particles were sieved using a < 75 µm test sieve in order to get a fine powder. The glass particles that did not go through the sieve were crushed and sieved once again; glass melting and powder processing was repeated until about 400 g powdered glasses for each composition were obtained. The powdered glasses were then passed over with a magnet in order to remove any metallic contamination arising from the percussion mortar. To homogenise the powder, dry milling was undertaken by loading each compositions of 400 g powdered glass into a polythene milling bottle (250 ml) and milling at 60 rpm for 8 h using Excal jar rolling mill. The homogenised powdered glasses were kept dry for further treatment.

3.4.4. Cold Press Sintering

Cold press sintering (CPS) was carried out using an ELITE, TSH 12/38/130 tube furnace. Due to the temperature indicated on the EUROTHERM digital screen being from a thermocouple placed on the outside of the alumina worktube, calibration of the temperature inside the tube was performed using K type thermocouple attached with multilogger thermometer, CHY 502A. The thermocouple used for this purpose had been previously calibrated using a standard heating source and was found to be accurate to ± 2°C. The calibration of the tube furnace involved taking the temperature reading at the centre of the alumina tube from RT to 1000°C at 100°C increments. The temperature data were plotted and the calibration line was drawn. Based on this calibration line, the true temperature inside the alumina tube was known for each desired sintering temperature.

In the CPS processing method, the intention was to study the effect of sintering temperatures and the effect of waste loading using various glasses and/or graphite glass compositions. The designation of the samples is indicated in Table 3-4.

Table 3-4: Samples designation for CPS processing, *x* – graphite loading, G – Graphite.

Designation	Composition (wt%)	
	Batch	Graphite loading
ABS	(100-*x*)ABS	*x* = 0
ABS*x*G	(100-*x*)ABS + *x*G	*x* = 5, 10, 15, 20, 25, 30, 35
CAS	(100-*x*)CAS	*x* = 0
CAS*x*G	(100-*x*)CAS + *x*G	*x* = 5, 10, 15, 20, 25, 30, 35
G11	(100-*x*)G11	*x* = 0
G11*x*G	(100-*x*)G11 + *x*G	*x* = 5, 10, 15, 20, 25, 30, 35
IP	(100-*x*)IP	*x* = 0
IP*x*G	(100-*x*)IP + *x*G	*x* = 5, 10, 15, 20, 25, 30, 35
OB	(100-*x*)OB	*x* = 0
OB*x*G	(100-*x*)OB + *x*G	*x* = 5, 10, 15, 20, 25, 30, 35

In all cases, 2 g batches consisting of powdered glass with or without graphite flake were mixed thoroughly in an agate mortar by gentle stirring using a spatula. The mixtures were stirred until no colour change could be seen, usually for about 5 min. The homogeneous mixtures were transferred into a 13 mm pellet mould and pressed with a load of 3 tons. The pressing procedure was similar to that used for the microwave samples and the details are described above in section 3.3.2. For each temperature interval, three pellets were placed on mullite plate designed to keep the samples horizontal throughout the sintering process (see Figure 3-4). The pellets were then sintered in flowing argon at various sintering temperatures for 2 hours with 5°C/min heating and cooling rates. The fast cooling and heating rates were used to minimise the oxidation of the graphite. The flowing argon gas during sintering was set at 0.25 l/min. The sintered samples were kept dry and characterised.

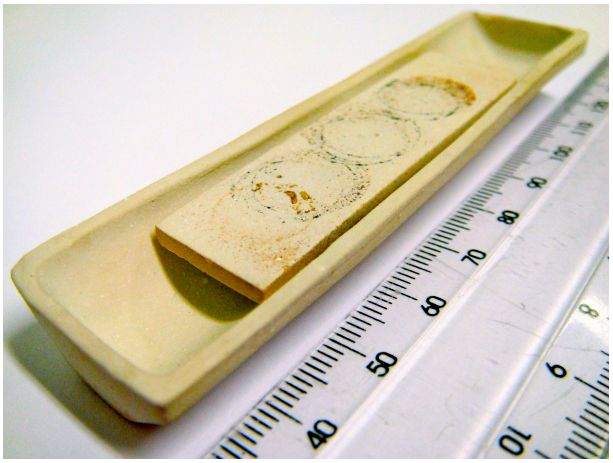

Figure 3-4: Mullite boat and plate used for CPS processing.

3.5. Spark Plasma Sintering Processing

Spark plasma sintering (SPS) was utilised to research the sintering behaviour of glass and graphite glass composites that had undergone fast sintering with application of pressure. The SPS machine and the tools used are illustrated in Figure 3-5. In this method, mixtures of powdered CAS glass (prepared in 3.4.3) and graphite flake were sintered at different temperatures and sintering times. The sintering process was performed under a static argon environment.

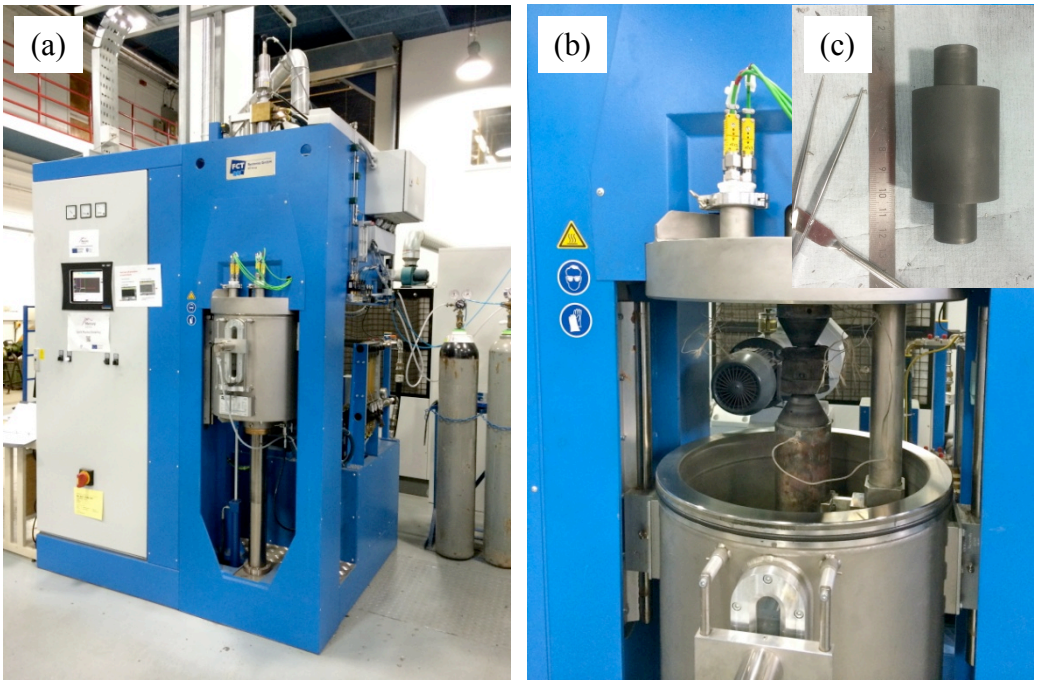

Figure 3-5: SPS machine, (a) main equipment, (b) close up of the furnace chamber, (c) 20 mm graphite mould.

For all cases, 5 g batches consisting of 70 wt% powdered CAS glass and 30 wt% graphite flakes were homogenised by gently stirring the mixture using a stainless steel spatula in an agate mortar. The mixtures were stirred for approximately 5 min after which no colour change of the mixtures could be observed. A graphite sheet was placed on the inner wall and the base of the bottom punch of the 20 mm graphite mould. The homogenised mixture was then transferred into the graphite mould and another graphite sheet was inserted on top of the sample. The reason for placing the graphite sheet between the mould and the sample is to protect the mould from contamination and improve the thermal transfer while sintering. The upper punch was then pushed into the mould and subsequently pressed at 1 ton using a SPECAC press, held at this pressure for 60 s before the pressure was released slowly. The exposed length of upper and bottom punches were kept similar (see Figure 3-5c). The graphite mould was insulated with fibreglass cloth and placed in the furnace chamber as shown in Figure 3-5b. The chamber was closed and the required sintering programs were created using the ECS recipe manager (version 4.0-build 12) on the control computer. An example of the program is presented in Table 3-5. The

program was then uploaded to the machine and the sintering of the sample was started. In all runs, only the temperature and sintering dwell time were varied; the maximum pressure was kept at 35 MPa, the heating rate was maintained at 200ºC/min and an identical cooling program was used. The obtained sintered samples were kept dried prior to characterisation.

Table 3-5: SPS sintering program for sample heated at 890°C for 20 min.

Segment	Segment time (min)	Temperature (ºC)	Pressure (MPa)	Environment
0	0	RT	0	Air
1	3	RT	16	Vacuum
2	1	450	16	Argon
3	1	450	16	Vacuum
4	2	450	16	Argon
5	4	450	16	Argon
6	2	890	35	Argon
7	20	890	35	Argon
8	1	Cooling to RT	16	Argon
9	10	Cooling to RT	16	Argon
10	0.17	RT	0	Air

3.6. Particle Size Analysis

Particle size of samples was examined using a COULTER LS 130 particle analyser. This instrument is capable of measuring particle sizes from 0.1 to 900 μm. For each measurement, the electrical offset, laser beam alignment and background were initially measured prior to sample loading. About 2 g of powdered glass was poured into the sample vessel containing water until a polarised intensity differential scattering (PIDS) obscuration between 40 to 60 % was achieved. This loading level is important to provide an acceptable signal-to-noise ratio in the detector channels. For graphite samples, the powders were mixed with glycerol before being measured. The glycerol was used to reduce the agglomeration between the particles and help the graphite powders disperse in the water. In all cases sonication was applied during loading, run and interval of the measurements.

The information about the particle size was based on the diffraction of laser light and the PIDS methods. Both of these lights were used to illuminate the particles in sequence to achieve high precision data. The additional PIDS method was needed in order to measure and improve the resolution of smaller particles *i.e.* < 0.4 μm. In principle, the diffraction of laser light method passed a 750 nm wavelength laser light through the suspended particles in the liquid which cause the light to be scattered. The incident light was then focused using a Fourier lens (focus signals from moving particles) to generate characteristic diffraction patterns that contain particle size information that were collected by arrays of phothodetectors (see Figure 3-6).

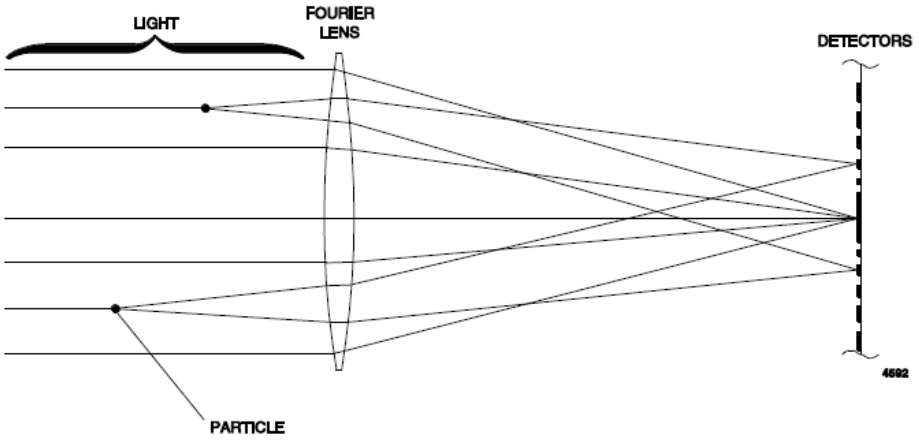

Figure 3-6: Interaction of scattered light with Fourier lens (taken from Beckman Coulter Inc. 2011).

The PIDS method, on the other hand, used an incandescent tungsten-halogen lamp with two polarising filters (vertical and horizontal) to provide monochromatic polarised light at three different wavelengths; 450, 600 and 900 nm. Although the interaction with samples is similar to the diffraction of laser light method, the PIDS photodetectors measure the pattern arising from differences in the scattering of vertically and horizontally polarised light for each wavelength. The signals for both methods were finally converted to digital signals and were analysed using the COULTER@LS version 2.09 software package. The analysis made was based on a Fraunhofer optical model to calculate particle size. Each sample measurement was repeated 10 times and each run was about 2 min. It should be pointed out that the analysis assumed the particles were spherical and that no agglomeration occurred during the course of the measurement.

3.7. Thermogravimetric Analysis

Thermogravimetric analysis (TGA) of graphite flakes was performed using a Perkin Elmer Pyris 1 TGA. This instrument was primarily used to determine the mass loss behaviour (mainly oxidation) of graphite flakes whilst being heat treated in different environments. In each measurement, approximately 25 mg of as received powdered graphite was placed into an alumina crucible and heated at a constant heating rate (10ºC/min) to 1000ºC in air or argon. The weight changes of the samples throughout the heating process were recorded using a high accuracy balance that was installed in the instrument. The sensitivity, accuracy and precision of the balance are 0.1 μg, > 0.02 % and 0.001 %, respectively. The obtained data were plotted as a function of weight change versus temperature and analysed using the Pyris software package (version 11.0.3.0470).

3.8. Differential Thermal Analysis

A Perkin Elmer simultaneous thermal analyser (STA 8000) was used to characterise the thermal properties of the prepared glasses, such as glass transition temperature (T_g) and crystallisation temperature (T_c). In all cases, approximately 25 mg of sieved powdered glass (< 75 μm) was placed in an alumina crucible and heated at 10°C/min from room temperature to 1000°C in argon, with aluminium oxide as a reference. The relative temperature differences (ΔT) between the sample and the reference material were taken every 0.1 s and plotted against temperature. The resultant curve provides information about exothermic and/or endothermic reactions in a sample over a temperature range. The T_g and T_c were carefully identified and taken as the extrapolated onset temperature using the Pyris software package (version 11.0.3.0470).

3.9. Dilatometry

The T_g's of ABS, CAS, G11 and IP glasses measured using STA 8000 were compared with T_g's obtained using a Netzsch DIL 402C dilatometer. The dilatometer is push rod type and the simplified schematic diagram can be seen in Figure 3-7. The principle of operation involves measuring the changes of sample length during temperature program and accurately recorded by

linear variable displacement transducer (LVDT) system. The sample holder and the front part of the pushrod were exposed to the temperature program during heating, which would cause an error in measuring the sample length. For this reason, baseline calibration was initially undertaken by heating a cylindrical recrystallised alumina standard to 900°C at a 3°C/min heating rate under flowing argon. The calibration data were uploaded in the TASC measurement program for each run.

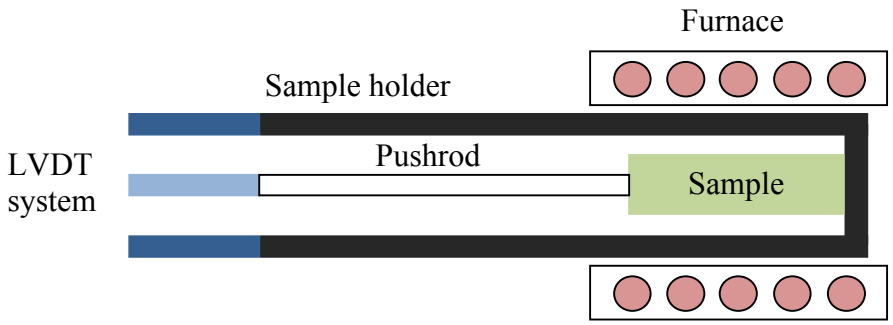

Figure 3-7: Cross-section schematic diagram of a pushrod dilatometer.

In all cases, 5×5×20 mm monoliths were prepared by cutting the annealed glasses using a diamond bladed slow saw. The glass monoliths were ground on all surfaces using 1200 grit grinding paper, which resulted in about 5 µm surface finish. Each monolith was then loaded into the dilatometer ensuring there was no gap between sample and pushrod. Samples were heated at 3°C/min under flowing argon and the instrument was set to automatically turn off when the dilatometric softening point was reached. The 3°C/min heating rate was used as this rate should give results comparable with the DTA measurements detailed in Section 3.8 (Mazurin 2007, Mazurin and Gankin 2008). The T_g values of the glasses were determined by using the Proteus software package.

3.10. Chemical Analysis

Chemical compositions of prepared glasses were investigated using both X-ray fluorescence (XRF) spectrometry and inductive couple plasma – optical emission spectrometry (ICP-OES). Due to the complications associated with ensuring complete sample dissolution and limited

access to the instruments, selected samples, specifically those containing B and Li, were sent to an external lab for XRF and ICP-OES analysis. For this purpose, approximately 10 g powdered samples (< 75 μm) were sent to AMG Superalloys UK Limited.

Chemical analyses of various glass samples were also been carried out using energy dispersive X-ray spectroscopy (EDS) in a JEOL JSM6400 electron microscope (see also section 3.17). In principle, the EDS is based on the analysis of the characteristic X-rays emitted when the incident electron knocked inner shell out from its orbit and the higher energy electron filled the vacancy to stabilise the configuration. For example, if the K shell electron of element is ejected by the incident electron, the L shell electron will fill the vacancy (KL transition) and emit a K_α X-ray unique to this element; other types of X-ray *i.e.* K_β, K_γ or L_α can be emitted depending on the transition of the electron. As the energy levels for each element are different, the element associated with the characteristic X-ray produced can be distinguished by comparing the data with an available database. In this study, all the EDS elemental analysis was undertaken using Oxford INCA software package.

3.11. Volume Shrinkage

The volume shrinkage of the sintered pellets formed using the CPS method was determined by measuring the thickness (height) and the diameter of the samples before and after the sintering process using calibrated digital callipers. These measurements were intended to estimate the volume of the final wasteform produced via various preparation techniques. The percentage volume shrinkage was calculated using

$$\%\ \text{volume shrinkage} = \left(\frac{\pi \left(\frac{D_i}{2} \right)^2 h_i - \pi \left(\frac{D_f}{2} \right)^2 h_f}{\pi \left(\frac{D_i}{2} \right)^2 h_i} \right) \times 100 \qquad [3\text{-}1]$$

where D_i, D_f, h_i, and h_f are the initial diameter, final diameter, initial height and final height of the samples, respectively.

3.12. Assessing Mass Loss

The change in sample mass after processing is important and should be compared with the theoretical evaluation to verify the loss of volatile materials as well as to have an indication of any other chemical reactions (oxidation and/or reduction of materials) that may have occurred during sintering. With this target in mind, the mass of samples (whether microwaved or conventionally sintered) was measured before and after melting/sintering using a high precision balance (± 0.0001 g). The percentage mass loss was computed by differentiating the masses as given by

$$\%\,\text{mass loss} = \left(\frac{m_i - m_f}{m_i} \right) \times 100 \qquad [3\text{-}2]$$

where m_i and m_f are the initial and final masses of the samples, respectively.

3.13. Density

The densities of the solid and powdered samples were recorded both by using Archimedes' principle (Mettler Toledo density balance, MS-DNY-43) and a Micromeritics Accupyc II 1340 helium gas pycnometer.

For the Archimedes measurements, distilled water (H_2O) was used as the immersion liquid. Although all the measurements were done at RT, slight changes of temperature will affect the density of distilled water, thus decreasing the accuracy of the measurement. Due to this reason, in each measurement, the initial temperature was measured using thermometer and inputted into the density balance. The selected bulk samples were weighted in air and after that submerged in distilled water to displace all the air from the samples. Bubbles that appeared on the surface of the sample were carefully removed using a rigger type brush. Only the stable weight of the sample in distilled water was taken. The sample density (ρ_{sample}) was then calculated automatically using the recommended equation from Mettler Toledo as follows:

$$\rho_{sample} = \frac{m_a}{m_a - m_w}\left(\rho_{water} - \rho_{air}\right) + \rho_{air} \qquad [3\text{-}3]$$

where m_a and m_w denote the mass of samples in air and mass of samples in water. The density of air (ρ_{air}) was assumed constant at 0.0012 g/cm^3; although this also varies with temperature, the effect should be very small. The density of distilled water (ρ_{water}) at various temperatures used in the software package (version V1.30) can be found in Appendix A1. For each sample the average of at least three measurements was calculated.

For the pycnometer measurements, samples were crushed and ground in a mortar using a pestle and sieved to < 75 μm. The known masses of powdered samples were inserted into a 1 cm^3 steel sample holder, placed in the sample chamber and purged 50 times with research grade helium gas (removing water and volatiles). The pressure of the gas in the sample chamber was set to 170 kPa. The gas molecules rapidly filled the pores of the sample; only solid phase of the sample displaces the gas. The gas was then discharged into a second empty chamber which allows computation of the sample solid phase volume using

$$V_{sample} = V_{cell} - V_{\exp}\left(\frac{P_1}{P_2} - 1\right) \qquad [3\text{-}4]$$

where V_{cell}, V_{exp}, P_1 and P_2 are sample chamber volume, expansion chamber volume, gauge pressure after fill and gauge pressure after expansion, respectively. The density was then calculated by dividing mass over volume of the sample. The density measurement was repeated 50 times and the average taken.

3.14. Porosity

Porosities in sintered samples, whether resulting from poor consolidation of the glass particles during sintering, limitations of sample processing, and/or from the effect of releasing gases (due to decomposition or oxidation of the materials), were determined by calculating the difference between the density of the bulk and powdered samples. The percentage of porosity is defined by

$$\% \text{ porosity} = \left(\frac{\rho_{powder} - \rho_{bulk}}{\rho_{powder}} \right) \times 100 \quad [3\text{-}5]$$

Where density of powder sample (ρ_{powder}) and density of bulk sample (ρ_{bulk}) are determined using gas pycnometer and Archimedes principle (refer to section 3.13).

3.15. X-ray Diffraction

Powder X-ray diffraction (XRD) was primarily conducted to confirm whether the glasses were X-ray amorphous and, if not, which crystalline phases had precipitated during the production of the glass composite materials. Siemens D500 and D5000 diffractometers with CuK_α (1.5406 Å) radiation operated at 40 kV and 30 mA were used. In theory, when the generated X-ray interacts with the planes of atoms, a fraction of the beam is transmitted, absorbed, scattered or diffracted by the samples. XRD is based on the diffraction of the incidence beam which is described using Bragg's law:

$$n\lambda = 2d \sin\theta \quad [3\text{-}6]$$

where n is an integer, λ is wavelength, d is spacing between atomic planes and θ is the angle of incidence. Two phenomena can be observed from the XRD data; sharp peaks if the X-ray beam diffracted by the regular lattice planes (crystalline materials) and/or a broad hump indicating diffuse scattering by the random orientated atoms (amorphous materials). The XRD data were collected by the detector using reflection geometry and the basic principle of the interaction between X-ray beam and the regular lattice planes is illustrated in Figure 3-8.

For all XRD measurements, only powdered samples that had been sieved to < 75 μm were analysed. The samples were placed in the sample holder and the top of the surface was flattened using a glass slide. The detector was scanned over a 2θ range from 10 to 80° at 1°/min intervals with a step size of 0.05°. In some cases, overnight XRD measurements were undertaken by using identical scan conditions but with increased scan time to improve resolution (1°/8min intervals).

The XRD data was analysed using PDF-4+ 2012 software package (version 4.12.0.4) of which utilised The International Centre for Diffraction Data (ICDD) database.

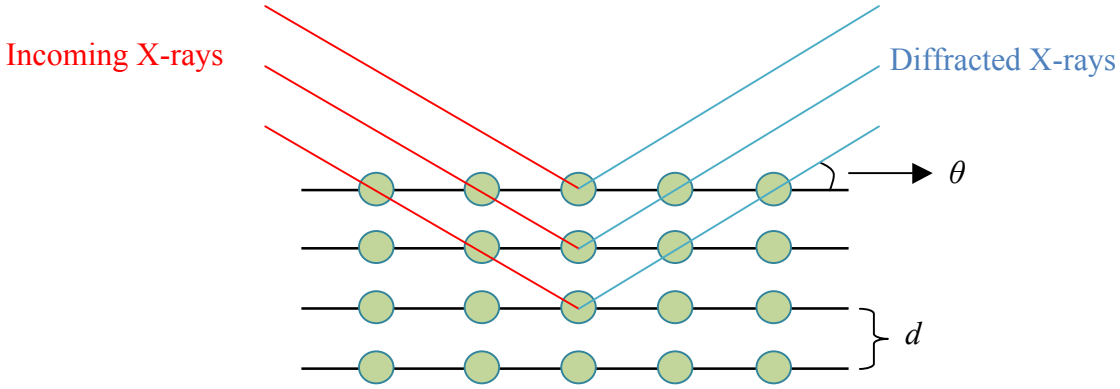

Figure 3-8: Schematic diagram showing the basic principles of X-ray diffraction.

3.16. Fourier Transform Infrared Spectroscopy

The types of the bonds contributing to the network structure of the samples were identified using a Perkin Elmer Frontier Fourier transform infrared spectrometer (FTIR). The FTIR spectrometer consists of four major spectrometer components: radiation source, interferometer, sample compartment, pyroelectric detector (triglycine sulphate, DTGS) and a computer to run the mathematical procedure called fast Fourier transform (FFT). The FTIR is based on the principle of Michelson interferometer and a block diagram of the instrument is shown in Figure 3-9.

The Michelson interferometer is a device that produces interference between two beams of light. The operation of the interferometer is as follows; the infrared beam generated from the source (various frequencies in infrared region) was split 50:50 by the beam splitter, one beam travelled to the stationary mirror and one to the moving mirror that introduced different optical path lengths, the beams were reflected by the mirrors and recombined to create an interference signal called an interferogram. The interferogram is a unique signal resulting from the constructive and destructive interferences (due to different optical paths) and contains all infrared frequencies. The interferogram passed through the sample and the resultant interferogram is detected using the pyroelectric detector. Each molecular bond will couple with a specific frequency of light

causing molecular bond vibrations and a signal in the interferogram. According to quantum mechanics, the molecular bonds vibrate by absorbing energy and excite from the lowest state to the highest (usually from the ground state to the first exited state). For a transition to be FTIR active, the molecule must undergo a dipole moment change during vibration. The resultant interferogram was finally Fourier transformed to generate intensity as a function of wavenumber (see example in Figure 3-10).

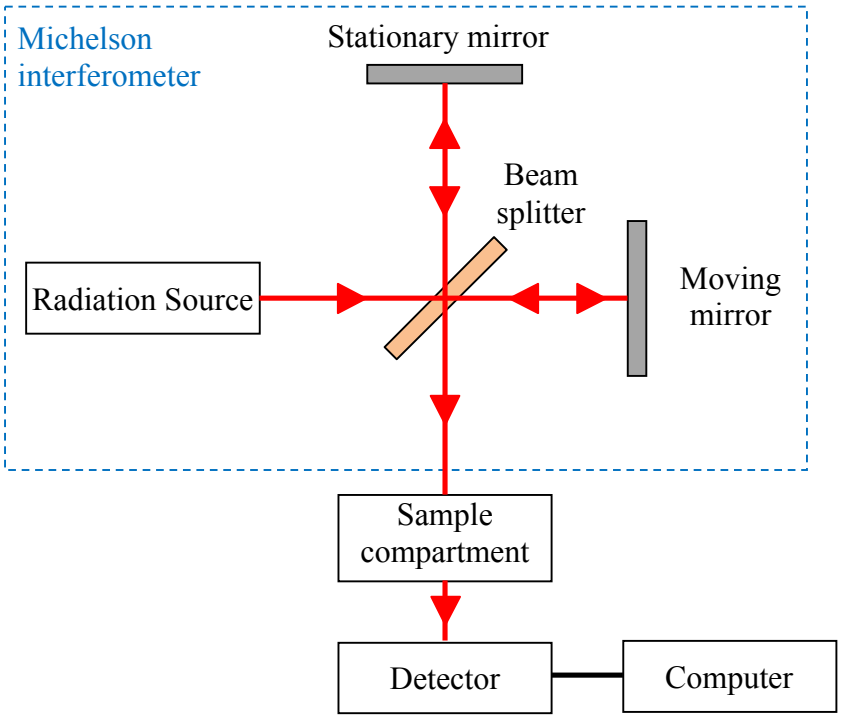

Figure 3-9: Basic configuration of FTIR spectrometer.

The samples to be analysed were prepared using the KBr disc method. This is due to the diamond attenuated total reflection (ATR) module that was available at the time being limited to detecting bands at lower wavenumbers, < 700 cm^{-1}. In all cases, 0.2 g of powder KBr were mixed with 0.002 g of sample, ground in an agate mortar with a pestle for 5 min to ensure the homogeneity of the mixture and pressed using a 10 mm diameter mould at 10 tons. The background scan was carried out without the sample prior to each measurement in order to calibrate the detector of the instrument. The prepared pellets were scanned using the FTIR from 400 to 4000 cm^{-1} wavenumbers and 20 spectra were accumulated for each to ensure high

accuracy of the data; each cycle was a complete scan of moving back and forth of the moving mirror. The obtained data were then analysed using the Spectrum software package (version 10.4.1.262) and compared with the data reported in the literature.

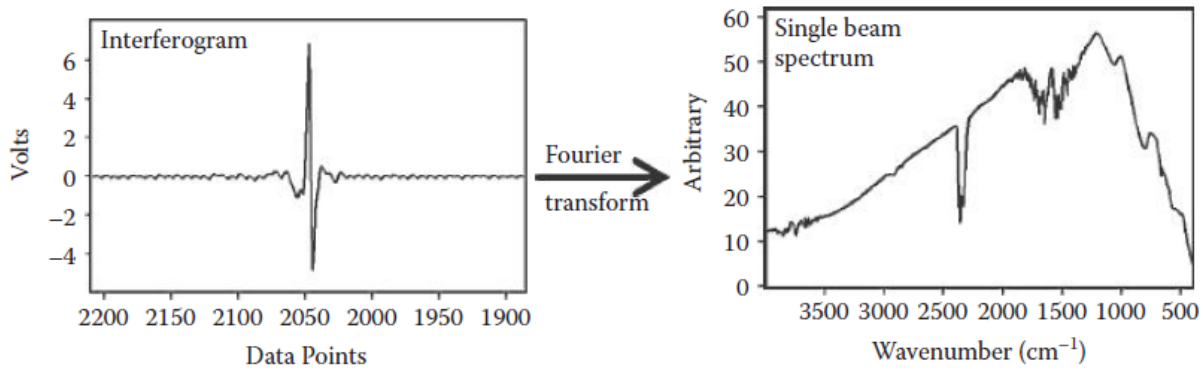

Figure 3-10: Fourier transform of measured interferogram yields a single beam spectrum (taken from Smith 2011).

3.17. Microscopy

The size of features that can be observed using a microscope is related to its resolving power which is the smallest separation at which two separate objects can be distinguished. The resolving power of a microscope is ultimately dependant on the wavelength of light. This is why an optical microscope (λ = 400-700 nm) has lower resolution compared to an electron microscope (λ < 1 nm). Although hugely different in resolution, optical and electron microscopes share similar basic principles; both of the microscopes use lenses to magnify an image of an object. In an optical microscope, the visible light is focused by glass objective lenses (very short focal length) and this magnifies an image of the sample. Apart from giving a low resolution image, the optical microscope offers significant advantages, such as no coating being required, producing a real colour image and being suitable for all kind of samples *i.e.* liquids, solids and living microorganism. Whilst in an electron microscope, the electron beam generated from tungsten-hairpin gun is focused using electromagnetic lenses (by changing the current through the objective lens coil) onto the surface of the sample. The interactions of the electron beam with

the surface of sample result in a range of signals being emitted and these signals are recorded by the detectors (see Figure 3-11).

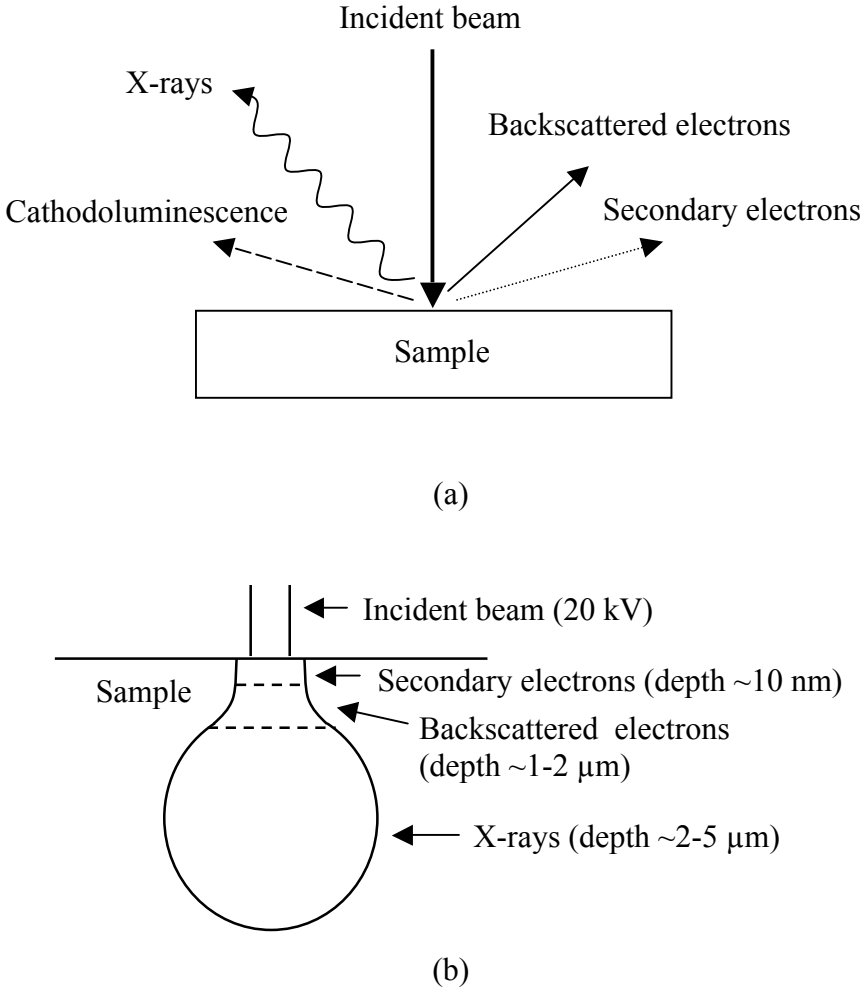

Figure 3-11: Showing (a) signals emitted from the interaction between electron beam and sample, (b) the interaction volume and the regions from which the signals may be detected (Goodhew *et al* 2001).

In this work, surface morphology and microstructural analysis were conducted using a Nikon ECLIPSE, LV150 optical microscope and a JEOL JSM6400 scanning electron microscope (SEM) equipped with an EDS. Samples were cut using a diamond bladed slow saw, cold mounted in epoxy resin and left to harden for 24 h. Mounted samples were ground flat by successive steps using 120, 400, 800 and 1200 grit abrasive papers. The samples were then

polished with 9, 6, 3 and 1 μm diamond pastes to achieve a mirror-like surface. After polishing, the samples were rinsed using acetone/isopropanol to accelerate the drying process. Polished samples were observed using an optical microscope to identify the bulk microstructures. Samples with interesting microstructures were then carbon coated, silver painted around the edge of the samples to improve the conductivity and kept dry prior to SEM examination. Secondary and backscattered images of the samples were collected along with elemental analysis by EDS. For semi-quantitative analysis using EDS, high purity cobalt was used as reference and the detector was calibrated every 5 semi-quantitative measurements.

In some cases, the samples observed using optical microscopy were also subjected to optical profilometer analysis. Essentially, the optical profilometer is the combination of an inferometer and optical microscope into one instrument. The optical profilometer analysis was undertaken in order to investigate the surface roughness of the samples and to observe the surface behaviour of glass/glass composites and graphite components.

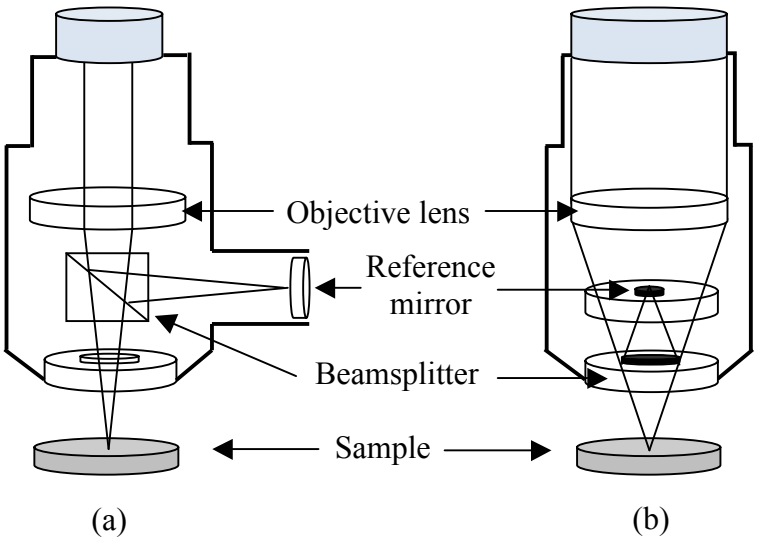

Figure 3-12: Typical microscope interferometry objectives, (a) Michelson-type objective, (b) Mirau-type objective, more detail in Niehues et al. (2012).

For these purposes, the samples were examined using a Veeco ContourGT optical profilometer and analysed using the BRUKER-vision64 (version 5.30 update 4) software package. The

working principle of a Veeco ContourGT optical profilometer is based on the interferometer device that splits a collimated beam of light (emitted from a halogen lamp) into two separate beams; where one beam is reflected from the sample under test and another one is reflected from the reference mirror. Both of the beams are then recombined to create an interference signal (bright and dark bands known as fringes) that make up the interferogram. The produced interferogram is detected by the charge-coupled device (CCD) detector and analysed using interferometric-phase mapping programs, which generates 3D image that represent the topography of the sample. The Veeco ContourGT optical profilometer is equipped with two types of interferometer devices that couple into the microscope objectives (see Figure 3-12); Michelson (for low magnification, 2-5×) and Mirau (for high magnification 10-100×).

3.18. Raman Spectroscopy

Raman and FTIR are two similar spectroscopic techniques; both probing the vibrations of molecular bonds. However, the selection rules are different so that weak bands in the FTIR spectroscopy may be strong in the Raman spectroscopy and vice versa. In Raman spectroscopy, the molecular transitions take place by changing the polarisability of molecule during the vibration, which means the electron cloud of the molecule must experience positional change (by an external electric field). Due to this advantage, Raman spectroscopy is widely used to study symmetrical molecules *e.g.* O_2.

In principle, a monochromatic laser is used to illuminate the sample, the interaction of the polarisable molecule with the incoming radiation creates an induced dipole moment in the molecule and the radiation emitted/scattered contains Rayleigh (elastic) and Raman (inelastic) scattering. Rayleigh scattering corresponds to the light scattered at the frequency of the incident radiation whilst Raman scattering is shifted in frequency, and hence energy, from the frequency of the incident radiation by the vibrational energy that is gained (Stokes Raman) or lost (anti-Stokes Raman) in the molecule. Both Rayleigh and Raman processes are depicted in Figure 3-13.

For the Raman spectroscopy experiments, samples prior or after SEM observation were used to confirm which molecular bonds of base glasses were present after sample processing. Samples

after SEM observation were re-polished back to 1 μm to remove the carbon coating on the sample. Raman spectra were obtained with a Renishaw Invia Raman spectrometer equipped with a CCD detector that was calibrated using Si (100). A monochromatic green laser (514.5 nm) operated at 20 mW power was focused on the flat sample (powdered samples were flatten using glass slit) surface using 50× objective lens. The spectra were scanned 20 times in an energy range of 0 - 4000 cm^{-1} with an exposure time of 60 s. Cosmic radiation was ignored in all spectra measurements.

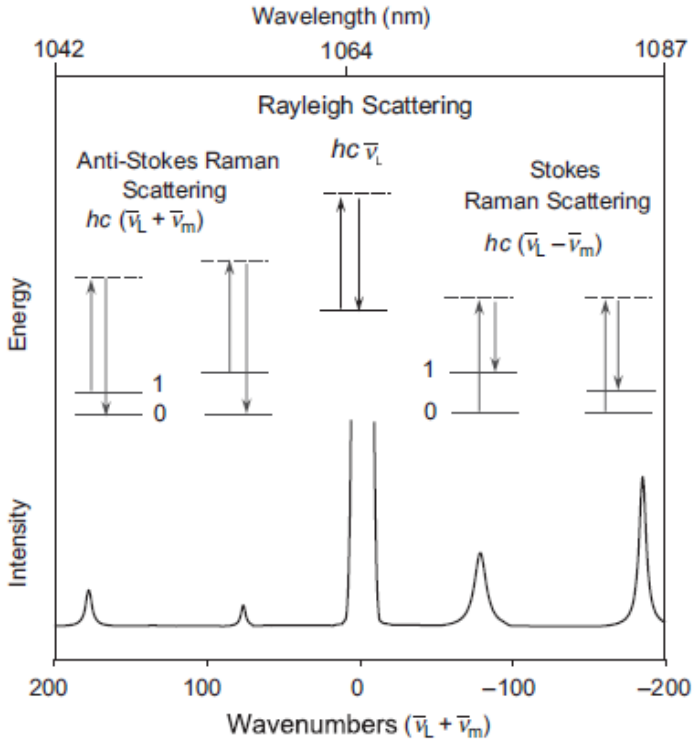

Figure 3-13: Illustration of Rayleigh scattering as well as Stokes and anti-Stokes Raman scattering (taken from Larkin 2011).

3.19. Mössbauer Spectroscopy

Since the discovery of the Mössbauer effect, which involves a nucleus embedded in a solid matrix emitting and absorbing gamma (γ) rays without recoil (recoil energy less than the lowest quantised lattice vibrational energy), many studies regarding the interaction between γ rays with materials primarily with the nuclei ^{57}Fe, ^{119}Sn, ^{151}Eu, ^{121}Sb and ^{161}Dy have been performed. In

this work, room temperature Mössbauer spectroscopy (WissEl MB-500 Mössbauer bench) was used to study the valency of the iron in iron-containing base glass and the graphite-glass composite samples. To achieve this aim, having a radioactive source in an excited state containing a similar isotope to the samples in a ground state is essential. For this purpose 25 mCi ^{57}Co prepared by diffusing ^{57}Co into a Rh matrix (so that the ^{57}Co atoms have the same local environment and the same nuclear energy) with a half live of ~271 days was used. The nuclear decay scheme of ^{57}Co to metastable state and finally to the ground state via a γ ray cascade is illustrated in Figure 3-14.

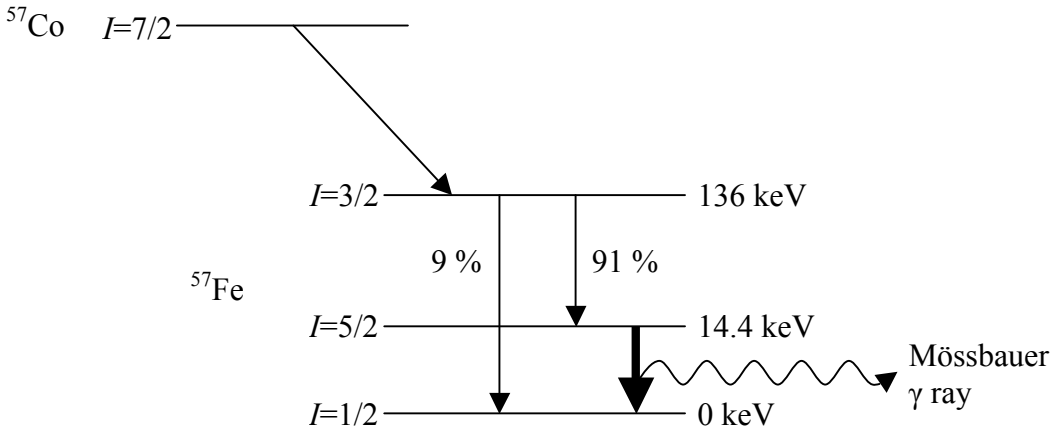

Figure 3-14: Schematic diagram of energy level of ^{57}Co to ^{57}Fe, *I* = spin state of the nucleus (Dickson and Berry 1986).

In principle, the 14.4 keV γ rays emitted from the source were passed through the sample by moving the source relative to the stationary sample with constant acceleration, resonance absorption occurred due to the emitted γ rays matching the nuclear transition energy in the sample and the resultant signals were detected by the proportional counter. The Mössbauer spectra obtained from the measurement consist of a plot of γ ray counts versus the velocity of the source with respect to the sample.

As the samples studied were non-magnetic the analysis of the Mössbauer spectra could be interpreted based on the electric monopole (Coulomb) interactions. Figure 3-15 shows a

schematic diagram of the situation where this electric monopole interaction is the only hyperfine interaction affecting the nuclear energy levels in the samples.

In every experiment, approximately 5 mg of powdered sample were loaded into the copper holder with a transparent perspex window. The velocity of the spectrometer was calibrated using a pure iron foil. The obtained calibration and experimental data were convoluted and analysed with extended Voigt-based fitting (xVBF) analysis using the Recoil software package (version 1.03). All the data were fitted by considering centre shift (CS) and quadrupole splitting (QS) values of desired glasses that have been reported in the literature. The relevant crystalline phases observed by XRD and crystallography data from ICDD database were also taken into account in the analysis.

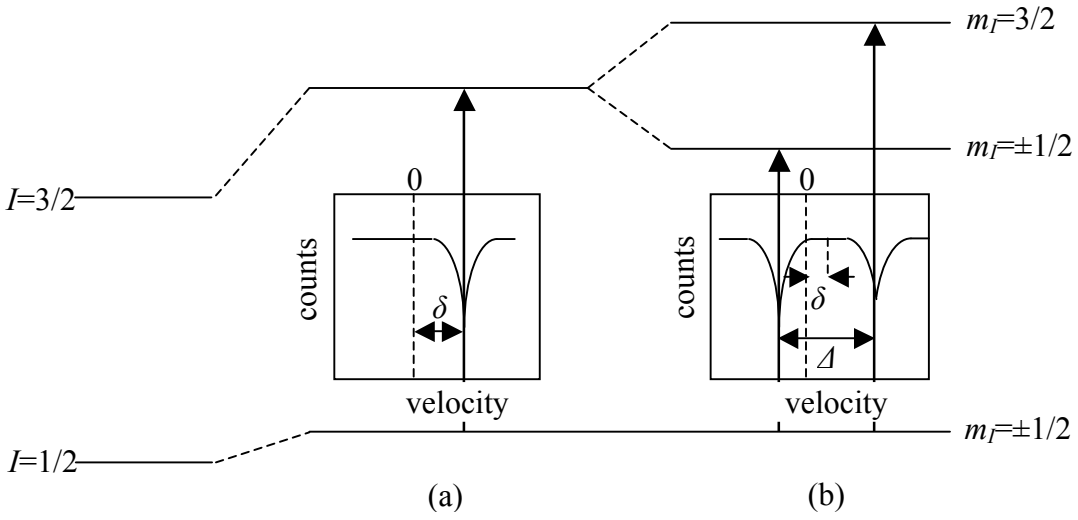

Figure 3-15: The effect of the nuclear energy level of ^{57}Fe, (a) the centre shift, δ, (b) the quadrapole spitting, Δ; I = spin state of the nucleus, m_I = magnetic quantum numbers (Dickson and Berry 1986).

3.20. Indirect Tensile Testing – Brazilian Method

The Brazilian test method is geotechnical laboratory test that is usually used for the measurement of indirect tensile strength of rocks. This method is also relevant to measure the tensile strength of concretes, ceramics and glass materials. In the Brazilian test method, a load is applied

continuously at a constant rate across the diameter of cylindrically shaped samples until failure occurs. The loading scheme for the test and the suggested ideal failure (Andreev 1991) of the sample is shown in Figure 3-16.

In this work, tensile strength of sintered samples produced using the CPS method was performed in a Zwick/Roell Z050 universal tester. The samples were placed vertically towards the upper and bottom punches of the instrument and subsequently loaded at a test speed of 0.5 mm/min. The tester was set to stop and return back to initial position after exceeding 20 mm deformation. At least 5 identical samples were tested and samples that did not break as stipulated for Brazilian indirect tensile tests were discarded. The force required for fracture for each sample was extracted from the testXpert II software and the average indirect tensile strength values were calculated using

$$\sigma_{sample} = \frac{F}{\pi r h} \qquad [3\text{-}7]$$

where F, r, and h are force, radius and height of the samples, respectively. The radius and height of the samples were measured using calibrated digital callipers.

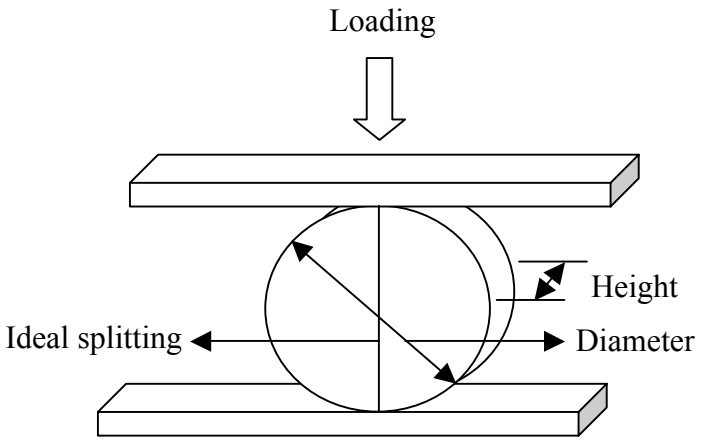

Figure 3-16: Loading scheme for the Brazilian test using a cylindrically shaped sample.

4. Results and Discussion I: Graphite Immobilisation in Iron Phosphate Glass Composite Materials Prepared using Microwave and Conventional Processing

4.1. Introduction

The objective of this chapter is to assess the potential of DMO processing for the production of wasteforms intended for the immobilisation of irradiated graphite waste. For comparison purposes, the well established conventional glass melting and CPS methods were used to produce equivalent samples to those successfully made using the DMO. A wide selection of characterisation techniques were implemented to investigate the properties of the produced glasses and graphite wasteforms. To simplify the presentation, the results have been divided into four sections: characterisation of graphite, characterisation of iron phosphate base glasses, characterisation of iron phosphate glass composites and Mössbauer spectroscopy analysis. This chapter is then followed by the discussion and summary sub-sections.

4.2. Characterisation of Graphite

As mentioned previously in Section 3.2, two types of graphite powder were utilised as an irradiated graphite waste simulant. Knowledge of the physical and chemical properties of the graphite powders is important in the production of graphite wasteforms. Due to this reason, the graphite powders have been characterised by means of particle size, density, TGA, XRD, FTIR and SEM with EDS analysis. All the obtained data are presented and discussed in this section.

4.2.1. Particle Size and Density

The particle size distributions of the specific graphite powders used in the DMO, CPS and SPS processing methods are summarised in Table 4-1. Although the average size of the particles based on volume considerations is comparable, equivalent to average diameters of 167 ± 8 or 145 ± 7 μm, on a number basis there were much greater numbers of small particles used in the DMO experiments with an average size of 0.24 ± 0.01 μm. It is worth noting that the presence of

the small particle size means that there is a high surface area and this may increase the possibility of graphite oxidation during sintering. The powder density of smaller size graphite was slightly larger, being about 2 % greater than the graphite used in the CPS and SPS processing. This can be understood as the large particles of graphite may contain more porosity and consequently lowering the powder density.

Table 4-1: Statistical particle size analysis and density of graphite powders.

Parameter	DMO		CPS, SPS	
	(Volume basis) Diameter /μm	(Number basis) Diameter /μm	(Volume basis) Diameter /μm	(Number basis) Diameter /μm
Average size	145 ± 7	0.24 ± 0.01	167 ± 8	4.59 ± 0.23
Size distribution				
10%	< 46.6 ± 2.3	< 0.11 ± 0.01	< 34.5 ± 1.7	< 1.62 ± 0.08
25%	< 86.5 ± 4.3	< 0.11 ± 0.01	< 73.6 ± 3.7	< 2.03 ± 0.10
50%	< 131.5 ± 6.6	< 0.14 ± 0.01	< 139.2 ± 6.7	< 2.87 ± 0.14
75%	< 189.9 ± 9.5	< 0.19 ± 0.01	< 229.6 ± 11.5	< 4.58 ± 0.23
90%	< 258.5 ± 12.9	< 0.28 ± 0.01	< 336.5 ± 16.8	< 8.44 ± 0.42
Density	2.3287 ± 0.0046 g/cm^3		2.2746 ± 0.0029 g/cm^3	

4.2.2. Effect of Heating under Air and Argon

The main issue in the production of graphite wasteform is the potential of the waste to oxidise to CO and/or CO_2 whilst being heat treated at low temperature. This behaviour can be seen in Figure 4-1, which demonstrates the oxidation reaction under air and argon (see below) resulting from continuous heating at 10°C/min. It is apparent that both of the graphite powders started to oxidise in air at temperatures as low as ~600°C, the percentage mass loss gradually increased after this temperature. It is hypothesised that if the lower heating rate and longer dwell time were used in the sintering process, it may also increase the loss of the graphite. This oxidation reaction is unacceptable, as if the irradiated graphite is considered, radionuclides such as ^{14}CO and $^{14}CO_2$

may be released to the biosphere. When the graphite powders are heated in argon, more than 95 % of the mass can be retained, suggesting that the presence of air is not possible if heating above 600°C is needed in the production of graphite wasteforms. The small loss of graphite under argon is probably due to the impurities in the gas (95 % pure according to manufacturer). It is also seen that the smaller particles of the graphite used in the DMO method resulted in a slight increase of the percentage mass loss in both heating environments. This is expected as the smaller particles have a large surface area and this promotes the oxidation reaction.

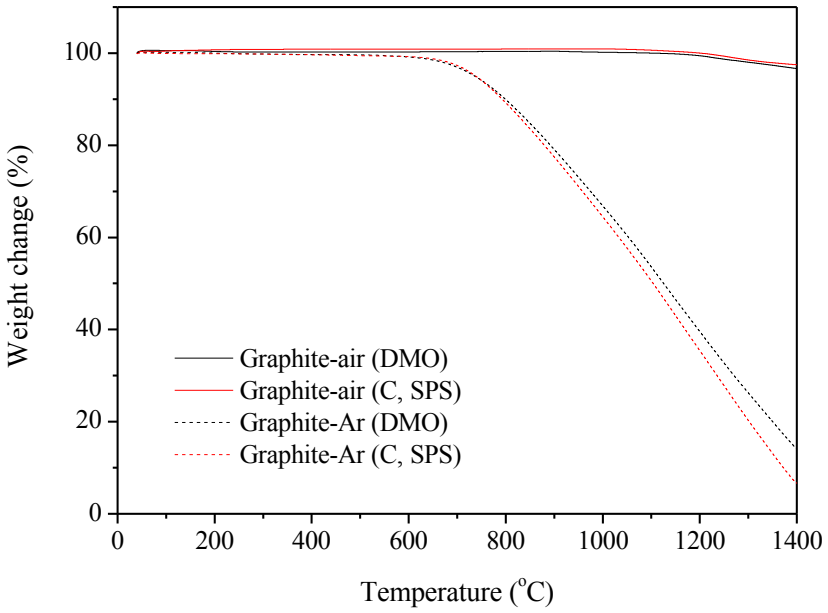

Figure 4-1: TGA of graphite powders measured under air and argon environments.

4.2.3. XRD

Figure 4-2a shows the normalised XRD patterns of graphite powders measured at room temperature. The diffractograms matched with PDF card 26-1076 and revealed the positions of the peaks for both of graphite powders are essentially identical; especially the maximum intensity peak is located at 26.5° 2θ. It is also evidenced in Figure 4-2a that the intensity of the secondary peak (54.6° 2θ) for graphite used in CPS and SPS processing is two magnitudes higher than the one used in DMO, suggesting a higher degree of crystallisation. Magnifying the diffractograms as shown in Figure 4-2b, peaks matched with sodalite ($Na_6Al_6(SiO_4)_6$, PDF card

04-009-5260) and some unknown peaks labelled with a star (*) were identified. It is thought that these peaks are due to contamination in the graphite powders. Comparing the diffractograms, it is clear that higher degree of sodalite crystallisation (as another 2 peaks were identified) is present in the graphite powder used in DMO processing. Due to the low intensity of the unknown peaks, the software could not identify these peaks. To address this issue, EDS analysis of the graphite powders was carried out and the results can be viewed in Section 4.2.5.

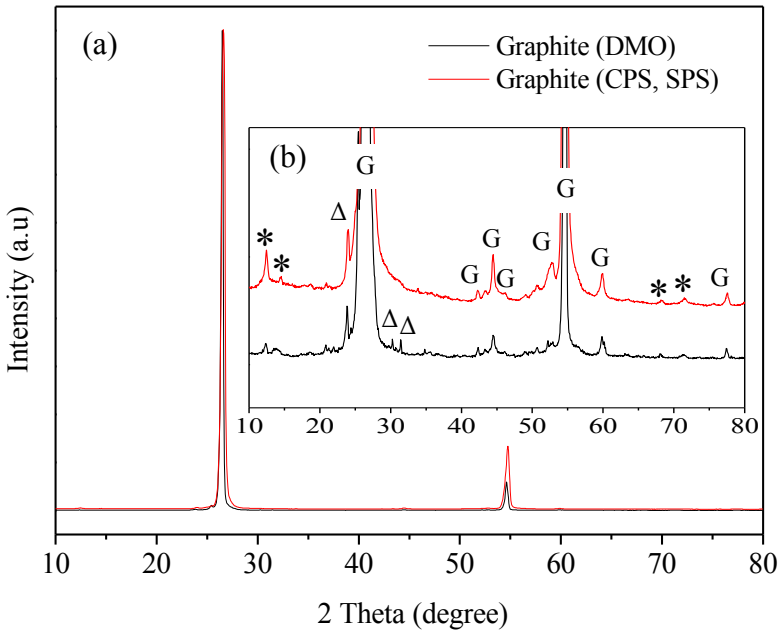

Figure 4-2: Normalised XRD patterns of graphite powders, (a) overall diffractograms, (b) close up of the diffractograms, * = unknown peak, Δ = $Na_6Al_6(SiO_4)_6$, G = graphite.

4.2.4. FTIR

The comparison of the FTIR spectra of both graphite powders used in this study is depicted in Figure 4-3. The absorption bands of the FTIR spectra are analysed based on the literature as follows: the band at about 771 cm^{-1} can be recognised as the stretching mode of C-H out-of-plane bending in *o*-substituted benzenes (Socrates 2004); the band at 1025 cm^{-1} is attributed to the vibration of C-H in plane bending in *p*-substituted benzenes (Socrates 2004) and may also correspond to the C-OH stretching mode (Yu *et al* 2014); the band at 1110 cm^{-1} is assigned as

the stretching mode of C-O, ketals and acetals (Socrates 2004, Wang and Dou 2012); the doublet observed at 1578-1635 cm^{-1} is believed to be due to C=C or C=O directly conjugated to the aromatic rings (Nakahara and Sanada 1995, Socrates 2004) and finally the band at 3430 cm^{-1} is associated with O-H stretching vibrations (Socrates 2004, Chen *et al* 2013b, Lipińska *et al* 2014, Olanipekun *et al* 2014). Theoretically, the FTIR spectrum of 100 % pure graphite is flat (without peaks) as no IR active functional group exists in this material (Choi *et al* 2010); another flat spectra of pure graphite with some contamination of C=C groups has been reported elsewhere (Yu *et al* 2014, Zhang *et al* 2014). Based on the FTIR analysis, it can be inferred that both of the graphite powders used in this study are not 100 % pure and are essentially contaminated with the hydrocarbon impurities.

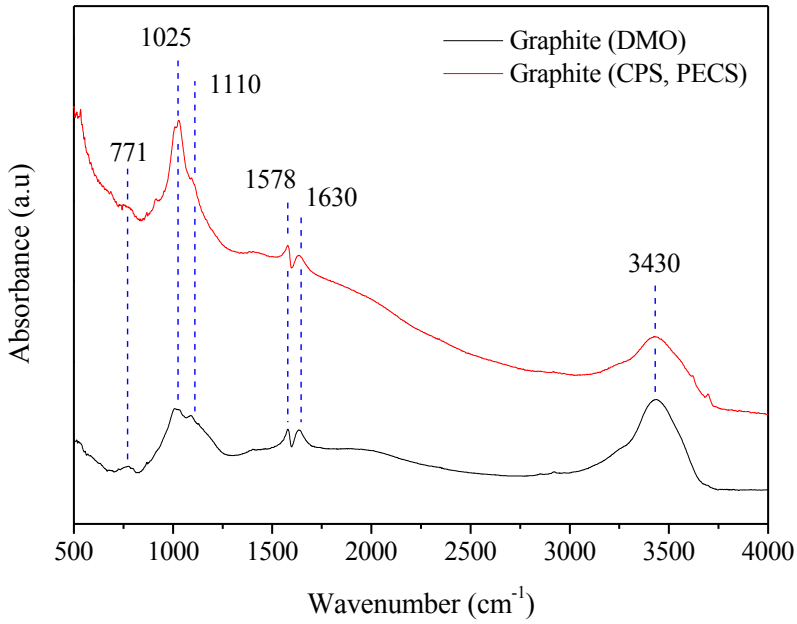

Figure 4-3: FTIR spectra of graphite powders.

4.2.5. Microstructure and EDS Analysis

The microstructure and compositional mapping analysis of the most contaminated graphite (used in DMO processing) are illustrated in Figure 4-4. SE image indicates that the graphite powder has an irregular shape with the average length of particles varying from 100 to 150 µm, which is consistent with the particle size analysis (Table 4-1). It is clearly seen that almost all particles

were identified as C (see Figure 4-4b). Based on the individual mapping images, minor contamination by chemicals such as Al, Si, S, Ca, Fe, K and Na can be distinguished. The similar position of Al, Si and Na species (see Figure 4-4Al, Si, Na) reflect the sodalite contamination that was previously detected in the XRD analysis (Section 4.2.3). Other contaminations may be recognised as calcium aluminosilicate and iron sulphide compounds. This statement is solely due to some elements being detected in a similar area; Al, Si, Ca (Figure 4-4Al, Si, Ca) and S, Fe (Figure 4-4S, Fe). Additionally, the Al, Si, S, Ca and Fe elements correlate well with the O. This leads to the suggestion that these elements may as well present as oxide phases.

The compositional mapping analysis of the graphite powders used in the CPS and SPS processing is shown in Figure 4-5. Basically, the elemental images exhibited identical contaminations albeit less detection of XRD peaks (refer Figure 4-2b). Larger particle size than graphite that utilised in DMO processing can be seen in the SE image (Figure 4-5a). This is also in agreement with the particle size analysis. Potential sodalite and calcium aluminosilicate compounds as well as the Al, Si, S, Ca and Fe correlate well with O are also detected in this graphite batch; refer Figure 4-5O, Al, Si, S, Ca, Fe and Na. However, the possibility of iron sulphide compound existed in DMO graphite is not visible in the mapping analysis of the new batch; Figure 4-5S and Fe show that Fe and S are present in different places.

Overall, the small contamination of both graphite samples detected by EDS analysis may at least explain the detection of unknown peaks in the XRD diffractograms. The impurities were thought to originate from the graphite manufacturing process; as-received graphite powders without any treatments were characterised. Although both of the graphite samples were mostly identified as C, it should be noted that this contamination will affect the production of wasteforms in this research.

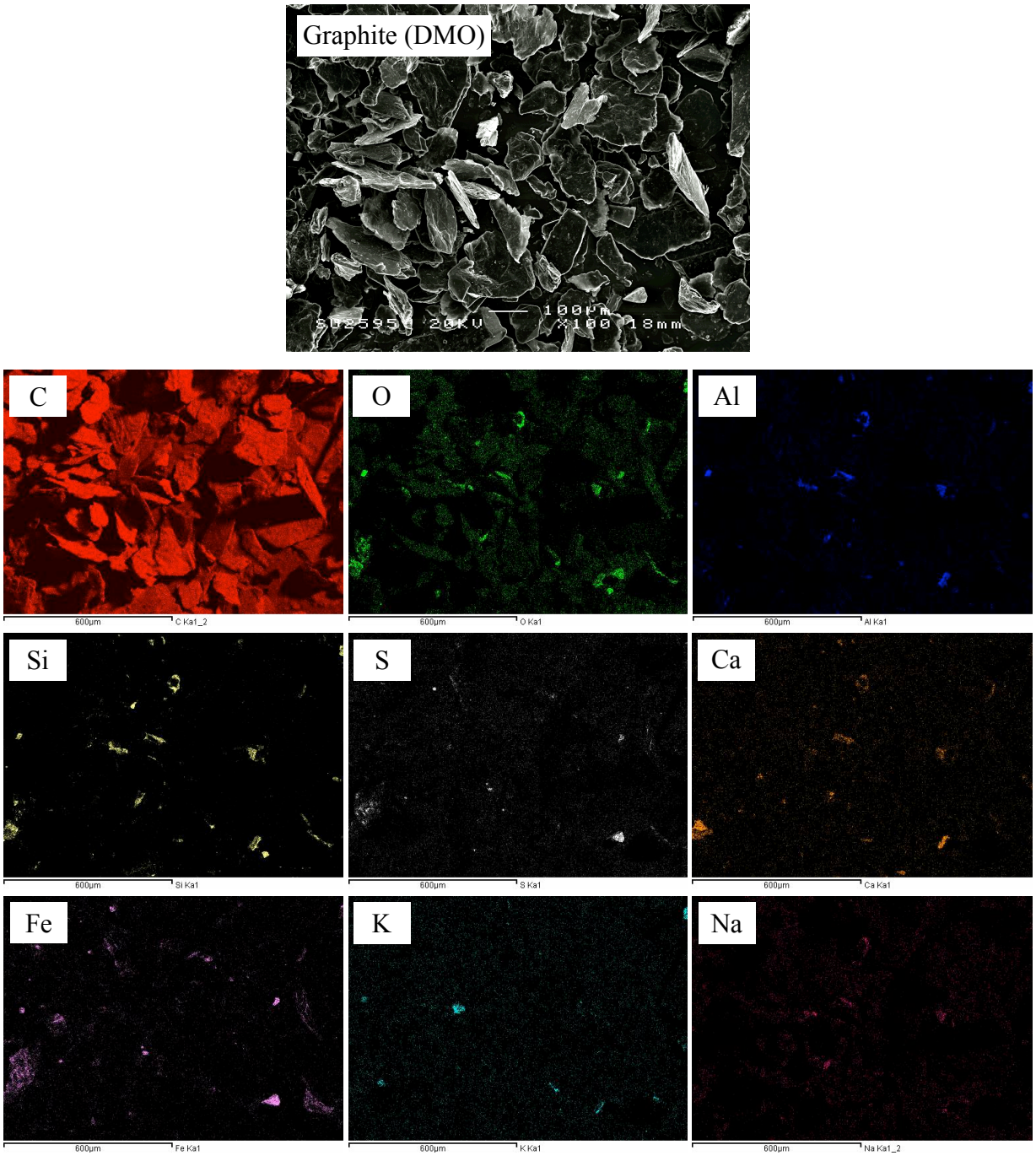

Figure 4-4: SE micrograph and individual compositional analysis of graphite powder used in DMO processing.

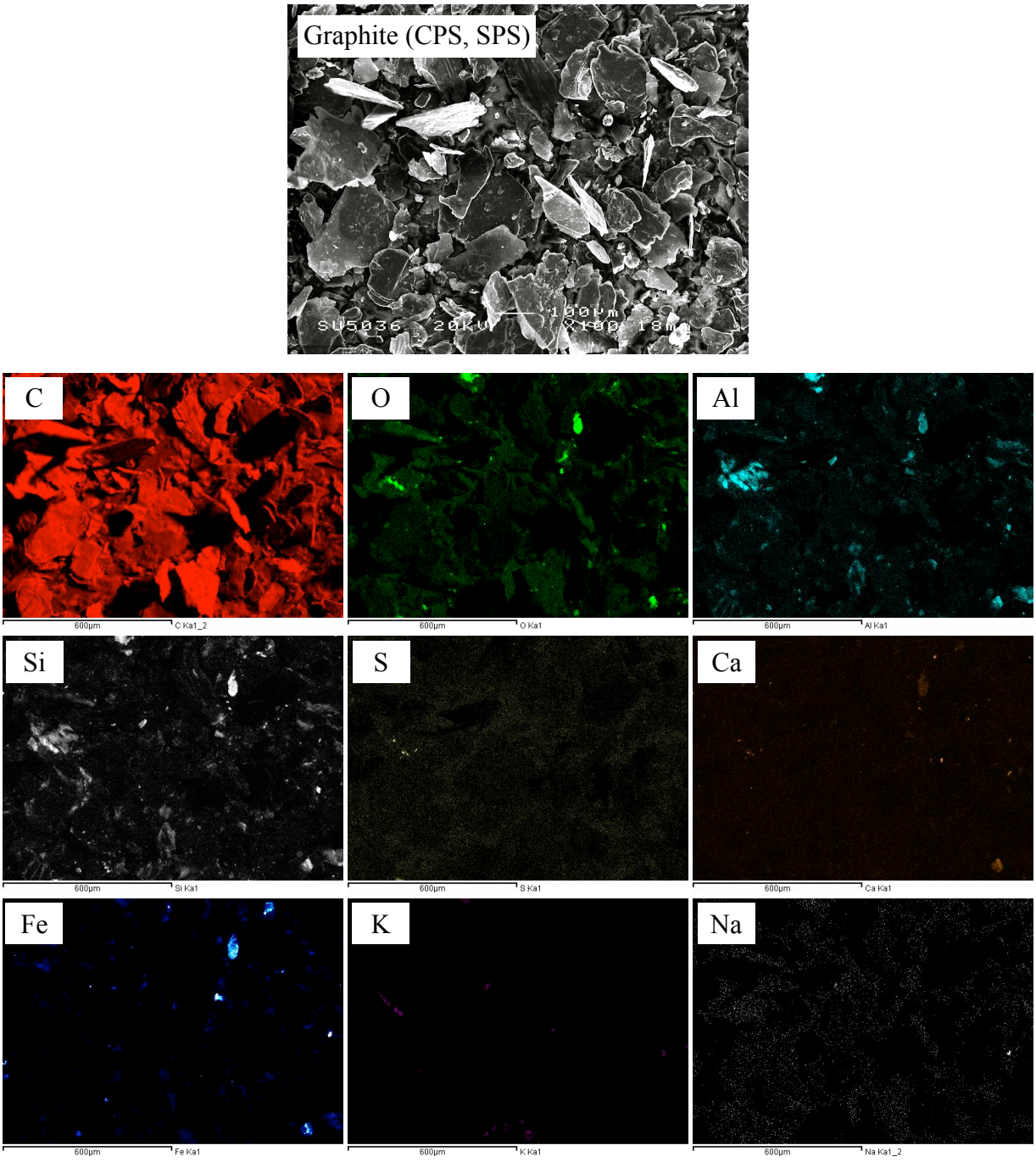

Figure 4-5: SE micrograph and individual compositional analysis of graphite powder used in CPS and SPS processing.

4.3. Characterisation of Iron Phosphate Base Glasses

This section describes various characterisation data of iron phosphate base glasses prepared using DMO and conventional melt processing. Note that only iron phosphate based glass without the addition of graphite is being discussed. In this particular section, the intention is to compare the properties of iron phosphate glasses formed using unconventional (microwave melting) and conventional melt processing methods.

4.3.1. Chemical and Physical Properties

Information about chemical and physical properties of the IP base glasses prepared using DMO and conventional processing methods is detailed in Table 4-2.

Table 4-2: Properties of iron phosphate glasses prepared using microwave and conventional melting methods.

Element	As batched	Microwave (EDS)		Conventional (EDS)
Fe (at.%)	12.90	13.78 ± 0.12	13.75 ± 0.07	13.43 ± 0.06
P (at.%)	19.35	19.88 ± 0.04	20.31 ± 0.03	20.64 ± 0.01
Al (at.%)	-	-	-	0.37 ± 0.04
Si (at.%)	-	0.95 ± 0.12	0.46 ± 0.04	-
O (at.%)	67.74	65.39 ± 0.03	65.47 ± 0.03	65.57 ± 0.01
Fe_2O_3 (mol %)	40.00	40.94 ± 0.44	40.37 ± 0.17	39.42 ± 0.09
P_2O_5 (mol %)	60.00	59.06 ± 0.64	59.63 ± 0.23	60.58 ± 0.14
Melting time (min)		8	20	180
Mass loss (%)		29.3 ± 2.9	28.6 ± 2.9	27.0 ± 2.7
T_g - DTA (ºC)		489 ± 5	490 ± 5	474 ± 5
Density (g/cm^3)		2.9955 ± 0.0005	3.0110 ± 0.0064	3.0904 ± 0.0004

In DMO processing, the raw materials of the glass were successfully transformed to glass after 8 minutes melting, with a black shiny solid being formed after rapid cooling of the melt. An

identically coloured glass was obtained from the conventional melt processing. The chemical composition analysis revealed that there is a lower amount of P in the microwaved iron phosphate glasses. This suggests that the higher heating rate during the microwave melting led to slightly increased P loss. Corrosion of the vitreous silicate or mullite crucibles by the glass melt at high temperatures was confirmed as some contamination by Si or Al was detected. The difference in the chemical compositions is in agreement with the mass loss data, which shows higher mass loss for the microwaved glasses. Despite the differing amounts of P in the glasses, T_g and powder density of iron phosphate glasses obtained from conventional and microwave melting were similar.

4.3.2. XRD

XRD patterns for the base iron phosphate glass prepared by means of DMO and conventional melting are shown in Figure 4-6.

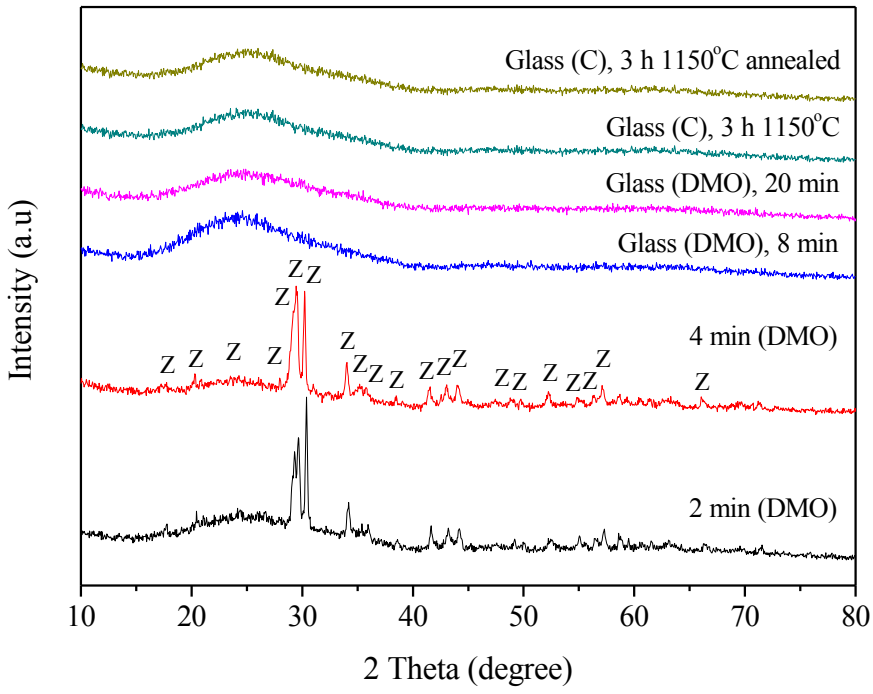

Figure 4-6: XRD patterns of iron phosphate glasses prepared by microwave and conventional heating, Z = $Fe_2(P_2O_7)$.

After microwaving for 2 and 4 minutes a number of peaks were observed which were matched with $Fe_2(P_2O_7)$, PDF card 04-009-4840. Traces of an amorphous phase were also detected in these samples. The intensity of some peaks decreased after 4 minutes of microwave heating, indicating a reduction in crystallinity. On further increasing the microwave times to 8 minutes or 20 minutes, the diffractogram shows diffuse scattering between 20 and 35° of 2θ and an absence of any distinct crystalline species. This is consistent with the presence of iron phosphate glass in the sample. A similar pattern was also obtained from iron phosphate glasses prepared by using conventional heating, whether involving rapid quenching into water or annealing of the cast glass.

4.3.3. FTIR

The FTIR spectra for the IP base glasses produced using DMO and conventional melting methods are displayed in Figure 4-7.

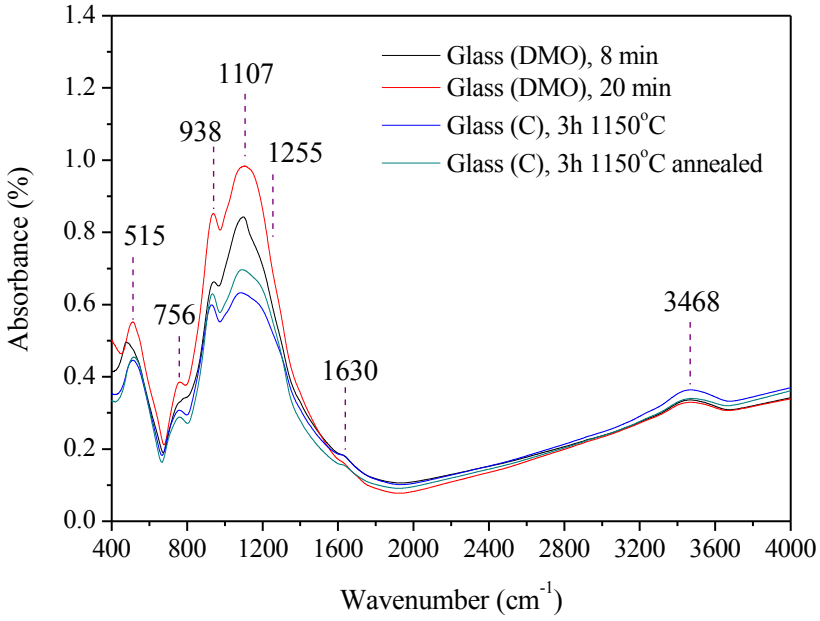

Figure 4-7: FTIR spectra of IP base glasses.

In general, the patterns of the spectra for all glasses have peaks at identical wave numbers implying all the glasses shared similar chemical functional groups. According to the literature,

the peaks can be assigned to specific bond vibrations that are consistent with iron phosphate glasses as follows: 515 cm^{-1} is due to overlapping vibrations of bending of O-P-O in P_2O_7 units, and of Fe-O bonds (Schofield 2011, Lai *et al* 2011a, Joseph *et al* 2012, Lai *et al* 2014); 756 cm^{-1} to symmetric stretching of P-O-P bridges (Kim and Day 2003, Schofield 2011, Lai *et al* 2011a, 2011b, 2014); 938 cm^{-1} is attributed to asymmetric stretching P-O-P bridges (Schofield 2011, Lai *et al* 2011b, 2014); 1107 cm^{-1} to P-O Q^1 terminal oxygens (Schofield 2011, Lai *et al* 2011a); 1255 cm^{-1} corresponds to P=O (Schofield 2011, Lai *et al* 2011a, 2014) and the rest of the peaks (1630 and 3468 cm^{-1}) are related to P-OH or water (Lai *et al* 2011a, 2011b).

4.4. Characterisation of Iron Phosphate Glass Composites

The characterisation data of produced iron phosphate glass composites containing 20 - 38 wt% graphite powder formed using DMO are discussed in this section. Selected DMO samples are compared with the samples made using the CPS method. This section is divided into 4 parts namely physical properties, XRD, FTIR, and finally microstructure and EDS analysis. The focus of this section is to identify the potential of DMO processing in the production of graphite wasteform based iron phosphate glass compositions.

4.4.1. Physical Properties

The mass loss of the microwaved IP20G glass composites is presented in Figure 4-8. Pellets microwaved for 1, 2 and 3 minutes show increasing mass losses of 17.6 ± 1.8, 24.1 ± 2.4 and 26.9 ± 2.7 %, indicating the removal of volatile elements. After 4 minutes microwave processing, the mass change of the microwave heated pellets was 28.2 ± 2.8 % and there was no significant change as the microwave processing time was increased from 4 to 20 minutes.

Figure 4-9 shows the variation in density of the pellets and powdered IP20G glass composites as a function of microwave processing time. In general, the bulk density of the pellets decreased gradually from the green state up to 3 minutes processing time, became stable for processing times varying from 4 to 12 minutes, increased slightly again between 12 and 14 minutes and reached its maximum value for processing times varying from 14 to 20 minutes. It is thought that

at this time frame (14 – 20 minutes) the glass component was partially liquid, which enabled some pore filling and leads to the release of entrapped gasses, thus increasing the bulk density of the composites. In contrast the density of the powdered iron phosphate glass composites gradually increased for processing times up to 4 minutes and thereafter was stable for processing times between 4 and 20 minutes.

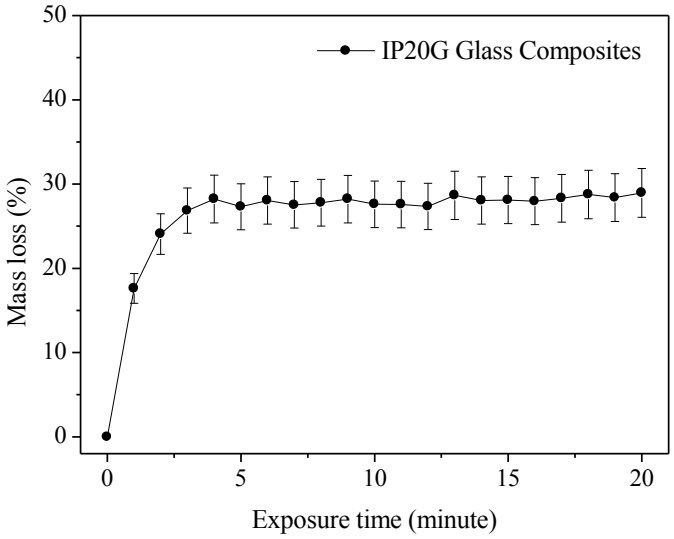

Figure 4-8: Mass loss of microwaved IP20G glass composites.

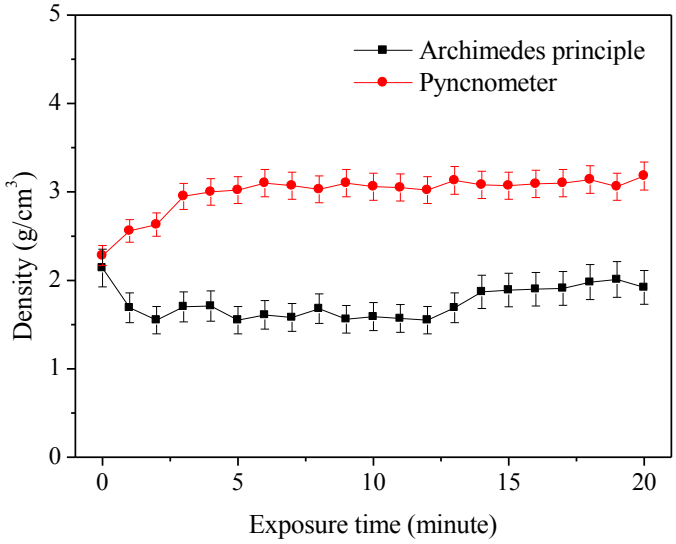

Figure 4-9: Bulk and powdered densities of microwaved IP20G glass composites at various exposure times.

From the density data, the porosity of the samples was calculated. As can be seen from Figure 4-10 it is apparent that the microwaved samples are highly porous with only a limited decrease in porosity for microwave processing times in excess of 14 minutes. Based on the physical properties of the IP20G series, it was inferred that 20 minutes is an adequate exposure time to complete the reaction of the iron phosphate glass composites for higher graphite loadings.

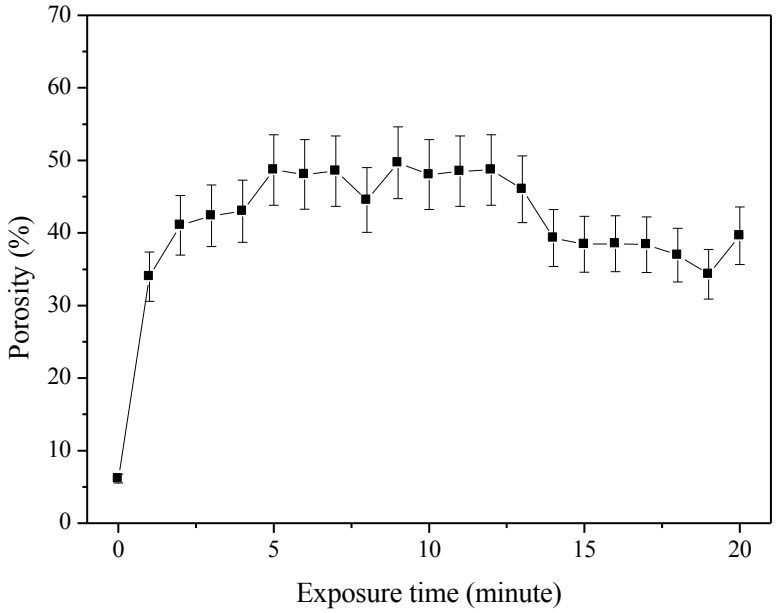

Figure 4-10: Porosity of microwaved IP20G glass composites at various exposure times.

The physical properties of iron phosphate composites containing various waste loadings and produced in various environments are listed in Table 4-3. It is found that similarly high porosity values were obtained from samples IP30G and IP38G. This not acceptable as the high porosity material will increase the volume and lower the mechanical properties as well as the chemical durability (when in contact with water) of the final wasteform, hence only limited analysis was conducted on these samples. Table 4-3 also shows that there is no significant difference between samples with a 20 wt% waste loading that have been microwave processed in air or in argon with both samples showing between 36 and 38 % porosity. In comparison IP20G samples that were conventionally sintered (CPS) at 770°C for 2 h exhibit much lower porosity levels of about 15 % (see Section 5.3 for detailed analysis of iron phosphate graphite-glass materials made using CPS).

Table 4-3: Physical properties of various iron phosphate glass composites.

Sample	Measured mass loss (%)	Bulk density (g/cm^3)	Powdered density (g/cm^3)	Porosity (%)
IP38G (DMO), 20 min	22.9 ± 2.3	1.6 ± 0.2	2.8 ± 0.1	42.8 ± 4.3
IP30G (DMO), 20 min	25.8 ± 2.6	1.6 ± 0.2	2.9 ± 0.1	45.8 ± 4.6
IP20G (DMO), 20 min	29.0 ± 2.9	1.9 ± 0.2	3.2 ± 0.2	36.9 ± 3.7
IP20G (DMO), 20 min (Ar)	29.2 ± 2.9	1.9 ± 0.2	3.0 ± 0.2	37.5 ± 3.8
IP20G (CPS), 2h 770°C (Ar)	0.6 ± 0.1	2.6 ± 0.3	3.1 ± 0.2	14.9 ± 1.5

4.4.2. XRD

Figure 4-11 shows the XRD patterns of IP20G glass composites produced using various exposure times, environments and sintering methods. Graphite peaks can be seen in all of the XRD patterns. For all of the microwaved samples, mixtures of FeP_2O_6 (PDF 04-009-5697), $Fe(PO_3)_3$ (PDF 00-038-0109) and $Fe_2(P_2O_7)$ (PDF 04-009-4840) together with graphite contamination of sodalite (refer section 4.2.3) were detected. In addition, traces of Fe_2O_3, $NH_4H_2PO_4$ and Fe_3O_4 were also identified in samples microwaved for 1 to 3 minutes. This agrees with the mass loss data that suggest decomposition of the raw materials occurs on this time scale. The formation of Fe_2O_3 at shorter exposure times was due to oxidation of Fe_3O_4. This oxidation process seems to occur during the initial rapid heating phase. Based on the diffractograms, it is seen that the peaks related to iron phosphate crystalline phases become sharper and more pronounced/dominant as the microwave processing time increases while heating under air. There is a slight decrease in the relative intensity of the iron phosphate phases in samples that were microwaved for 20 minutes under argon. Identical crystalline phases, but with more clearly defined XRD patterns, were also found for the IP20G sample that was conventionally sintered at 770°C for 2 hours in argon. Similar crystallisation data were obtained for samples that contained 30 and 38 wt% graphite although, as expected, the intensities of the graphite peaks increased with increasing waste loading. It is worth noting that the diffuse scattering pattern located between 20 and 35° of 2θ was present in all diffractograms. However, in this case the diffuse scattering patterns are not visible in Figure 4-11 due to the intensity scale used.

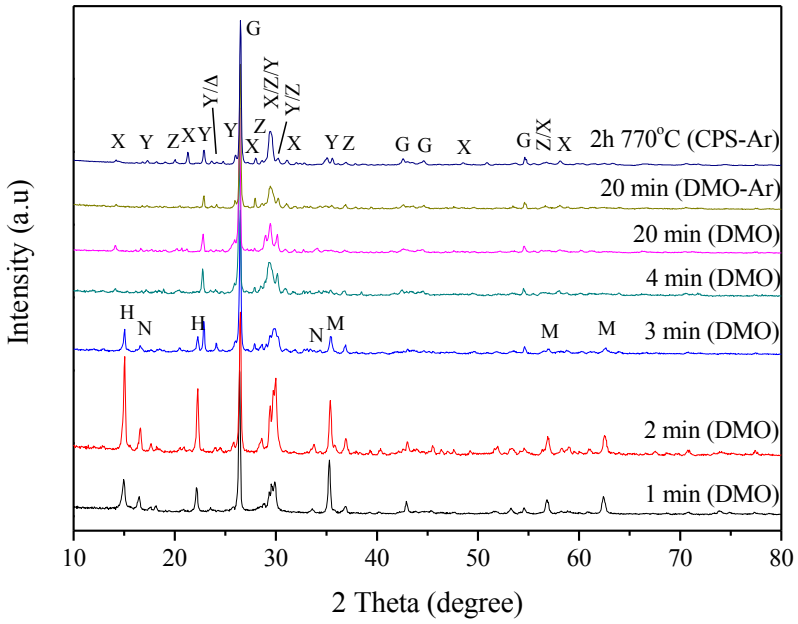

Figure 4-11: Normalised XRD patterns of IP20G glass composites, H = Fe_2O_3, N = $NH_4H_2PO_4$, M = Fe_3O_4, X = FeP_2O_6, Y = $Fe(PO_3)_3$, Z = $Fe_2(P_2O_7)$, Δ = $Na_6Al_6(SiO_4)_6$, G = Graphite.

4.4.3. FTIR

According to the XRD analysis it is expected that the FTIR spectra of the iron phosphate glass composites will have contributions from the glass, crystalline phases and graphite. The aforementioned spectra obtained from IP20G samples prepared using DMO and CPS methods are presented in Figure 4-12. By considering the information in Section 4.2.4 and 4.3.3, the contributions of graphite and IP glass can be distinguished and are labelled as G and I. The rest of the peaks are thought to be from crystalline phases that precipitated during sintering. Overall, there is no significant difference in the position of the peaks for all the IP20G composites. The peaks have been assigned as follows: 504 cm^{-1} is due to O-P=O bending vibrations (Abid *et al* 2003), 563 cm^{-1} to the O-P-O bending mode (Lai *et al* 2014), 601 cm^{-1} is due to Fe-O vibrations, and can be observed if Fe_2O_3 content greater than 20 mol % (Jermoumi *et al* 2002), 714 cm^{-1} to P-O-P bridge symmetric stretching (Karabulut *et al* 2003), 920 cm^{-1} to P-O-P asymmetric stretching in Q^0 units (Lai *et al* 2014), 1005 and 1145 cm^{-1} are the vibrations of $P\text{-}O^-$ groups, chain terminator (Hafid *et al* 2002), 1184 cm^{-1} to asymmetric and symmetric vibrations of $(PO_2)^-$

in Q^2 units (Moguš-Milanković *et al* 2004) and finally 1231 cm^{-1} to P=O in Q^3 groups (Bingham *et al* 2005).

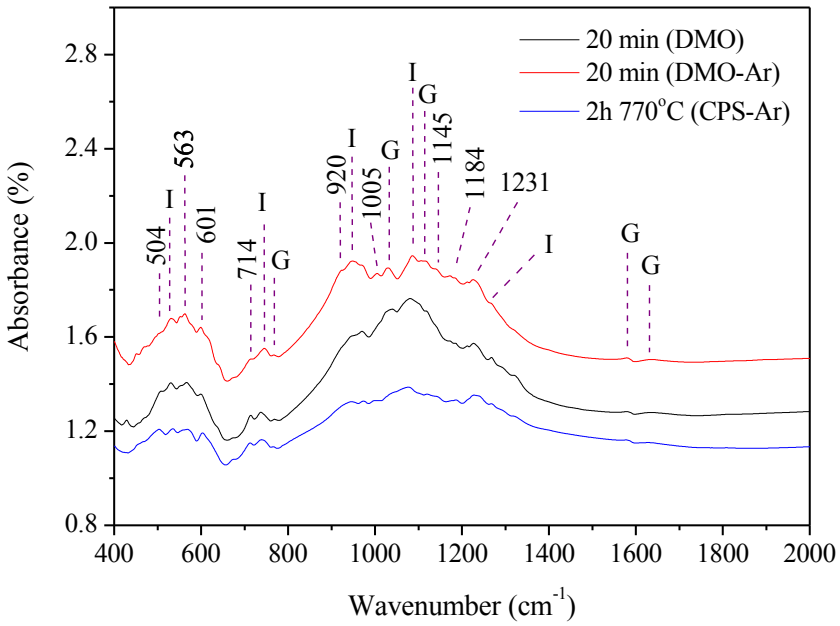

Figure 4-12: FTIR spectra of IP20G glass composites, I = contribution from IP glass, G = contribution from graphite.

4.4.4. Microstructure and EDS Analysis

The nature of the produced pellets from both microwave and CPS processing as well as the optical microscope images of the samples are shown in Figure 4-13. It is clear that the use of raw materials (iron and phosphate precursors) in microwave processing affects the structural integrity of the pellets; some material has formed a liquid phase on top of the sample whilst microwaving (Pellet a); this is most probably caused by the aggression of the released gases that occurred in the decomposition process of the raw materials. By using pre-made iron phosphate glass powder (Pellet b) in CPS processing, this effect is negligible, presumably because there are no volatile materials apart from graphite in the sample. Optical images of the microwaved IP20G at 20 minutes confirm the high amount of porosity compared to the equivalent sample composition prepared using CPS (see optical microscope images, Figure 14-13a and 14-13b).

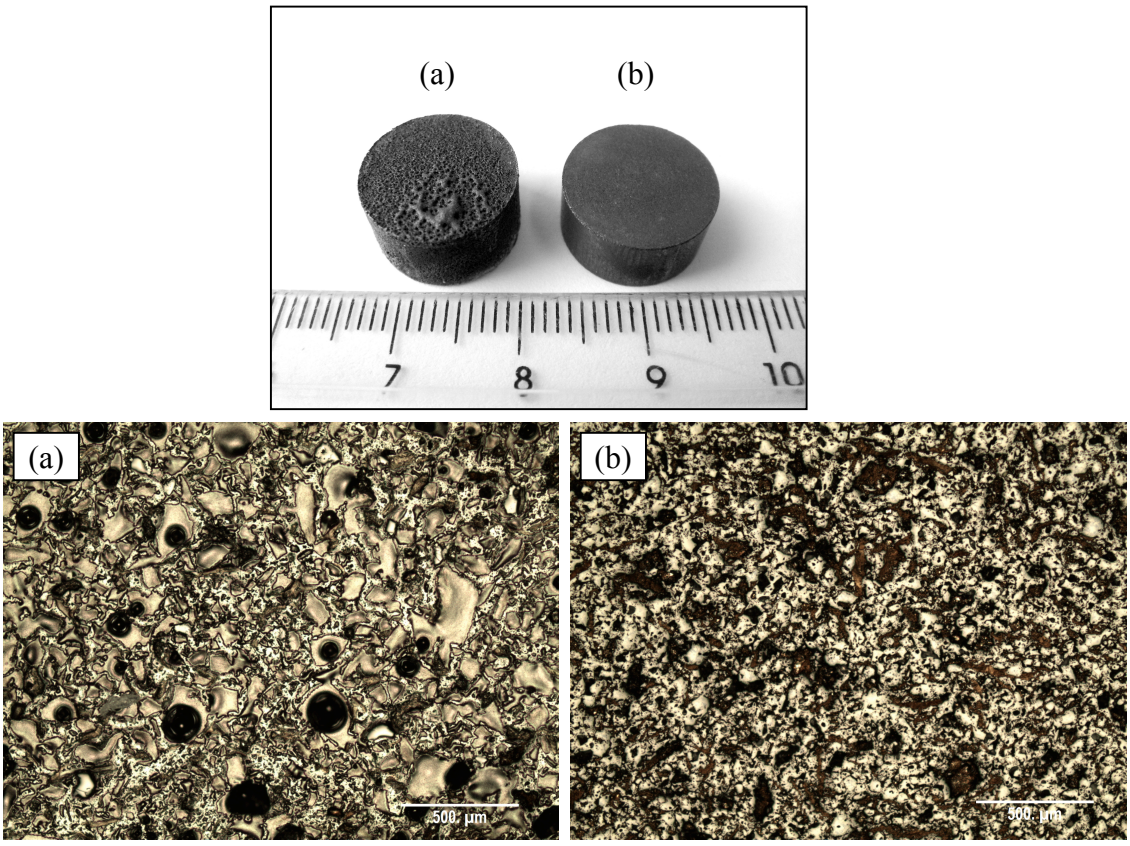

Figure 4-13: Photographic and OM images of iron phosphate glass composites (a) IP20G (DMO), 20 min (b) IP20G (CPS), 2h 770°C (Ar).

Figure 4-14 exhibits SEM micrographs of iron phosphate phases encapsulating the graphite particles. For all of the microwaved samples, it is apparent that some of the graphite has oxidised, with the effect of this oxidation process being indicated by the spherical porosity on the graphite particles (indicated by arrows). Figures 4-14c and 4-14d confirm the presence of extensive porosity in the microwaved IP30G and IP38G samples; an evidence of graphite particles pull out from grinding and polishing process is also shown in Figure 4-14c. A reduction of porosity can be seen by comparing micrographs for samples processed for 20 minutes in air using the DMO (Figure 4-14a) with those processed for 2 hours using CPS under argon (Figure 4-14e). The microstructures of samples microwaved for 20 minutes under air or argon were found to be similar (see Figure 4-14a and 4-14b). The extent of the crystalline phases as against glassy phases encapsulating the graphite particles seems to be higher for the conventionally sintered samples than in those prepared using a DMO (compare Figure 4-14a with 4-14d).

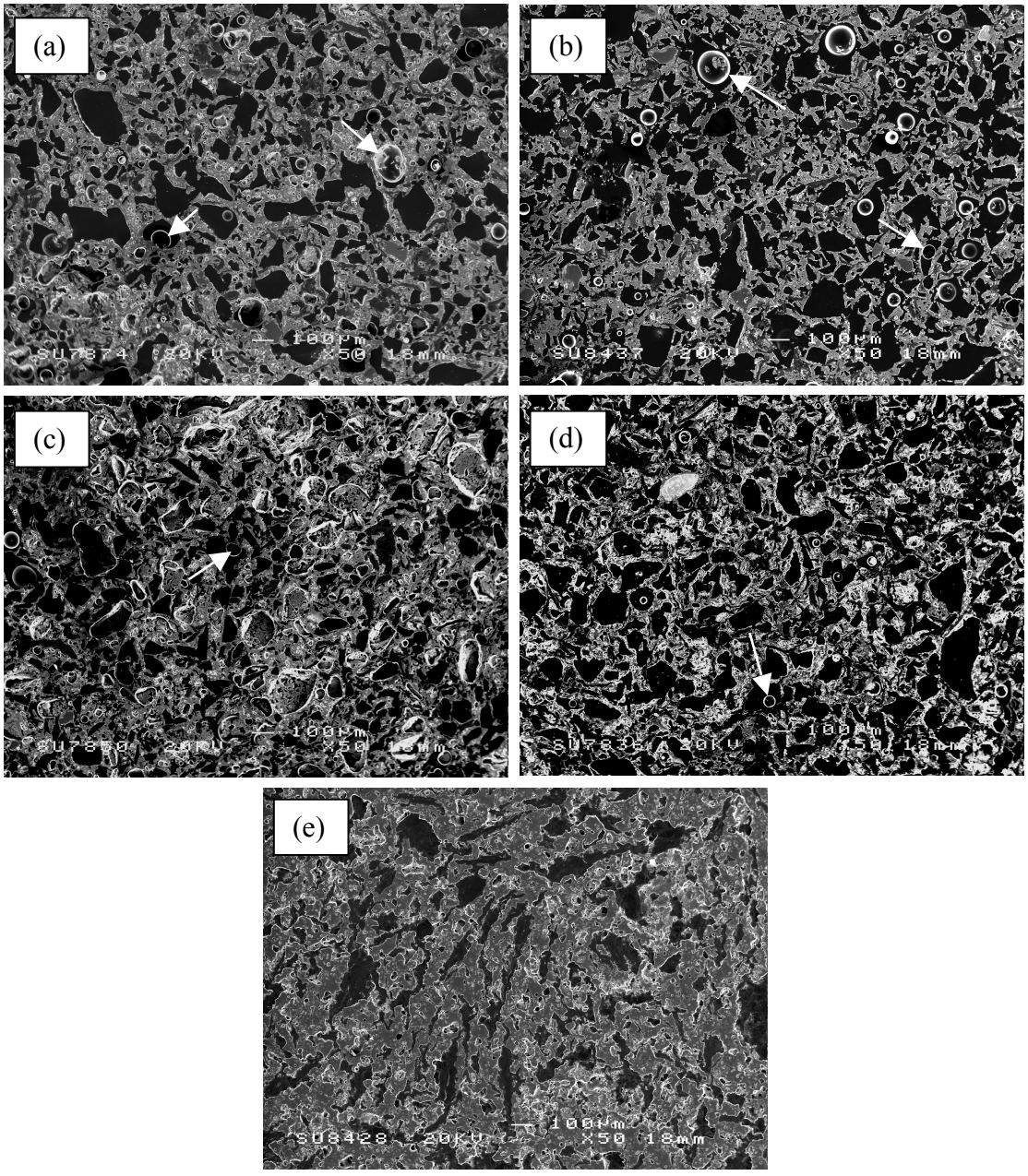

Figure 4-14: SEM micrographs of iron phosphate glass composites, (a) IP20G (DMO), 20 min, (b) IP20G (DMO), 20 min (Ar), (c) IP30G (DMO), 20 min , (d) IP38G (DMO), 20 min, (e) IP20G (CPS), 2h 770°C (Ar).

When using raw materials in DMO processing and pre-made glass in CPS processing, the distribution of Fe and P is homogeneously encapsulating graphite particles. This can be clearly seen by comparing the compositional mapping analysis in Figure 4-15 with Figure 4-16. It is

worth noting that the graphite particles in both samples are completely separated from the iron phosphate phases, suggesting encapsulation and that no chemical reaction between these materials occurred during sintering.

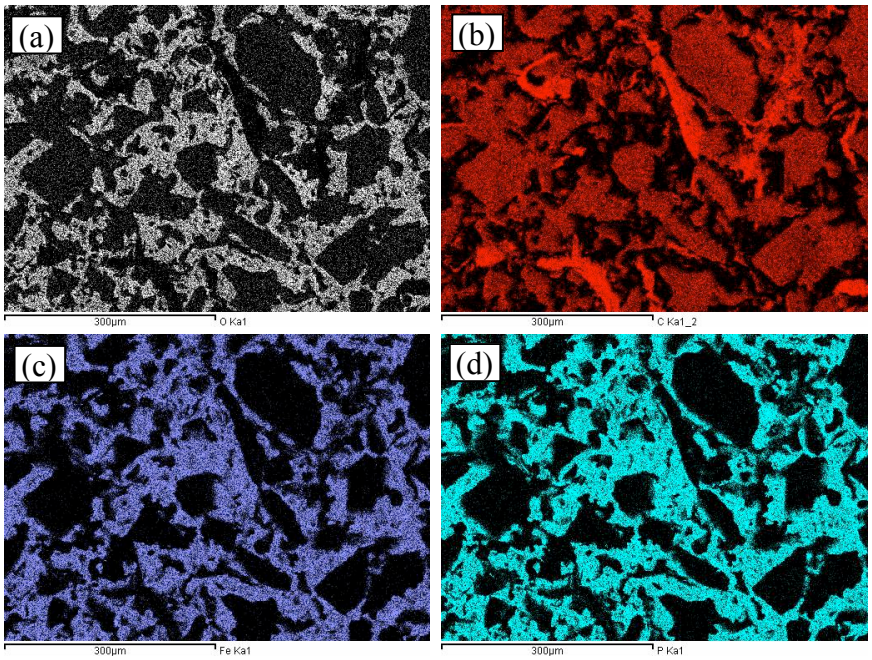

Figure 4-15: Elemental mapping analysis of IP20G (DMO), 20 min, (a) O, (b) C, (c) Fe, (d) P.

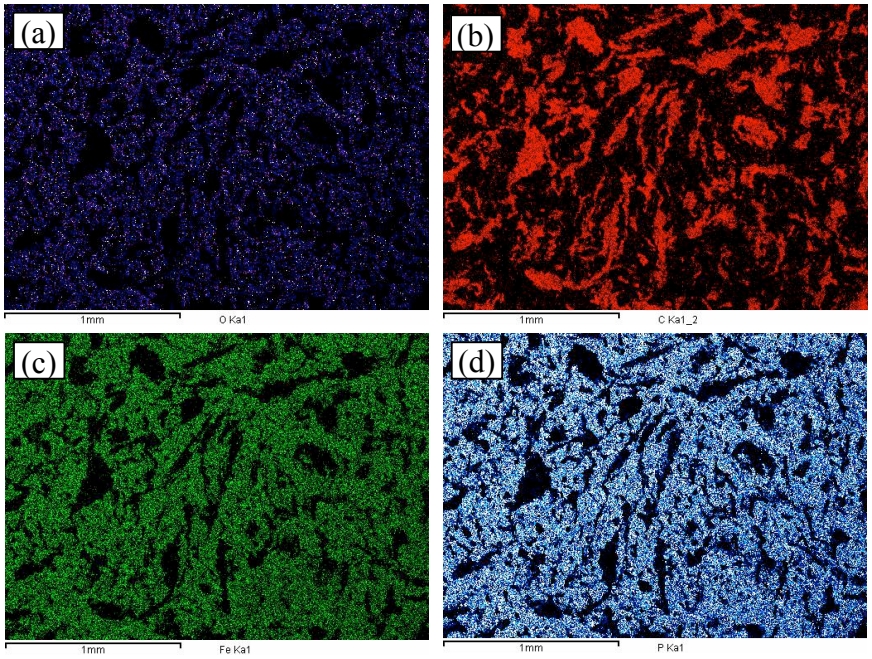

Figure 4-16: Elemental mapping analysis of IP20G (CPS), 2h 770°C (Ar), (a) O, (b) C, (c) Fe, (d) P.

Higher magnification SEM images suggest that at least 3 different components are present in the samples (see Figure 4-17). The black regions were confirmed to be graphite by EDS analysis. From the EDS spectra, areas A and C contain Fe and P, whereas areas B and D also contain Si, Al and/or Ca. Based on compositional mapping analysis of the graphite Al, Si and Ca are confirmed to originate from graphite (Section 4.2.5); Al or Si may also result from contamination of the crucibles (Table 4-1). It is clear that the phosphate and iron ratios were in line with the XRD analysis. The measured P:Fe ratios can be matched with crystalline phases identified by XRD as follows: FeP_2O_6 (Fe:P = 1:2) - areas $A/A_1/A_2$, $Fe(PO_3)_3$ (Fe:P = 1:3) - areas $B/B_1/D$ and $Fe_2(P_2O_7)$ (Fe:P = 1:1) - area C.

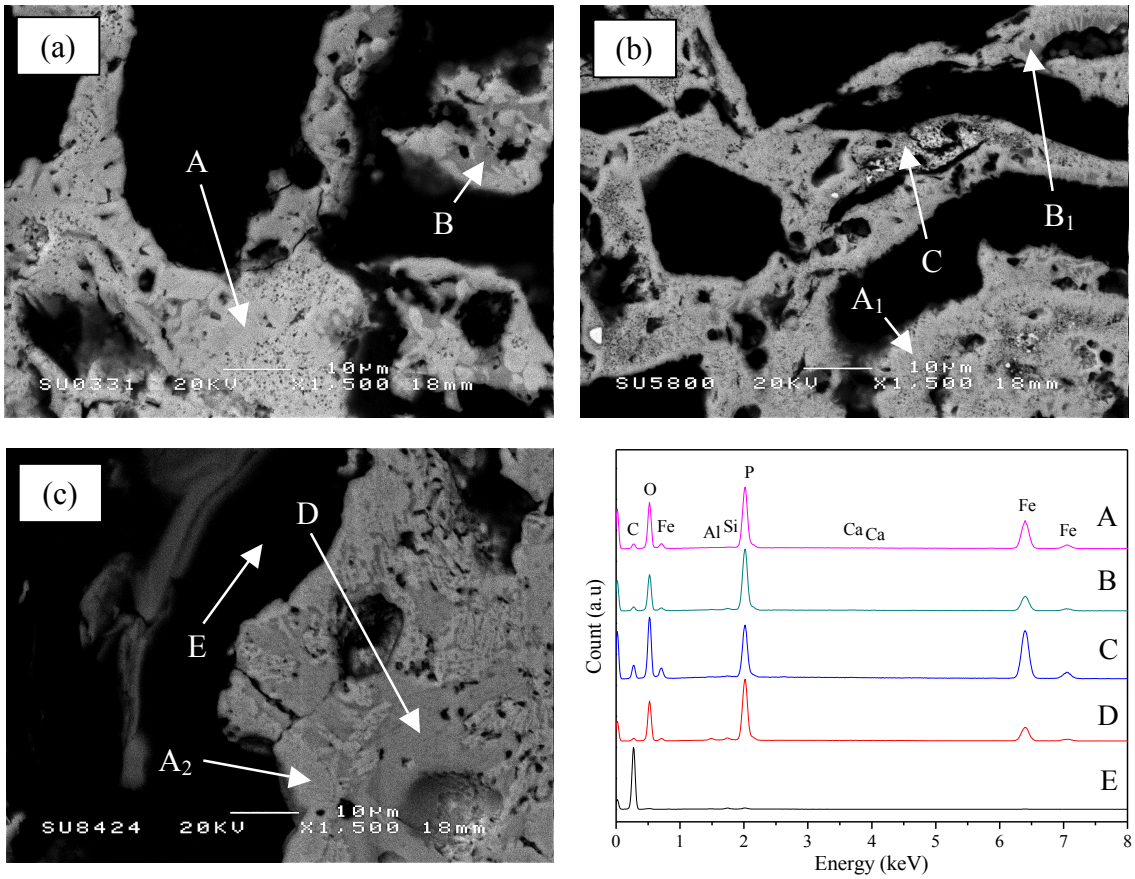

Figure 4-17: Backscattered electron SEM micrographs and normalised EDS spectra of iron phosphate glass composites, (a) IP20G (DMO), 20 min, (b) IP20G (DMO), 20 min (Ar), (c) IP20G (CPS), 2h 770°C (Ar).

4.5. Mössbauer Spectroscopy Analysis

Figure 4-18 indicates the fitted Mössbauer spectra for selected glasses and IP20G composite materials. The fitted Mössbauer parameters are given in Table 4-4. Fe^{2+} and Fe^{3+} were assigned by considering the work of Darby-Dyar et al. (Dyar *et al* 2006). Mössbauer parameters from the literature for iron phosphate glasses (Forder *et al* 2012), FeP_2O_6 (Ericsson *et al* 1990), $Fe(PO_3)_3$ (Elbouaanani *et al* 1999) and $Fe_2(P_2O_6)$ (Ericsson *et al* 1990, Millet *et al* 1989) were used as references in the fitting. The magnetite used in this work matched with PDF card 19-629, and contained 69 % Fe^{3+} and 31 % Fe^{2+}.

Some reduction of Fe^{3+} to Fe^{2+} occurred during the initial stages of glass processing (when no carbon was present) whether this involved 8 minutes in a microwave or 3 hours in a conventional melting furnace. This reducing environment occurred due to the presence of NH_3 generated from the decomposition of the ammonium dihydrogen phosphate used as a phosphate source. As the microwave melting time increased to 20 minutes, the amount of Fe^{3+} increased significantly, indicating that a longer melting time leads to oxidation of iron. It is found that rapid quenching or annealed glasses prepared using conventional glass melting resulted in a similar $Fe^{2+}/\Sigma Fe$ ratio. The iron phosphate composite materials, on the other hand, had much more complicated Mössbauer spectra due to the contribution of Fe^{2+} and Fe^{3+} in glassy and crystalline phases. Generally, IP20G samples prepared using both DMO and CPS methods shows that some iron has been reduced, consistent with loss of graphite. It is clear that the reduction of iron occurred to a greater extent in the IP20G (DMO) composite microwaved for 20 minutes in air compared to the equivalent sample that was microwaved for 20 minutes under argon with the $Fe^{2+}/\Sigma Fe$ ratios being 62 to 51 % respectively. A decreased amount of crystalline phases and increased glassy content were also seen in sample that was microwaved under argon. Comparing the microwaved composites with composites prepared using CPS, the contributions of glassy phase was dominant rather than crystalline phases. This is in line with the XRD analysis that indicated more intense and sharper crystallisation peaks for the CPS composites. It is also worth noting that one unknown quadrupole was fitted to the CPS composite data. This phase was not detected in XRD analysis and due to the high value of QS, it is assigned as Fe^{2+}.

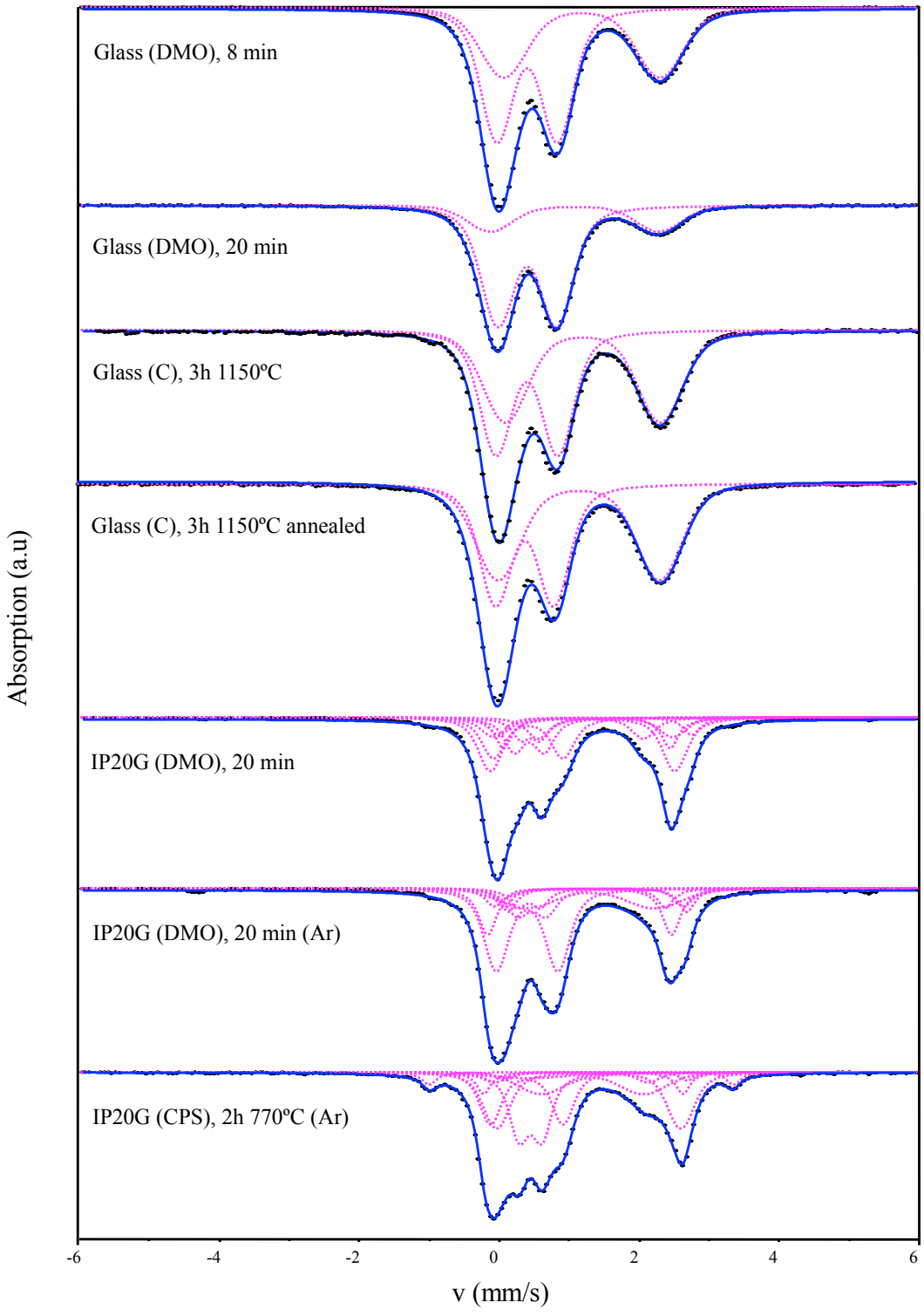

Figure 4-18: Mössbauer spectra of glass and glass composite samples formed using microwave and conventional melting/sintering methods.

Table 4-4: Mössbauer parameters (±0.02 mm/s) of glass and IP20G samples produced by microwave and conventional heating (CS = centre shift, QS = quadrupole splitting, FWHM = full width half maximum).

Sample	CS (mm/s)	QS (mm/s)	FWHM (mm/s)	Assigned phase	Area (%)	Site	$(Fe^{2+}/\Sigma Fe) \times 100$ %
Glass (DMO), 8 min	0.40	0.87	0.14	Glass	58	Fe^{3+}	42
	1.19	2.23	0.14	Glass	42	Fe^{2+}	
Glass (DMO), 20 min	0.40	0.84	0.14	Glass	77	Fe^{3+}	23
	1.08	2.41	0.14	Glass	23	Fe^{2+}	
Glass (C), 3 h 1150˚C	0.40	0.89	0.14	Glass	50	Fe^{3+}	50
	1.20	2.21	0.14	Glass	50	Fe^{2+}	
Glass (C), 3 h 1150˚C annealed	0.42	0.83	0.15	Glass	48	Fe^{3+}	50
	1.19	2.30	0.15	Glass	52	Fe^{2+}	
IP20G (DMO), 20 min	0.42	0.99	0.15	Glass	18	Fe^{3+}	62
	1.21	2.55	0.15	Glass	10	Fe^{2+}	
	1.31	1.50	0.15	FeP_2O_6	10	Fe^{2+}	
	1.19	2.64	0.15	FeP_2O_6	25	Fe^{2+}	
	0.43	0.42	0.15	$Fe(PO_3)_3$	13	Fe^{3+}	
	0.45	0.28	0.15	$Fe(PO_3)_3$	7	Fe^{3+}	
	1.25	2.38	0.15	$Fe_2(P_2O_7)$	11	Fe^{2+}	
	1.37	2.76	0.15	$Fe_2(P_2O_7)$	6	Fe^{2+}	
IP20G (DMO), 20 min (Ar)	0.40	0.88	0.14	Glass	33	Fe^{3+}	51
	1.22	2.31	0.14	Glass	6	Fe^{2+}	
	1.31	1.84	0.14	FeP_2O_6	16	Fe^{2+}	
	1.15	2.63	0.14	FeP_2O_6	16	Fe^{2+}	
	0.47	0.41	0.14	$Fe(PO_3)_3$	10	Fe^{3+}	
	0.43	0.36	0.14	$Fe(PO_3)_3$	6	Fe^{3+}	
	1.29	2.70	0.14	$Fe_2(P_2O_7)$	6	Fe^{2+}	
	1.41	2.55	0.14	$Fe_2(P_2O_7)$	7	Fe^{2+}	
IP20G (CPS), 2 h 770˚C (Ar)	0.40	1.04	0.12	Glass	19	Fe^{3+}	57
	1.03	2.20	0.12	Glass	4	Fe^{2+}	
	1.33	1.47	0.12	FeP_2O_6	15	Fe^{2+}	
	1.28	2.63	0.12	FeP_2O_6	25	Fe^{2+}	
	0.45	0.33	0.12	$Fe(PO_3)_3$	21	Fe^{3+}	
	0.42	0.39	0.12	$Fe(PO_3)_3$	3	Fe^{3+}	
	1.20	2.85	0.12	$Fe_2(P_2O_7)$	6	Fe^{2+}	
	1.39	2.60	0.12	$Fe_2(P_2O_7)$	2	Fe^{2+}	
	1.18	4.35	0.12	Unknown	4	Fe^{2+}	

4.6. Discussion

Microwave and conventional melting resulted in iron phosphate glasses with largely similar physical and structural properties, although the microwaved samples retained slightly less phosphorus than the conventionally melted samples, which is consistent with other reported studies (Bingham *et al* 2006, 2009). Due to the similar properties of the glasses prepared by the two methods, it is suggested that the temperature reached in the microwave processing is around 1150°C. If it is assumed that all of the ammonium dihydrogen phosphate completes the decomposition processes during microwave heating *i.e.*

$$2\left[NH_4H_2PO_4\right] \xrightarrow{\Delta Q} P_2O_5 + 2NH_3 + 3H_2O \qquad [4\text{-}1]$$

then a theoretical mass loss of glass during melting can be calculated based on an assumed iron oxidation state; the two extreme cases being all of the iron being present as Fe^{3+} *i.e.*

$$4Fe_3O_4 + O_2 \xrightarrow{\Delta Q} 6Fe_2O_3 \qquad [4\text{-}2]$$

or all of the iron being present in the Fe^{2+} *i.e.*

$$2Fe_3O_4 \xrightarrow{\Delta Q} 6FeO + O_2 \qquad [4\text{-}3]$$

The former case gives a theoretical mass loss of 25.4 % whereas the latter gives a theoretical mass loss of 28.6 %. In practice the actual mass loss of glass after 20 minutes in the DMO is in line with the larger of these two values being 28.6 ± 2.9 %, suggesting that all of the iron is present as Fe^{2+}. In contrast the Mössbauer results indicate $Fe^{2+}/\Sigma Fe = 0.23$ for this sample (see Table 4-4), which suggests that the weight loss should be less than 28.6 %. The glass prepared using conventional melting on the other hand agrees with the theoretical mass loss rather than that calculated based on the Mössbauer data. The cause of this discrepancy is not clear although it may be associated with the slightly lower amount of P_2O_5 in the microwaved glass (see Table

4-2). Therefore the experimental value of the mass loss for the base glass has been used in determining the extent of graphite loss from the microwaved composites.

The mass loss from the glass composites prepared in the DMO has been compared with the *measured* mass loss for full transformation of the raw materials to glass by microwave melting. This comparison indicates that for the microwaved IP20G samples formed in air and argon, up to 4.8 and 5.0 % of the total mass loss is due to oxidation of graphite, whereas these losses are reduced to 4.2 and 3.7 % for the IP30G and IP38G samples respectively. In contrast the IP20G samples sintered at 770°C using CPS had a much lower total mass loss about 0.6 %, which is equivalent to 0.4 % of graphite loss (considering the mass loss of glass component) whilst sintering. Although the properties of graphite used in the DMO processing was confirmed to accelerate the graphite oxidation (small particles size and higher mass loss measured using TGA), the use of the CPS method is far superior in term of the physical integrity of the produced samples (higher bulk density and lower amount of porosity).

Considering the obtained iron phosphate glasses, it is accepted that a higher Fe^{3+} content will increase the connectivity of the glass network and its chemical durability (Forder *et al* 2012, Cassingham *et al* 2008). In this work, it is shown that the glass processed by microwave melting for 20 minutes has an increased amount of Fe^{3+} namely 77 % compared to 50 % in the level in the glass melted conventionally at 1150°C for 3 hours. Thus it is shown that the use of microwave glass melting (at least in the laboratory) can reduce the processing time from hours to minutes, hence if it could be successfully scaled up and used in waste vitrification, use of a microwave furnace will both potentially save energy and be cost effective.

To understand the effect of microwave heating on graphite-glass composite production, the production of iron phosphate glass composites that contained 20 wt% graphite was studied in detail. It is worthy of note that for samples that contained only 10 wt% of graphite the microwaved samples did not retain the cylindrical shape of the initial pellets. At this level of graphite loading melting of the glass forming components clearly takes place. In contrast at 20 wt% loading or greater it was found that the amount of sintering (or melting) was reduced; it seems that increasing the graphite content effectively prevents flow and/or passivates the effects

of the electromagnetic field in the DMO. The addition of 30 and 38 wt% of graphite resulted in still greater amounts of porosity and reduced the density of the microwaved pellets. This suggests that only the iron phosphate raw material, specifically the Fe_3O_4, couples with the electromagnetic waves, not the graphite *i.e.* the graphite does not act as a susceptor in this situation. To investigate this hypothesis, the reaction of loose powdered graphite and pressed powdered graphite pellets in the DMO has been examined. The loose graphite powder glowed red in less than 1 minute when exposed to microwaves but there was little obvious change in the pressed pellets when exposed to microwave radiation. Although graphite powder is a microwave suscepting material, our experiments suggest that the graphite only exhibits surface heating when pressed into pellets. This behaviour is related to the penetration depth of the microwaves. It is well known that most metals couple with microwaves in powder form, usually on the micron scale. Similar behaviour is also seen in the present study (see Table 4-1 for particle size analysis). This phenomenon was also reported by Rajkumar and Aravindan (Rajkumar and Aravindan 2009), who found that graphite couples with microwaves when the particle size is of the same order of penetration depth *i.e.* about 30 μm.

Comparing iron phosphate glass composites heated for 20 minutes in the DMO with CPS iron phosphate glass composites shows that similar FTIR spectra and phase assemblages (with some small differences in amounts) were obtained in both cases. However, from the Mössbauer analysis it was clear that different amounts of glassy and crystalline phases were produced in the composite materials, whether formed by microwave heating or the CPS method. Due to the similarity of crystalline phases observed in the two cases, it is suggested that a sintering temperature of approximately 770-870°C may have been achieved in DMO, although no direct measurements of this temperature have been made.

It was originally hoped that the short processing time in a microwave oven would limit or prevent oxidation of any graphite incorporated into the glass however, in practice greater graphite loss was found in the microwaved samples. As noted above a high percentage of graphite has oxidised during the microwave heating process; the oxygen source is likely to be the iron oxide as essentially the same result was obtained for samples microwaved under argon. This is a reflection of the use of Fe_3O_4 as a suscepting raw material for glass composite production in

the DMO, whereas the CPS process utilised pre-made glass. As expected, greater reduction of iron to form crystalline materials was seen when the samples were microwaved in air rather than in argon. Overall the Mössbauer analysis indicates that the graphite-glass composite materials sintered using DMO or CPS methods resulted in the formation of FeP_2O_6 and $Fe_2(P_2O_6)$, indicating an increase in the total amount of Fe^{2+}.

The primary aim was to produce a graphite wasteform whilst minimising the oxidation of graphite. In this work, it is found that the most promising sample was prepared by using CPS method, loaded with 20 wt% graphite and heated at 770°C for 2 hours (Ar) with graphite losses of about 0.4 %, respectively. It is also found that > 90 % graphite oxidised when heated at 770°C in air whereas this was not the case when heating was carried out under argon indicating that Ar successfully prevents graphite oxidation despite the potential for a redox coupling involving graphite and the iron oxide redox in the glass. Although complete encapsulation of graphite by the iron phosphate glass was not achieved in either case, less oxidation of the graphite, a wasteform greater densification and thus less porosity were obtained by CPS, suggesting that CPS is a better method than microwave heating for the production of graphite-glass composites for the encapsulation of irradiated graphite waste.

4.7. Summary

The use of microwave and conventional sintering processing with an iron phosphate base glass to produce stable graphite-glass composite materials for the immobilisation of irradiated graphite waste has been investigated. The base glass, $40Fe_2O_3 – 60P_2O_5$ (mol%) was successfully prepared by both conventional and microwave glass melting with the rapid microwave glass melting process resulting in a small loss of P from the final glass. Graphite-glass composite production using microwave processing was less successful, with the decomposition of iron phosphate raw materials and the graphite impeding densification resulting in porous wasteforms regardless of whether the process was conducted in air or under Ar.

Some oxidation of graphite by reduction of iron was identified via microstructural and Mössbauer investigations of microwaved iron phosphate glass composites; heating in either air

or argon made little difference to the results. About 5 % of total mass loss is due to graphite oxidation in the microwave samples loaded with 20 wt% graphite. Increased waste loading of the samples led to greater amounts of porosity. Mössbauer analysis confirmed that the oxidation of graphite happens via reduction of iron during processing. The most promising sample was that conventionally heated in argon at 770°C for 2 hours. This sample successfully encapsulated 20 wt% graphite particles in iron phosphate crystalline phases and resulted in about 0.4 % oxidation of graphite with much lower porosity levels compared to the microwaved samples. Overall however the porosity levels in this sample are probably too high for viable wasteform production.

5. Results and Discussion II: The Production of Various Graphite -glass Composites by CPS Method for the Immobilisation of Irradiated Graphite Waste

5.1. Introduction

In Chapter 4, it was shown that the use of CPS method is more promising than the microwave method for the immobilisation of graphite in iron phosphate glass composite materials. This led to the work in Chapter 5 which aims to explore and access the potential of the CPS method in production of graphite wasteforms using various glass systems. Although some data with regard to iron phosphate glass and iron phosphate glass composites prepared using conventional melting and CPS have been discussed previously, these materials are studied in greater detail and used to draw comparisons with other selected glass compositions. This chapter is divided into five main sections: characterisation of base glasses, the effects of sintering temperatures on graphite-glass composites, the effects of waste loading on graphite-glass composites, discussion and summary.

5.2. Characterisation of Base Glasses

Laboratory made glasses namely alumino-borosilicate (ABS), calcium aluminosilicate (CAS), alkali borosilicate (G11) and iron phosphate (IP) were successfully prepared using conventional melt processing. Natural obsidian glass has also been researched in this chapter. This is due to its interesting properties (*i.e.* reasonably high chemical durability) and to investigate the use of a natural glass for the immobilisation of graphite waste. Photos of the annealed manufactured glasses and as-received obsidian glasses are shown in Figure 5-1. The ABS and CAS glass appeared transparent with ABS being colourless and CAS slightly yellowish. The other glasses are opaque and black in colour. For each laboratory-made glass composition, the obtained glasses whether annealed or rapid quenched into water were found to be visibly similar in colour, apart from G11 and IP glass frits that were green, particularly in thin section. To understand the physical, chemical and structural properties of the glasses, various characterisation methods/techniques such as XRF, ICP, EDS, density measurement, DTA, dilatometry, particle size, XRD, FTIR and Raman have been employed and the results are summarised in this section.

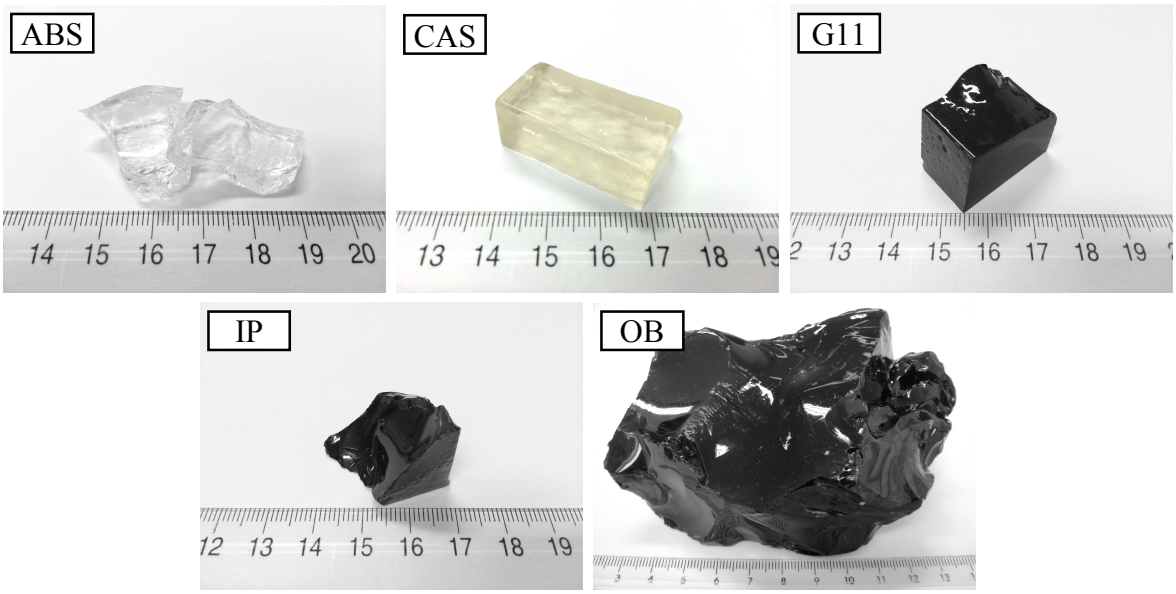

Figure 5-1: Photographic images of ABS, CAS, G11, IP and OB base glasses.

5.2.1. Chemical Composition and Physical Properties

The results of chemical composition, density, T_g and particle size of the base glasses are detailed in Table 5-1. For the chemical composition analysis, multiple measurement techniques which are XRF, ICP and EDS have been conducted. In general, XRF and EDS were used to detect all the elements in the base glasses and ICP was used for the identification of light elements (B and Li) that present in ABS and G11 base glasses. According to the measured data (data were normalised and shown in brackets), it is clear that all the nominal elements in ABS, CAS, G11 and IP glasses were detected and the values except Al_2O_3 are below 5 % measurement error. For OB glass, the normalised EDS and XRF data are also similar apart from Cl, which was only detected in the EDS analysis. Al_2O_3 crucibles were used to prepare ABS glass, a platinum crucible was used for CAS glass and mullite crucibles were used for G11 and IP glasses. It should be noted here that the use of alumina and mullite crucibles in glass melting leads to an increase in the Al_2O_3 content of the prepared glasses. There is no contamination detected in CAS glass due to the use of a Pt crucible. It is found that the Al_2O_3 content increases about 0.76 mol % in ABS, 0.47 mol % in G11 and 1.07 mol % in IP glasses. The highest Al_2O_3 contamination in IP glass indicates that the melts created during glass melting were highly corrosive.

The density data for bulk and powdered glasses were measured using Archimedes' principle and gas pycnometry. Based on the results, for each glass composition, similar bulk and powder density data were found, despite the different state of the samples and measurement techniques used. This is in agreement with the obtained glasses, which appeared dense without any visible porosity.

The T_g values of the base glasses measured using DTA and dilatometry (DIL 420C) were found to be slightly different. It is worth noting that the heating rates used in the DTA and dilatometry experiments are compatible as suggested in the literature (Mazurin 2007). As seen in Table 5-1, the T_g measured using dilatometry were found approximately ± 6 % different from the DTA data. Although powdered and monolith samples were used in the DTA and dilatometry measurements, it is believed that the samples are similar in phase and structure. Furthermore, the annealing temperatures used for the preparation of each monolith samples are around T_g and this should not alter the glass structure. The discrepancy in the T_g values obtained by the two techniques is discussed in Section 5.5.

All the laboratory made glass frits and as-received obsidian glasses were crushed manually into powder, sieved < 75 μm and dry milled for 8 h before being used in the production of graphite-glass composites. In all cases, similar crushing and milling methods were applied. However the particle size analysis suggest slight differences in values for each glass composition, whether considering the volume or number basis (see Table 5-1). This can be understood in that each glass compositions had different hardness and toughness values, which lead to the different distribution of particle sizes of powdered glasses. It should be noted that the small particle size leads to high surface area and will promote sintering; the CPS method depends on reducing the free energy of the system. Furthermore, the closer the particle to one another, the shorter the diffusion path will be and consequently speed up the sintering kinetics (*i.e.* surface diffusion and viscous flow) resulting in a dense sintered product with minimal porosity (Kang 2005).

Table 5-1: Chemical composition and physical properties of ABS, CAS, G11, IP and OB base glasses.

Oxide (mol %)	ABS Nominal (XRF & ICP)	CAS Nominal (EDS)	G11 Nominal (XRF & ICP)	IP Nominal (EDS)	OB EDS (XRF)
Al_2O_3	5.29 (6.05)	7.17 (7.25)	2.59 (3.06)	- (1.07)	8.36 (8.36)
B_2O_3	7.48 (7.43)	-	9.24 (9.62)	-	-
BaO	- (< 0.02)	-	- (< 0.02)	-	- (< 0.02)
CaO	3.02 (3.02)	51.40 (49.92)	- (< 0.06)	-	0.87 (0.86)
Cl	-	-	-	-	0.57
Cr_2O_3	- (< 0.02)	-	- (< 0.02)	-	- (< 0.02)
Fe_2O_3	- (< 0.02)	-	4.96 (5.10)	60.00 (59.93)	0.61 (0.74)
K_2O	- (< 0.03)	-	- (0.11)	-	3.47 (3.70)
Li_2O	-	-	9.69 (9.29)	-	-
MgO	1.56 (1.56)	-	- (< 0.08)	-	- (< 0.08)
Mn_3O_4	- (< 0.01)	-	- (< 0.02)	-	- (< 0.02)
Na_2O	7.48 (7.40)	-	15.57 (15.13)	-	4.43 (4.48)
P_2O_5	- (< 0.02)	-	- (< 0.02)	40.00 (39.00)	- (< 0.02)
SiO_2	75.17 (74.26)	41.43 (42.83)	57.95 (57.30)	-	81.70 (81.52)
SrO	- (< 0.03)	-	- (< 0.03)	-	- (< 0.03)
TiO_2	- (< 0.04)	-	- (< 0.04)	-	- (0.07)
V_2O_5	- (< 0.02)	-	- (< 0.02)	-	- (< 0.02)
ZnO	- (< 0.04)	-	- (< 0.04)	-	- (< 0.04)
ZrO_2	- (< 0.03)	-	- (< 0.03)	-	- (< 0.03)
Density					
Bulk (g/cm^3)	2.318 ± 0.116	2.908 ± 0.145	2.584 ± 0.129	3.152 ± 0.158	2.357 ± 0.118
Powder (g/cm^3)	2.3099 ± 0.0025	2.8781 ± 0.0093	2.5729 ± 0.0056	3.1614 ± 0.0009	2.3601 ± 0.0029
T_g					
DTA (ºC)	588 ± 5	792 ± 5	411 ± 5	474 ± 5	659 ± 5
DIL 420C (ºC)	610 ± 5	784 ± 5	434 ± 5	457 ± 5	-
Average particle size (diameter / μm)					
Volume basis	34.7 ± 1.7	38.8 ± 1.9	35.0 ± 1.8	34.8 ± 1.7	32.0 ± 1.6
Number basis	0.93 ± 0.05	0.76 ± 0.04	0.81 ± 0.04	0.76 ± 0.04	0.91 ± 0.05

5.2.2. XRD

Figure 5-2 presents the overnight XRD patterns of the powdered glasses. CAS, IP and OB diffractograms exhibit diffuse scattering behaviour without any evidence of crystalline peaks.

This confirmed that the glasses were X-ray amorphous. Similar diffuse scattering behaviour can be seen in the ABS and G11 diffractograms but in these diffractograms, a weak β-quartz peak (SiO_2, PDF card 01-086-1562) is detected at ~ 27.3° *2θ*. It is believed that this SiO_2 peak might represent the SiO_2 from batch that was not properly dissolved whilst glass melting. Overall the intensity of the SiO_2 peak is very low and it is assumed that the content of crystalline phase in the glasses is less than 5 %.

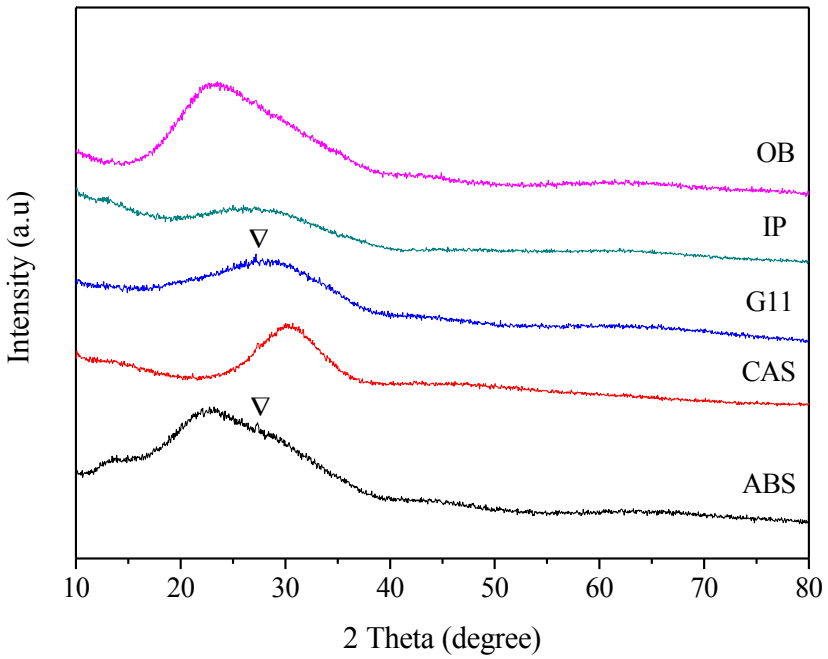

Figure 5-2: XRD patterns of powdered ABS, CAS, G11, IP and OB base glasses, ∇ = SiO_2.

5.2.3. FTIR Spectroscopy

The FTIR spectra of powdered glasses recorded from 400 - 4000 cm^{-1} using KBr disc method are shown in Figure 5-3. The data from 2000-3000 cm^{-1} were removed from the graph as no absorption bands were detected in this region. In all spectra, bands at 1640 and 3467 cm^{-1} correspond to the bending and stretching vibration modes of O-H in hydroxyl groups or water molecules in the samples. The assignments of other FTIR bands for each glass were made on the basis of previous literature that specifically related to the tested glasses.

For ABS spectrum, six main absorption bands located at 460, 697, 792, 1060 with a shoulder at 1175 and 1414 cm^{-1} have been identified. The band at 462 cm^{-1} is assigned to Si-O-Si and O-Si-O bending vibrations of bridging oxygens Q^4 (Gaafar and Marzouk 2007, Song *et al* 2009, Saddeek *et al* 2010, Bootjomchai *et al* 2012, Marzouk *et al* 2013). It is also suggested that there is a contribution of B-O-B linkages overlapping at this particular band (Gaafar and Marzouk 2007, Bootjomchai *et al* 2012). Bands at 697 and 792 cm^{-1} are attributed to bending vibrations of B-O-B (BO_3) and B-O-B (BO_4) (Darwish and Gomaa 2006, McGann *et al* 2012) overlapping with stretching vibrations of Al-O-Al in [AlO_4] tetrahedron (Song *et al* 2009). The band at 1060 cm^{-1} is assigned to stretching vibrations of Si-O-Si in [SiO_4] tetrahedra (Gaafar and Marzouk 2007, Song *et al* 2009, Saddeek *et al* 2010) and a shoulder arising at 1175 cm^{-1} is associated with stretching vibrations of Si-O-NBO in Q^3 structural units (El-Egili 2003, Bingham and Jackson 2008) overlapping with stretching vibrations of bridging oxygens of BO_3 triangles (Gaafar and Marzouk 2007). The broad band at 1414 cm^{-1} is assigned to stretching vibrations of NBOs of BO_3 triangles (Gaafar and Marzouk 2007, Song *et al* 2009, Saddeek *et al* 2010).

Four absorption bands observed in CAS spectrum can be assigned to the following vibration modes: 503 cm^{-1} to bending vibrations of Si-O-(Si, Al) (Huang and Behrman 1991, Środa and Paluszkiewicz 2008, Mahdy and Ibrahim 2012, Garcia-lodeiro *et al* 2014), however it may also be attributed to symmetric stretching of Al-O-Al in [AlO_6] (Środa and Paluszkiewicz 2008); 696 cm^{-1} to symmetrical stretching of Si-O-(Si, Al) (Środa and Paluszkiewicz 2008) overlapping with stretching vibration of Al-O-Al in [AlO_4] tetrahedra (Huang and Behrman 1991, Środa and Paluszkiewicz 2008, Sontakke *et al* 2009, Garcia-lodeiro *et al* 2014); broad shoulder at 876 cm^{-1} is due to the asymmetric stretching of Si-O bond involving NBO atoms of [SiO_4] tetrahedra Q^3, *i.e.* Si-O tetrahedra with two corners shared with Al-O or Ca-O polyhedra (Huang and Behrman 1991, Środa and Paluszkiewicz 2008, Sontakke *et al* 2009) and the band at 967 cm^{-1} is attributed to the asymmetric stretching of Si-O bond involving BO atoms of [SiO_4] tetrahedra Q^2 (Środa and Paluszkiewicz 2008, Sontakke *et al* 2009).

In G11 spectrum, the vibration modes of the bands can be assigned as follows: 458 cm^{-1} to bending vibrations of Si-O-Si and O-Si-O related to bridging oxygens Q^4 overlapped with B-O-B linkages (Marzouk *et al* 2013); 726 cm^{-1} is due to bending vibrations of B-O-B of BO_3 triangles

overlapped with Al-O-Al in [AlO_4] tetrahedra (Song *et al* 2009), it is also thought that this band was developed from the overlapping contribution of bending vibrations of B-O-B (BO_4); 991 cm^{-1} is due to the stretching vibrations of Si-O-Si of [SiO_4] tetrahedra (MacDonald *et al* 2000, McGann *et al* 2012) and finally the band at 1409 cm^{-1} is due to the stretching vibrations of NBOs in BO_3 triangles, respectively (Gaafar and Marzouk 2007, Song *et al* 2009, Saddeek *et al* 2010, McGann *et al* 2012).

The FTIR spectrum resulted from the different batches of powdered IP glass formed using similar conventional melting were found to be identical, with the differences in the bands position being approximately ± 7 cm^{-1}. This implies that the new batch of IP glass had similar chemical functional groups. To avoid repetition of the data, the FTIR spectrum of the IP glass produced using conventional melting can be viewed in the previous chapter (see Section 4.3.3, Figure 4-7).

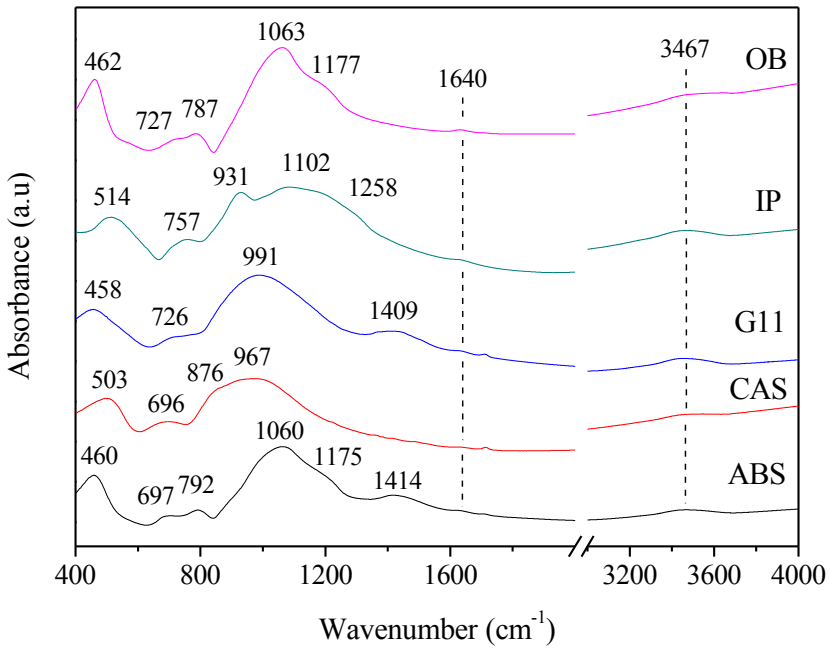

Figure 5-3: FTIR spectra of powdered ABS, CAS, G11, IP and OB base glasses.

It can be seen from the OB spectrum that the bands positioned at 462, 1063 and 1177 cm^{-1} are comparable with the ABS spectrum, suggesting some similarity in the structure of these glasses.

Based on the chemical composition analysis (see Table 5-1), which indicates the absence of B_2O_3, it is believed that there is no contribution of boron structural units in OB glass. With this in mind, the absorption bands of OB glass can be assigned as follow: 462 cm^{-1} is attributed to Si-O-Si and O-Si-O bending vibrations of bridging oxygens Q^4 (Gaafar and Marzouk 2007, Song *et al* 2009, Saddeek *et al* 2010, Bootjomchai *et al* 2012, Marzouk *et al* 2013); 727 cm^{-1} is associated with symmetrical stretching modes of Si-O-(Si, Al) (Środa and Paluszkiewicz 2008); 787 cm^{-1} corresponds to Al-O-Al in [AlO_4] tetrahedra (Huang and Behrman 1991, Środa and Paluszkiewicz 2008, Sontakke *et al* 2009, Garcia-lodeiro *et al* 2014); 1063 cm^{-1} is due to stretching vibrations of Si-O-Si in [SiO_4] tetrahedra (Gaafar and Marzouk 2007, Song *et al* 2009, Saddeek *et al* 2010) and finally a shoulder at 1177 cm^{-1} is related to a stretching vibration of Si-O-NBO in Q^3 structural unit (El-Egili 2003, Bingham and Jackson 2008).

5.2.4. Raman Spectroscopy

Raman spectra of powdered base glasses from the low to mid-range frequency band (0 – 2000 cm^{-1}) are presented in Figure 5-4. Spectra from 2000 – 4000 cm^{-1} were removed from the graph as there are no features detected in this frequency region. Similar to the FTIR data, the Raman bands have been assigned to specific bond vibrations that have been reported in the literature for the tested glasses. In the Raman spectra of the powdered base glasses, it is seen that the luminescence or fluorescence background increase started at ~1600, 1200 and 800 cm^{-1} for ABS, CAS and OB spectra respectively. This is unexpected and the downside of this phenomenon is that this luminescence covered the Raman spectra, which in this case heavily affects the CAS and OB glasses. Very minimal luminescence background was detected in the G11 and IP spectra.

Considering the ABS spectrum, seven distinct features located at 82, 465, 601, 800, 1065, 1180 and 1446 cm^{-1} are identified. The peak at 82 cm^{-1} is attributed to the 'boson peak' resulting from vibrational excitations made up of acoustic phonons, which are scattered strongly from elastic inhomogeneities in the disordered glass structure (Schroeder *et al* 2004). The low frequency envelope measured from ~200 – 650 cm^{-1} with the detection of a peak centred at 465 cm^{-1} and accompanied with a shoulder at 601 cm^{-1} can be assigned as follows: the band at 465 cm^{-1} is due to contributions from mixed stretching-bending vibration modes of Si/B-O-Si/B bridging bonds

overlapping with breathing vibrations of 4-fold (D_1) silicate rings. The shoulder at 601 cm^{-1} is due to the breathing vibrations of 3-fold (D_2) silicate rings, D_1 and D_2 also known as defect modes (Furukawa *et al* 1981, Galeener 1982, Mercier *et al* 2009, McKeown *et al* 2010, Kalampounias 2011, Kjeldsen *et al* 2013, Winterstein-Beckmann *et al* 2014). The shoulder at 601 cm^{-1} may also overlap with Al-O-Al vibrational modes of AlO_4 tetrahedra (Rupesh Kumar *et al* 2013). The band at 800 cm^{-1} is assigned to Si-O-Si bending modes (Kamitsos 1996, Kalampounias 2011, Winterstein-beckmann *et al* 2014) overlapped with breathing modes of boroxol rings (Kumar *et al* 2013, Winterstein-beckmann *et al* 2014). The broad band located at 1065 cm^{-1} with a shoulder at 1180 cm^{-1} is attributed to asymmetric stretching modes of Si-O-Si bridges in a fully polymerised silicate network, which specifically related to the characteristic vibrations of Q^3 and Q^4 species (Kamitsos 1996, McKeown *et al* 2010, Rupesh Kumar *et al* 2013). A broad, weak intensity band at 1446 cm-^{1} is associated to B-O stretching vibrations in BO_3 and BO_2O^- trigonal borate units (Mckeown *et al* 2010, Kumar *et al* 2013, Winterstein-beckmann *et al* 2014).

In CAS spectrum, several Raman bands can be distinguished in the lower frequency region (< 800 cm^{-1}), which are individually positioned at 126, 223, 383, 586 and 683 cm^{-1}. The most distinctive band was detected at about 936 cm^{-1} with a trace of a shoulder at 1038 cm^{-1}. The band at 126 cm^{-1} is assigned to the 'boson peak'. The weak bands centred at 223 and 383 cm^{-1} are possibly contributions of Al-O bending vibrations of AlO_4 tetrahedra and Al-O symmetric stretching of AlO_6^{3-} octahedra respectively (Kamitsos *et al* 1994). The band at 586 cm^{-1} can be interpreted as being due to the presence of Al-O-Al bridges (Mcmillan *et al* 1982, Seifert *et al* 1982, Neuville *et al* 2004, 2006). The band at 683 cm^{-1} has a similar intensity with the previous band detected at 586 cm^{-1} and the appearance of this band is ascribed as Al-O stretching vibrations of AlO_4 tetrahedra (Kamitsos *et al* 1994, McMillan and Piriou 1982). The band peaking at 936 cm^{-1} with a trace of a shoulder at 1038 cm^{-1} is associated with Si-O stretching vibrations of SiO_4 tetrahedra involving NBO atoms of SiO_4 tetrahedra, particularly related to Q^2 and Q^3 species (McMillan 1984, Kamitsos *et al* 1994). It is also suggested in the literature that these bands (936 and 1038 cm^{-1}) are due to the stretching vibrations of SiO_4 tetrahedra bound to one and two Al atoms (McMillan and Piriou 1982, Mysen *et al* 1982, Neuville *et al* 2004).

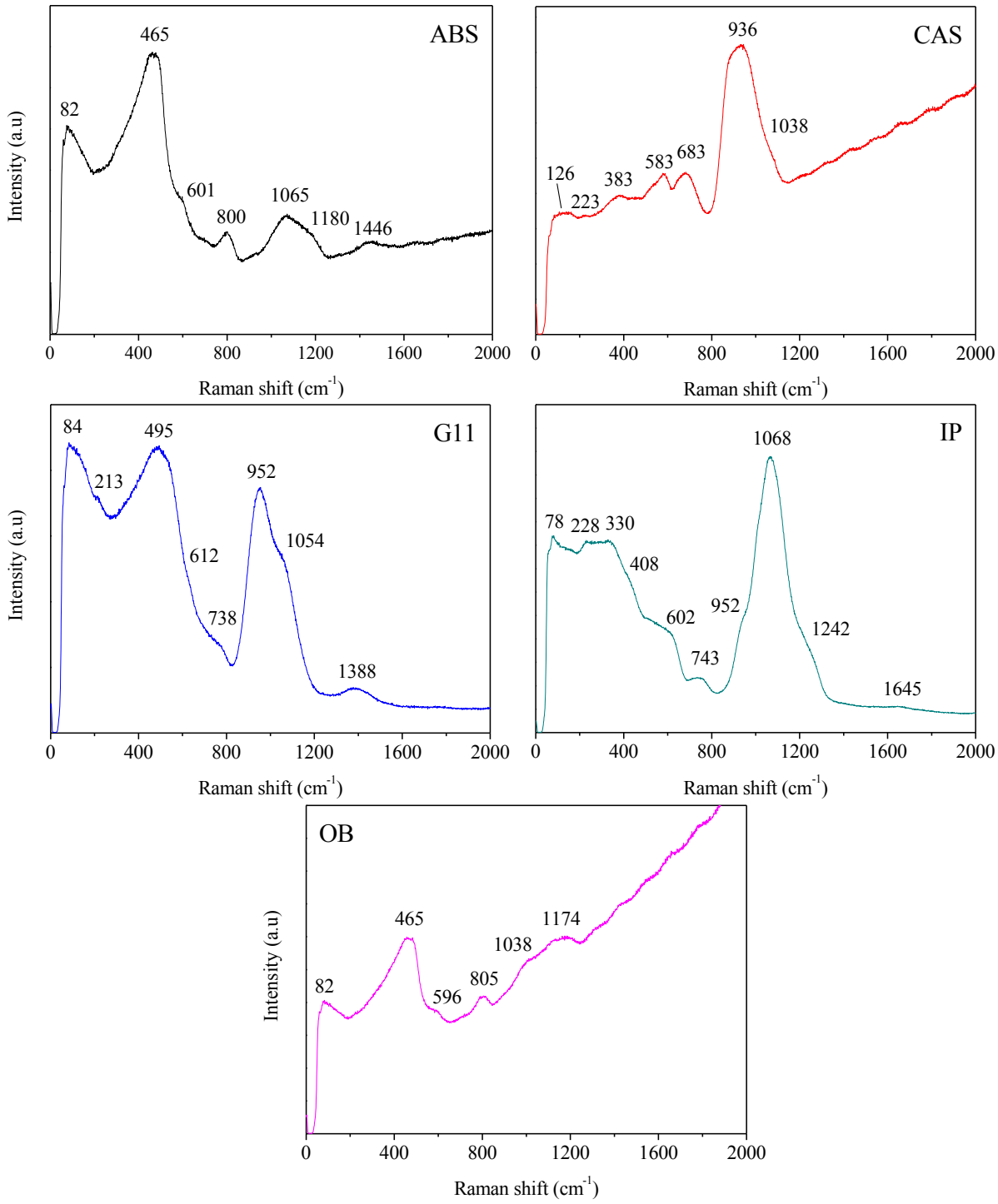

Figure 5-4: Raman spectra of powdered ABS, CAS, G11, IP and OB base glasses.

For G11 glass, the 'boson peak' is located at 84 cm^{-1}. The position of the low frequency and mid-range frequency of Raman bands in G11 spectrum are similar to those seen in ABS and CAS glasses. This is due to the fact that the G11 glass is an alkali borosilicate glass with additions of Li and Fe. Thus, the structure of this glass is comparable to the structure of ABS and CAS glasses. In this case, the bands at ~495, 612 and 1388 cm^{-1} are assigned similarly to the bands detected at ~465, 601 and 1446 cm^{-1} in the ABS glass spectrum. The bands at ~952 and 1054 cm^{-1} are analogous to the bands at about 936 and 1038 cm^{-1} in the CAS glass spectrum. However, the increased amount of B in G11 glass (refer table 5-1) gives rise to the broad band at about 738 cm^{-1}. This band is attributed to the breathing mode of three-membered borate rings with $[BO_4]^-$ tetrahedral units (Winterstein-beckmann *et al* 2014). It also has been reported that this band may overlap with Al-O stretching vibration modes of AlO_4 tetrahedra (Neuville *et al* 2006, Rupesh Kumar *et al* 2013).

The Raman features of IP glass spectrum are observed at ~78, 228, 330, 408, 602, 743, 952, 1068, 1242 and 1645 cm^{-1}. It is apparent that the 'boson peak' for this glass is located at about 78 cm^{-1}. The bands at lower Raman frequency range, between 200 and 800 cm^{-1} can be assigned as follows: 228 cm^{-1} corresponds to network vibrations and P-O-P bending modes (Chakraborty and Arora 2012, Qian *et al* 2012); 330 cm^{-1} is due to bending vibrations of PO_4 tetrahedra with a cation as modifier (Chakraborty and Arora 2012, Lai *et al* 2014); a shoulder at 408 cm^{-1} is due to the O-P-O bending vibrations of Q^0 units (Moguš-Milanković *et al* 2004, Chakraborty and Arora 2012, Joseph *et al* 2012); a broad shoulder at 602 cm^{-1} is associated with P-O-P symmetric stretching of bridging oxygen atoms in Q^2 units (Moguš-Milanković *et al* 2004, Bingham *et al* 2009, Qian *et al* 2012) and the band at 743 cm^{-1} is assigned to symmetric stretching of P-O-P bridging bonds in the Q^1 $(P_2O_7)^{4-}$ structural units (Moguš-Milanković *et al* 2004, Lai *et al* 2011b, Chakraborty and Arora 2012, Premila *et al* 2012, Qian *et al* 2012, Ma *et al* 2014). In the mid-range Raman frequency ~800-1400 cm^{-1}, it is clear that there are three distinct features positioned at 952, 1068 and 1242 cm^{-1} in the spectrum envelope. The shoulder at 952 cm^{-1} is assigned to the asymmetric stretching of Q^0 tetrahedra of $(PO_4)^{3-}$ monomer units (Moguš-Milanković *et al* 2004, Lai *et al* 2011b, Chakraborty and Arora 2012, Premila *et al* 2012, Qian *et al* 2012, Ma *et al* 2014). The most prominent band at 1068 cm^{-1} is attributed to the asymmetric stretching modes of Q^1 tetrahedra of $(P_2O_7)^{4-}$ structural units, implying there is a large number of

pyrophosphate groups in the network of this glass (Moguš-Milanković *et al* 2004, Chakraborty and Arora 2012, Joseph *et al* 2012). A shoulder trace at 1242 cm^{-1} is associated with asymmetric stretching vibrations of Q^2 tetrahedra, $(PO_3)^-$ metaphosphate groups (Lai *et al* 2011b). Finally the weak band located at 1645 cm^{-1} is due to the bending vibrations of H-O-H indicating the presence of water (Mysen 1990).

In agreement with FTIR analysis, the Raman spectrum of OB glass shows largely similar positions of the bands to those of the ABS spectrum. The difference in the bands position compared to the ABS is ± 6 cm^{-1} apart from the band located at 1038 cm^{-1}, which is found to be shifted to a lower Raman frequency (by about 27 cm^{-1}). It is worth noting that the OB spectrum here is identical to the previous Raman study of a similar obsidian sample originated from Lipari, Italy (White and Minser 1984). Due to the similarity of OB and ABS spectra, the bands of OB spectrum are assigned based on the ABS analysis and the assignment is as follows: the peak at 82 cm^{-1} is attributed to the 'boson peak'; the band at 465 cm^{-1} to contributions from mixed stretching-bending vibration modes of Si-O-Si bridging bonds overlapped with breathing vibrations of 4-fold (D_1) silicate rings; a shoulder at 601 cm^{-1} is due to the breathing vibrations of 3-fold (D_2) silicate rings; the band at 800 cm^{-1} is assigned to Si-O-Si bending modes and finally the band located at 1065 cm^{-1} accompanied with a shoulder at 1180 cm^{-1} are assigned to asymmetric stretching modes of Si-O-Si bridges in a fully polymerised silicate network that related to Q^3 and Q^4 units.

5.3. The Effects of Sintering Temperature on Graphite-glass Composites

In this section, the effects of sintering temperatures on various systems of compacted powdered glasses with the addition of 20 wt% graphite in argon environment are studied. The compacted graphite-glass composites were sintered from 50°C above T_g to a range of higher temperatures all of which were below 1000°C. The sintered products of the ABS20G and CAS20G series can be seen in Figure 5-5. In terms of the colour of the samples, the final product of G1120G, IP20G and OB20G series were found to be visually similar to the ABS20G and CAS20G series respectively. To determine the effect of sintering temperatures at various temperatures on graphite-glass composites, a range of analysis methods have been implemented including the

analysis of volume shrinkage, mass loss, density, porosity, crystal phase, microstructure with elemental analysis and the investigation of iron valence behaviour in the samples. All the data obtained from these analyses are detailed in this section.

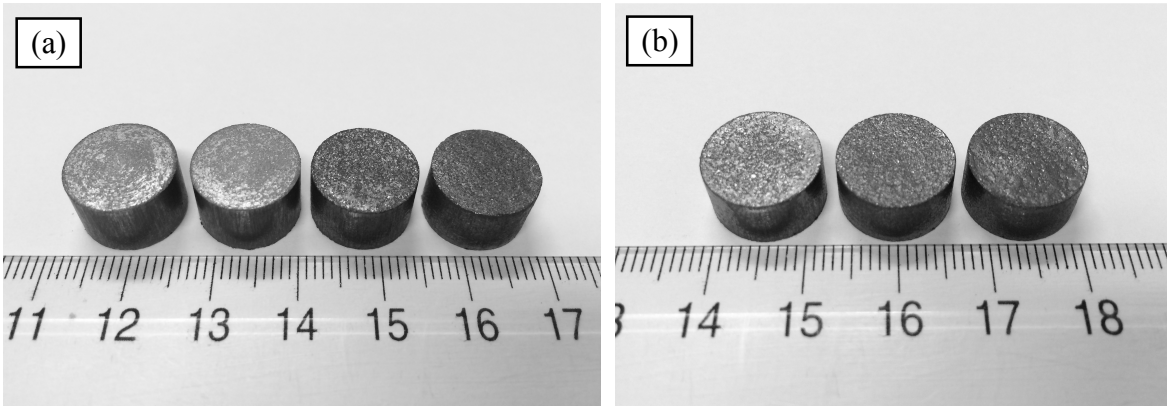

Figure 5-5: Selected photographic images of graphite-glass composites formed at various temperatures, (a) ABS20G series, from left to right: 638°C, 690°C, 790°C, 854°C, (b) CAS20G series, from left to right: 842°C, 890°C, 990°C.

5.3.1. Volume Shrinkage

Figure 5-6 shows the variation of volume shrinkage of graphite-glass composites with increasing sintering temperatures. It is apparent that overall trends of volume shrinkage for all graphite-glass composites are similar except the OB series; the trend shows an increase of volume shrinkage from T_g, which reaches a maximum at 790, 890, 560 and 770°C for the ABS20G, CAS20G, G1120G and IP20G series respectively and subsequently a decrease at the highest sintering temperatures for each series. For the OB20G series, the maximum is at 960°C and the general trend is comparable to the other series except that the volume shrinkage has small negative values at the lower sintering temperatures, between 700 and 800°C. This indicates that the samples have expanded and it is believed that is due to the release of some gases from volatile components (Westrich *et al* 1988, Dunbar and Kyle 1992, Barclay and Carroll 1996, Lowenstern *et al* 2012) and/or graphite during sintering. The maximum value of volume

shrinkage is found to be 8.4 ± 0.2 %, 6.1 ± 0.2, 5.3 ± 0.1, 4.2 ± 0.2 and 2.0 ± 0.2 % for the ABS20G, G1120G, CAS20G, OB20G and IP20G series respectively.

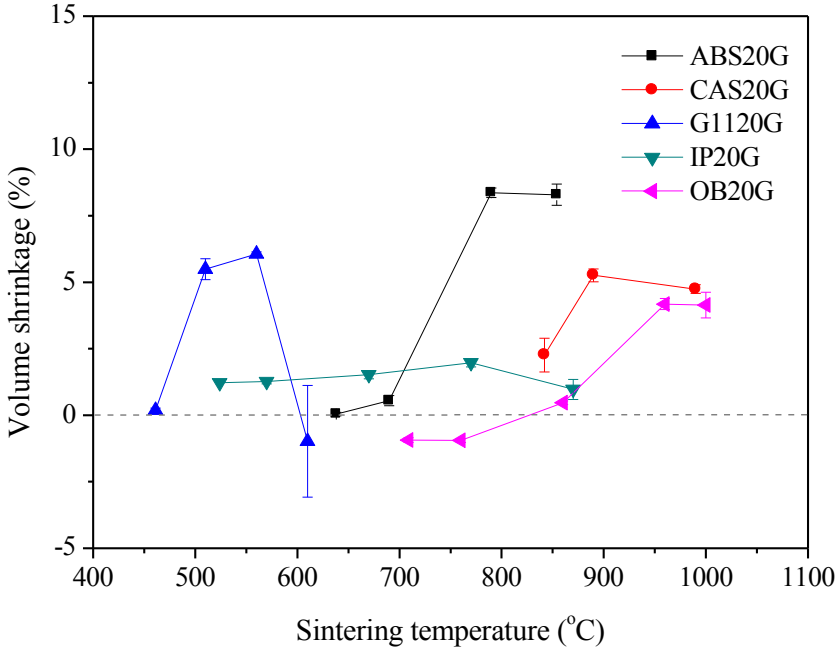

Figure 5-6: Volume shrinkage of graphite-glass composites (20 wt% graphite loading) formed at various sintering temperatures.

5.3.2. Mass Loss

The total mass loss calculated from the different mass between green and final product of graphite-glass composites is shown in Figure 5-7. In general, the trend of total mass loss for all series indicates a linear increase with increasing sintering temperature. Only IP20G samples sintered at 890°C showed a significant mass loss about 2 %. From the data, it is worth noting that low mass loss values are obtained from CAS20G and G1120G series, suggesting less oxidation of graphite occurred in these samples despite the high temperatures that were used to sinter the CAS series. It is known from Chapter 4 that the iron content in iron phosphate glass composites can be reduced by graphite when sintered at 770°C. Based on this information, it is inferred that more iron reduction reactions take place at 890°C. A detailed study of iron valence behaviour in selected samples is discussed later in Section 5.3.7.

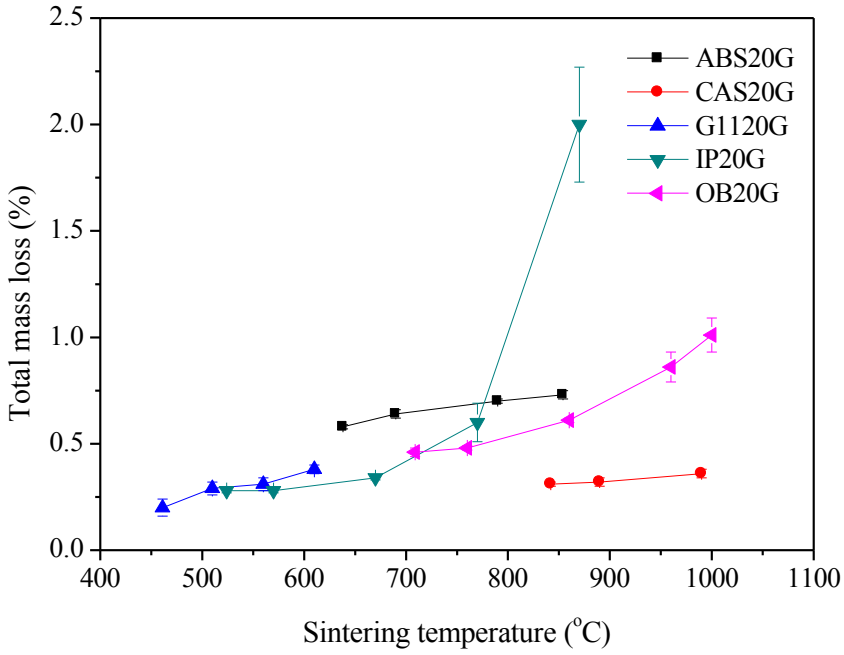

Figure 5-7: Total mass loss of graphite-glass composites (20 wt% graphite loading) formed at various sintering temperatures.

5.3.3. Density and Porosity

The bulk density of compacted powdered glass depends mostly on porosity, which was created whilst consolidation of particles takes place during sintering or from the effect of releasing gases. In this work, the bulk and powder densities of sintered graphite-glass composites were determined in order to predict the porosity.

Figure 5-8 shows the bulk density of various graphite-glass composite samples. It is apparent that the trend of bulk density is similar for all graphite-glass composite series; with bulk density decreasing with increasing sintering temperatures. This suggests that the porosity generated in the samples is increased with increasing sintering temperatures.

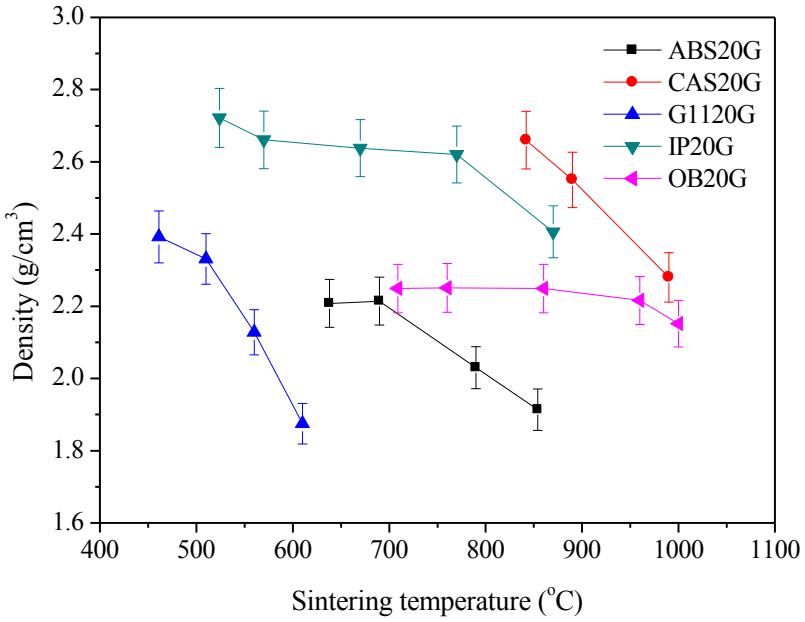

Figure 5-8: Bulk density of graphite-glass composites (20 wt% graphite loading) formed at various sintering temperatures.

When the powder density is considered (see Figure 5-9), it is observed that the trends are similar for IP20G and CAS20G series; both series show increased values of powder density as the sintering temperature increases, with a maximum at 770 and 890°C and a slight decrease at greater sintering temperatures, respectively. For the G1120G series, the powder densities are reasonably similar at about 2.54 g/cm^3 at the first three sintering temperatures and then decrease at 610°C. The reason for these trends is most probably because some of the materials in the glass composite systems exhibit crystallisation and may increase or decrease the powder density of the samples (see Figures 5-12, 5-13 and 5-14). No significant differences are identified in the powder densities of the ABS20G and OB20G series over the sintering temperatures studied. Due to the similarity of the powder density trends for the ABS20G and OB20G series, it is expected that there is no significant change in terms of the crystallisation of the materials upon sintering at various temperatures. It is worth noting here that the error for each powder density measurement is very small approximately < 0.0050 g/cm^3, hence the error bars are not visible in the graph.

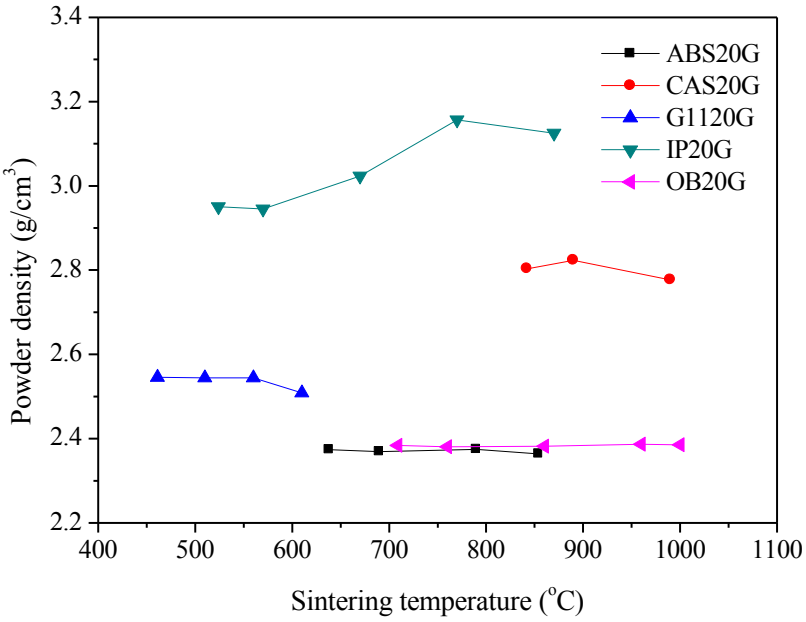

Figure 5-9: Powder density of graphite-glass composites (20 wt% graphite loading) formed at various sintering temperatures, error bar < 0.0050 g/cm^3.

The porosity based on the difference between bulk and powder densities was calculated and the data are presented in Figure 5-10. There are two main factors that may lead to the generation of porosity; the oxidation of graphite by oxygen in the glass or air that was trapped in the samples during pressing and the reduction of iron (for iron-containing base glasses). The trend of porosity in all graphite-glass composites series shows an increasing value with increasing sintering temperature. The increasing trend of porosity is paralleled by an increasing trend of total mass loss and decreasing trend of bulk density for all graphite-glass composite series. From the graph, the porosity generated at maximum volume shrinkage for each series is as follows: 14.5 ± 1.9 % for ABS20G sintered at 790°C, 9.7 ± 1.2 % for CAS20G sintered at 890°C, 16.4 ± 2.0 % for G1120G sintered at 560°C, 17.0 ± 2.2 % for IP20G sintered at 770°C and 7.1 ± 0.7 % for OB20G sintered at 960°C. It is found that the porosity generated in OB20G series is much lower compared to the other graphite-glass composite systems, consistent with the detection of small particle size (Table 5.1) which is hypothesised to promote sintering. This may lead to the development of improved wasteforms, although more analysis related to crystalline phase,

microstructure, iron valency and investigation of mechanical properties must be carried out to support this claim.

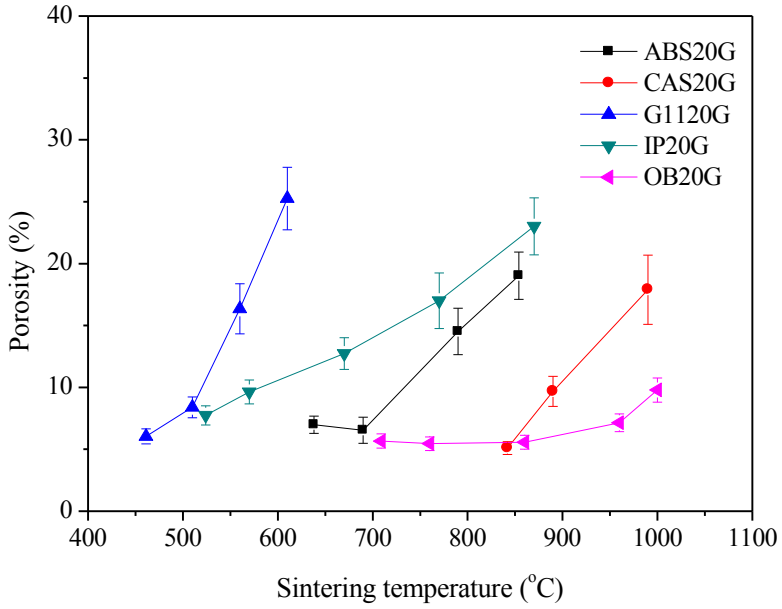

Figure 5-10: Total porosity of graphite-glass composites (20 wt% graphite loading) formed at various sintering temperatures.

5.3.4. XRD

XRD measurements were undertaken to determine the crystalline phases that potentially precipitated in all graphite-glass composites during sintering processing. Note that, in all XRD patterns, Δ is sodalite, $Na_6Al_6(SiO_4)_6$, which originated from the contamination of the graphite raw material (Section 4.2.3). XRD patterns of ABS and ABS20G samples sintered at various sintering temperatures are shown in Figure 5-11. For ABS20G samples sintered at 638, 690 and 790°C, the XRD patterns show diffuse scattering characteristics (amorphous phase) with the detection of identical graphite peaks in all samples. This suggests that there is no alteration of phase, whether considering the glass component or the graphite particles. The diffuse scattering pattern of sintered ABS and sintered ABS20G at 790°C were largely similar; both remain amorphous except that graphite peaks appear in ABS20G samples. At 854°C sintering temperature, similar diffuse scattering and graphite peaks along with some crystalline peaks were

identified. The peaks are assigned with β-quartz (SiO_2, PDF card 01-086-1564) and unknown peak (*). The SiO_2 is thought to originate from the glass components rather than contamination from graphite (no detection of these peaks at lower sintering temperatures). The intensity of the graphite peaks was similar in all ABS20G samples; changing the sintering temperature does not affect the intensity of the peaks.

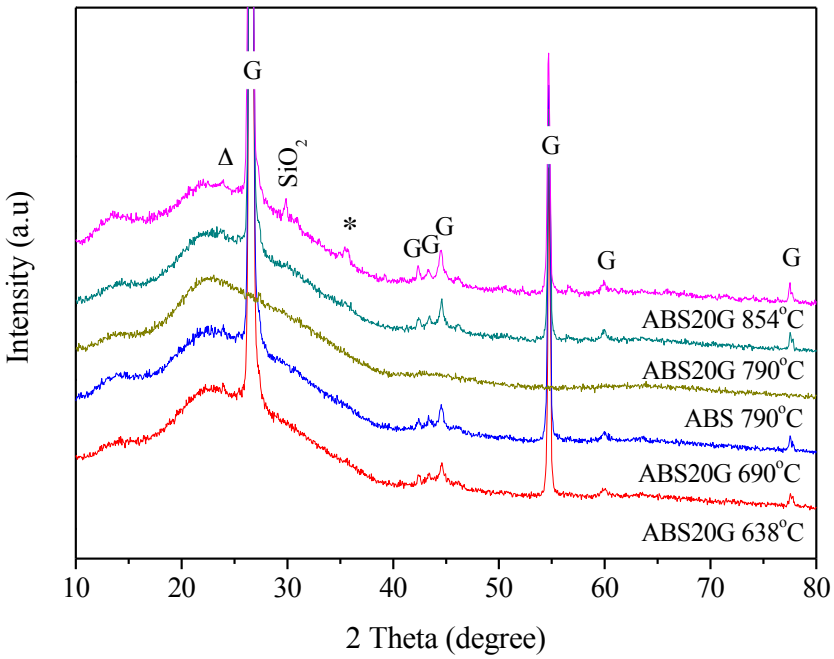

Figure 5-11: XRD patterns of sintered ABS glass and ABS20G heated at various sintering temperatures, G = graphite, Δ = $Na_6Al_6(SiO_4)_6$, SiO_2 = β-quartz, * = unknown peak.

The XRD patterns of sintered CAS and CAS20G samples are displayed in Figure 5-12. At 842°C, the XRD pattern of CAS20G sample indicates diffuse scattering behaviour between 20 and 40° of 2θ with the detection of graphite peaks. As the sintering temperature increases to 890°C, identical crystallisation peaks are detected in the sintered CAS and CAS20G samples. These crystallisation peaks are attributed to larnite (Ca_2SiO_4, PDF card 00-033-0302). Further increasing the sintering temperature of CAS20G sample to 990°C gives rise to the formation of new crystalline phases along with the detection of identical graphite peaks. The new phases are assigned to gehlenite ($Ca_2(Al(AlSi)O_7)$, PDF card 01-075-1677), kilchoanite ($Ca_6(SiO_4)(Si_3O_{10})$, PDF card 00-029-0370) and traces of β-quartz (SiO_2, PDF card 01-086-1564). From the XRD

analysis, the most intense gehlenite peak is significantly higher than the most intense peaks of kilchoanite and β-quartz, suggesting that the gehlenite, phase may be dominant in this sample, although quantitative XRD would be needed to confirm this. It is also worth noting that the diffuse scattering characteristic of the glass component is present in all samples. However, the intensity of the amorphous hump is decreased with increasing sintering temperature, implying a smaller contribution/amount of glassy phase in samples sintered at higher temperatures.

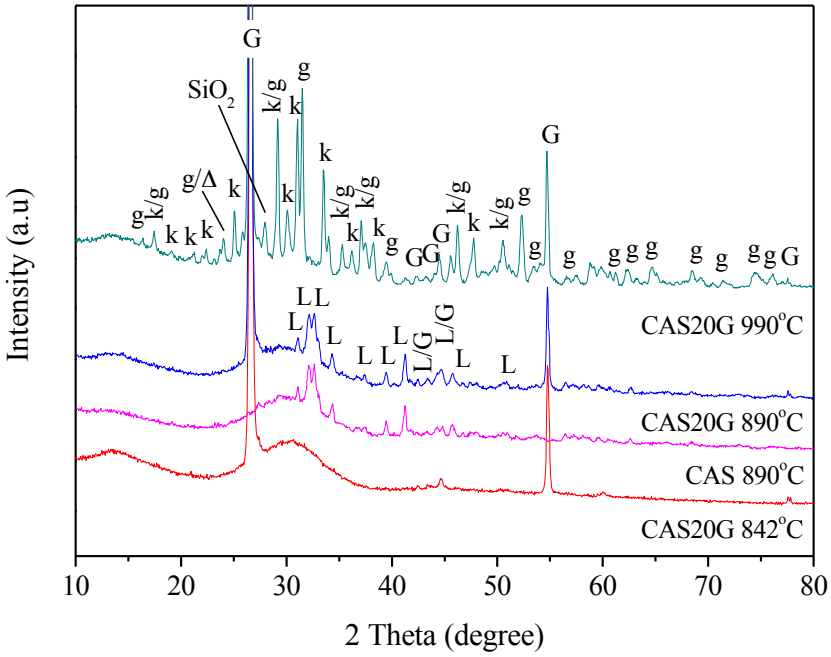

Figure 5-12: XRD patterns of sintered CAS glass and CAS20G heated at various sintering temperatures, G = graphite, L = Ca_2SiO_4, g = $Ca_2(Al(AlSi)O_7)$, k = $Ca_6(SiO_4)(Si_3O_{10})$, Δ = $Na_6Al_6(SiO_4)_6$.

Figure 5-13 shows XRD patterns of sintered G11 and G1120G at various sintering temperatures. In the graph, it is obvious that the glass component of G1120G samples sintered at 461 and 510°C remains unchanged and no significant differences in the graphite peaks can be observed. Comparing G11 and G1120G sintered at 560°C, it is apparent that both diffractograms show identical diffuse scattering patterns with similar crystalline peaks assigned to lithium silicate (Li_2SiO_3, PDF card 04-008-3005). The missing graphite peaks in the sintered G11 sample is due to the fact that this sample was intentionally made without the addition of graphite. Further

development of the Li_2SiO_3 crystalline phase (the intensity of the peaks increase), precipitation of β-quartz (SiO_2, PDF card 01-086-1564), unknown peak (*), an identical diffuse scattering pattern and identical graphite peaks can be seen in sample sintered at 610°C. Overall, it is confirmed that there is no change in terms of intensity and position of graphite peaks in all sintered G1120G samples. Only the glass component crystallises to Li_2SiO_3 and SiO_2 on sintering at 610°C.

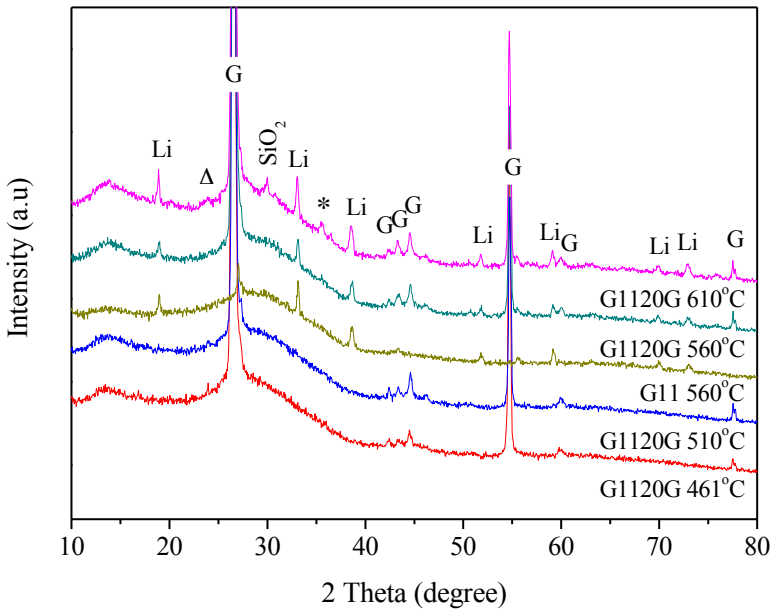

Figure 5-13: XRD patterns of sintered G11 glass and G1120G heated at various sintering temperatures, G = graphite, Li = Li_2SiO_3, Δ = $Na_6Al_6(SiO_4)_6$, SiO_2 = β-quartz, * = unknown peak.

In the XRD patterns of IP and IP20G, there are several contributions of iron phosphate crystalline phases namely FeP_2O_6, $Fe(PO_3)_3$ and $Fe_2(P_2O_7)$ mixed together with the contribution of iron phosphate glass and/or graphite. It should be mentioned here that IP20G sample sintered at 770°C has been compared with the microwave samples in Section 4.4.2. This is due to the fact that this sample gave the highest volume shrinkage and a reasonably low total mass loss, and has thus been selected as the best sample in the IP20G series. The XRD patterns of sintered IP and the complete series of IP20G are presented in Figure 5-14. Considering the IP20G diffractograms from 524 to 870°C, it can be seen that the most intense peak (labelled as X) belongs to FeP_2O_6

(~29° *2θ*) and shows an increasing trend, suggesting the development of this phase, which becomes dominant in the samples sintered at higher temperatures (670-870°C). The contribution of $Fe_2(P_2O_7)$, labelled as Z turns out to be less dominant as some peaks disappear and this can be clearly seen by comparing the IP20G diffractograms from 524-770°C. For $Fe(PO_3)_3$ a crystalline phase (labelled as Y), has its most intense peak located at ~23° *2θ*, which is detected in the IP20G sample sintered at 670˚C. The intensity of this peak is slightly decreased in the sintered sample with graphite loading (compare IP and IP20G sample sintered at 770°C) and completely disappears in the IP20G sample sintered at 870°C. This indicates a larger contribution of $Fe(PO_3)_3$ crystals in the IP samples with the content of the phases probably following the order IP 770°C > IP20G 770°C > IP20G 870°C. Besides the different intensities of the $Fe(PO_3)_3$ peak and no detection of graphite in IP sample, the IP and IP20G diffractograms sintered at 770°C were found to be otherwise identical to each other. Based on the most intense peak of the FeP_2O_6, $Fe_2(P_2O_7)$ and $Fe(PO_3)_3$ crystalline phases, it is found that the amounts of the phases in IP20G sample sintered at 770 and 870°C follows the order of FeP_2O_6 > $Fe(PO_3)_3$ > $Fe_2(P_2O_7)$ and FeP_2O_6 > $Fe_2(P_2O_7)$ > $Fe(PO_3)_3$ respectively.

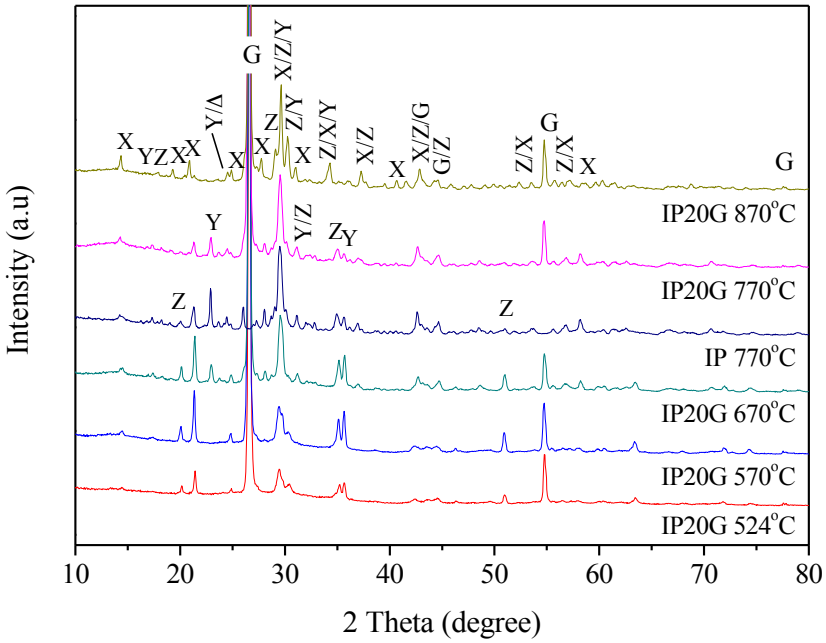

Figure 5-14: XRD patterns of sintered IP glass and IP20G heated at various sintering temperatures G = Graphite, X = FeP_2O_6, Y = $Fe(PO_3)_3$, Z = $Fe_2(P_2O_7)$, Δ = $Na_6Al_6(SiO_4)_6$.

Figure 5-15 shows the XRD patterns of OB and OB20G series sintered above the T_g of the glass component. The diffuse scattering characteristic and 100 % intensity of graphite peak has been confirmed to be similar in all the sintered OB20G samples. However, the increase in the graphite peak at ~45° of 2θ from low to high sintering temperatures is not clearly understood; although the degree of crystallisation of graphite may increase in the samples sintered to high temperature. It is noticeable that all the diffractograms are identical apart from the missing graphite peaks in the sintered OB sample. Among all the studied graphite-glass composite systems, the ABS20G and OB20G series are considered as the most resistant to crystallisation; the crystallisation behaviour of both series are in agreement with the powder density data (see Figure 5-9). This implies that the graphite is immobilised in a glassy system for the ABS20G and OB20G series rather than a glass-ceramic system as seen for the CAS20G, G1120G and IP20G series.

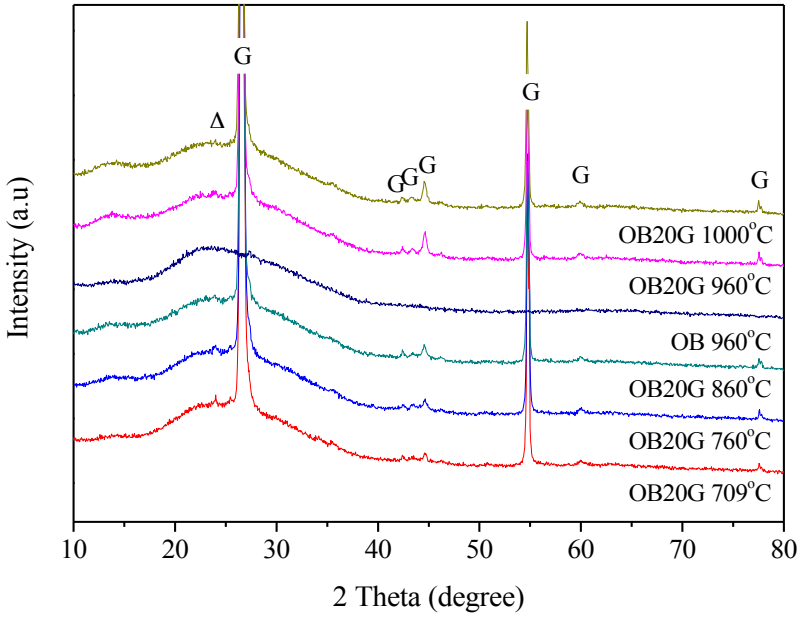

Figure 5-15: XRD patterns of sintered OB glass and OB20G heated at various sintering temperatures, G = graphite, Δ = $Na_6Al_6(SiO_4)_6$.

5.3.5. Optical Microscopy and Optical Profilometry

The images related to the surface morphology and surface roughness of the selected graphite-glass composites are shown in Figure 5-16 and Figure 5-17. As can be seen in the optical

microscope images, the surface morphology of all sintered samples is visually similar. The IP20G sample has been previously observed using optical microscopy (see Section 4.4.4, Figure 4-13) and the image of a different sample batch shown here has a similar morphology. Based on the optical microscope images, the feature observed as grey in colour with rounded/bevel-like edges are thought to be the glass component and the graphite is seen as black and bright white in colour. The reason graphite appears as a bright white feature in some samples is due to the fact that the particles were pressed and this created mirror surfaces. These mirror surface particles reflect the light from the optical microscope. According to the 3D images, the characteristics of the surface can be assigned as follow: the flat surface is the glass or glass-ceramic phases and the rough surface with measured depth in range of 5 - 20 µm is the graphite. It is obvious from the optical microscope and optical profilometer 3D images that the graphite components are not level with the glass and/or glass-ceramic components, implying some of the graphite has been removed from the surface. This event has been confirmed by grinding and polishing processes, which results in the presence of graphite on the polishing cloth.

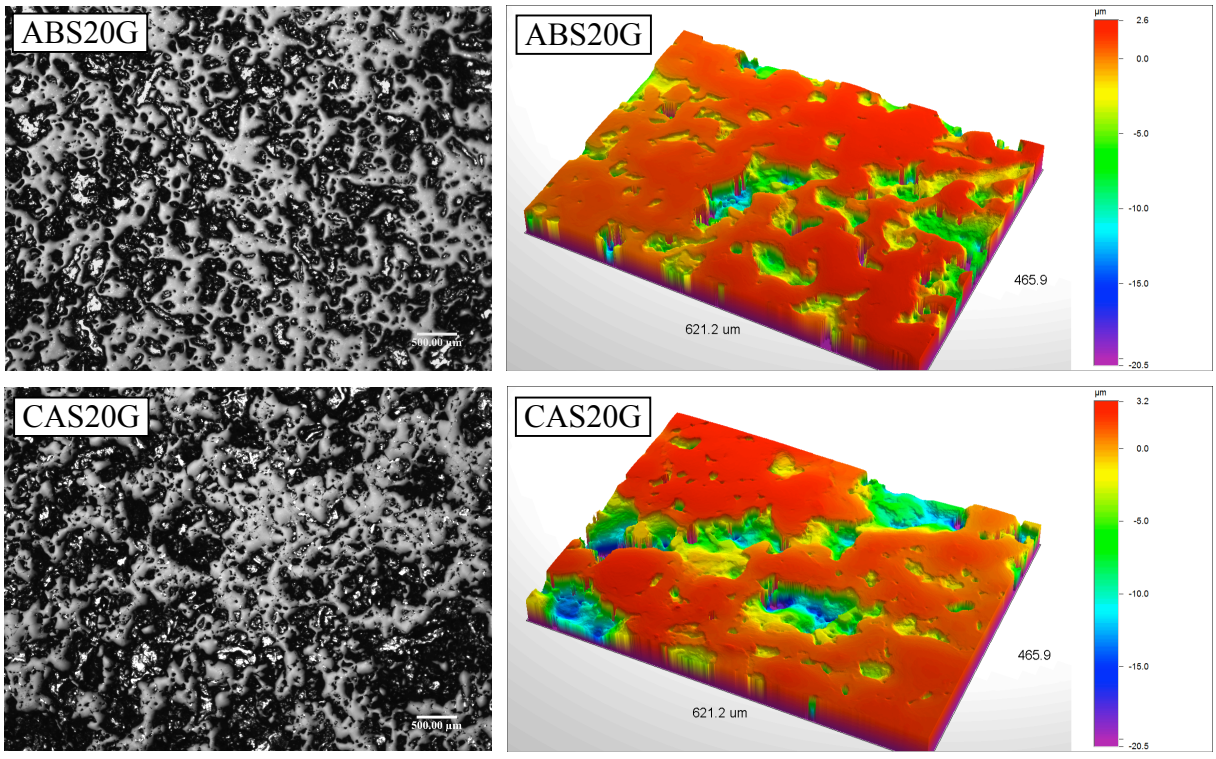

Figure 5-16: Optical microscope and optical profilometer images of selected graphite-glass composites formed at various sintering temperatures, ABS20G - 790°C, CAS20G - 890°C.

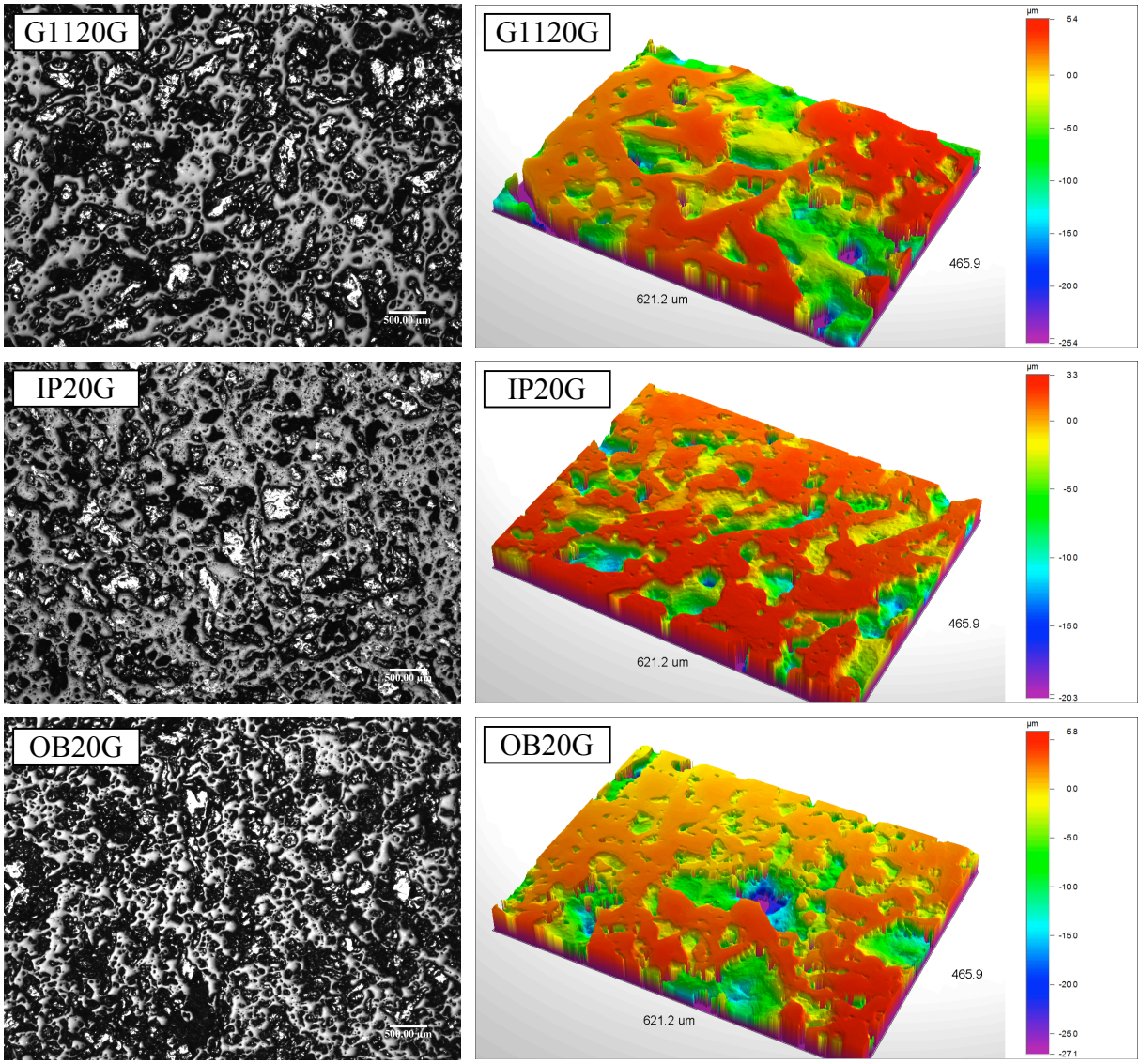

Figure 5-17: Optical microscope and optical profilometer images of selected graphite-glass composites formed at various sintering temperatures, G1120G - 560°C, IP20G - 770°C, OB20G - 960°C.

5.3.6. SEM and EDS

With the XRD results in mind, the primary interest in this section is to investigate the microstructure and the presence of crystalline phases, particularly in the high magnification SEM images of sintered graphite-glass composites. In all images, the black regions have been

confirmed to be graphite. To avoid repetition, the IP20G samples sintered at 770°C are not shown here and the image analysis can be viewed in Section 4.4.4, Figure 4-14e. Low magnification of SE and BE images of selected graphite-glass composite samples are shown in Figure 5-18 and Figure 5-19. In agreement with the porosity data, SE images of sintered ABS20G, G1120G and IP20G samples indicate more micro-sized porosity compared to the SE images of sintered CAS20G and OB20G samples. It is evident in the BE images that different size of graphite particles (black region) were successfully encapsulated by the glass and/or glass-ceramic materials. It is also clear that the graphite particles have irregular shapes and sizes are comparable with the previous particle size analysis (Section 4.2.1). It is worth noting that the area of SE and BE images are taken selectively from the whole surface of the samples; the amount of graphite shown in the image might not represent the total amount of graphite loaded in the samples.

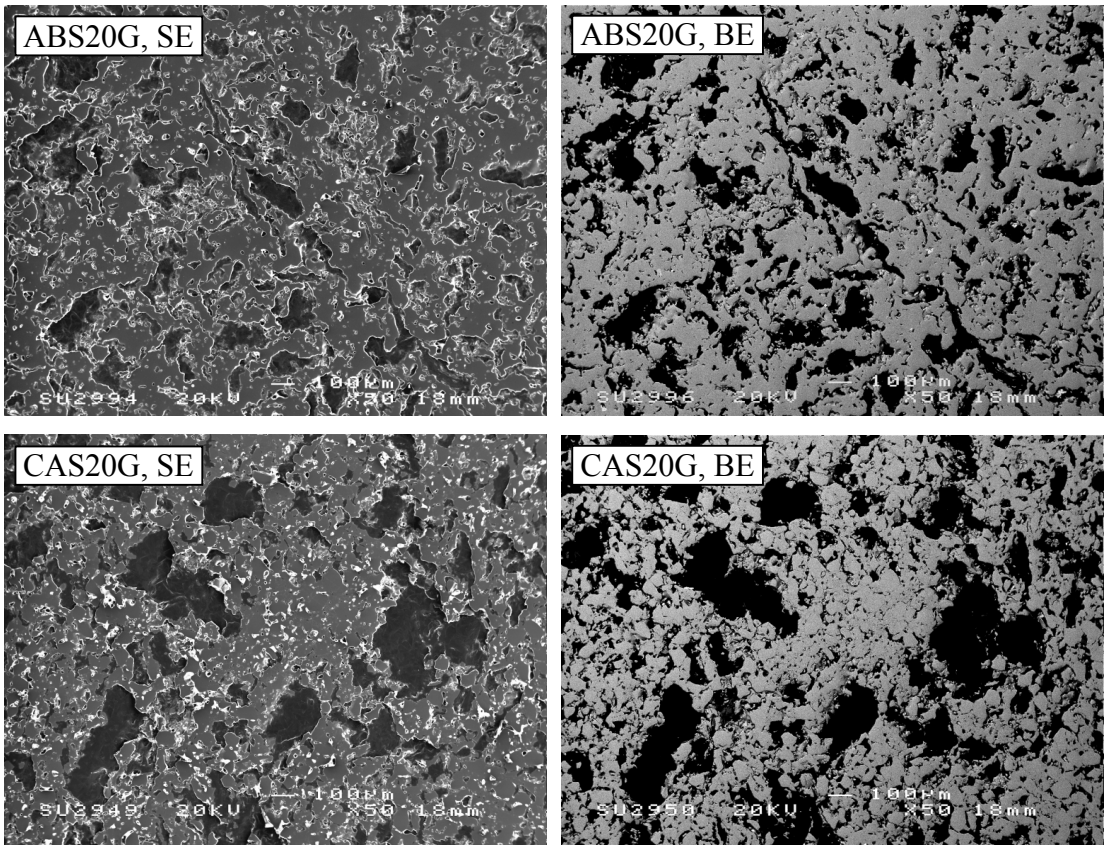

Figure 5-18: Complementary SE (left) and BE (right) images of selected graphite-glass composites prepared at various sintering temperatures, ABS20G - 790°C, CAS20G - 890°C.

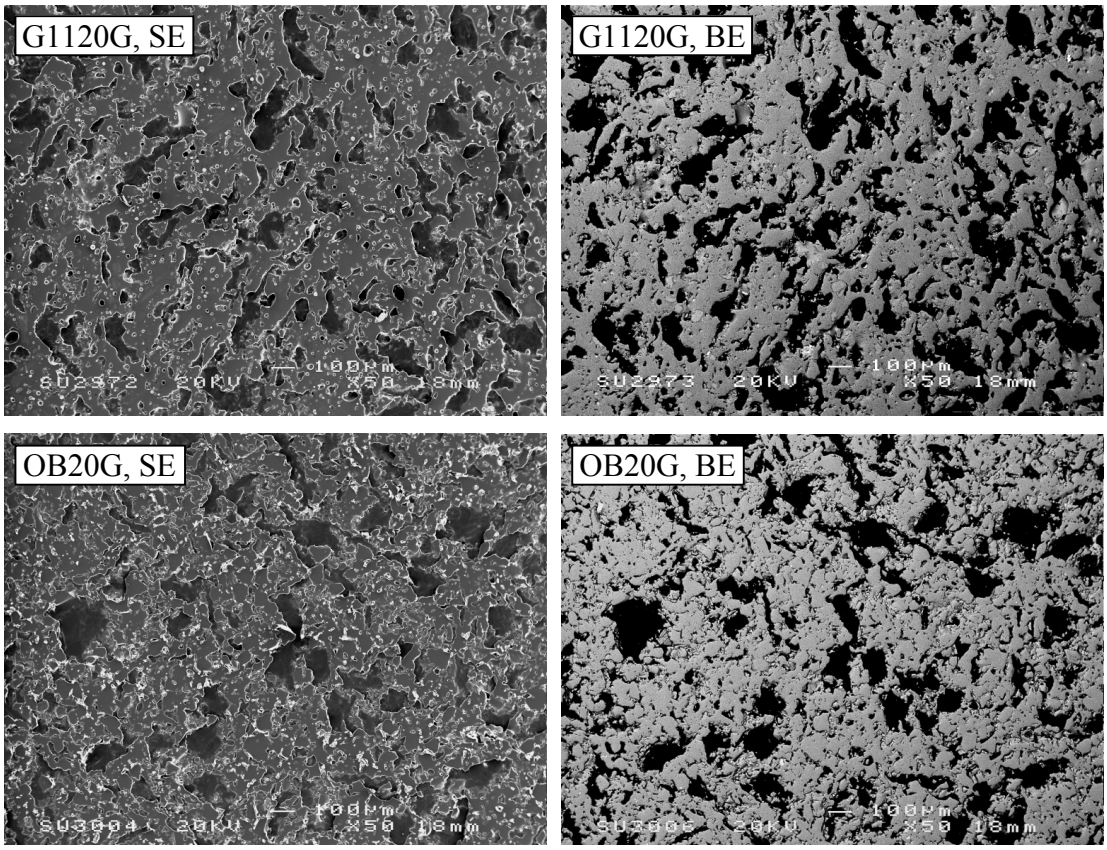

Figure 5-19: Complementary SE (left) and BE (right) images of selected graphite-glass composites prepared at various sintering temperatures, ABS20G - 790°C, CAS20G - 890°C, G1120G - 560°C, IP20G - 770°C, OB20G - 960°C.

As can be seen in Figure 5-20ABS20G, three distinctive features labelled A, B and C were identified in sample sintered at 790°C. Based on the EDS analysis, the features can be interpreted as follows: area A contains similar elements to the glass except boron which cannot be detected by EDS; area B contains similar elements to area A along with traces of Fe and area C is found to be rich in calcium. When the XRD results are considered, area A, B and C can be assigned to ABS glass, contamination from the graphite (also see Section 4.2.5) and possibly of $CaCO_3$ precursor from batch, due to similar microstructure as seen in literature (Amjad and Zuhl 2006) or initial development of a CaO crystalline phase.

Contributions of glass, graphite and larnite are expected in the sintered CAS20G at 890°C. From the low and high magnification BE images (see Figure 5-20CAS20Ga and Figure 5-20CAS20Gb), at least three distinct features can be distinguished; graphite, needle-like crystals and crystalline free regions. The needle-like randomly dispersed feature on the surface of glass particles are believed to be larnite, (area D). The grey region without any precipitation of needle-like crystals is assigned to CAS glass (area E). However, there is no significant difference in the EDS spectra obtained from both crystal and glassy areas (compare spectra D and E).

For G1120G samples sintered at 560°C, the XRD analysis suggests the existence of Li_2SiO_3 mixed with the amorphous phases. Identification of this phase using EDS analysis is not possible; EDS cannot detect elements that have a lower atomic mass than sodium. Due to this reason the investigation of the Li_2SiO_3 phase is limited to the BE image (Figure 5-20G1120G). From the BE image and EDS spectra, area F can be assigned to the glass with rich iron content. Area G is pointed at the middle of the spherical porosity and the EDS spectrum suggests the presence of a large amount of iron mixed with traces of glass. In area H, all the chemical compositions are present in the EDS spectrum and the EDS analysis on the similar area (results not shown) resulted in similar result, hence it is assigned to the glass. The spherical porosity with the detection of a large amount of iron might represent the effect of iron reduction (further explanation in Section 5.5). In this reaction, CO_2 is released and may create spherical porosity that is similar to area G. It is also worth noting that some darker grey areas can be observed in the image; the areas have been measured using EDS but the spectrum was found to be identical with the spectrum obtained from area H. As Li_2SiO_3 phase is present (based on XRD results), the darker grey areas may be due to the contribution of Li_2SiO_3 crystals mixed with the amorphous phase.

In the BE image of OB20G sintered at 960°C (Figure 5-20OB20G), no crystalline features can be found and this is consistent with the XRD analysis. All the elements present in the glass have been detected in the EDS spectrum. Comparing the BE image of OB20G and ABS20G, it can be observed that the microstructures of these sample are largely similar to each other except some contaminations are seen in the ABS20G image.

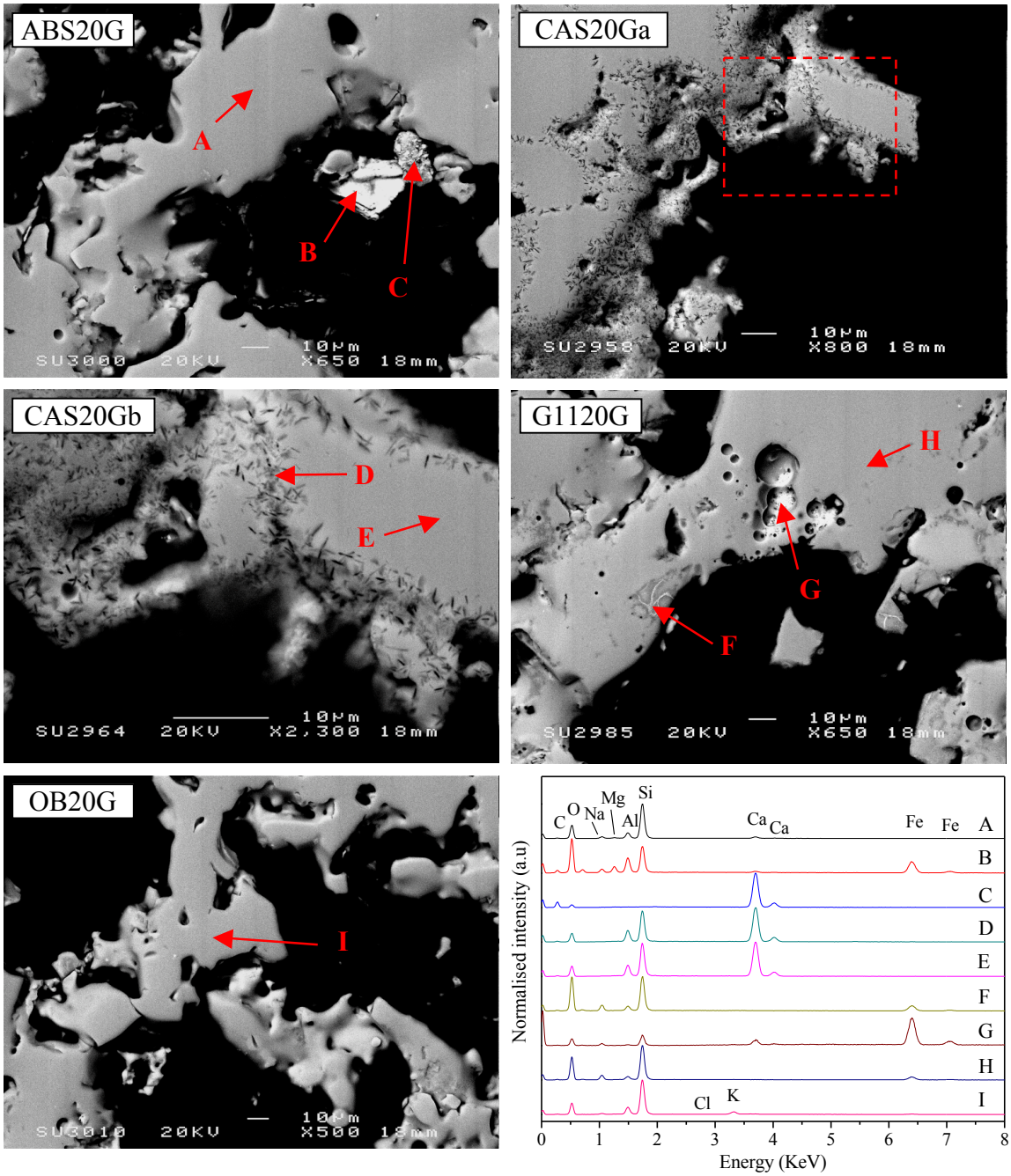

Figure 5-20: BE images and normalised EDS spectra of graphite-glass composites formed at the optimum sintering temperature.

To understand the interaction/reaction of glass or glass-ceramics with the graphite at various sintering temperatures, the samples that yielded maximum volume shrinkage for each series were subjected to line scan analysis. The line scan is very sensitive to the surface roughness of the

samples and the intensity of each spectrum is highly dependent on the depth of the surface profile. The results of the line scan analysis for ABS20G, CAS20G, G1120G, IP20G and OB20G are presented in Figures 5-21 to 5-25. All the line scans show there is no C in the glass and/or glass-ceramic matrix regions. It is also seen that all the expected elements of the glass or glass ceramic are detected by the EDS apart from the OB20G samples that revealed two amorphous phases that appear to be silicate and sodium aluminosilicate, respectively. Due to the similarity of the results, it can be inferred that there is no interaction between the graphite and glass/glass-ceramics particles in all sintered samples except for the possiblity of graphite oxidation (Figure 5-7) and the corresponding reduction of iron in G1120G, IP20G and OB20G samples. The evidence of iron reduction was observed in the BE images analysis of sintered G1120G at 560°C (Figure 5-20G1120G) and in previous Mössbauer analysis of sintered IP20G at 770°C (Section 4.5). There is no clear evidence of iron reduction in OB20G sample; this sample will be analysed further in Section 5.3.7. Overall, it can be seen from the results that the glass/glass-ceramics components are well attached to the graphite and the line scans data at ~2000× magnification implying that no chemical reaction between the materials occurred apart from some potential graphite oxidation and iron reduction.

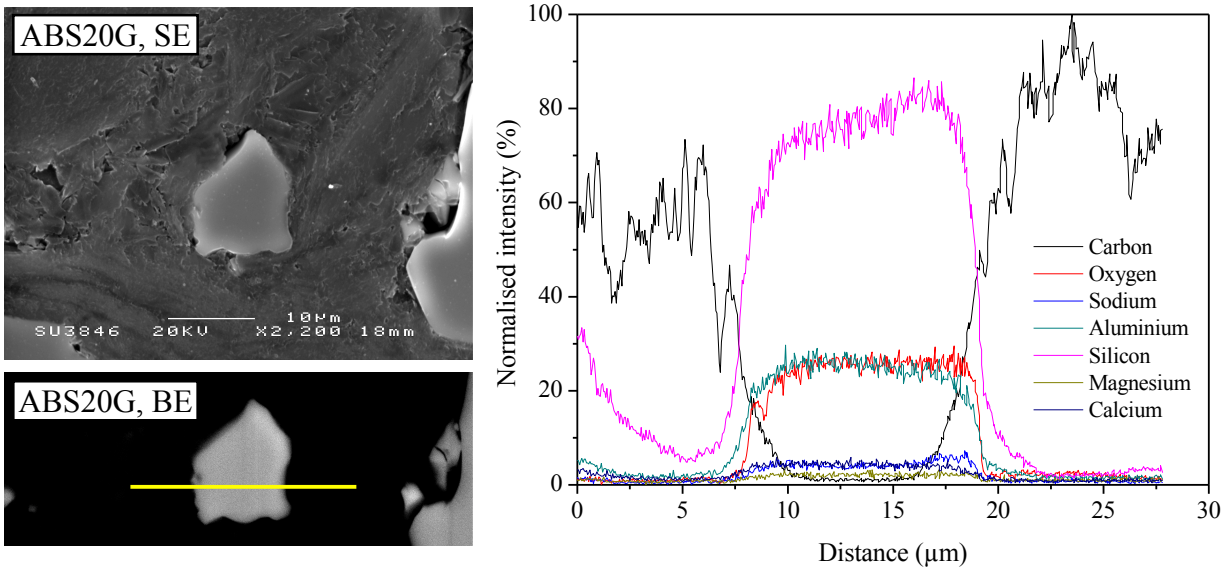

Figure 5-21: SE, BE images and normalised EDS line scan of ABS20G sintered at 790°C. Yellow line indicates the line scan.

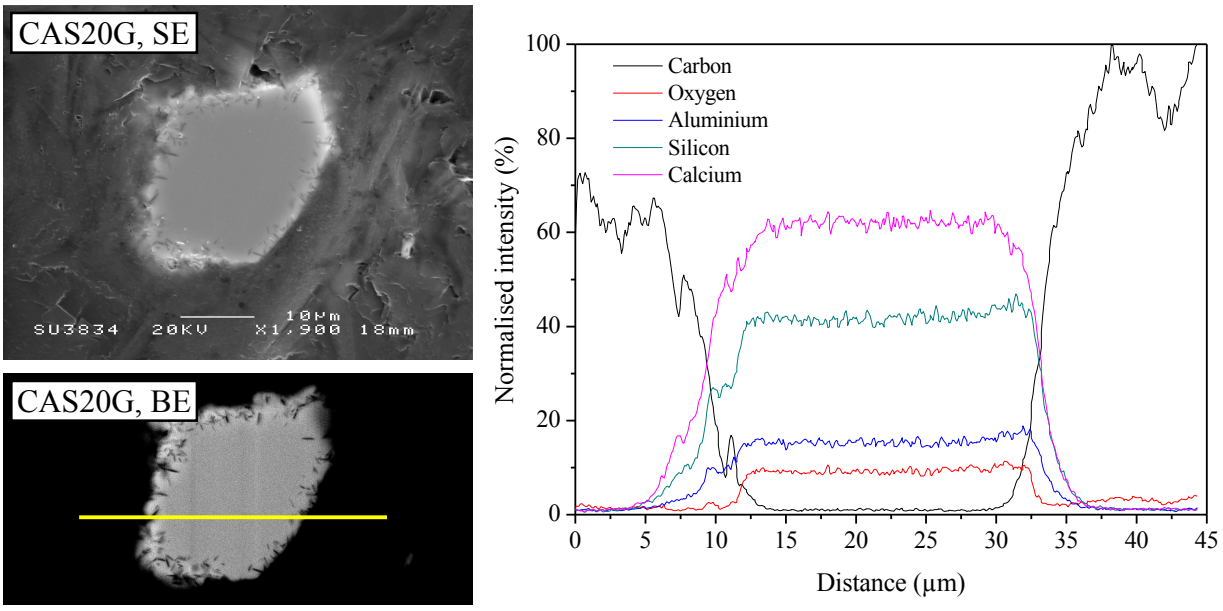

Figure 5-22: SE, BE images and normalised EDS line scan of CAS20G sintered at 890°C. Yellow line indicates the line scan.

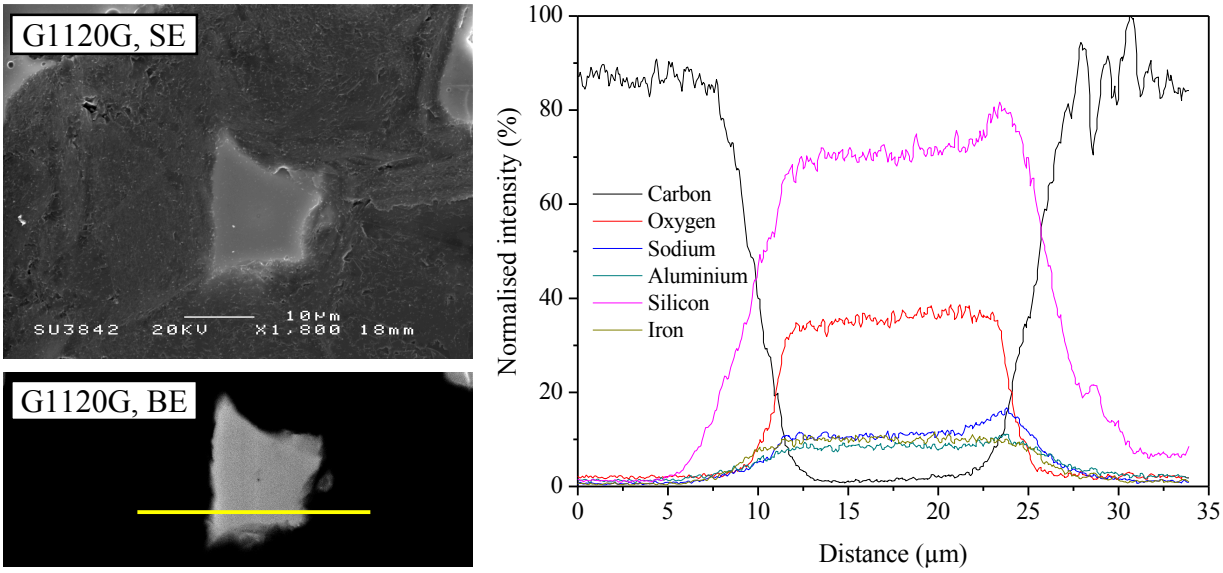

Figure 5-23: SE, BE images and normalised EDS line scan of G1120G sintered at 560°C. Yellow line indicates the line scan.

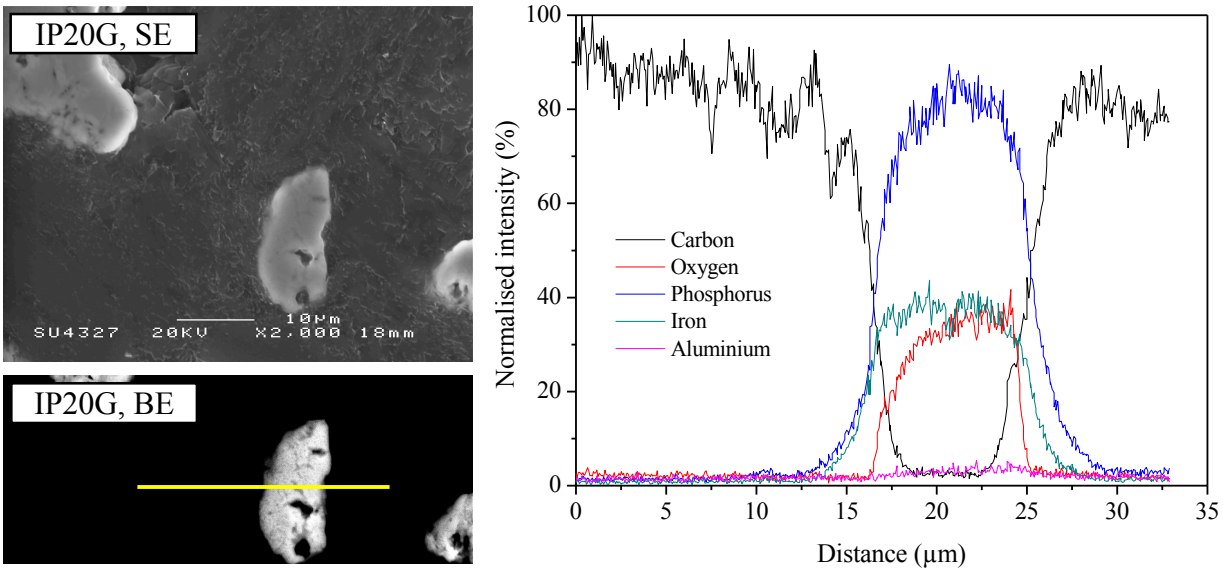

Figure 5-24: SE, BE images and normalised EDS line scan of IP20G sintered at 770°C. Yellow line indicates the line scan.

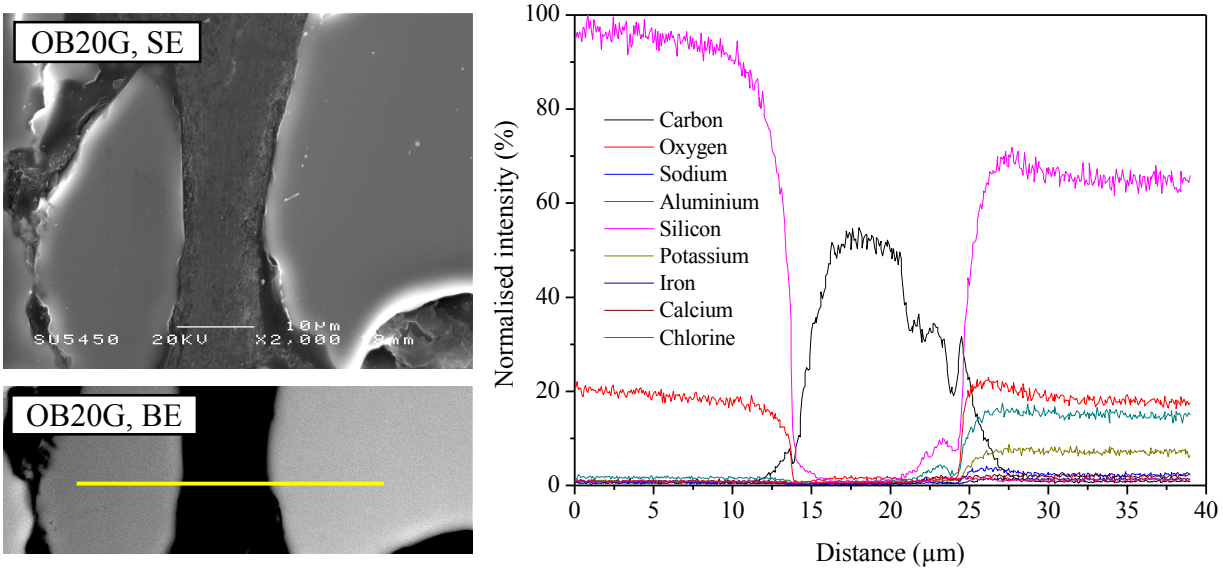

Figure 5-25: SE, BE images and normalised EDS line scan of OB20G sintered at 960°C. Yellow line indicates the line scan.

5.3.7. Mössbauer Spectroscopy

The fitted Mössbauer spectra analysed using Recoil software and the Mössbauer parameters of selected graphite-glass composites are shown in Figure 5-26 and Table 5-2 respectively. Only the samples that yielded maximum volume shrinkage are analysed in this section; the results on equivalent sample for IP20G can be seen in Section 4.5. The Mössbauer data of IP20G sintered at 890°C is presented here due to the total mass loss data for this sample (Section 5.3.2) which was significantly higher than in the other samples. From the spectra, two doublets have been fitted for glass samples to represent the contribution of Fe^{3+} and Fe^{2+}. For the IP20G samples sintered at 890°C, a similar approach used in the previous study (Chapter 4) is applied to quantify the contribution of glass and iron phosphate crystalline phases.

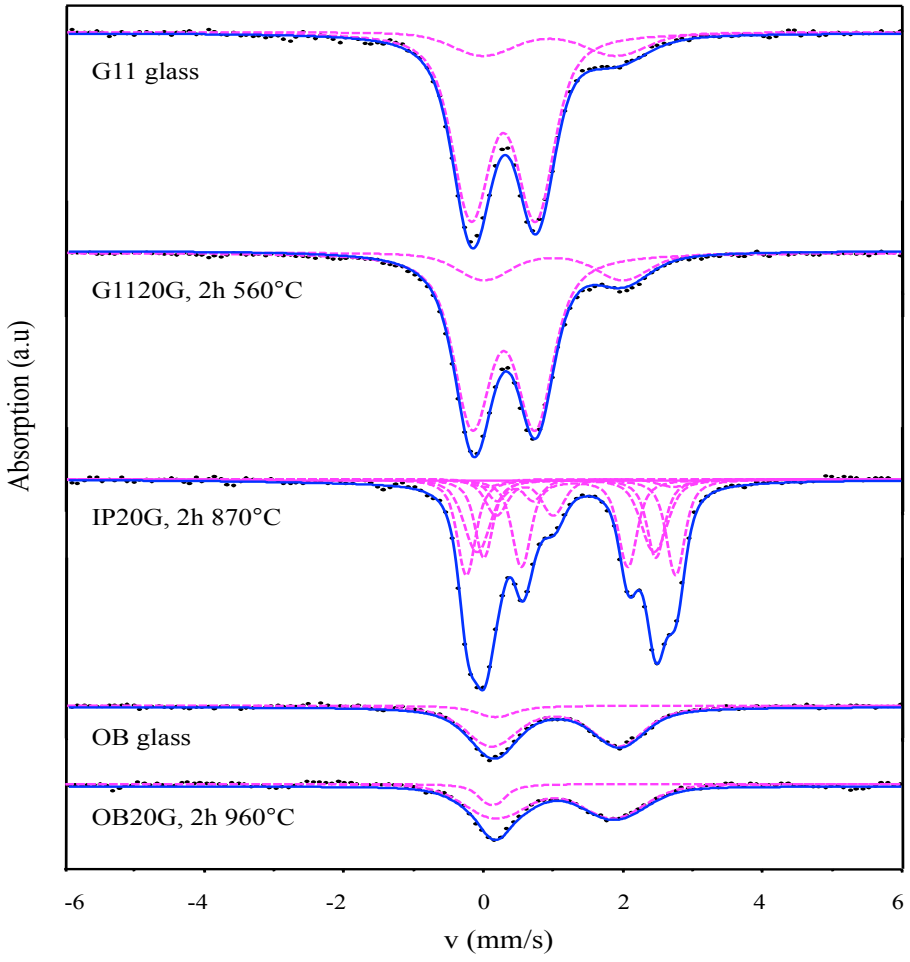

Figure 5-26: Mössbauer spectra of powdered base glasses and sintered graphite-glass composites.

As can be seen in Table 5-2, there is evidence that 2 % of Fe^{3+} has been reduced to Fe^{2+} in going from the G11 to G1120G samples. This explains the detection of porosity with iron content in the microstructural analysis of sintered G1120G at 560°C. For IP20G sample sintered at 870°C, 85 % of Fe^{2+} is detected. The amount of Fe^{2+} is increased by 28 % from the previous sintering temperature at 770°C. Further comparing both IP20G samples, it is found that the contribution of Fe^{3+} and Fe^{2+} in the glass is decreased and gives rise to more contribution of crystalline phases at 890°C; increased contribution of FeP_2O_6 and $Fe_2(P_2O_7)$ and decreased contribution of $Fe(PO_3)_3$ can be observed. These findings are in agreement with the total mass loss data and the XRD analysis.

Table 5-2: Mössbauer parameters (± 0.02 mm/s) of powdered base glasses and sintered graphite-glass composites (CS = centre shift, QS = quadrupole splitting, FWHM = full width half maximum).

Sample	CS (mm/s)	QS (mm/s)	FWHM (mm/s)	Assigned phase	Area (%)	Site	$(Fe^{2+}/\Sigma Fe) \times 100$ %
G11 glass	0.27	0.93	0.19	Glass	84	Fe^{3+}	16
	0.94	1.92	0.19	Glass	16	Fe^{2+}	
G1120G, 2h 560°C	0.28	0.90	0.22	Glass	82	Fe^{3+}	18
	0.99	2.00	0.22	Glass	18	Fe^{2+}	
IP20G, 2h 870°C	0.35	1.26	0.10	Glass	8	Fe^{3+}	85
	1.16	2.49	0.10	Glass	10	Fe^{2+}	
	1.34	1.44	0.10	FeP_2O_6	16	Fe^{2+}	
	1.24	2.76	0.10	FeP_2O_6	36	Fe^{2+}	
	0.30	0.41	0.10	$Fe(PO_3)_3$	4	Fe^{3+}	
	0.84	0.84	0.10	$Fe(PO_3)_3$	3	Fe^{3+}	
	1.18	1.85	0.10	$Fe_2(P_2O_7)$	7	Fe^{2+}	
	1.35	2.49	0.10	$Fe_2(P_2O_7)$	16	Fe^{2+}	
OB glass	0.16	0.21	0.27	Glass	10	Fe^{3+}	90
	1.02	1.82	0.27	Glass	90	Fe^{2+}	
OB20G, 2h 960°C	0.14	0.17	0.15	Glass	13	Fe^{3+}	87
	1.03	1.68	0.15	Glass	87	Fe^{2+}	

In OB glass, Mössbauer analysis suggests that the Fe^{2+} is dominant with the total value about 90 %. This may be due to the fact that the OB glass was formed in the presence of various reducing agents. As the OB glass is sintered with 20 wt% graphite loading, 3 % of the Fe^{2+} in the glass was oxidised to Fe^{3+}, suggesting that no reduction of iron by graphite occurred in this sample.

5.4. The Effects of Waste Loading on Graphite-glass Composites

In this section, further investigation is undertaken to identify the effect of waste loading on graphite-glass composite samples prepared using the CPS method. From the previous analysis, it is found that the main factors that need to be clarified in order to identify the waste loading limit in the glass composite system are as follows: the volume shrinkage of the graphite-glass composites, the mass loss of graphite, the porosity generated in the graphite-glass composites and the mechanical properties of the final wasteforms. The sintering temperatures that yielded maximum volume shrinkage (based on samples loaded with 20 wt% graphite) were used to sinter the graphite-glass composites with varying graphite loading from 5-35 wt%. A photographic image of the selected samples is shown in Figure 5-27.

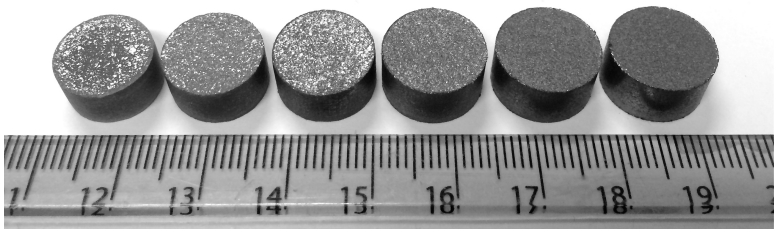

Figure 5-27: Photographic image of CAS series sintered at 890°C (from left to right: 5, 10, 15, 20, 25, 30, 35 % graphite loading), similar images were obtained for the other series.

It must be noted that two assumptions have been made in this section. The crystalline phase of the samples is assumed to be similar; *i.e.* changing the waste loadings does not affect the phase of the samples. This assumption has been made as it is evident that the sintered glass and sintered graphite-glass composites loaded with 20 wt % graphite do not show any significant differences

in their XRD patterns (Section 5.3.4). The second assumption is that a similar microstructure is obtained with the amount of graphite seen depending on the waste loading. The work is not focussed on the microstructural study due to the fact that the glass/glass-ceramic component does not react with the graphite, only graphite oxidation and reduction of iron occurred in samples that involved G11 and IP base glasses. Due to the potentially increased graphite loss, it is inferred that these samples are not suitable to immobilise graphite. However, for the sake of comparison, these samples were also investigated in this section.

5.4.1. Volume Shrinkage

The volume shrinkage as a function of graphite loading is shown in Figure 5-28.

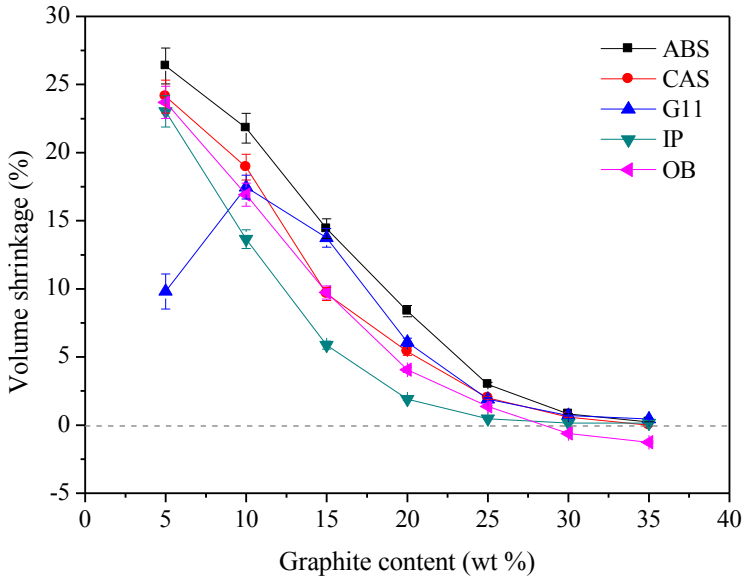

Figure 5-28: Volume shrinkage versus various waste loading of graphite-glass composites formed at selected sintering temperature: ABS - 790°C, CAS - 890°C, G11 - 560°C, IP - 770°C, OB - 960°C.

In all graphite-glass composite series, it is seen that the volume shrinkage decreased from 5-35 % graphite loading. However this is not the case for the G115G sample; a lower volume shrinkage of about 9.8 % was found at 5 % graphite loading. This may be due to the glass particles having become sufficiently fluid whilst sintering and it is observed that 5 % graphite loading is not

adequate to hold the shape of the pellet (pellet became bloated), thus giving the lower volume shrinkage value. From the graph, it is apparent that the OB30G and OB35G samples indicate negative values of volume shrinkage, suggesting the samples have slightly expanded. The reason for the expansion behaviour might be due to the effect of excessive amount of graphite oxidation (also boating effect caused by significant amount of gas diffusion). Overall, apart from the G115G sample, it is clear that the trend of volume shrinkage for all series is similar despite the different base glasses used.

5.4.2. Mass Loss

The variations of total mass loss measured in various graphite-glass composites samples with varying waste loading are presented in Figure 5-29. It is clear from the graph that each series of the samples has a similar total mass loss trend; the total mass loss increases with increasing graphite loading. Although similar trends were found in all series, the highest total mass loss throughout the various graphite loadings is detected in the OB series. As mentioned before, this phenomenon may be due to the release of volatile components in OB glass together with potential graphite oxidation to CO and/or CO_2. This finding is in agreement with the volume shrinkage data and the volume expansion of OB30G and OB35G samples. The total mass loss of CAS and G11 series are comparable to each other and yielded the lowest total mass loss compared to the other sample series. In all series, the total mass loss data were thought to originate from the mixed contributions of gases released from the glass (*i.e.* moisture, volatile elements in OB glass) and graphite (*i.e.* graphite oxidation, reduction of iron by graphite).

In order to identify the graphite loss in all samples, each total mass loss value has been subtracted from the mass loss of the sintered base glasses prepared using similar method to the graphite-glass composite samples. The graphite loss data for each sample is presented in Figure 5-30. Based on the data, the mass loss of graphite is small and in general < 0.8 %. It is worth noting that the studied sample is small; for example 0.8 % is equivalent to ~0.016 g graphite loss. In all series, the trend of the graphite loss increases with increasing graphite loading. It is notable that the graphite losses in ABS, IP and OB series vary at lower waste loadings but exhibit similar mass losses at 30 and 35 % graphite loadings where the values are about 0.6 and 0.7 %

respectively. Similarly with the total mass loss data, the lowest graphite losses in the region of 20-35 wt% graphite loading are seen in the CAS and G11 series.

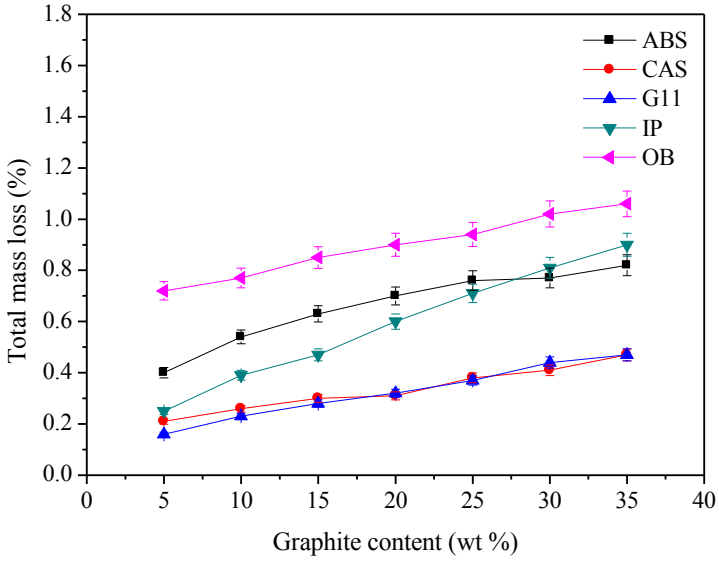

Figure 5-29: Total mass loss versus various waste loadings of graphite-glass composites formed at selected sintering temperatures: ABS - 790°C, CAS - 890°C, G11 - 560°C, IP - 770°C, OB - 960°C.

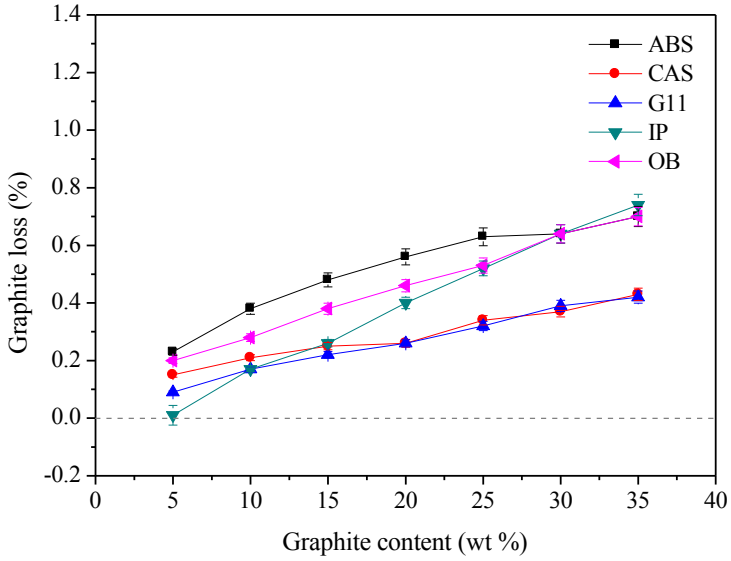

Figure 5-30: Percentage of graphite loss after considering the losses from the sintered base glasses.

5.4.3. Density and Porosity

The bulk density of the prepared graphite-glass composites with varying waste loadings is displayed in Figure 5-31. The trends of the bulk density of CAS and IP graphite-glass composite series were found to be similar with both showing a decrease in bulk density with increasing graphite loading. This is in agreement with the mass loss data of these samples. For the G11 series, the bulk density data seem to fluctuate below 20 wt% and afterward increase steadily to 35 % graphite loading. The reason for this could be the porosity that is generated whilst undertaken the sintering process. Comparing the trend in bulk density of the ABS and OB series, it is seen that the trend is reasonably flat. There is no significant changes can be found in the density values for each series except the slight decrease of the density of the ABS series, which can be observed from 5-20 wt% graphite loadings.

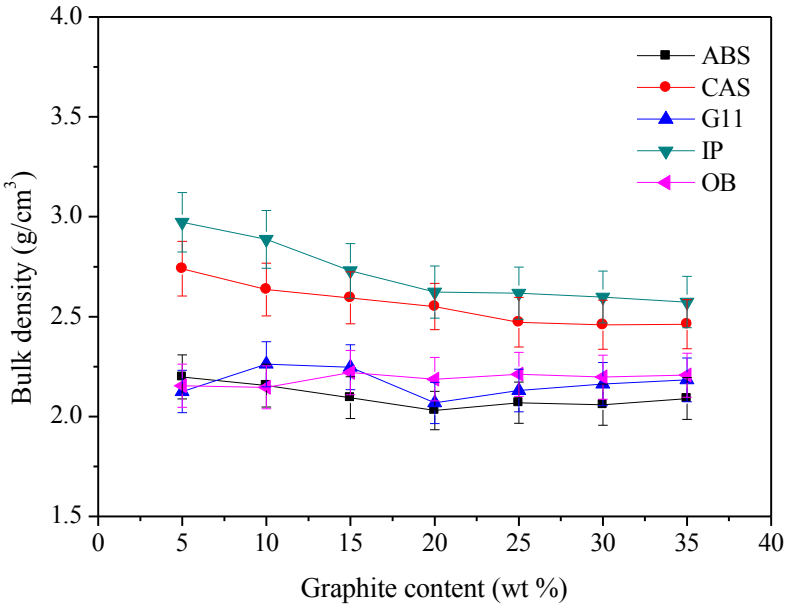

Figure 5-31: Bulk density versus various waste loadings of graphite-glass composites formed at selected sintering temperature: ABS - 790°C, CAS - 890°C, G11 - 560°C, IP - 770°C, OB - 960°C.

Figure 5-32 shows the measured powder density of graphite-glass composite samples prepared with various graphite loadings. The overall trend of powder density in all series is decreasing

with the increase of graphite loading. This is expected as the density of graphite is lower than the density of the glasses. In this case the greater addition of graphite in the samples will further reduce the powder density of the graphite-glass composites. It is also seen in the graph that the powder density data of the ABS and OB series are similar.

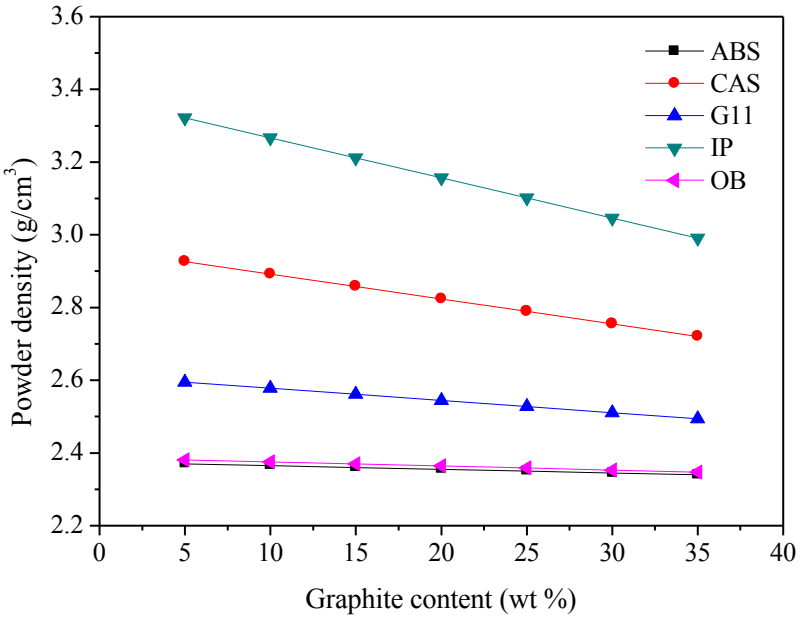

Figure 5-32: Powder densities versus various waste loadings of graphite-glass composites formed at selected sintering temperature: ABS - 790°C, CAS - 890°C, G11 - 560°C, IP - 770°C, OB - 960°C.

Figure 5-33 shows the complication of porosity data as a function of graphite loading. In general, the trend of porosity for ABS, G11 and IP series is found to be similar apart from the G115G sample; the trend shows increasing porosity from 5-20 wt% and afterwards decreases gradually to 35 % graphite loading. As G115G sample is considered, the high value of porosity is in agreement with the low value of volume shrinkage (see Section 5.4.1). For CAS series, the trend of the porosity is found to increase from 5-25 % and decreases steadily towards 35 % graphite loading. The trend of porosity for OB series, on the other hand, was found to decrease from 5-15 %, increase slightly at 20 wt% and afterward was found to be stable from 25-35 % graphite loading. Overall, the highest percentage of porosity is found in the G11 and IP series, followed

with ABS, CAS and OB series respectively. Based on the graph, it is observed that the porosity tends to decrease at high waste loading (> 20 wt %). This phenomenon may be related to the soft nature of the graphite particles that potentially filled the voids during the pressing of the green body; when graphite powder is pressed at 3 tons (does not involve sintering), 94.55 % of theoretical density is achieved.

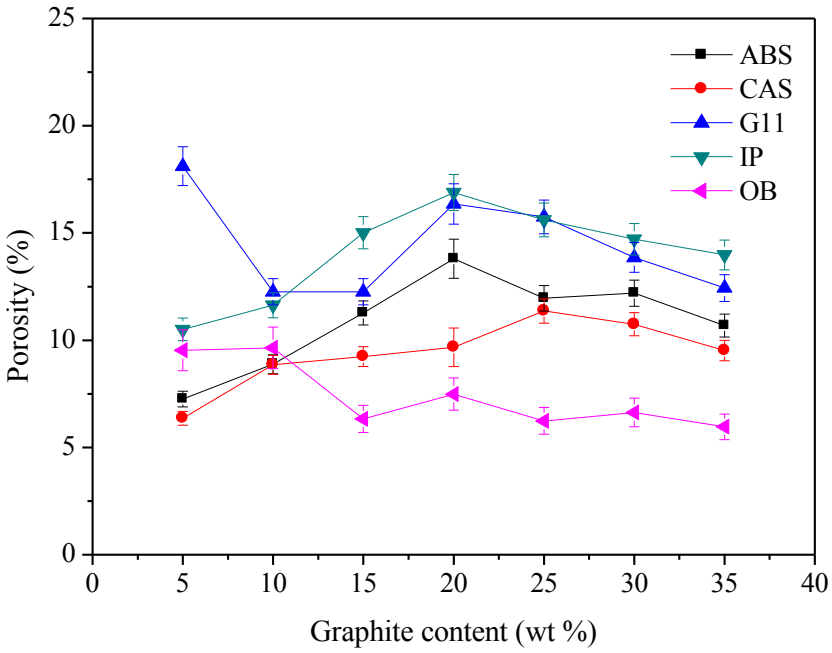

Figure 5-33: Porosity versus various waste loading of graphite-glass composites formed at selected sintering temperature: ABS - 790°C, CAS - 890°C, G11 - 560°C, IP - 770°C, OB - 960°C.

5.4.4. Indirect Tensile Testing

The indirect tensile strength as a function of graphite loading is presented in Figure 5-34. In this particular characterisation, 175 samples have been tested and the data at each point represents the average of 5 successful measurements. It can be seen that a large scatter was found with lower waste loadings of < 15 %. This is due the shape of the samples being slightly concave, which leads to an increase in the measurement error. The concave shape is thought to be due to the effect of gravity during the sintering process. The values of indirect tensile strength in all series

fluctuate below 20 wt% graphite loading, however, the overall trend indicates that the indirect tensile strength decreases with increasing graphite loading. At above 15 wt% graphite loading, the data are more consistent and it is clear that IP and OB series yield the lowest value of the indirect tensile strength compared to the other series. The ABS, CAS and G11 series show similar indirect tensile strength data with the values about 6, 5 and 4 MPa at 25, 30 and 35 % graphite loading respectively. It is worth noting that the graphite is easily removed from the samples that yielded indirect tensile strength values below 5 MPa.

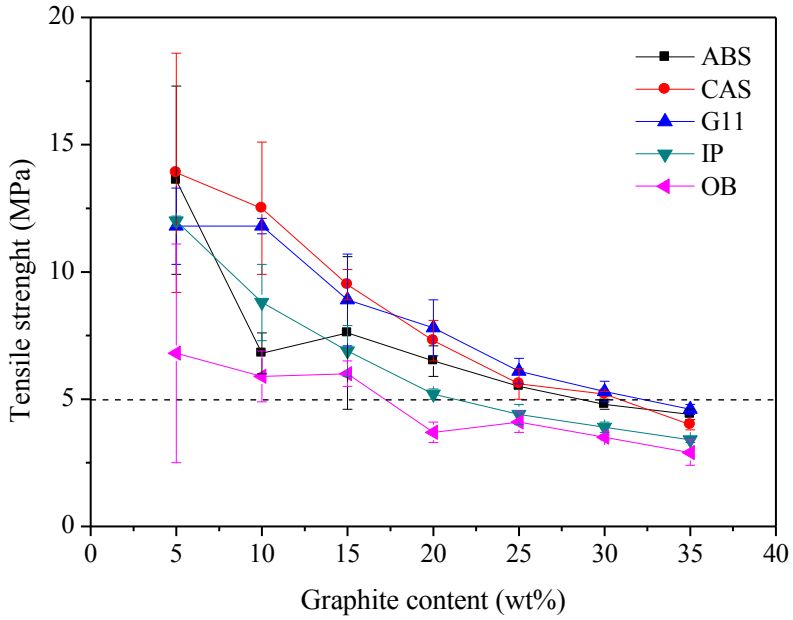

Figure 5-34: Indirect tensile strength versus graphite loading of graphite-glass composites formed at selected sintering temperature: ABS - 790°C, CAS - 890°C, G11 - 560°C, IP - 770°C, OB - 960°C.

5.5. Discussion

In this work, the use of ABS, CAS, G11, IP and natural OB as base glasses for the immobilisation of simulant irradiated graphite have been studied. The selected base glasses have been previously shown to be capable of immobilising nuclear wastes and have potential for dealing with problematic irradiated graphite waste. For example, ABS glass has been identified

as a promising candidate to immobilise TRISO fuel generated from HTR reactors (Heath *et al* 2013); CAS glass as a composition to incorporate Cl originating from pyrochemical reprocessing (Schofield *et al* 2009, Schofield 2011); G11 glass has been suggested as a host glass for ILW and is resistant to gamma radiation (Bingham *et al* 2012, McGann *et al* 2012) and IP glass has been widely researched for HLW immobilisation (Day *et al* 1998, Marasinghe *et al* 2000). Moreover, OB has been considered due to its high durability (Ericson *et al* 1975); obsidians can survive up to millions of years in the natural environment (Vogel *et al* 2006, Morgan *et al* 2009).

From the elemental analysis, similar chemical compositions to those batched were found in all the in-house produced glasses except for contamination of Al_2O_3 from the alumina and mullite crucibles. Although the use of a Pt crucible can avoid contamination while preparing the glasses, this crucible is not suitable for making large amounts of glass (ABS), coloured glass (G11) and highly corrosive melts (IP). This is due to the fact that the Pt crucible used had low volume, coloured glass will complicate the cleaning process and IP melts react with the crucible. Among all the studied base glasses, the IP melts created during glass melting have been confirmed as being extremely corrosive as this glass yielded the highest Al_2O_3 contamination about 1.07 mol %. This corrosive nature of IP glass is in agreement with the literature related to iron phosphate glass (Donald 2010). The EDS elemental analysis suggested that Cl is present in the OB glass. Although there is no clear evidence, it is believed that Cl is the reason why the OB glass aggressively reacts at temperatures of ~700-1000°C (expended and bubbling), which made the dilatometry measurement impossible.

According to the density analysis, it is suggested that the lowest amount of porosity is developed in the annealed base glasses, which was found to be < 1 %. The prepared base glasses have been confirmed to be predominantly amorphous with a negligible detection of SiO_2 crystalline phase (β-quartz) in ABS and G11 glasses. In thermal analysis, the T_g value of each base glass measured with DTA and dilatometer were found not similar; the difference in T_g values for each glass is about ± 6 %. This is not expected, however, the reason for such different values may be due to the use of powdered glass frits for DTA measurements and polished annealed monoliths for dilatometry measurements. Whilst there is no problem using the powdered glass for DTA measurements, it is thought that the sample dimensions prepared for the dilatometry

measurements was not perfect, thus less accuracy on sample expansion reading, which consequently creates measurement error. In agreement with literature, the T_g values of some glasses measured using dilatometry were found fluctuated in value compared to the T_g obtained from DTA technique (Mazurin 2007).

The FTIR and Raman spectra of each base glass revealed largely similar detection of molecular bonds. The only advantage of using Raman spectroscopy is that the spectra show more clear detection of silicate ring defect modes in the lower frequency region of the ABS, G11 and OB spectra. Based on the FTIR and Raman analysis, the elements acting as network formers in each glass is identified as follow: ABS - Si, B, Al, CAS - Si, Al, G11 - Si, B, Al, IP - P, Fe (intermediate) and OB - Si, Al; other elements detected in the glasses are network modifiers. Besides no detection of B network in OB glass, both FTIR and Raman spectra of ABS and OB glasses were comparable (compare FTIR and Raman spectra in Figure 5-3 and 5-4) and the data suggested that these glasses shared similar structural properties. This finding is consistent with the similar results of density and chemical composition of these glasses. Although Cl, K_2O and Fe_2O_3 are detected in OB glass, it is believed that these elements act as network modifiers, hence, are not detected in FTIR and Raman spectra. In addition, the Cl element might as well substitute with O and this leads to the same outcome.

Based on the physical properties of graphite-glass composites (loaded with 20 % graphite) sintered from 50°C above T_g to various high temperatures and specifically from the maxima of the volume shrinkage values, it can be inferred that the best sintering temperatures for ABS20G, CAS20G, G1120G, IP20G and OB20G samples are 790, 890, 560, 770 and 960°C respectively. The mass loss, density and porosity data for each series of graphite-glass composites confirmed that gas release occurred during the sintering process. Furthermore, in all graphite-glass composites series, gas release was found to increase significantly with increase of sintering temperature/graphite loading. Although all the sintering was undertaken in closed systems with flowing argon gas, it is suggested that some oxygen may be present whilst sintering process take place and consequently promotes the oxidation of graphite. The presence of oxygen in the system may originate from different sources as follows:

i. Impurities in the argon gas. The manufacturer claimed that the gas is 95 % pure; the other 5 % may contain air.
ii. There is abundance of oxygen in the glass network and sintering to high temperatures give rise to the rearrangement of the molecules; this process may release the oxygen.
iii. The air that is trapped in the void between glass and graphite particle created whilst pressing the samples.

As the presence of oxygen is considered, it is suggested that two main reactions occurred that lead to the possibility of releasing CO_2 and CO whilst undertaken the sintering process; when the samples are in excess of oxygen,

$$C + O_2 \xrightarrow{\Delta Q} CO_2 \qquad [5\text{-}1]$$

and when the air and/or oxygen supply is restricted to the samples, incomplete combustion can occur as

$$2C + O_2 \xrightarrow{\Delta Q} 2CO. \qquad [5\text{-}2]$$

In the base glasses that contain considerably large amounts of iron, in this case G11, and IP, the reduction of iron, from Fe^{3+} to Fe^{2+} also contributes to the release of gases. The reaction that would occur in the presence of CO in the G1120G and IP20G graphite-glass composite samples is given by

$$Fe_3O_4 + CO \xrightarrow{\Delta Q} 3FeO + CO_2. \qquad [5\text{-}3]$$

This finding is supported by the significant increase of mass loss data, detection of porosity related to iron reduction in SEM images and the increase of Fe^{2+} component in Mössbauer data. Specifically, for IP20G and G1120G samples that yielded maximum volume shrinkage, the Mössbauer analysis confirmed the 7 and 2 % increase of Fe^{2+} compared to the base glass of these samples. This suggested that the reduction reaction occurred in the samples and led to the loss of graphite as well as releasing CO_2, hence increasing the total porosity of the samples. Severe

reduction of iron is found in IP20G samples sintered at 870°C with the highest mass loss among all graphite-glass composite series (about 2 %). This in agreement with the literature that suggested iron reduction heavily occurs in this temperature region (Hisa *et al* 2004, Mondal *et al* 2004, Piotrowski *et al* 2005). In the OB20G sample series, the Mössbauer data suggests that the iron content was largely present as Fe^{2+} in the base glass and 3 % of it oxidised to Fe^{3+} when sintered at 960°C. This suggested that less release of gas occurred which is in line with the low values of total mass loss and porosity of this sample. The equation for this reaction is given by

$$4FeO + O_2 \xrightarrow{\Delta Q} 2Fe_2O_3 . \qquad [5\text{-}4]$$

In crystalline phase analysis, the glass component in all graphite-glass composites is found to crystallise on sintering at high temperatures. Referring to the samples that yielded maximum volume shrinkage, it is found that graphite is immobilised in glass system for ABS20G and OB20G and in glass-ceramics system for CAS20G, G1120G and IP20G respectively. The comparison between sintered glass and sintered graphite glass composites for each sample revealed similar detection of crystalline phases (refer Section 5.3.4). It is also found that there is no signification change in the graphite peaks in all sintered samples. This clearly indicates that the presence of graphite does not affect the crystallisation of the glass component. The XRD data is backed up by the SEM and EDS analysis. Based on the SEM images, all detected crystalline phases from XRD analysis are identified apart from the undetectable lithium silicate phase.

The surface analysis of all potential samples indicated that some of the graphite particles have been removed whilst undertaken grinding and polishing processes. This finding suggests that the soft characteristic of graphite remains similar; pressing the samples at 3 tons and sintered at high temperature does not affect the soft characteristic of the graphite. Despite the fact that some graphite is removed, the glass and/or glass-ceramic components indicate better mechanical strength on the surface and this has been confirmed by optical profilometer images (refer Figures 5-16 and 5-17).

The SEM with EDS analysis confirms that reduction of iron occurred in G1120G and IP20G samples. From the microstructure of the samples, the porosity seen in the images is also in

agreement with the porosity data; G1120G, IP20G and ABS20G samples indicate more micro size porosity compared to the CAS20G and OB20G samples (Figure 5-18 and 5-19). The increase of porosity in G1120G and IP20G series is in line with the occurrence of iron reduction. The detection of high levels of porosity in ABS20G samples is not clear. However, it is believed due to the decomposition of unreacted $CaCO_3$ precursor together with the influence of Ca species (perhaps present as $CaCO_3$) from graphite contamination that favours to form CaO (see Section 5.3.6, Figure 5-20ABS20G), leading to the release of CO_2 therefore increasing the total porosity.

From the investigation of graphite-glass composites with varying waste loading, it is found that the volume shrinkage decreases with increasing waste loading. This suggests that the graphite particles remained in a similar state as in the green body; only glass particles softened with temperature and become sufficiently liquid to fill the porosity in the samples. From the mass loss data, a minimal amount of graphite is oxidised from CAS and G11 series, however, the porosity data suggest a large amount of porosity in the G11 series (refer Figure 5-33). This is due to the effect of iron reduction in this sample (more porosity generated). The OB series indicated minimum porosity compared to the other sample but in terms of the mass loss, this series yielded high graphite loss and considerably lower indirect tensile strengths. In regard to all the data, it is suggested that the potential base glass to immobilise graphite is CAS. This is due to this glass yielding minimum graphite loss and acceptable indirect tensile strength at a waste loading of 30 wt%. In addition, iron is not present in this glass and this is advantageous for the immobilisation of graphite.

5.6. Summary

Considering all the data discussed in this chapter, it is concluded that the use of a base glass containing iron is not suitable for the immobilisation of graphite. This is due to the reduction of iron in this glass promoting the development of porosity and may reduce the corrosion and leaching resistance of the wasteform. The most promising sample is found to be CAS30G with graphite loss, porosity and indirect tensile strength of 0.37 %, 10.74 % and 5.2 MPa respectively. However the porosity generated in this sample is still too high for viable wasteform production. Overall, the CPS method used in this chapter is seen to be ineffective to immobilise simulant

irradiated graphite waste. Thus for further investigatation, sintering under pressure with an inert environment (*e.g.* argon, vacuum) must be considered.

6. Results and Discussion III: The Immobilisation of Simulant Irradiated Graphite in Calcium Aluminosilicate Glass Composites Using Spark Plasma Sintering

6.1. Introduction

As mentioned in Section 3.5, the SPS method utilises pulsed electric current (on-off DC) to generate heat and offers sintering processing under pressure in a static argon environment. The fast sintering process and the application of pressure arising from the SPS method were hypothesised to be advantageous for the immobilisation of irradiated graphite; this method may reduce the amount of porosity which has been identified as a major problem in graphite-glass composites that were formed using microwave (Chapter 4) and CPS (Chapter 5) processing. In this novel investigation, the prepared samples were characterised using various analytical methods including density, porosity, XRD, optical microscope, SEM equipped with EDS, optical profilometry and indirect tensile testing. The sintering parameters of SPS processing such as sintering temperatures and sintering dwell time together with the investigation of graphite loading limit in the CAS glass system are studied in this chapter.

6.2. Sintering Profile of SPS

Figure 6-1 presents the typical temperature, pressure, piston displacement and average speed characteristics that were recorded in-situ during the preparation of the CAS30G sample using the SPS method. The sintering profile was initialised at 450°C with an applied pressure of 16 MPa. This pre-sintering stage is necessary in order to remove the residual air trapped between the particles and also to ensure both upper and bottom punches are aligned parallel to each other. At about 5 min processing time, the temperature and pressure are programmed to increase simultaneously to 890°C with a maximum pressure of 35 MPa. The heating rate of the sintering process was maintained at ~200°C/min. The densification mainly began during the heating stage as the measured displacement and average speed of the pistons increased significantly when the maximum sintering temperature and pressure were reached; this event occurred in all samples sintered by using SPS method. The negative displacement at around ~6 min processing time

appears to be associated with the thermal expansion of the samples, graphite sheet, graphite mould, graphite spacers and/or pistons (Córdoba *et al* 2013, Huang *et al* 2013, Hussainova *et al* 2014). The displacement and the average speed of the pistons did not significantly change during the sintering dwell time (20 min) and rapid cooling process. However, a slight increase of the displacement value can be observed from ~7.5 min to the end of the sintering process. The displacement increases slowly and steadily at this time period, implying continued densification of the sample. This may occur when the CAS glass component reached a partially solid-liquid state and potentially further filled the porosity. The measured displacement and shrinkage rate of CAS30G sample are found to be 2.50 mm and 10.35 mm/min respectively.

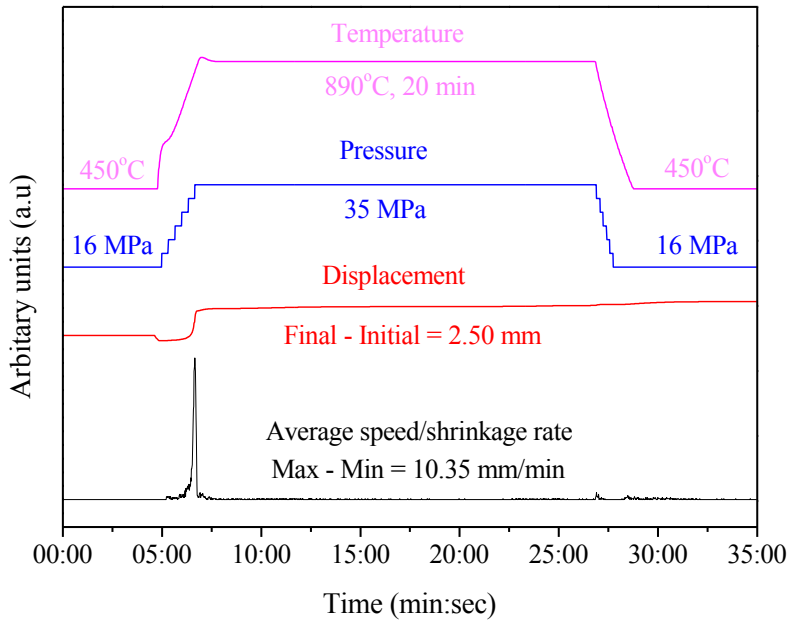

Figure 6-1: Sintering profile of CAS30G sample recorded in-situ during SPS experiment.

For all samples prepared using the SPS method, similar pre-sintering treatments, heating rates, pressure profiles and cooling processes to that described were used. The displacement and the average speed of the pistons were monitored throughout the preparation process and these parameters may shed some light about the shrinkage, density and porosity behaviour of the samples whilst undertaking SPS processing. However, based on the analysis of the displacement and the average speed of all samples, it is found that the patterns of both sets of data were not coherent with the fundamental theory of densification *i.e.* the displacement of the CAS30G

samples should increase with the increasing sintering dwell times (sintered at 890°C - this temperature resulted in the highest density value of sintered glass) and become constant at some point where densification is completed; the data recorded in-situ suggesting some fluctuation of the displacement and average speed values. This behaviour is due to the complication of some samples that are present in a solid-liquid state whilst sintering and which can leak through the small slits between graphite dies. In addition, the green body samples were enveloped with the graphite sheet in order to increase the lifetime of the graphite mould and improve the heat transfer mechanism. The inconsistent thickness of graphite sheet might also influence the displacement and average speed data. Thus, in this work, the data have been replaced with the measured bulk and powder density as well as the analysis of the calculated porosity of the samples.

6.3. Sintered CAS Glass Prepared using CPS and SPS Methods

In this section, the sintered CAS base glass powder compact prepared without the addition of graphite using CPS method is compared with the equivalent sample produced using the SPS method. The purpose of this comparison is to understand the effectiveness of the SPS method, and whether it is suitable for the immobilisation of irradiated graphite. It is worth noting that a similar sintering temperature (890°C) with dwell times of 2 h and 20 min respectively were used for the preparation of sintered CAS glass using CPS and SPS methods. The thermal analysis, XRD, FTIR and Raman analysis of the powdered CAS glass were discussed in Section 5.2.

6.3.1. Density and Porosity

The averaged density and porosity data of sintered CAS samples formed using the CPS and SPS methods are detailed in Table 6-1. The SPS sample has higher powder and bulk density values and a lower porosity than the CPS sample. This data indicates greater densification was achieved in the SPS sample compared to the CPS sample, which was sintered for a longer time. It can be seen that the SPS method successfully reduced most of the porosity in sintered CAS sample and this is a good indication for producing a better wasteform, especially when the simulant graphite waste is introduced into the system.

Table 6-1: Density and porosity data of sintered CAS glasses prepared using CPS and SPS methods.

Parameter	CAS 890°C (2h, CPS)	CAS 890°C (20 min, SPS)
Powder density (g/cm^3)	2.9607 ± 0.0028	2.9955 ± 0.0025
Bulk density (g/cm^3)	2.809 ± 0.140	2.957 ± 0.148
Porosity (%)	5.1 ± 0.1	1.3 ± 0.2

6.3.2. XRD

Figure 6-2 compares the normalised XRD patterns measured from the sintered CAS samples prepared using SPS and CPS methods. From the XRD analysis, it is found that the same crystalline phase is precipitated in both samples; all peaks matched with larnite (Ca_2SiO_4, PDF card 00-033-0302).

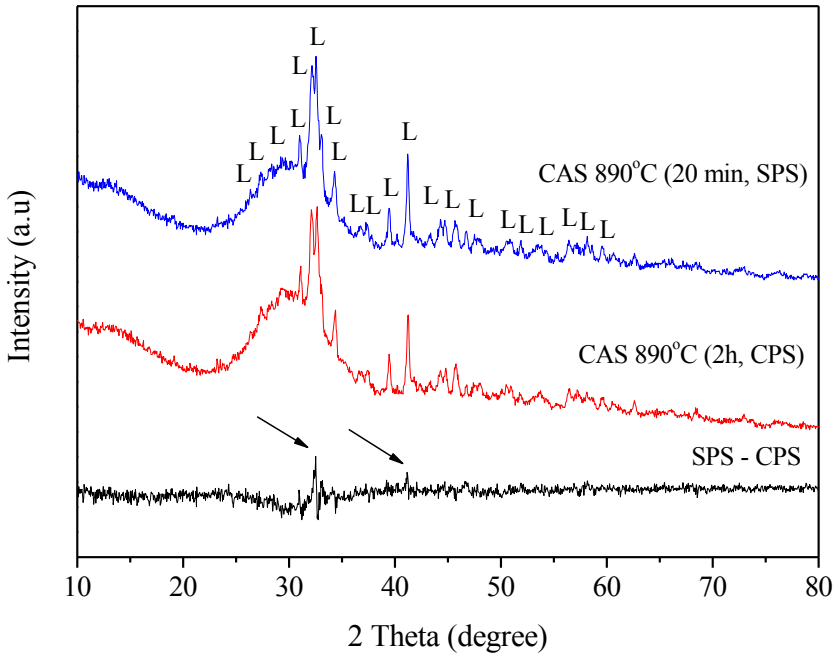

Figure 6-2: Normalised XRD patterns of sintered CAS glasses prepared using SPS and CPS methods, L = Ca_2SiO_4.

The difference pattern indicates that the intensity of larnite peaks located at ~32.5 and ~41.1° of *2θ* (indicated by arrows) is increased in the SPS diffractogram. Another distinctive feature in the difference pattern is the occurrence of a negative diffuse scattering characteristic (inverted amorphous hump) located between 25 and 35° *2θ*. These phenomena suggest that more crystalline phase and less glassy phase was present in the SPS sample. According to the PDF card, the density of larnite is 3.28 g/cm^3 and the measured powder density of the CAS glass using pycnometry is 2.89 g/cm^3 (refer Table 5-1). Based on this data, the crystalline phase analysis can be directly related to the measured density (Table 6-1), as the SPS sample has a density exceeding that of the pure glass and CPS sample. Indeed, this event is believed due to the slight reduction of glassy phase that favoured formation of larnite crystals.

6.3.3. Optical Microscopy

Figure 6-3 shows low and high magnification optical micrographs of sintered CAS glasses produced using the CPS and SPS methods. As can be seen in the low magnification images (Figure 6-3a and Figure 6-3c), it is obvious that there is a larger amount of isolated porosity in the CPS sample compared to the SPS sample. The size of porosity in CPS samples is in range between ~1 and 100 μm. In contrast, limited porosity is detected in the SPS sample (arrowed) with an average diameter of < 5 μm. The low magnification images also indicate that the grains appeared similar to the original glass particles but that there are crystalline ingrowths. Apart from the difference in porosity, it can be seen that some areas appeared lighter in colour in the SPS sample (see Figure 6-3c). The lighter features are thought to be the crystal-free regions with a mirror-like finished surface that reflect light of the microscope. This has been confirmed in the high magnification image (Figure 6-3d) that is focused on a lighter feature, labelled X; the grey area without any crystalline feature is assumed to be a glass region (refer Figure 6-4 for the EDS data). The ingrowth of the crystalline features appears to be completed at region Y. However, the orientation of the particle may have affected the image. It is arguable that the particle (area Y) is fully crystallised or the particle is ground and polished at the top surface, which at this region is dominated by the crystalline material. Comparing both high magnification images of the CPS (Figure 6-3b) and SPS (Figure 6-3d) samples, it can be observed that the SPS sample is heavily crystallised whereas any crystal growth in the CPS sample appears to be confined to the

grain boundaries. It is also seen that the needle-like feature occurred in the SPS sample seems to be longer in length compared to the ones that occurred in the CPS sample. Based on the XRD analysis it is suggested that the needle-like feature that randomly dispersed on the surface of the particles in both samples are larnite crystals.

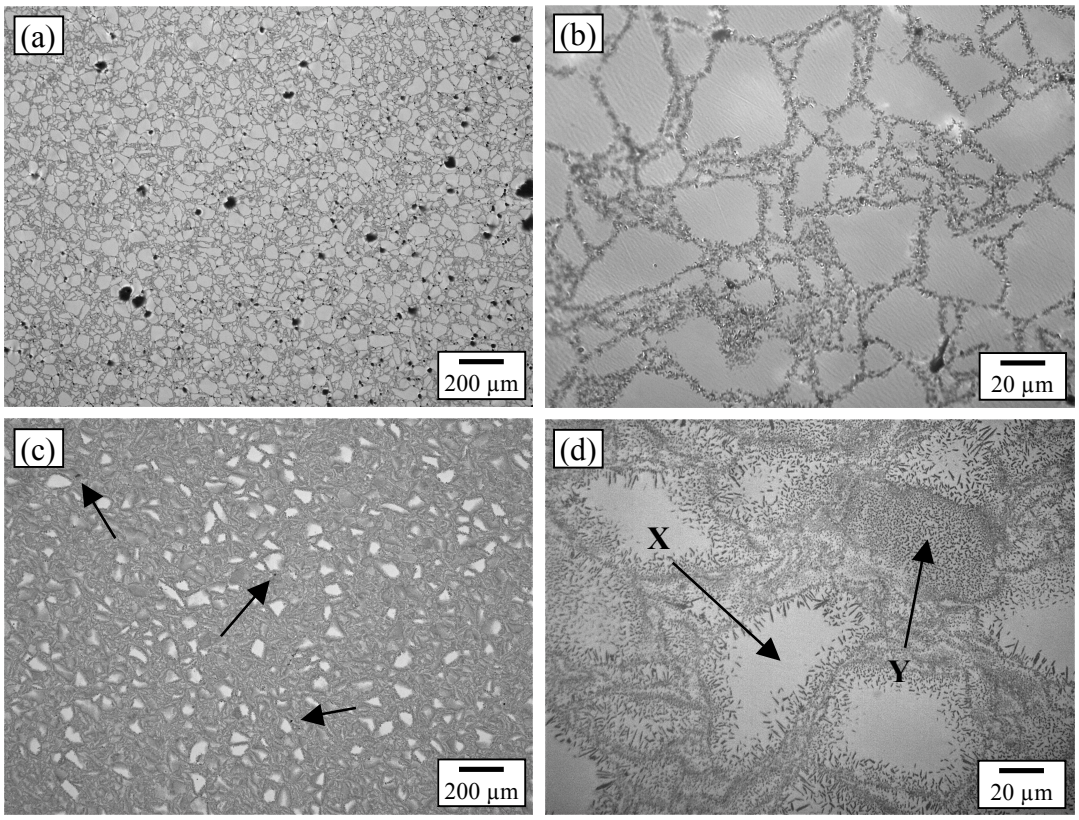

Figure 6-3: Optical micrographs of CAS glasses sintered at 890°C, (a) overview of CPS sample, (b) high magnification of CPS sample, (c) Overview of SPS sample, (d) High magnification of SPS sample.

6.3.4. SEM and EDS

The SEM micrographs and EDS analysis of sintered CAS formed using CPS and SPS methods are presented in Figure 6-4. It should be noted that the magnification of the SEM micrographs are not similar for the CPS and SPS samples; features in SPS samples are too big which makes high magnification images not suitable for the purposes of comparison. In general, the SE images

show similar features namely isolated porosity, crystalline larnite and a glassy phase to that observed in the optical micrographs.

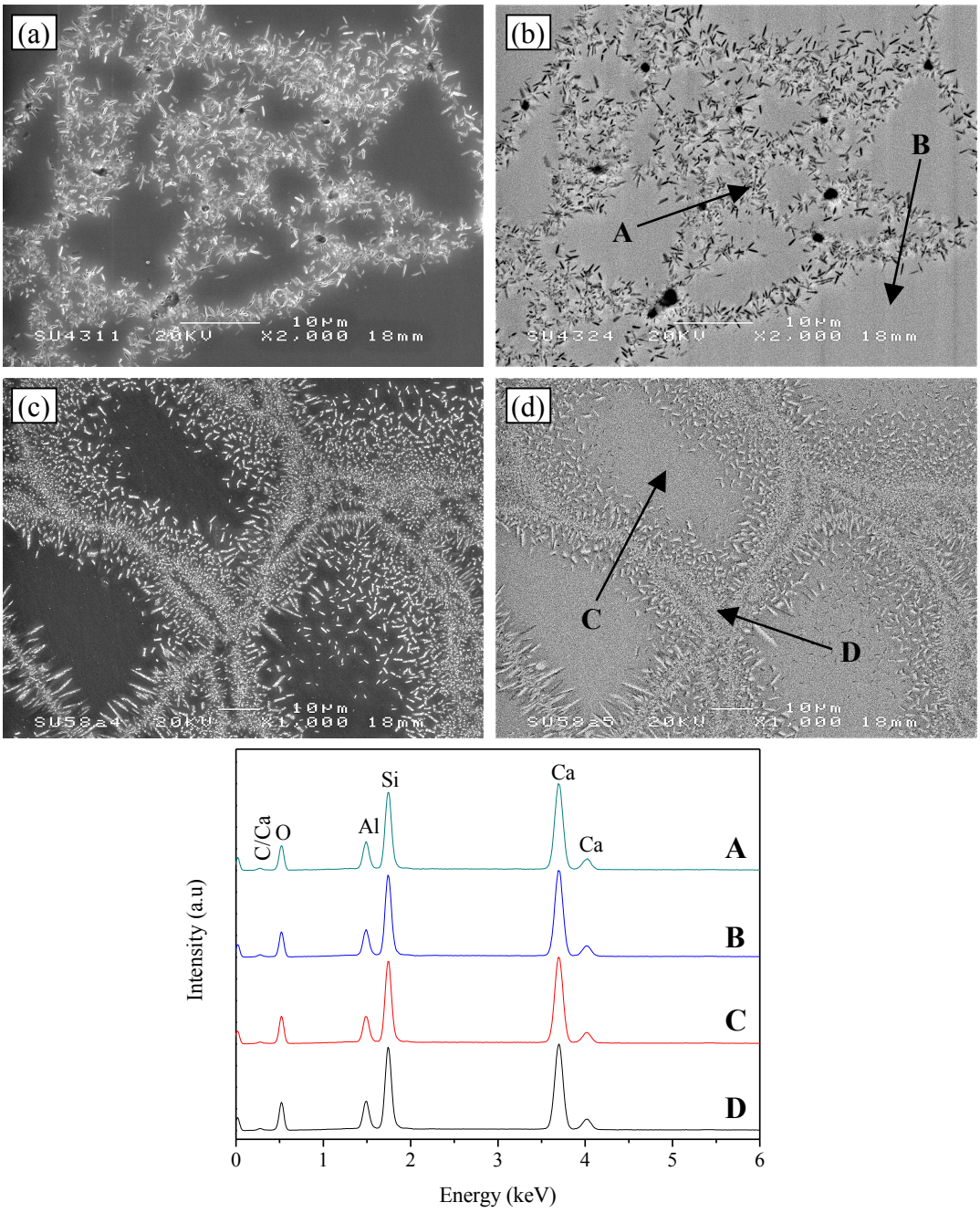

Figure 6-4: SEM micrographs and normalised EDS analysis of CAS glasses sintered at 890°C, (a) SE images of CPS sample, (b) BE image of CPS sample, (c) SE image of SPS sample, (d) BE image of SPS sample.

On comparing the BE micrographs of the samples, it is noticeable that the crystalline region of the CPS sample (area A) appeared black in colour whereas the equivalent region of the SPS sample (area D) was seen as light grey. The difference contrast in these images is attributed to the uneven surface of the CPS sample; the depth of profile of needle-like crystals were slightly lower than the glass region and this leads to the detection of elements with lower atomic number (in this case is gas, also note that EDS is not capable of detecting light elements < Na), hence appeared black in colour. This phenomenon may also explain the porosity region that appeared black in Figure 6-4b. As seen in optical microscope images, the SEM micrographs also indicate similar behaviour of crystal growth of larnite crystalline phase; the crystals seem to grow from the surface toward the centre of CAS glass particles. The EDS data suggest that there is no difference in the chemical elements present in the crystalline or glassy regions, whether the sample was prepared using CPS or SPS. However this is probably due to the EDS technique that measures over an interaction volume (details in Section 3.17) which is larger than the features observed.

6.4. The Effect of Sintering Temperatures on CAS30G Composites

In this section, CAS30G composite samples sintered at various sintering temperatures from ~T_g to < 1000°C using SPS are examined. The dwell time at the maximum sintering temperature for all samples was kept at 20 min. Where possible, the data obtained from the CAS30G samples sintered via SPS are compared with that of an equivalent sample formed using CPS.

Figure 6-5: A CAS30G sample sintered at 890C for 20 min using SPS.

A photographic image of the CAS30G sample sintered at 890°C for 20 min using SPS is presented in Figure 6-5. It is worth noting that the graphite sheet has been removed and the sample has been ground using 1200 grit grinding paper for further analysis. For other SPS samples sintered at various temperatures, a similar treatment was applied and the colour of all sintered samples was found to be similar.

6.4.1. Density and Porosity

The measured bulk and powder densities of CAS30G samples sintered at various sintering temperatures using SPS are shown in Figure 6-6. It is apparent that the trends in both bulk and powder density of the samples are similar; the density increased from 790 to 890°C and decreased slightly at the maximum sintering temperature (note that the scale of the *y*-axis is reasonably small). The highest bulk and powder densities are found with the SPS samples sintered at 890°C, with measured density values of 2.69 and 2.72 g/cm^3 respectively. In comparison, the bulk and powder densities of the equivalent CAS30G samples formed using CPS (sintered at 890°C for 2h) are 2.46 and 2.75 g/cm^3. Indeed the powder density of both samples were about similar, regardless of the differences in the sintering method used. Overall, the powder density data shown in Figure 6-6 are found to be higher than the Archimedes density and this suggests that porosity is present in the samples.

The porosity data calculated based on the difference between the powder and bulk densities are shown in Figure 6-7. It can be seen that the porosity is constant within error from 790 to 840°C and afterwards increased steadily as sintering temperature increased from 840 to 940°C. Comparing the porosity of the CAS30G sample (1.18 %) that gave highest density value with the equivalent CAS30G sample (10.74 %) sintered at 2h using the CPS (both sintered at 890°C), it is found that 89 % of porosity has been removed in the CAS30G sample formed at 20 min using SPS. This shows that the use of SPS is more feasible for the production of graphite-glass wasteforms than the use of CPS.

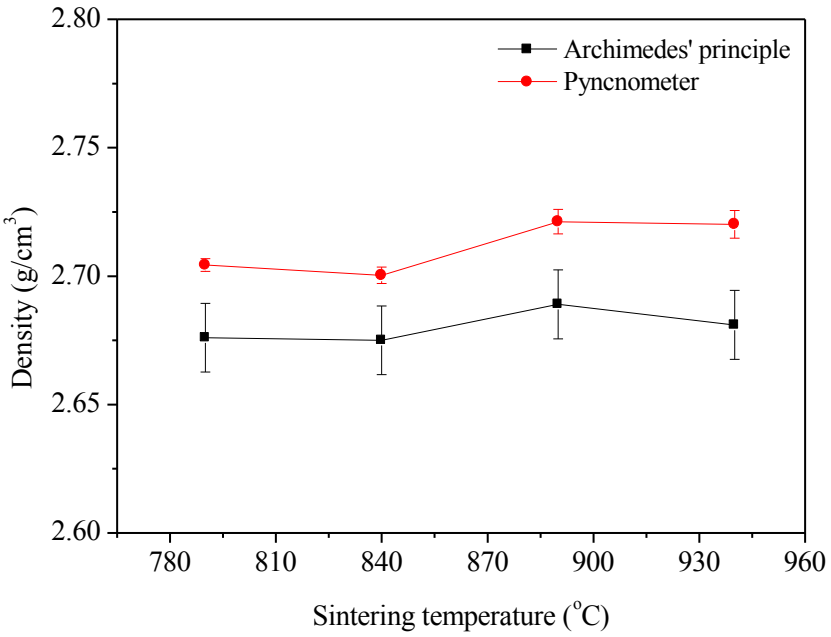

Figure 6-6: Bulk and powder density of CAS30G sintered at various temperatures for 20 min using SPS method.

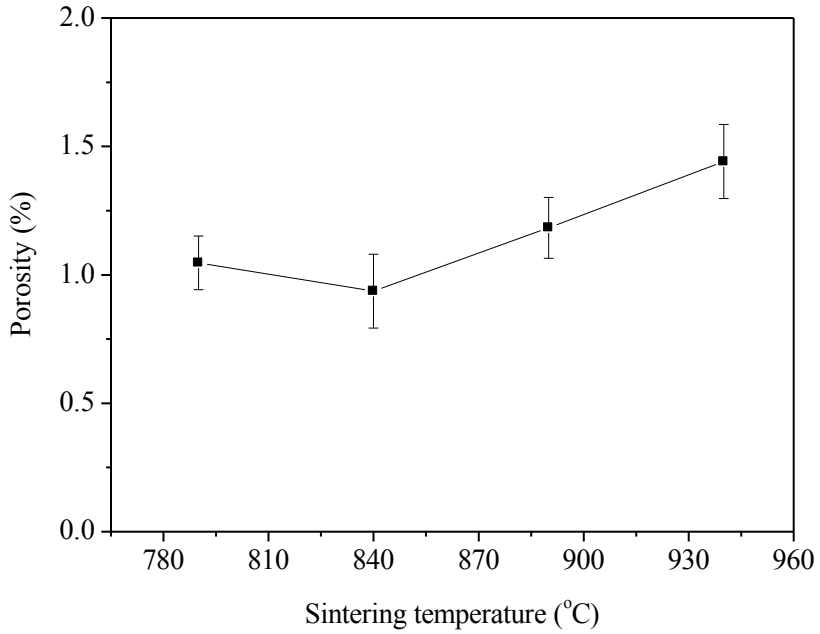

Figure 6-7: Porosity of CAS30G sintered at various sintering temperatures for 20 min using SPS method.

6.4.2. XRD

Figure 6-8 shows the crystalline phases that precipitated in all of the CAS30G samples made using SPS and a comparison of the data for the sample that had the highest density values with respect to the equivalent sample prepared using CPS. It should be noted that the sodalite ($Na_6Al_6(SiO_4)_6$, PDF card 04-009-5260) phase marked as Δ were detected in all diffractograms; this phase originated from the contamination of the graphite raw material (refer Section 4.2.3).

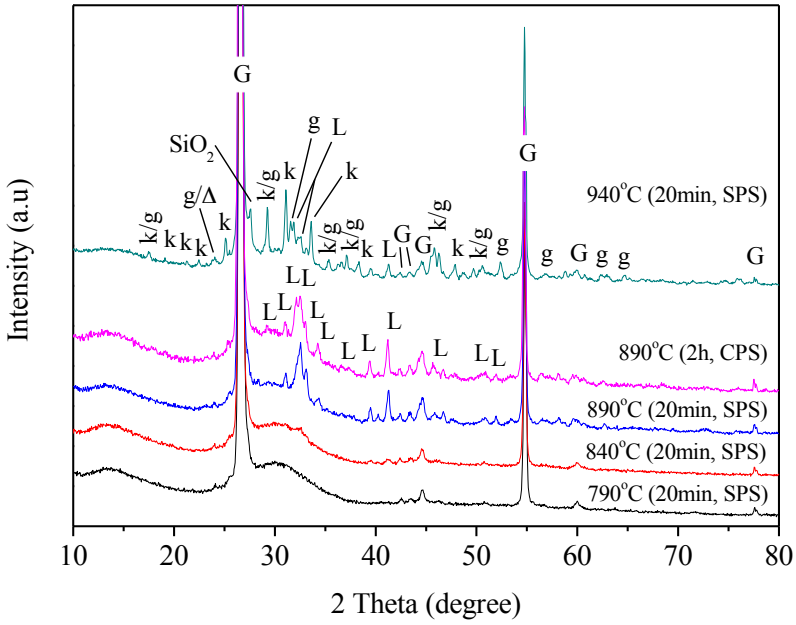

Figure 6-8: Normalised XRD patterns of CAS30G samples sintered using SPS and CPS method, G = graphite, L = Ca_2SiO_4, k = $Ca_6(SiO_4)(Si_3O_{10})$, g = $Ca_2(Al(AlSi)O_7)$, Δ = $Na_6Al_6(SiO_4)_6$, SiO_2 = β-quartz.

As the sample was sintered at ~T_g, the XRD pattern reveals that the glass component tends to remain amorphous upon sintering, along with the detection of graphite (PDF card 26-1076). When the sintering temperature is increased to 840°C, a similar pattern can be observed along with an indication of a weak peak located at ~32.5° of 2θ. In reference to the PDF card, this weak peak is positioned at the same place as the 100 % intensity peak for larnite (Ca_2SiO_4, PDF card 00-033-0302). On further increasing the sintering temperature to 890°C, it is clear that

mixture of an amorphous phase, graphite and larnite are present in the sample. Similar phases were detected in the equivalent samples prepared using CPS. However, the 100 % intensity peak of larnite was found to be more pronounced in the sample prepared using SPS. This may suggest that the degree of crystallisation of larnite is higher in the SPS sample compared to the CPS sample sintered at 890°C. At the maximum sintering temperature of 940°C, a more complex mixture of an amorphous phase, graphite, larnite, SiO_2 (β-quartz, PDF card 01-086-1564), gehlenite ($Ca_2(Al(AlSi)O_7)$, PDF card 01-075-1677) and kilchoanite ($Ca_6(SiO_4)(Si_3O_{10})$, PDF card 00-029-0370) is obtained. Based on the comparison of the maximum intensity peaks of larnite, gehlenite and kilchoanite, these crystal phases are present in the following order kilchoanite > gehlenite > larnite, although quantitative XRD measurements should be considered to identify the percentages of each phases.

6.5. The Effect of Sintering Dwell Time on CAS30G Composites

The effect of sintering dwell time in the production of CAS30G samples with the aim of identifying the optimum sintering parameter for SPS is described in this section. All the CAS30G samples discussed in this section were sintered at 890°C using SPS and prepared at various sintering dwell times ranging from 3 to 30 minutes. The sintering temperature of 890°C was used due to the fact that CAS30G sample sintered at this temperature produces the highest bulk and powder density values (Figure 6-6).

6.5.1. Density and Porosity

The pattern of bulk and powder densities of obtained CAS30G samples formed using SPS method is presented in Figure 6-9. Generally, both bulk and powder densities of the samples are found to be similar with the variation of the measured density values from 2.69 to 2.72 g/cm^3. The bulk density values are increased from 3 to 15 minutes, slightly decreased at 20 minutes, increased again at 25 minutes and after which it was stable to 30 minutes sintering dwell time. For the powder density of similar samples, it can be observed that the density increased from 3 - 5 minutes, decreased linearly from 5 - 20 minutes, increased again from 20 - 25 minutes and no significant change of the density data was found between 25 and 30 minute sintering dwell times.

Although the changes in the density values in bulk and powder density is very small, it is suggested that such variations are due to the release of air that trapped between the glass and/or graphite particles. The degree of crystallisation may also responsible for the slight increase of bulk and powder densities from 20 - 30 minutes. Furthermore, it is clear that the difference in the bulk and powder density data slightly fluctuated from 3 - 20 minutes and afterwards the difference in the densities remains similar.

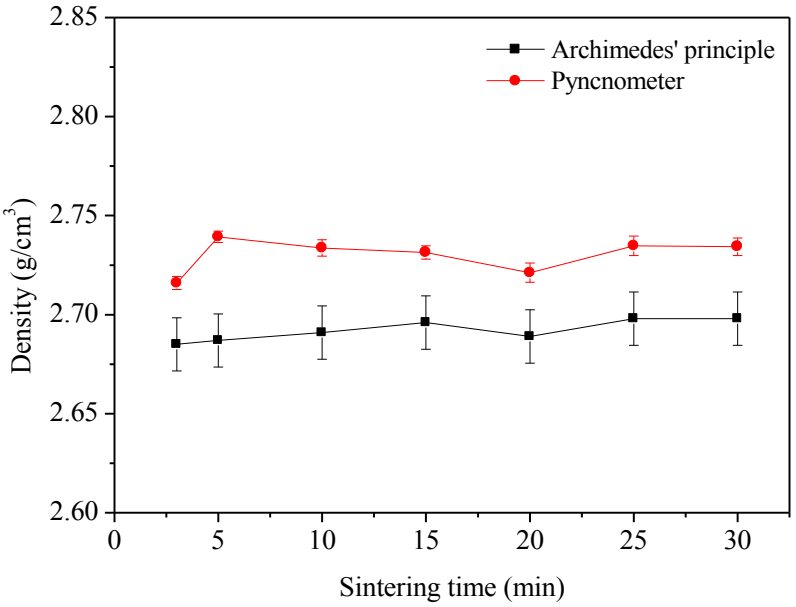

Figure 6-9: Bulk and powder density of CAS30G samples prepared at various sintering dwell times.

From the percentage differences in the density values measured on each CAS30G sample, the porosity data are obtained and presented in Figure 6-10. The porosity is increased from 3 - 5 minutes, decreased steadily from 5 - 20 minutes, increased again from 20 - 25 minutes and was stable from 25 - 30 minutes sintering dwell times. The porosity data revealed that the removal of air and/or porosity from the green body was completed at 20 minutes. This leads to the suggestion that 20 minutes sintering dwell time is adequate to produce a CAS30G sample with a reasonably low amount of porosity: 1.18 % at 20 minutes. The slight increase of porosity from 20 - 30 minutes dwell time may be attributed to the generation of porosity created from the oxidation of graphite, which presumably occurred through the scavenging the oxygen from the

glassy component; this event was evidenced and discussed earlier in Chapter 5. Although there is the possibility of the graphite oxidation in the samples, the low percentage of porosity data suggested that the graphite oxidation in the samples made using SPS is negligible.

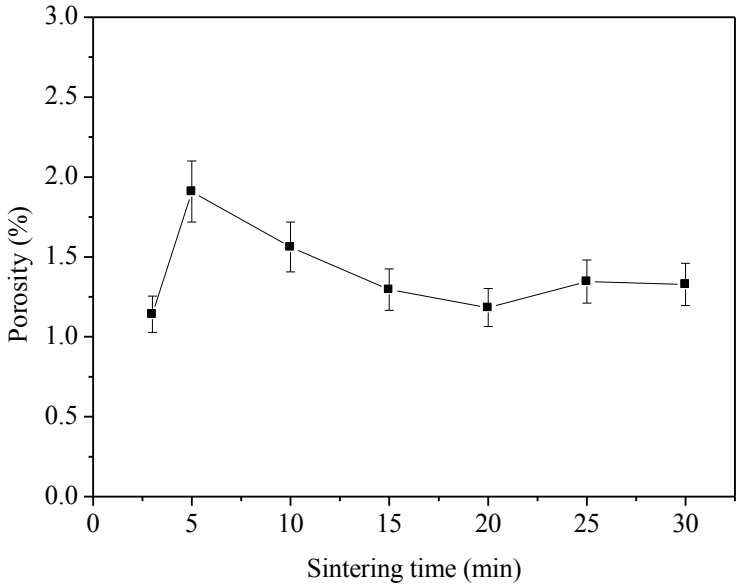

Figure 6-10: Percentage porosity in CAS30G samples prepared with various sintering dwell times using SPS.

6.5.2. XRD

Figure 6-11 presents the XRD patterns measured from CAS30G samples sintered for various dwell times. Note that due to the larger scale used, the contamination phase of sodalite ($Na_6Al_6(SiO_4)_6$, PDF card 04-009-5260) originating from the graphite is less visible. It is obvious that a similar mixture of amorphous material, graphite and larnite (Ca_2SiO_4, PDF card 00-033-0302) is present in all CAS30G samples. Comparing Figure 6-8 and Figure 6-11 shows that the development of crystalline material in CAS30G system is highly dependent on the sintering temperature as similar phases were detected in all samples. The only difference in the time series XRD patterns is the intensity of larnite crystalline peaks, which increased with increasing sintering dwell time, especially the 100 % intensity peaks located at ~32.5° 2θ. This suggests that the degree of crystallisation of larnite crystalline phase increased from 3 to 30 minute sintering dwell times.

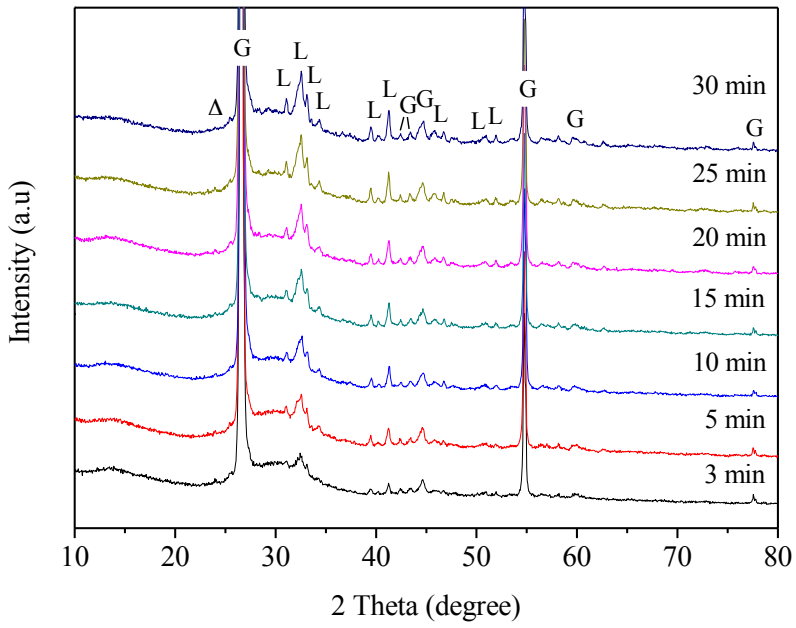

Figure 6-11: Normalised XRD patterns of CAS30G samples prepared at various sintering dwell times, G = graphite, L = Ca_2SiO_4, Δ = $Na_6Al_6(SiO_4)_6$.

6.6. Microstructural Analysis of CAS30G Composites

Based on the findings in Section 6.4 and 6.5, it was concluded that the best CAS30G composite material is produced by SPS processing at 890°C with a sintering dwell time of 20 minutes. This is due to the fact that at these sintering parameters, a high density and low porosity CAS30G composite is obtained. In this section, the microstructure of mentioned CAS30G composite sample is compared with the sample that prepared using CPS method (sintered at 890°C for 2 hours).

6.6.1. Optical Microscopy and Optical Profilometry

As seen in Figure 6-12, the top view of the CAS30G sample formed using CPS revealed that some amount of graphite has been removed from the surface of the sample. The counterpart image obtained from optical profilometry also implies similar removal behaviour with the

measured depth of profile in the graphite regions being in the range of 5 - 25 µm. In the cross sectional view of the sample, it can be observed from the optical microscope that some graphite is retained on the sample, which can be observed as light grey features (marked by arrow). Less removal of graphite is evident in the cross sectional view of the optical profilometer image with a measured depth of profile at graphite regions being about 5 - 20 µm. From the optical microscope and optical profilometer images of the samples, it is inferred that more graphite is being removed by grinding and polishing of the sample from the top surface compared to the cross sectional surface, regardless of the fact that similar grinding and polishing methods were applied on both surfaces. This graphite removal is in agreement with the previous study of the mixtures of CAS glass and graphite in Section 5.3.5.

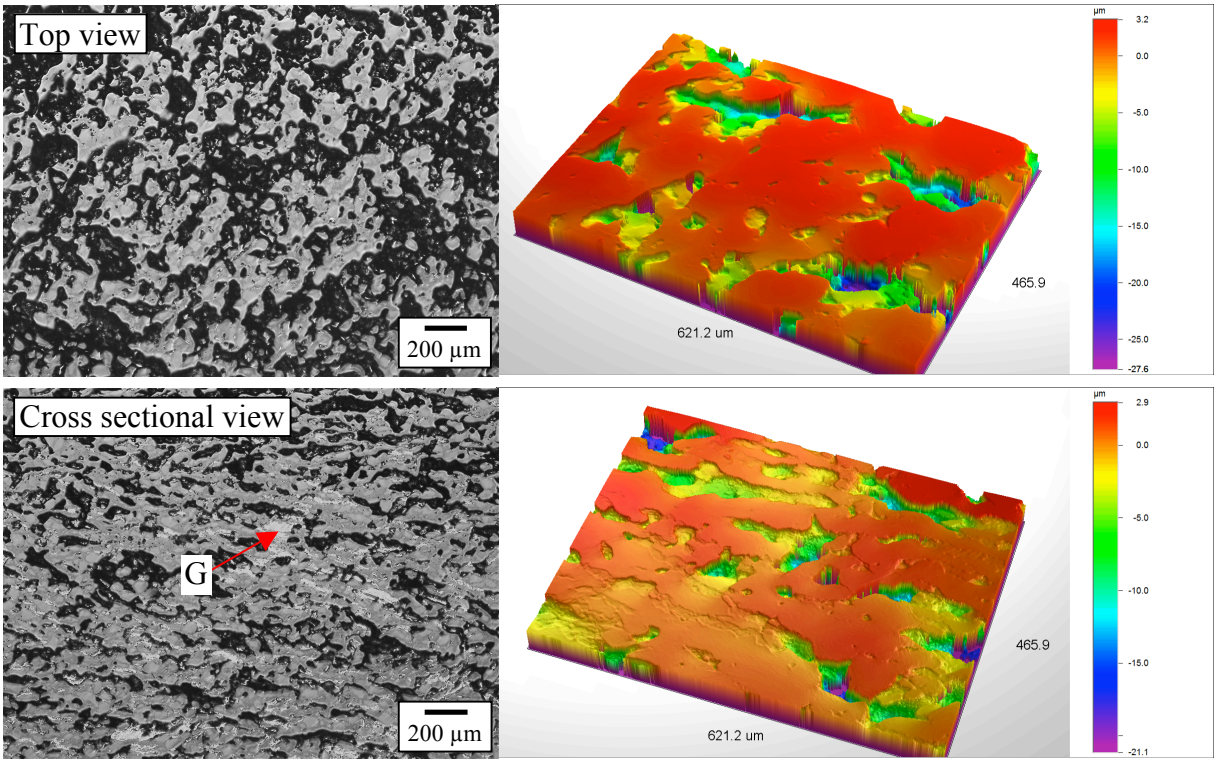

Figure 6-12: Optical microscope and optical profilometer images of a CAS30G sample prepared using CPS, sintered at 890°C for 2 h.

Similar analysis techniques were conducted on CAS30G sample prepared using SPS. In Figure 6-13, it is clear that the effect of pressure in the SPS transformed the microstructure of the

sample, which can be seen in both top view and cross sectional view. The CAS glass ceramic regions in the top view were seen to be flatter (larger area) and the graphite regions in the cross sectional view were found more compact compared to the images of CAS30G sample prepared using CPS. The cross sectional optical micrograph shows that the graphite sheet does not react with the CAS30G and the black regions are not porosity; in this case the black regions have been thoroughly observed and it seems that the regions are due to particles pull out caused from the grinding and polishing processes. From the analysis of the optical and optical profilometer images, some graphite has also been removed on both top and cross section surfaces of the sample. However, in comparison with the CPS sample, this graphite removal is reduced, as the measured depth of profile in the top and cross sections of the surfaces are in range of ~2 - 18 µm and ~0.5 - 3.5 µm respectively. This is again a good indication of encapsulation of graphite in glass system and leads to the suggestion that the pressure assisted SPS is a better processing method for retaining graphite in glass composite materials.

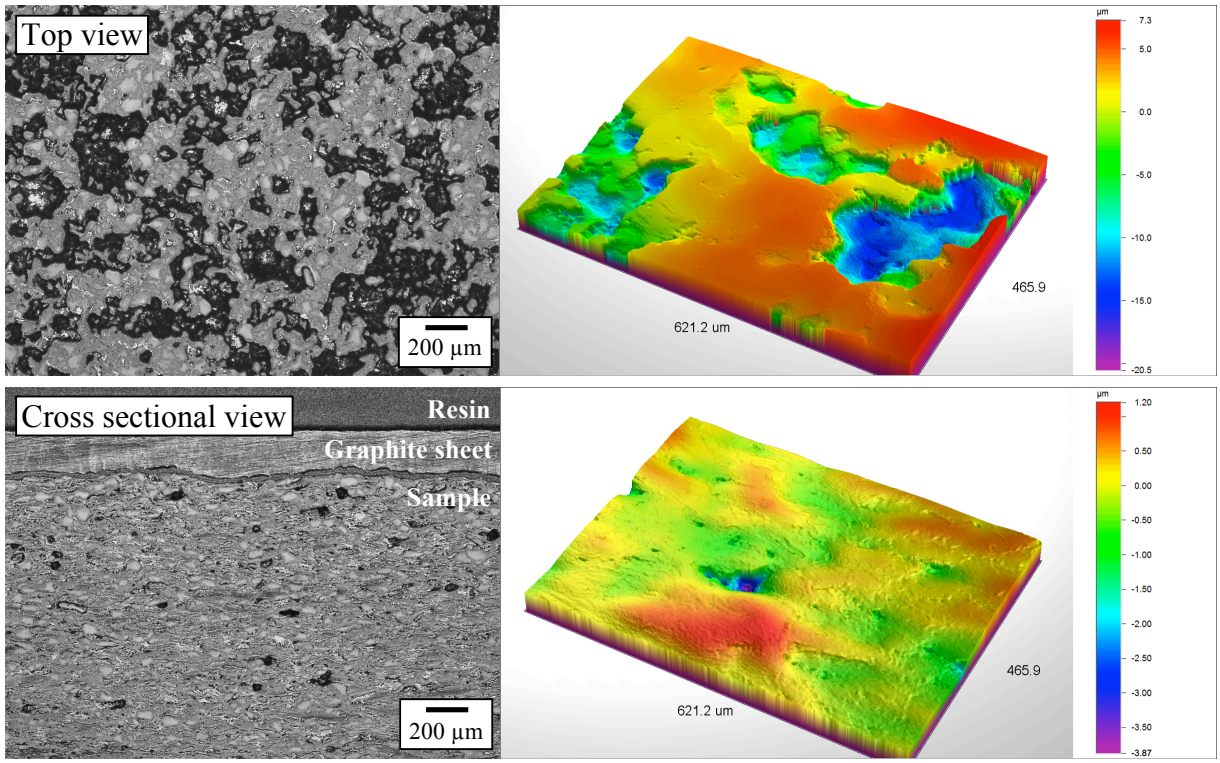

Figure 6-13: Optical microscope and optical profilometer images of a CAS30G sample prepared using SPS method, sintered at 890°C for 20 min.

6.6.2. SEM and EDS

Figure 6-14 compares BE and SE micrographs of CAS30G samples sintered at 890°C for 2 h and 20 min using CPS and SPS methods. Essentially, the top and cross sectional view of BE micrographs are in agreement with the optical microscopy images. In the BE micrographs, additional information about the elemental composition of graphite and CAS glass ceramic can be distinguished. It is clearly seen that the graphite component is encapsulated by the CAS glass ceramic component. Similar to the analysis of the optical microscope images, the effect of the pressure is also observed in top and cross sectional views of the BE micrographs; the CAS glass ceramic component is flatter (larger area) and the graphite sandwiched between the CAS glass ceramic components is more compact with respect to the CAS30G samples formed using the CPS method. This pressure effect that increases the driving force for pore removal is most probably the reason why the SPS made sample had a very low porosity (Figure 6-7 and 6-10).

Comparing the higher magnification SE micrographs (taken from the cross section surface), the most distinct feature that can be seen in the micrographs is the behaviour of the larnite crystallisation. It is apparent that the degree of crystallisation is higher in the CAS30G sample formed using SPS compared to the sample formed using CPS (compare Figure 6-14e and 6-14f). As mentioned previously, there is no evidence in the micrographs to suggest the needle-like features observed in the SE micrographs are definitely the larnite crystalline phase. However, by considering the XRD patterns of CAS30G samples, it can be concluded that the needle-like features are larnite crystals. Overall, apart from the behaviour of graphite (pressure effect), the crystallisation of larnite crystalline phase seen in the CAS30G sintered at 890°C using CPS (2 h) and SPS (20 min) methods are in line with the sintered glasses, which were previously discussed in Sections 6.3.3 and 6.3.4.

Further investigation on the CAS30G sample prepared using SPS was carried out using the EDS mapping analysis. As seen in Figure 6-15, all the expected chemical elements namely graphite (C) and CAS glass (Ca, Al, Si, O) are detected. The trace of Fe is believed originated from the contamination of the graphite (see chapter 4, Section 4.2.5). This statement is supported with the Fe elemental image, which revealed the area of Fe is located at the graphite regions (see Figure

6-15C and Figure 6-15Fe). Based on the elemental mapping analysis, there is no evidence of chemical bonding or chemical reaction occurred between graphite and CAS glass ceramic components. This is consistent with the XRD data and further confirmed that the graphite has been encapsulated with the CAS glass ceramic materials without any chemical interactions.

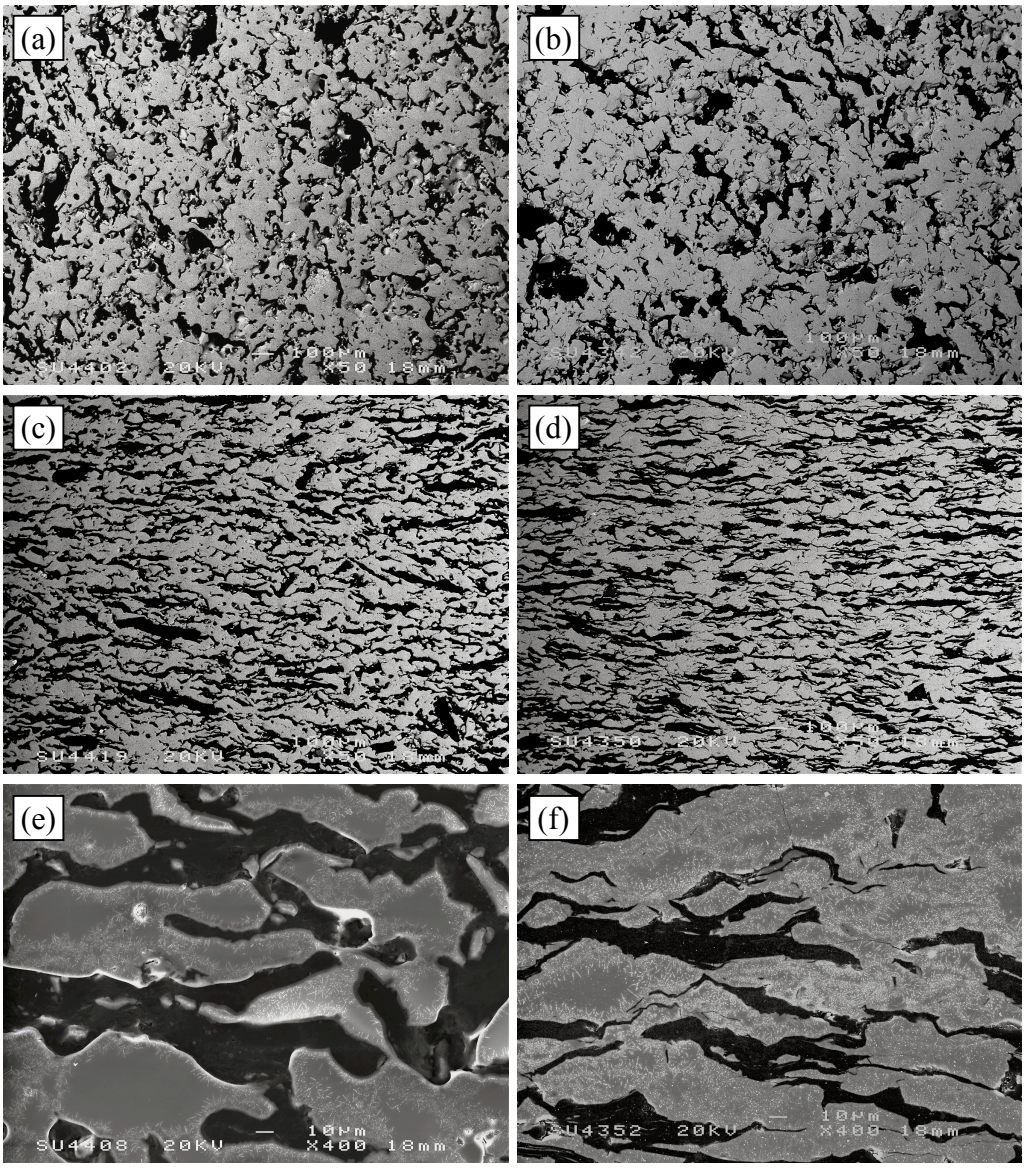

Figure 6-14: BE and SE micrographs of CAS30G samples prepared using CPS and SPS methods, (a) top view of CPS sample, (b) top view of SPS sample, (c) cross sectional view of CPS sample, (d) cross sectional view of SPS sample, (e) close-up view of CPS sample, (f) close-up view of SPS sample.

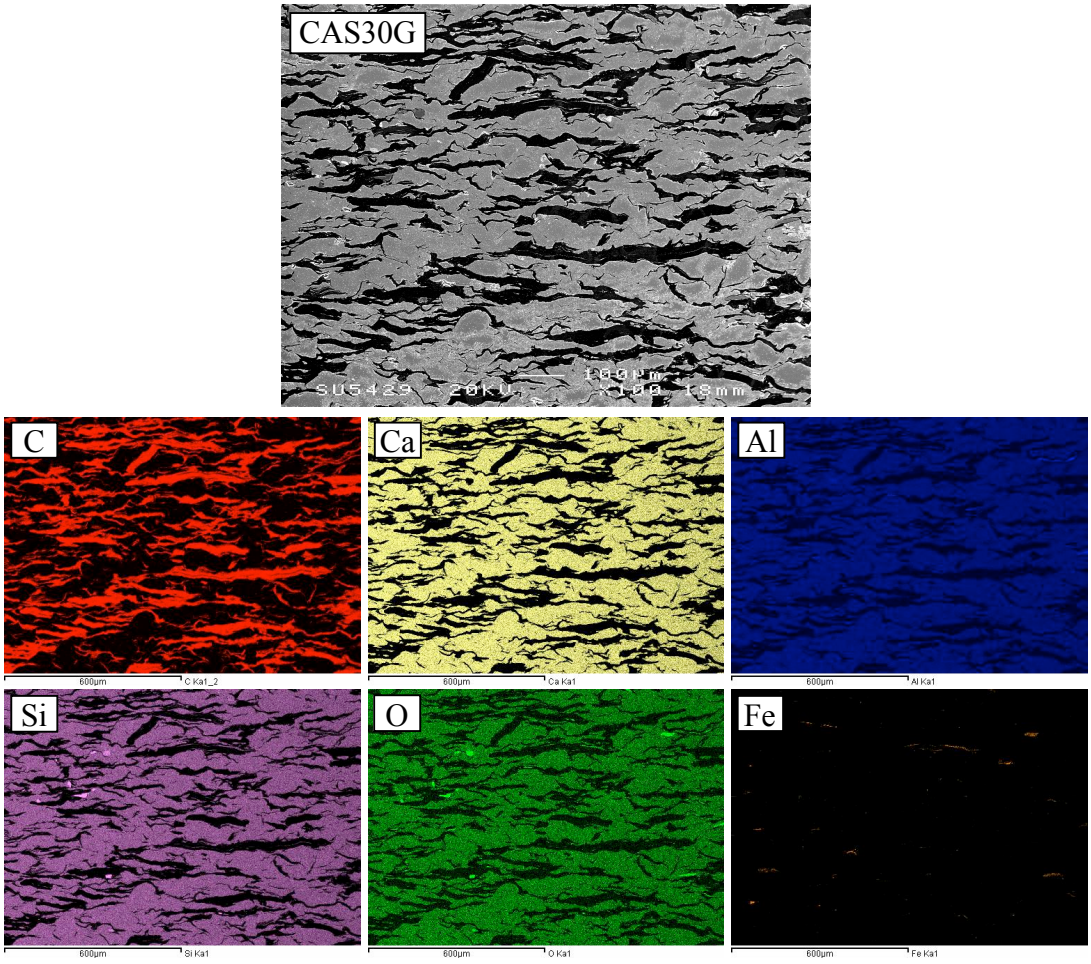

Figure 6-15: EDS mapping analysis on cross section of CAS30G sample prepared using SPS method, sintered at 890°C for 20 min.

6.7. The Effect of Waste Loading on CAS Glass Composites

In this section, various waste loadings ranging from 30 - 90 wt% of graphite powder have been loaded into the powdered CAS glass system and sintered at 890°C for 20 minutes using SPS. The aim of this investigation is to find out how waste loading affecting the density, porosity and the tensile strength of the samples. The XRD and microstructure analyses have not been studied here due to the crystallisation of the material being dependent primarily on the sintering temperature, sintering method; no chemical reaction occurs between the CAS components (glassy and/or

crystalline phases) and graphite. As seen above sintered CAS glass with or without graphite contains the same phases (see Sections 6.3.2, 6.4.2 and 6.5.2).

Figure 6-16 shows a photograph of the samples taken after the graphite sheet has been removed by grinding process. It can be observed that the surfaces of CAS30G and CAS50G are smoother than those of CAS70G and CAS90G. It is clear that some scratches appeared on the surface of CAS70G and CAS90G samples, suggesting that these samples have poorer mechanical properties. Based on the observation whilst undertaking grinding process, the graphite component was more easily removed from the CAS70G and CAS90G samples.

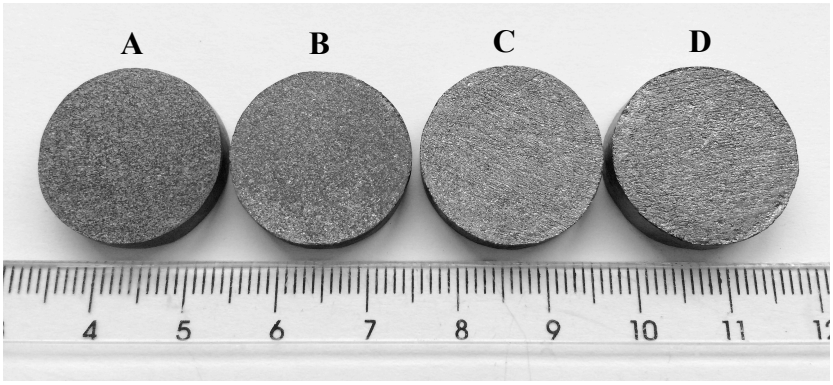

Figure 6-16: Photographic images of graphite-glass composites, A = CAS30G, B = CAS50G, C = CAS70G, D = CAS90G.

6.7.1. Density and Porosity

Figure 6-17 shows the bulk and powder densities of graphite-glass composites prepared with various graphite loadings. The trends of bulk and powder densities of the samples are similar with both decreasing with increasing graphite loading. This is expected as the density of graphite is lower than the glass ceramic component. Thus the increase in graphite content will lower the total densities of the samples. From the data, it is clear that the difference in the bulk and powder densities is more pronounced when the graphite content is increased from 30 to 90 wt%. The calculated theoretical density of CAS30G, CAS50G, CAS70G and CAS90G samples prepared using SPS is about 99.82, 96.12, 94.64 and 93.51 % respectively. In comparison, the CAS30G

sample prepared using CPS only achieved 89.26 % of the theoretical density, which is much lower than the highest waste loaded sample prepared using the SPS method.

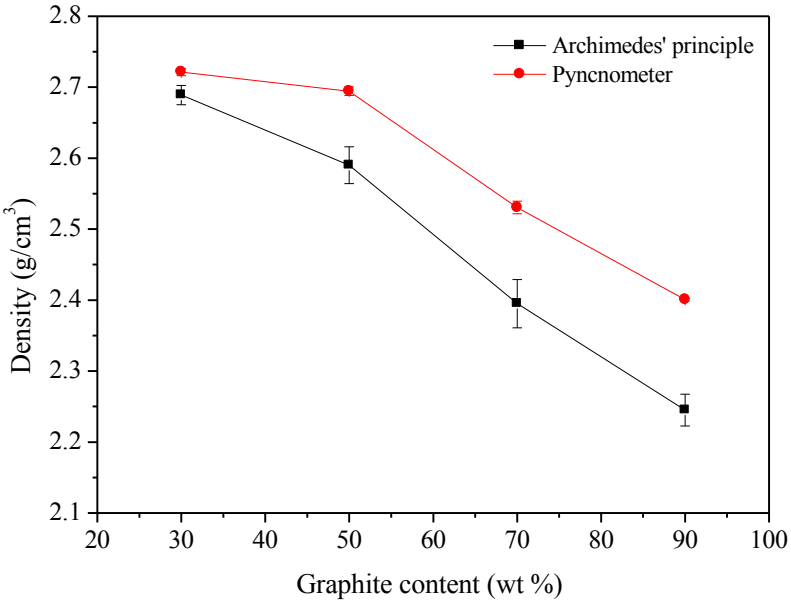

Figure 6-17: Bulk and powder density of graphite-glass composites prepared from mixtures of CAS glass and graphite.

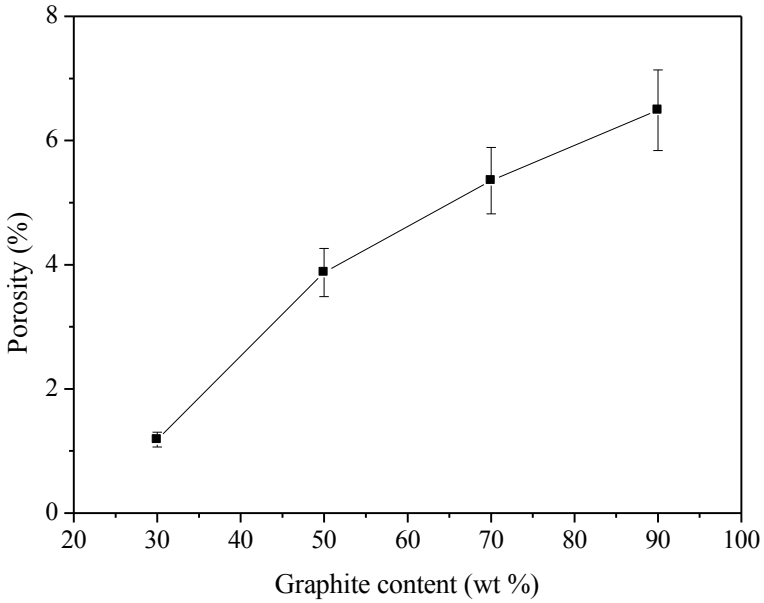

Figure 6-18: Porosity of prepared graphite-glass composites with various graphite loadings.

Figure 6-18 shows that the porosity increases monotonically with increased graphite loading. This is in agreement with the trends of the density data. Although at 90 wt% graphite loading, it is interesting that the measured porosity is low, about 6.5 %. In comparison with the CPS method that was previously studied using various glass systems in Chapter 5, it is confirmed that the SPS method is advantageous for reducing porosity of the graphite-glass composites based on the CAS glass system.

6.7.2. Indirect Tensile Testing

Figure 6-19 presents the tensile strength data for all SPS made glass-composites samples with various graphite loadings; an average of five measurements was taken at each data point. It should be noted that all the samples were carefully ground with 1200 grit grinding paper and the cylindrical shape of the compacted samples was preserved as accurately as possible, otherwise the shape of the sample (if not cylindrical in shape) will affect the tensile strength measurement *i.e.* the splitting of the sample will not follow the requirement of the test (details information in Section 3.20).

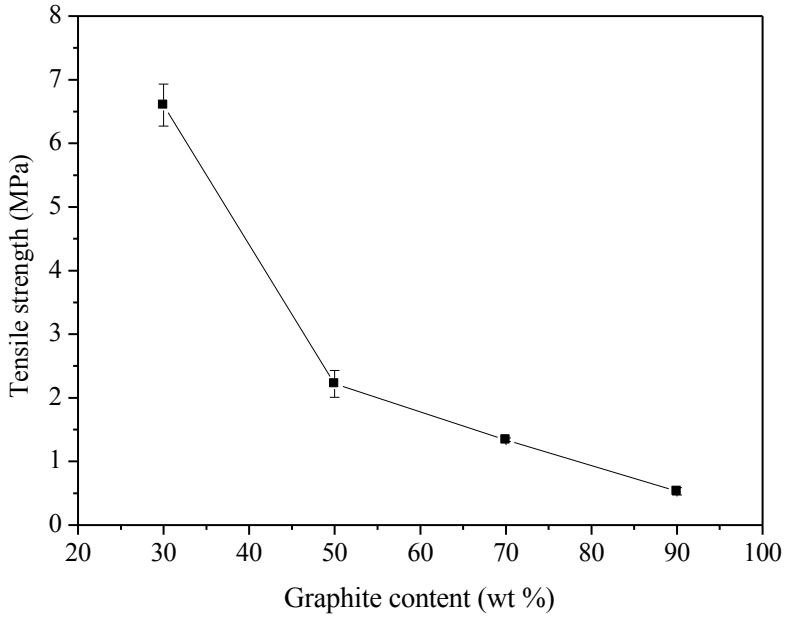

Figure 6-19: Indirect tensile strength of graphite-glass composites loaded with various graphite loadings.

From the graph, the tensile strength is found to decrease as the graphite content is increased from 30 to 90 wt%. As seen in Figure 6-16, the surface of samples loaded with 30 and 50 wt% graphite are smoother (without visible scratches) than samples loaded with 70 and 90 wt% graphite, which may, at least partially explain the lower strength values. These results suggest that the graphite loadings of 70 and 90 wt% are too high and the mechanical integrity of the samples is not suitable for the production of nuclear wasteforms. In comparison with the CAS30G sample made using CPS method, the tensile strength of CAS30G formed using SPS is 1.4 MPa higher than that of the sample prepared using CPS. This further implies that the SPS is a better method for the production of graphite-glass composite materials.

6.8. Discussion

The scope of this chapter is to assess the use of the SPS processing method for the production of graphite-glass wasteforms based on the CAS glass system. Essentially, the SPS method is a relatively new approach to sintering and since the 1990s SPS has been applied in the production of various materials *i.e.* glass, ceramics, composites and metallic alloys (Suárez *et al* 2013, Xie 2013). In spite of the fact that many studies have been undertaken in the recent years, the interaction of the materials with the sintering mechanism of SPS is not yet fully understood (Saheb *et al* 2012, Guillon *et al* 2014). The SPS method has attracted many researchers due to the following advantages; 1) it can form dense materials at relatively low temperatures; 2) it provides the application of pressure whilst undertaking sintering process; 3) sintering parameters and sintering environment are changeable as needed and finally 4) the whole sample processing time is much shorter compared to conventional and hot isostatic pressing (Sahin *et al* 2012, Fredrick *et al* 2013, Guyon *et al* 2013). Due to the stated advantages, the SPS method is seen to be attractive for the immobilisation of problematic nuclear graphite waste. The crucial aim is to reduce the porosity of graphite-glass composites and also to minimise graphite oxidation whilst retaining the mechanical strength of the samples.

In this contribution, it has been demonstrated that the SPS method is superior to the CPS method and successfully reduced the porosity of produced glass composite and graphite-glass composite materials based on the CAS glass system. The reduction of porosity in the obtained samples is

directly related to the transport mechanisms involved during sintering processing. Basically, in the initial stage of viscous glass sintering, the surface transport mechanism is mainly dominated by surface diffusion and can be described by considering the neck formation between the two identical glass spheres. The neck growth does not affect the densification (due to no change in particle spacing) as the mass flow originates and terminates on the particle surface. The early stage of viscous glass sintering has been modelled by Frenkel (1945) and the model is valid roughly for the first 10 % of linear shrinkage. This model takes into account the neck formation of spherical, monodispersed particles by viscous flow and assumed the remaining parts of the particles retain their spherical shape as they approach one another (Ristić and Milosević 2006). It is worth noting that this model was not particularly developed to analye the case of viscous glass sintering, however the Frenkel model is the most applicable to the initial stage of viscous glass sintering. In the final stage of viscous glass sintering, the bulk transport mechanism known as viscous flow occurs and leads to the system densification. The driving force for this flow is surface tension that varies as a function of surface curvature of which connecting the rate of shear strain with the shear stress. The material flows toward the particle necks and fills into the pores as the pores become spherical and reduce in size, thus densifying the powder compact. A model for the final stage of viscous glass sintering has been developed by Mackenzie & Shuttleworth (1949). This model successfully explained the sintering of glasses and suggested that the densification rate will increase if the external pressure is applied to a compact whilst undertaking sintering process.

With both models in mind, it is believed that the neck formation may occur in the early stage of the CAS glass sintering using the CPS method. However, the optical micrograph of sintered CAS glass (see Figure 6-3a and 6-3b) shows that the sample exhibits surface crystallisation, suggesting at the later stage the glass particle starts to crystallise when sintering. Although the CAS glass obeys the law of deformation for a solid with Newtonian viscosity, the surface crystallisation hinders the viscous flow mechanism; as the crystallised particles do not flow (Prado and Zanotto 2002, Chen *et al* 2013a). In this case, the vacancy diffusion mechanism probably plays an important role for the densification of the sintered CAS glass using CPS. The sintering process of sintered CAS glass using CPS can be simplified as follow: (a) when two glass particles are bought into contact, neck formation with high curvature forms (b) due to

surface crystallisation, the concentration of vacancies in the neck region is higher than the surface far away from the neck, leading to a driving force for diffusion; the vacancies moving away from the neck caused the material to move towards the neck. Note that the concentration of the vacancies is strongly dependent on the surface stress (c) and that a grain boundary acts as a sink for vacancies resulting a flux toward itself and allowing for their accumulation and collapse. This leads to the vacancies moving toward and into the grain boundary from nearby surface regions, balanced by the rate of collapse along the grain boundary and caused by an inward motion of the particles; this motion is known as the plating velocity of the particles (d) eventually, the mentioned vacancy diffusion mechanisms result in system shrinkage or densification (Djohari *et al* 2009, Djohari and Derby 2009). Based on the experiments reported here, the transport mechanisms are in agreement with the results of sintered CAS glass using CPS; the plating velocity is also observed in Figure 6-3b, which at some areas shows the migration/spreading of non-crystallised materials to the adjacent particle, breaking the grain boundary and crystalline line. It is also seen that the sintered CAS glass compact using CPS achieved 94.9 % theoretical density. In contrast, the sintered CAS glass compact using pressure assisted SPS increased in density to 98.7 % theoretical density. The increase value of theoretical density complements the Mackenzie & Shuttleworth model and is also in line with the study of glass sintering with concurrent crystallisation (Prado and Zanotto 2002, Djohari *et al* 2009, Djohari and Derby 2009).

The larnite crystals in sintered CAS glass compacts produced using SPS were found to be more developed than those in the equivalent sample made using CPS; the needle-like features are longer in length, suggesting an increased rate of crystal growth. This is thought due to the efficiency of the heating mechanism in SPS. In SPS, a pulsed electric current is passed through the graphite mould and directly interacts with the sample by joule heating together with the electrical field diffusion effect (Birkel *et al* 2013, Rizzo *et al* 2014), also refer Section 2.5.4. This leads to homogeneous heating with very minimal energy loss. In contrast in the CPS method, the heat transfer mechanism is mainly by conduction and heat is being transferred from the heat source to the surface of sample. This gives less efficient heat transfer when the system contains large amounts of porosity; gases are much less conductive than solids. From the obtained powder

density data of sintered CAS glass compacts, the larnite crystalline material can be quantified using the law of mixtures that gives

$$\rho_t = \rho_g\left(\frac{V_g}{V_g + V_c}\right) + \rho_c\left(\frac{V_c}{V_g + V_c}\right). \quad [6\text{-}1]$$

Equation 6-1 can be rewritten as follow

$$\rho_t = \rho_g(f) + \rho_c(1 - f) \quad [6\text{-}2]$$

where ρ_t is the density of sintered CAS glass, ρ_g is the density of CAS glass, ρ_c is the density of larnite, V_g is the volume of glass, V_c is the volume of crystal and f is the volume fraction of glassy material in the sintered body (refer Table 6-1 and Section 6.3.2 for the density data). Based on Equation 6-2, the volume fraction of larnite was calculated and found to be ~17.9 and 28.2 % for sintered CAS glass compacts formed using CPS and SPS methods, respectively. These values are in agreement with the obtained physical and microstructure data (Section 6.3).

When the graphite is present in the CAS glass system, the results revealed that the properties of sintered CAS and CAS30G samples are largely similar whether CPS or SPS is used. The major difference between the sintered CAS glass and CAS30G samples made using CPS and SPS is the amount of porosity, which is high in CPS samples and reasonably low in SPS samples. This confirmed that external pressure provided an increased driving force for densification and this leads to the reduction of porosity; in this case, similar porosity values are identified in sintered CAS and CAS30G samples formed using SPS. In addition, a low amount of porosity in nuclear wasteform is very important as this will avoid any penetration of ground water or aquatic phases into the wasteform (Fachinger *et al* 2012), hence potentially increasing the lifetime and/or chemical durability. The maximum graphite loading in CAS glass system is suggested to be between 30 and 50 wt%. CAS30G and CAS50G achieved 98.82 and 93.51 % theoretical density, 1.18 and 6.49 % porosity and 6.6 and 2.2 MPa tensile strength. These data are comparable with the recent United States Patent (family ID - 42285667) on the production of graphite-glass

composite materials using hot isostatic processing (Hrovat *et al* 2013). The patent indicates that their graphite-glass samples achieved about 95 - 97 % of theoretical density with 5 - 2 % of porosity. The clear advantage of CAS30G and CAS50G made using SPS is the reduced processing time, which is less than 40 minutes.

In this chapter, it has been shown that the SPS method can be used to encapsulate irradiated graphite waste with several advantages including low porosity, limited loss of graphite, no reaction occurring between the graphite and glass binder, and acceptable mechanical properties. Consequently, these parameters lead to the better properties of wasteform for long term disposal, ideally in a deep geological disposal facility. However, SPS processing method is not feasible due to the huge volume of irradiated graphite waste, accounted worldwide about 260 000 tonnes (refer Figure 2-6). The SPS machine used in this study can only produce < 500 g graphite-glass sample at a time. It is suggested that SPS method may of be use only for immobilising contaminated irradiated graphite with high level waste; as graphite is chemically stable, the remaining irradiated graphite waste can be treated as low level waste and disposed near surface.

6.9. Summary

The aim of the study has been achieved with the production of low porosity CAS and CAS(30-50)G composite materials using SPS. SPS is advantageous as it gives fast sintering due to the application of pressure, which in this work efficiently reduced the porosity with negligible loss of graphite. Overall, the data suggest that the samples produced using the SPS method are better in terms of physical, crystal growth, microstructure and tensile strength data compared to the samples those sintered using CPS. The graphite loading limit is suggested to be between 30 and 50 wt% to avoid significantly compromising the wasteform properties. The CAS50G composite is acceptable for the encapsulation of graphite with a measured porosity and tensile strength are about 3.87 g/cm^3 and 2.22 MPa respectively. Improvements in the density, porosity and the tensile strength of CAS50G sample may possible by increasing the pressure whilst undertaking the SPS process. However, due to time constraints, this investigation was not carried out and should be considered in future work.

7. Conclusions and Suggestions for Further Work

7.1. Introduction

The use of microwave heating, CPS and SPS as potential processing methods for the production of graphite-glass wasteforms have been investigated in Chapters 4, 5 and 6 respectively. Various base glass compositions have been used to encapsulate different waste loadings of graphite simulants, only some of which were found to possess suitable physical and chemical properties to be potential nuclear wasteforms. In this chapter, the key findings obtained from all result and discussion chapters are summarised and suggestions for future work are outlined for further research. Although this present research does not completely solve the immobilisation problems of the irradiated graphite waste, it is believed that the knowledge from this thesis contributes to the development of a route for the immobilisation of active irradiated graphite waste.

7.2. Contamination of Graphite Simulants in Graphite-glass Wasteforms

The contamination present in the irradiated graphite originating from the purification process at manufacturing stage, is without a doubt, a major problem that leads to the creation of problematic radionuclides (*e.g.* ^{16}Cl) resulting from the long term exposure to neutrons in the nuclear power plant. Other contaminations from nuclear reactor components during operation and nuclear incident also cause difficulties in the irradiated graphite waste management (*e.g.* ^{60}Co, ^{63}Ni, ^{55}Fe, fission products). In this study (Section 4.2), it was identified that the graphite simulants used were contaminated with various chemical elements namely O, Al, Si, S, Ca, Fe, K and Na as well as various hydrocarbon impurities. Sodalite present in the graphite simulant raw materials did not react with the base glasses; this phase can be seen in all the graphite-glass samples produced (evidence in Figure 4-11, 5-12, 5-13, 5-14, 5-15, 6-8, 6-11). Less problematic species such as Al, Si and Ca, probably in oxide form, are found incorporated with glassy materials as shown by the EDS elemental analysis; traces of such elements are identified in the glassy regions (Figure 4-17, 5-20). This is the advantage of using glass materials as they potentially encapsulate and/or incorporate such phase/elements in more stable glassy structure. From the results of this study it can be concluded that one should pay attention to the amounts of

O and Fe (3+ oxidation state) in the active irradiated graphite waste; large amounts of these elements could release ^{14}C (via the formation of ^{14}CO, $^{14}CO_2$) and promote porosity when thermally treated in glass materials. This consequently decreases the mechanical properties of the graphite wasteforms and will complicate the handling and transportation process. High porosity of graphite wasteforms is unacceptable as it can accelerate the migration of radionuclides when brought into contact with aquatic phases.

7.3. Graphite Immobilisation using Microwave Processing

At the beginning of the study, microwave processing was thought to be beneficial as it can melt or sinter the glass materials in a short processing time, typically a matter of minutes. This was seen to be advantageous for the immobilisation of irradiated graphite waste as the short processing time could reduce the oxidation rate of graphite. The main challenge of using microwave processing is to identify the materials that can act as a heat source in the glass systems (microwave absorber materials). Significant amount of time was given to identify the heat source that coupled with the microwave energy, however, only the iron phosphate glass composition was found suitable for use in the microwave processing. Magnetite was chosen as the heat source and at this stage, it is foreseen that this element can potentially accelerate the oxidation of graphite via iron reduction reaction. Nevertheless, the study was carried out to understand the effect of iron reduction reaction on graphite wasteforms produced using microwave processing.

Based on the investigation in Chapter 4, it can be concluded that the microwave processing is promising only in the production of glass materials; iron phosphate glasses were produced at 8 minutes with equivalent physical and chemical properties to glass sample prepared for 3 h using conventional melt processing (Table 4-2). However this is not the case for the graphite-glass composites based iron phosphate composition. The best graphite-glass composites (20 wt% waste loading – IP20G) formed after 20 minutes microwaving and the sample properties are unacceptable for the nuclear graphite wasteform; although produced in short processing time, the sample had ~37 % porosity and 5 % of the total mass loss was due to the graphite oxidation. Microwaving this sample in Ar did not give significant improvements. Increasing graphite

loading in the system led to a greater amount of porosity. The high porosity and graphite loss in the microwaved graphite-glass composites are due the release of a considerable amount of gases (NH_3, H_2O, CO, CO_2) which resulted from the decomposition of iron phosphate raw materials, the presence of oxygen in the sample and the environment as well as reduction of Fe^{3+} to Fe^{2+}. The comparison between the graphite-glass composite (20 % waste loading – IP20G) samples formed using microwave and CPS revealed that the CPS sample produced utilising pre-made glass had better properties; ~15 % porosity and only 0.4 % graphite oxidation from the total mass loss (Table 4-3). Hence the use of microwave processing by utilising magnetite as a heat source is seen not suitable for the production of nuclear graphite wasteforms.

7.4. Graphite Immobilisation in Various Glass Compositions by CPS

In Chapter 5, powdered base glasses namely ABS, CAS, G11, IP and natural OB were used as a host to encapsulate various graphite loadings using CPS method. A wide selection of characterisation techniques were conducted on the produced graphite-glass composites. The aim was to identify the potential of each glass in the production of graphite wasteforms, particularly in investigating the loss of graphite, amount of porosity, crystallisation behaviour, role of iron in pre-made glass, reaction of glass component with graphite and tensile strength of the obtained graphite-glass samples. From the extensive data analysis, the work in Chapter 5 can be summarised as follows:

The CPS method utilised a controlled Ar environment which was effective in reducing the graphite oxidation reaction; the graphite losses for all CPS samples sintered at optimum sintering temperatures were found generally to be < 0.8 % from the total mass loss (Figure 5-30). Although the mass loss of the graphite is low, the presence of Fe^{3+} in the glass led to similar iron reduction which accelerated the loss of graphite at temperatures around 870°C; it was also observed that the sample that initially had high amount of Fe^{2+} tended to oxidise to Fe^{3+}. Mossbauer analysis suggested that the reduction of iron occurred in G1120G and IP20G samples and in sintered OB20G sample, the iron was found to be oxidised (see Table 5-2). Both reactions potentially lead to increases in the total porosity of the samples. This complexity of iron

oxidation and/or reduction reaction(s) further suggests that the presence of this element is not suitable for the production of graphite-glass wasteforms.

The total porosity of all graphite-glass composite materials from low to high follows the order OB series < CAS series < ABS series < G11 series < IP series respectively (Figure 5-33). The total porosity of the produced graphite-glass composites loaded with 20-35 wt % graphite simulant were found to be in the range of 6-17 %. The low porosity in the OB, CAS and ABS series samples was due to the absence of iron reduction reaction. However, the porosity of these samples with such a low waste loading still seems too high for viable graphite glass wasteforms.

From the crystallisation analysis of all graphite-glass composite materials, the ABS and OB series were identified as the most resistant to crystallisation compared to the CAS series, which crystallised to larnite phase at the optimum sintering temperature. It is known that the crystallisation of the materials might slow down the sintering kinetics, limiting the flow of the glass materials while sintering and resulting in not properly filled the pores. However, from the data, this effect is difficult to observe as the generation of porosity in the graphite-glass samples mostly occurred due to the releasing of gaseous species (see Section 5-5). Investigation of the reaction of glass materials with graphite revealed that that there no chemical bonding between the graphite and the glass occurred in all graphite-glass composite series. The acceptable tensile strength of the graphite-glass composite samples made using CPS is suggested to be > 5 MPa, otherwise graphite particle could be easily removed from the samples' surface.

Overall the research in Chapter 5 leads to the conclusion that the use of CPS method is ineffective due to the production of high porosity graphite-glass composite materials. The important parameters worthy of attention for the graphite encapsulation in glass materials are: (a) all the thermal processing must be carried out in inert environment *i.e.* Ar, vacuum, (b) glass materials must not contain element that induces graphite oxidation *i.e.* iron as well as (c) the need for external pressure whilst sintering to reduce the porosity of the graphite-glass composite materials.

7.5. Graphite Immobilisation in CAS Glass Composites using SPS

The use of SPS method utilising external pressure was found to be promising and capable of producing low porosity graphite-glass wasteforms based on CAS glass systems. The SPS method successfully encapsulated graphite in CAS composite materials and the samples possessed better physical, crystal growth, microstructure and tensile strength properties compared to the samples sintered using CPS. The whole processing time is short being < 40 minutes and this is advantageous as low processing time reduced the oxidation of graphite during the thermally treatment. Whilst sintering the compacted CAS glass samples, larnite was formed and impedes viscous flow as shown in the samples that were prepared using CPS; a residue of isolated porosities is also seen in the microstructure analysis of the obtained sample (Figure 6-3a, 6-3b). This effect however is negligible in the sample made using SPS; the constant pressure given during heating forces the sample to achieve densification and thus resulting in low total porosity (Figure 6-3c, 6-3d).

For graphite-glass composite samples prepared using SPS, the graphite loss of the samples cannot be measured. However, the data could be estimated from the similar sample produced using CPS: graphite loss from total mass for CAS30G is 0.37 %. It should be noted that CAS30G sample prepared using SPS is produced in less than 40 minutes, the graphite loss should be less that the mentioned figure. Nevertheless, the microstructure analysis suggested that the porosity in the SPS made samples is low (Figure 6-8). Furthermore, similar to CPS method, no chemical bonding was identified between CAS glass composite and graphite. The waste loading limit is suggested to be in the range 30-50 wt% and the key properties of the potential graphite-glass composite materials based CAS glass compositions are as follows: CAS30G – 2.69 g/cm^3 bulk density, 1.1 % porosity, 6.6 MPa tensile strength; CAS50G – 2.59 g/cm^3 bulk density, 3.9 % porosity, 2.22 MPa tensile strength.

7.6. Future Work and Recommendations

The work undertaken in this thesis has highlighted the potential use of SPS to produce graphite-glass composite wasteforms with acceptable properties. It is clearly demonstrated that inert

environment and application of pressure are necessary in the production of graphite-glass wasteforms. However, several future investigations should be considered in order to optimise the physical and chemical properties of the graphite-glass composite samples as follows:

- Analysis of the gas species released during thermal treatments that imitate the sintering profile of SPS method should improve understanding on the mass loss behaviour of the graphite-glass composite materials. This can be carried out using TG-MS and TG-FTIR analytical techniques.
- The maximum pressure used in the study is 35 MPa. From the observations made during the course of study, the pressure can be increased and this may further reduce the total porosity of the graphite-glass composite sample. The graphite loading probably can be increased with the presence of higher pressure.
- There is an interest in using G11 glass with the iron content removed as a host for the production of graphite-glass materials using SPS method; this is due to the potential of this glass to incorporate a wide range of chemical elements, which might be suitable for the encapsulation of highly contaminated irradiated graphite waste. Essentially by removing the iron content from the glass, the composition will be similar to the borosilicate used for the vitrification of the HLW in the UK.
- In general, physical and chemical properties of irradiated graphite waste in nature are not consistent; it depends on the waste origin and how the irradiated graphite is treated in the nuclear power reactors. This is one of the major challenges in the immobilisation of irradiated graphite waste, however, it is interesting if one could demonstrate the production of graphite-glass composite materials using active waste and compare the result to that obtained data in this thesis.
- Finally, the chemical durability study should be undertaken on the ideal graphite-glass wasteforms; the environment of deep geological facility *i.e.* temperature, pressure and the groundwater behaviour/flow must be carefully considered. The chemical durability of the graphite-glass wasteforms produced using CPS and SPS can also be evaluated and should make clear whether the latter method is necessary to immobilise irradiated graphite waste.

References

Abdelouas A, Noirault S and Grambow B 2006 Immobilization of inert TRISO coated fuel in glass for geological disposal *J. Nucl. Mater.* **358** 1–9

Abid M, Et-tabirou M and Taibi M 2003 Structure and DC conductivity of lead sodium ultraphosphate glasses *Mater. Sci. Eng. B* **97** 20–4

Adamantiades A and Kessides I 2009 Nuclear power for sustainable development: current status and future prospects *Energy Policy* **37** 5149–66

Almeida F J M, Martinelli J R and Partiti C S M 2007 Characterization of iron phosphate glasses prepared by microwave heating *J. Non. Cryst. Solids* **353** 4783–91

Amjad Z and Zuhl R 2006 Kinetic and morphological investigation on the precipitation of calcium carbonate in the presence of inhibitors *Corrosion NACExpo 2006, 61st annual conference & exposition* p 6385

Andreev G E 1991 A review of the Brazilian test for rock tensile strength determination. Part I: calculation formula *Min. Sci. Technol.* **13** 445–56

Banhart F 1999 Irradiation effects in carbon nanostructures *Reports Prog. Phys.* **62** 1181–221

Barclay J and Carroll M 1996 Pre-eruptive volatile content and degassing history of an evolving peralkaline volcano *J. Volcanol. Geotherm. Res.* **74** 75–87

Bayliss S, Ewart F T, Howse R M, Dmith-Briggs J L, Thomason H P and Wilmott H A 1987 The solubility and sorption of lead-210 and carbon-14 in a near-field environment *Scientific Basis for Nuclear Waste Management XI, MRS Proceedings* vol 112 pp 33–42

Beckman Coulter Inc. 2011 Coulter LS series, product manual *TECDOC PN 4237214EA* 4–3

Béghein P, Berlioux G, Mesnildot B Du, Hiltmann F and Melin M 2012 NBG-17 - An improved graphite grade for HTRs and VHTRs *Nucl. Eng. Des.* **251** 146–9

Bingham P A, Hand R J and Forder S D 2006 Doping of iron phosphate glasses with Al_2O_3, SiO_2 or B_2O_3 for improved thermal stability *Mater. Res. Bull.* **41** 1622–30

Bingham P A, Hand R J, Forder S D and Lavaysierre A 2005 Vitrified metal finishing wastes: II. Thermal and structural characterisation *J. Hazard. Mater.* **122** 129–38

Bingham P A, Hand R J, Hannant O M, Forder S D and Kilcoyne S H 2009 Effects of modifier additions on the thermal properties, chemical durability, oxidation state and structure of iron phosphate glasses *J. Non. Cryst. Solids* **355** 1526–38

Bingham P A, Hyatt N C and Hand R J 2012 Vitrification of UK intermediate level radioactive wastes arising from site decommissioning: property modelling and selection of candidate host glass compositions *Glas. Technol. Eur. J. Glas. Sci. Technol. A* **53** 83–100

Bingham P a. and Jackson C M 2008 Roman blue-green bottle glass: chemical-optical analysis and high temperature viscosity modelling *J. Archaeol. Sci.* **35** 302–9

Birkel C S, Douglas J E, Lettiere B R, Seward G, Zhang Y, Pollock T M, Seshadri R and Stucky G D 2013 Influence of Ni nanoparticle addition and spark plasma sintering on the TiNiSn–Ni system: Structure, microstructure, and thermoelectric properties *Solid State Sci.* **26** 16–22

Bootjomchai C, Laopaiboon J, Nontachat S, Tipparach U and Laopaiboon R 2012 Structural investigation of borosilicate recycled-barium – bismuth glasses under the influence of gamma-irradiation through ultrasonic and FTIR studies *Nucl. Eng. Des.* **248** 28–34

Brown F J, Palmer J D and Wood P 1999 Derivation of a radionuclide inventory for irradiated graphite-chlorine-36 Inventory determination *Proc. IAEA Tech. Comm. Meet.* 143–52

Burchell T D 1999 *Carbon materiales for advanced technologies* (Pergamon: Elsevier Science Ltd., Oxford)

Burchell T D 2012 *Comprehensive nuclear materials: radiation effects in graphite* vol 4, ed R J M Konings (Elsevier Science Ltd., Oxford)

Burchell T D, Eatherly W P, Robbins J M and Strizak J P 1992 The effect of neutron irradiation on the structure and properties of carbon-carbon composite materials *J. Nucl. Mater.* **191-194** 295–9

Burchell T D and Snead L L 2007 The effect of neutron irradiation damage on the properties of grade NBG-10 graphite *J. Nucl. Mater.* **371** 18–27

Cassingham N J, Bingham P A, Hand R J and Forder S D 2008 Property modification of a high level nuclear waste borosilicate glass through the addition of Fe_2O_3 *Glas. Technol.* **49** 21–6

Chadwick J 1932 The existence of a neutron *Proc. R. Soc. A Math. Phys. Eng. Sci.* **136** 692–708

Chakraborty S and Arora A K 2012 Temperature evolution of Raman spectrum of iron phosphate glass *Vib. Spectrosc.* **61** 99–104

Chen Q, Tang C Y, Chan K C and Liu L 2013a Viscous flow during spark plasma sintering of Ti-based metallic glassy powders *J. Alloys Compd.* **557** 98–101

Chen Z, Lu P, Zhu H, Du B, Xie T, Wang W and Xu M 2013b AC impedance investigation and charge–discharge performance of NaOH surface-modified natural graphite *Electrochim. Acta* **102** 44–50

Choi E-Y, Han T H, Hong J, Kim J E, Lee S H, Kim H W and Kim S O 2010 Noncovalent functionalization of graphene with end-functional polymers *J. Mater. Chem.* **20** 1907–12 Online: See Supplementary Info

Cochran T B, Feiveson H A, Patterson W, Pshakin G, Ramana M V, Schneider M, Suzuki T and Hippel F V 2010 *Fast Breeder Reactor Programs: History and Status* vol 8 (International Panel on Fissile Materials)

Córdoba J M, Chicardi E, Poyato R, Gotor F J, Medri V, Guicciardi S and Melandri C 2013 Spark plasma sintering of $Ti_xTa_{1-x}C_{0.5}N_{0.5}$-based cermets: Effects of processing conditions on chemistry, microstructure and mechanical properties *Chem. Eng. J.* **230** 558–66

CoRWM 2006 Managing our radioactive waste safely: CoRWM's recommendations to government *CoRWM Doc 700*

Darwish H and Gomaa M M 2006 Effect of compositional changes on the structure and properties of alkali-alumino borosilicate glasses *J. Mater. Sci. Mater. Electron.* **17** 35–42

Day D E, Wu Z, Ray C S and Hrma P 1998 Chemically durable iron phosphate glass wasteforms *J. Non. Cryst. Solids* **241** 1–12

DECC 2013 Consultation review of the siting process for a geological disposal facility *URN 13D/250*

DECC 2014 Implementing geological disposal: a framework for the long-term management of higher activity radioactive waste *URN 14D/235*

Defra, BERR and the devolved administrations for Wales and Northen Ireland 2008 Managing radioactive waste safely: a framework for implementing geological disposal *Cm 7386*

Defra, DTI and Administrations D 2007 Policy for the long term management of solid low level radioactive waste in the United Kingdom *PB 12522*

Dickson D P E and Berry F J 1986 *Mossbauer spectroscopy* (Cambridge University Press)

Djohari H and Derby J J 2009 Transport mechanisms and densification during sintering: II. Grain boundaries *Chem. Eng. Sci.* **64** 3810–6

Djohari H, Martínez-Herrera J I and Derby J J 2009 Transport mechanisms and densification during sintering: I. Viscous flow versus vacancy diffusion *Chem. Eng. Sci.* **64** 3799–809

Donald I W 2010 *Waste immobilization in glass and ceramic based hosts: radioactive, toxic and hazardous wastes* (John Wiley & Sons Ltd, West Sussex)

Donald I W, Metcalfe B L and Taylor R N J 1997 Review: the immobilization of high level radioactive wastes using ceramics and glasses *J. Mater. Sci.* **32** 5851–87

Dubourg M 1998 Technologies fro gas cooled reactor decommissioning, fuel storage and waste disposal: the carbon 14 Cycle *IAEA TECDOC 1043* 233–7

Duderstadt J J and Hamilton L J 1976 *Nuclear reactor analysis* (John Wiley and Sons, Inc., New York)

Dunbar N W and Kyle P R 1992 Volatile contents of obsidian clasts in tephra from the Taupo Volcanic Zone, New Zealand: Implications to eruptive processes *J. Volcanol. Geotherm. Res.* **49** 127–45

Dunzik-Gougar M Lou and Smith T E 2014 Removal of carbon-14 from irradiated graphite *J. Nucl. Mater.* **451** 328–35

Dyar M D, Agresti D G, Schaefer M W, Grant C A and Sklute E C 2006 Mössbauer spectroscopy of earth and planetary materials *Annu. Rev. Earth Planet. Sci.* **34** 83–125

Einstein A 1905 Does the inertia of a body depend upon its energy-content? (Ist die Trägheit eines Körpers von seinem Energieinhalt abhängig?) *Ann. Phys.* 1–3

Elbouaanani L K, Malaman B and Gérardin R 1999 Structure refinement and magnetic properties of C–$Fe(PO_3)_3$ studied by neutron diffraction and Mössbauer techniques *J. Solid State Chem.* **148** 455–63

El-Egili K 2003 Infrared studies of $Na_2O - B_2O_3 - SiO_2$ and $Al_2O_3 - Na_2O - B_2O_3 - SiO_2$ glasses *Phys. B* **325** 340–8

Ericson J E, Makishima A, Mackenzie J D and Berger R 1975 Chemical and physical properties of obsidian: a naturally occuring glass *J. Non. Cryst. Solids* **17** 129–42

Ericsson T, Nord A G, Ahmed M M O, Gismelseed A and Khangi F 1990 $Fe_2P_2O_7$ and $Fe_2P_4O_{12}$ studied between 5–800 K *Hyperfine Interact.* **57** 2179–86

Fachinger J 2012 *Comprehensive nuclear materials: Graphite* vol 5, ed R J M Konings (Elsevier Science Ltd., Oxford)

Fachinger J, Grosse K H, Hrovat M and Seemann R 2012 Utilization of HTR reflector graphite as embedding matrix for radioactive waste *Nucl. Eng. Des.* **251** 235–8

Fachinger J, von Lensa W and Podruhzina T 2008 Decontamination of nuclear graphite *Nucl. Eng. Des.* **238** 3086–91

Forder S D, Bingham P A, McGann O J, Stennett M C and Hyatt N C 2012 Mössbauer studies of materials used to immobilise industrial wastes *Hyperfine Interact.* **217** 83–90

Fredrick D M, Gash A E, Landingham R L, Satcher J H and Munir Z a. 2013 Sol gel synthesis and spark plasma sintering of lanthana-doped alumina glass *J. Non. Cryst. Solids* **363** 64–9

Frenkel J 1945 Viscous flow of crystalline bodies under the action of surface tension *J. Phys. USSR* **9** 385–91

Frisch O R 1939 Physical evidence for the division of heavy nuclei under neutron bombardment *Nature* **143** 276–276

Furukawa T, Fox K E and White W B 1981 Raman spectroscopic investigation of the structure of silicate glasses. III. Raman intensities and structural units in sodium silicate glasses *J. Chem. Phys.* **75** 3226

Gaafar M S and Marzouk S Y 2007 Mechanical and structural studies on sodium borosilicate glasses doped with Er_2O_3 using ultrasonic velocity and FTIR spectroscopy *Phys. B* **388** 294–302

Galeener F L 1982 Planar rings in glasses *Solid State Commun.* **44** 1037–40

Garcia-lodeiro I, Fernández-jimenez A, Pena P and Palomo A 2014 Alkaline activation of synthetic aluminosilicate glass *Ceram. Int.* **40** 5547–58

Girke N A, Bushuev A V, Kozhin A F, Petrova E V, Aleeva T B and Zubarev V N 2012 ^{14}C in spent graphite from uranium-graphite reactors at the Siberian chemical combine *At. Energy* **112** 63–6

Goodhew P J, Humphreys F J and Beanland R 2001 *Electron microscopy and analysis* (Taylor & Francis, London)

Goodwin C, Barkatt A and Al-Sheikhly M 2014 On the mechanism of the interactions of neutrons and gamma radiation with nuclear graphite-implications to HTGRs *Radiat. Phys. Chem.* **97** 38–47

Greenwood N N and Earnshaw A 1997 *Chemistry of the elements* (Butterworth-Heinemann, Oxford)

Guillon O, Gonzalez-Julian J, Dargatz B, Kessel T, Schierning G, Räthel J and Herrmann M 2014 Field-assisted sintering technology/spark plasma sintering: mechanisms, materials, and technology developments *Adv. Eng. Mater.* **16** 830–49

Guiroy J J 1995 Graphite waste incineration in a fluidized bed *Spec. Meet. Graph. moderator lifecycle Behav.* 193–203

Guyon J, Hazotte A, Monchoux J P and Bouzy E 2013 Effect of powder state on spark plasma sintering of TiAl alloys *Intermetallics* **34** 94–100

Hafid M, Jermoumi T, Toreis N and Ghailassi T 2002 Structure of $(45-x)Na_2O–xBaO–5ZnO–50P_2O_5$ glasses studied by DSC and infrared spectroscopy *Mater. Lett.* **56** 486–90

Hall G, Marsden B J and Fok S L 2006 The microstructural modelling of nuclear grade graphite *J. Nucl. Mater.* **353** 12–8

Haynes W M 2014 *CRC handbook of chemistry and physics, 95th edition, 2014-2015* (CRC Press/Taylor and Francis, Boca Raton, FL)

Heath P G, Corkhill C L, Stennett M C, Hand R J, Meyer W C H M and Hyatt N C 2013 Encapsulation of TRISO particle fuel in durable soda-lime-silicate glasses *J. Nucl. Mater.* **436** 139–49

Heggie M I, Suarez-Martinez I, Davidson C and Haffenden G 2011 Buckle, ruck and tuck: a proposed new model for the response of graphite to neutron irradiation *J. Nucl. Mater.* **413** 150–5

Her Majesty's Stationery Office 1995 Review of radioactive waste management policy: final conclusions *Cm 2919*

Hietanfn R, Jaakkola T and Miettinen J K 1984 Sorption of cesium, strontiuli, iodine and carbon in concrete and sand *Scientific Basis for Nuclear Waste Management VIII, MRS Proceedings* vol 44 pp 891–8

Hisa M, Tsutsumi A and Akiyama T 2004 Reduction of iron oxides by nano-sized graphite particles observed in pre-oxidized iron carbide at temperatures around 873 K *Mater. Trans.* **45** 1907–10

Hrovat M, Grosse K-H and Seemann R 2013 Matrix material comprising graphite and an inorganic binder suited for final disposal of radioactive waste, a process for producing the same and its processing and use *US Patent, US 8502009 B2*

Huang C and Behrman E C 1991 Structure and properties of calcium aluminosilicate glasses *J. Non. Cryst. Solids* **128** 310–21

Huang S, Swarnakar A K, Vanmeensel K and Vleugels J 2013 Diamond dispersed Si3N4 composites obtained by pulsed electric current sintering *J. Eur. Ceram. Soc.* **33** 1237–47

Huang W, Day D E, Ray C S, Kim C-W and Mogus-Milankovic A 2004 Vitrification of high chrome oxide nuclear waste in iron phosphate glasses *J. Nucl. Mater.* **327** 46–57

Huang W-H, Tsai S-C, Yang C-W and Kai J-J 2014 The relationship between microstructure and oxidation effects of selected IG- and NBG-grade nuclear graphites *J. Nucl. Mater.* **454** 149–58

Hussainova I, Voltšihhin N, Cura E and Hannula S-P 2014 Densification and characterization of spark plasma sintered ZrC–ZrO_2 composites *Mater. Sci. Eng. A* **597** 75–81

IAEA 2013 Annual report 2013 *GC(58)/3*

IAEA 2006 Characterization, treatment and conditioning of radioactive graphite from decommissioning of nuclear reactors *TECDOC 1521*

IAEA 2011 Disposal of radioactive waste: specific safety requirements *No. SSR-5*

IAEA 2014a Energy, electricity and nuclear power estimates for the period up to 2050 *Ref. Data Ser. No. 1, 2014 Ed.*

IAEA 2000 Irradiation damage in graphite due to fast neutrons in fission and fusion systems *TECDOC 1154*

IAEA 2004 Management of waste containing tritium and carbon-14 *Tech. Reports Ser. No. 421*

IAEA 2007 Nuclear power plant design charateristics: structure of nuclear power plant design characteristics in the IAEA power reactor information system (PRIS) *TECDOC 1544*

IAEA 2014b Nuclear power reactor in the world *Ref. Data Ser. No. 2, 2014 Ed.*

IAEA 2010 Progress in radioactive graphite waste management *TECDOC 1647*

IEA 2014a Key world energy statistics *Inernational Energy Agency*

IEA 2014b World energy outlook *Inernational Energy Agency*

IUPAC 1997 *Compendium of chemical terminology (the "gold book")* ed A D McNaught, A Wilkinson and A Jenkins (Blackwell Scientific Publications, Oxford)

Jermoumi T, Hafid M, Niegisch N, Mennig M, Sabir A and Toreis N 2002 Properties of $(0.5-x)Zn–xFe_2O_3–0.5P_2O_5$ glasses *Mater. Res. Bull.* **37** 49–57

Joseph K, Premila M, Amarendra G, Govindan Kutty K V, Sundar C S and Vasudeva Rao P R 2012 Structure of cesium loaded iron phosphate glasses: an infrared and Raman spectroscopy study *J. Nucl. Mater.* **420** 49–53

Kalampounias A G 2011 IR and Raman spectroscopic studies of sol–gel derived alkaline-earth *Bull. Mater. Sci.* **34** 299–303

Kamitsos E 1996 Reply to "Comment on Infrared-reflectance spectra of heat-treated, sol-gel-derived silica" *Phys. Rev. B* **53** 14659–62

Kamitsos E I, Kapoutsis J A, Jain H and Hsieh C H 1994 Vibrational study of the role of trivalent ions in sodium trisilicate glass *J. Non. Cryst. Solids* **171** 31–45

Kang S-J L 2005 *Sintering: densification, grain growth and microstructure* (Elsevier Butterworth-Heinemann, Oxford)

Karabulut M, Metwalli E, Day D E and Brow R K 2003 Mössbauer and IR investigations of iron ultraphosphate glasses *J. Non. Cryst. Solids* **328** 199–206

Karlina O K, Klimov V L, Ojovan M I, Pavlova G Y, Dmitriev S A and Yurchenko A Y 2005 Immobilization of carbon-14 from reactor graphite waste by use of self-sustaining reaction in the C–Al–TiO_2 system *J. Nucl. Mater.* **345** 84–5

Kelly B T 1981 *Physics of graphite* (Applied Science Publishers, London)

Kelly B T and Burchell T D 1994 Structure-related property changes in polycrystalline graphite under neutron irradiation *Carbon N. Y.* **32** 499–505

Kharissova O V., Kharisov B I and Valdés J J R 2010 Review: the use of microwave irradiation in the processing of glasses and their composites *Ind. Eng. Chem. Res.* **49** 1457–66

Kim C-W and Day D E 2003 Immobilization of Hanford LAW in iron phosphate glasses *J. Non. Cryst. Solids* **331** 20–31

Kim T, Lee J and Lee K-H 2014 Microwave heating of carbon-based solid materials *Carbon Lett.* **15** 15–24

Kjeldsen J, Smedskjaer M M, Mauro J C, Youngman R E, Huang L and Yue Y 2013 Mixed alkaline earth effect in sodium aluminosilicate glasses *J. Non. Cryst. Solids* **369** 61–8

Lai Y, Liang X, Yang S, Liu P, Zeng Y and Hu C 2014 Raman and FTIR spectra of CeO_2 and Gd_2O_3 in iron phosphate glasses *J. Alloys Compd.* **617** 597–601

Lai Y, Liang X, Yin G, Yang S, Wang J, Zhu H and Yu H 2011a Infrared spectra of iron phosphate glasses with gadolinium oxide *J. Mol. Struct.* **1004** 188–92

Lai Y M, Liang X F, Yang S Y, Wang J X, Cao L H and Dai B 2011b Raman and FTIR spectra of iron phosphate glasses containing cerium *J. Mol. Struct.* **992** 84–8

Larkin P J 2011 *"IR and Raman spectroscopy - principles and spectral interpretation"* (Elsevier, USA)

Lee W E, Ojovan M I and Jantzen C M 2013 *Radioactive waste management and contaminated site clean-Up* (Woodhead Publishing Limited, Cambridge)

Lewis E E 2008 *Fundamentals of nuclear reactor physics* (Academic Press/Elsevier, Burlington, MA)

Lim Y S, Chi S H and Cho K Y 2008 Change of properties after oxidation of IG-11 graphite by air and CO_2 gas *J. Nucl. Mater.* **374** 123–8

Lipińska M E, Novais J P, Rebelo S L H, Bachiller-Baeza B, Rodríguez-Ramos I, Guerrero-Ruiz A and Freire C 2014 Microwave-assisted silylation of graphite oxide and iron(III) porphyrin intercalation *Polyhedron* **81** 475–84

Lowenstern J B, Bleick H, Vazquez J a., Castro J M and Larson P B 2012 Degassing of Cl, F, Li, and Be during extrusion and crystallization of the rhyolite dome at Volcán Chaitén, Chile during 2008 and 2009 *Bull. Volcanol.* **74** 2303–19

Ma L, Brow R K and Choudhury A 2014 Structural study of Na_2O–FeO–Fe_2O_3–P_2O_5 glasses by Raman and Mössbauer spectroscopy *J. Non. Cryst. Solids* **402** 64–73

MacDonald S A, Schardt C R, Masiello D J and Simmons J H 2000 Dispersion analysis of FTIR reflection measurements in silicate glasses *J. Non. Cryst. Solids* **275** 72–82

Mackenzie J K and Shuttleworth R 1949 A phenomenological theory of sintering *Proc. Phys. Soc. Sect. B* **62** 833–52

Magnox and NDA 2013 Intermediate level waste (ILW) storage and fuel element debris (FED) treatment optimisation study Online: http://www.nda.gov.uk/publication/intermediate-level-waste-ilw-storage-and-fuel-element-debris-fed-treatment-optimisation-study/

Mahdy E A and Ibrahim S 2012 Influence of Y_2O_3 on the structure and properties of calcium magnesium aluminosilicate glasses *J. Mol. Struct.* **1027** 81–6

Marasinghe G K, Karabulut M, Ray C S, Day D E, Shuh D K, Allen P O, Saboungi M L, Grimsditch M and Haeffner D 2000 Properties and structure of vitrified iron phosphate nuclear wasteforms *J. Non. Cryst. Solids* **263** 146–54

Márquez E, Piña G, Rodriguez M, Fachinger J, Grosse K, Luis J, Nieto L, Gracian M Q and Seemann R 2011 GRAFEC: a new spanish program to investigate waste management options for radioactive graphite *WM2012 Conference, February 26 – March 1, 2011, Phoenix, Arizona, USA*

Marzouk S Y, Seoudi R, Said D A and Mabrouk M S 2013 Linear and non-linear optics and FTIR characteristics of borosilicate glasses doped with gadolinium ions *Opt. Mater. (Amst).* **35** 2077–84

Mazo M A, Palencia C, Nistal A, Rubio F, Rubio J and Oteo J L 2012 Dense bulk silicon oxycarbide glasses obtained by spark plasma sintering *J. Eur. Ceram. Soc.* **32** 3369–78

Mazurin O V. 2007 Problems of compatibility of the values of glass transition temperatures published in the world literature *Glas. Phys. Chem.* **33** 22–36

Mazurin O V. and Gankin Y V. 2008 Glass transition temperature: problems of measurement procedures *Glass Technology: European Journal of Glass Science and Technology Part A* vol 49 pp 229–33

McGann O J, Bingham P A, Hand R J, Gandy A S, Kavčič M, Žitnik M, Bučar K, Edge R and Hyatt N C 2012 The effects of γ-radiation on model vitreous wasteforms intended for the disposal of intermediate and high level radioactive wastes in the United Kingdom *J. Nucl. Mater.* **429** 353–67

McGann O J and Ojovan M I 2011 The synthesis of graphite–glass composites intended for the immobilisation of waste irradiated graphite *J. Nucl. Mater.* **413** 47–52

Mcgill S L, Walkiewicz W E and Clark A E 1995 Microwave heating of chemicals and minerals *Rep. Investig. 9518*

McKeown D A, Buechele A C, Viragh C and Pegg I L 2010 Raman and X-ray absorption spectroscopic studies of hydrothermally altered alkali-borosilicate nuclear waste glass *J. Nucl. Mater.* **399** 13–25

McMillan P 1984 Structural studies of silicate glasses and melts-applications and limitations of Raman spectroscopy *Am. Mineral.* **69** 622–44

McMillan P and Piriou B 1982 The structures and vibrational spectra of crystals and glasses in the silica-alumina system *J. Non. Cryst. Solids* **53** 279–98

Mcmillan P, Piriou B and Navrotsky A 1982 A Raman spectroscopic study of glasses along the joins silica-calcium aluminate, silica-sodium aluminate, and silica-potassium aluminate *Geochim. Cosmochim. Acta*

Meitner L and Frisch O R 1939 Breaking up is easy - nuclear fission discovered *Nature* **143** 239–40

Menéndez J a., Arenillas A, Fidalgo B, Fernández Y, Zubizarreta L, Calvo E G and Bermúdez J M 2010 Microwave heating processes involving carbon materials *Fuel Process. Technol.* **91** 1–8

Menyah K and Wolde-Rufael Y 2010 CO_2 emissions, nuclear energy, renewable energy and economic growth in the US *Energy Policy* **38** 2911–5

Mercier M, Di Muro A, Giordano D, Métrich N, Lesne P, Pichavant M, Scaillet B, Clocchiatti R and Montagnac G 2009 Influence of glass polymerisation and oxidation on micro-Raman water analysis in alumino-silicate glasses *Geochim. Cosmochim. Acta* **73** 197–217

Meredith R J 1998 *Engineers' handbook of industrial microwave heating* (The Institution of Electrical Engineers, London)

Millet J M, Virely C, Forissier M, Bussière P and Vedrine J C 1989 Mössbauer spectroscopic study of iron phosphate catalysts used in selective oxidation *Hyperfine Interact.* **46** 619–28

Moguš-Milanković A, Šantić A, Reis S T, Furić K and Day D E 2004 Mixed ion–polaron transport in Na_2O–PbO–Fe_2O_3–P_2O_5 glasses *J. Non. Cryst. Solids* **342** 97–109

Mondal K, Lorethova H, Hippo E, Wiltowski T and Lalvani S B 2004 Reduction of iron oxide in carbon monoxide atmosphere-reaction controlled kinetics *Fuel Process. Technol.* **86** 33–47

Morgan L E, Renne P R, Taylor R E and WoldeGabriel G 2009 Archaeological age constraints from extrusion ages of obsidian: examples from the middle Awash, Ethiopia *Quat. Geochronol.* **4** 193–203

Mughabghab S F, Divadeenam M, Holden N E, Kinsey R R and McLane V 1981 *Neutron cross section series* ed S F Mughabghab, R R Kinsey and C L Dunford (Academic Press Inc. (London) Ltd.)

Mysen B O 1990 Interaction between water and melt in the system $CaAl_2O_4$-SiO_2-H_2O *Chem. Geol.* **88** 223–43

Mysen B O, Virgo D and Seifert F A 1982 The stucture of silicate melts: implications for chemical and physical properties of natural magma *Rev. Geophys. Sp. Phys.* **20** 353–83

Nakahara M and Sanada Y 1995 FT-IR ATR spectroscopy of the edge surface of pyrolytic graphite and its surface/PVC interface *J. Mater. Sci.* **30** 4363–8

NDA 2011 UK Management of solid low level radioactive waste from the nuclear industry: low level waste strategic review *NLWS/LLWR/16*

NDA 2009 UK radioactive higher activity waste storage review UK radioactive higher activity waste storage review Online: http://www.nda.gov.uk/publication/uk-radioactive-higher-activity-waste-storage-review-march-2009/

NDA 2010 UK strategy for the management of solid low level radioactive waste from the nuclear industry Online: http://www.nda.gov.uk/publication/uk-strategy-for-the-management-of-solid-low-level-radioactive-waste-from-the-nuclear-industry-august-2010/

NDA and DECC 2013 Radioactive wastes in the UK: a summary of the 2013 inventory Online: https://www.nda.gov.uk/wp-content/uploads/sites/2/2014/02/14D039-NDASTSTY140006-UKRWI-2013-High-Level-Summary.pdf

Neuville D, Cormier L and Massiot D 2006 Al coordination and speciation in calcium aluminosilicate glasses: Effects of composition determined by 27Al MQ-MAS NMR and Raman spectroscopy *Chem. Geol.* **229** 173–85

Neuville D R, Cormier L and Massiot D 2004 Al environment in tectosilicate and peraluminous glasses: A 27Al MQ-MAS NMR, Raman, and XANES investigation *Geochim. Cosmochim. Acta* **68** 5071–9

Niehues J, Lehmann P and Xie W 2012 Low coherent Linnik interferometer optimized for use in nano-measuring machines *Meas. Sci. Technol.* **23** 125002

Nightingale R E 1963 *Nuclear graphite* vol 47 (Academic Press Inc. (London) Ltd)

OECD, NEA and IEA 2015 Technology roadmap: nuclear energy Online: https://www.iea.org/publications/freepublications/publication/TechnologyRoadmapNuclearEnergy.pdf

OECD Nuclear Energy Agency 2014 Technology roadmap update for generation IV nuclear energy systems Online: https://www.gen-4.org/gif/upload/docs/application/pdf/2014-03/gif-tru2014.pdf

Ojovan M I 2011 *Handbook of advanced radioactive waste conditioning technologies* (Woodhead Publishing Limited, Cambridge)

Ojovan M I and Lee W E 2005 *An introduction to nuclear waste immobilisation* (Elsevier Ltd., Oxford)

Olanipekun O, Oyefusi A, Neelgund G M and Oki A 2014 Adsorption of lead over graphite oxide. *Spectrochim. Acta. A. Mol. Biomol. Spectrosc.* **118** 857–60

Pichon C, Guy C and Comte J 2008 ^{36}Cl and ^{14}C behaviour in UNGG graphite during leaching experiments *Commun. Ref. number* 1–5

Pierson H O 1993 *Handbook of carbon, graphite, diamond and fullerenes: properties, processing and applications* (Noyes Publications, New Jersey)

Piotrowski K, Wiltowski T, Mondal K, Stonawski L, Szymański T and Dasgupta D 2005 Simultaneous influence of gas mixture composition and process temperature on $Fe_2O_3 \rightarrow FeO$ reduction kinetics - Neural network modeling *Brazilian J. Chem. Eng.* **22** 419–32

Plodinec M J 2000 Borosilicate glasses for nuclear waste imobilisation *Glas. Technol.* **41** 186–92

Podruzhina T 2004 Graphite as radioactive waste; corrosion behaviour under final repository conditions and thermal treatment *Inst. für Sicherheitsforsch. und Reakt. Jül-4166*

Prado M O and Zanotto E D 2002 Glass sintering with concurrent crystallization *Comptes Rendus Chim.* **5** 773–86

Premila M, Abhaya S, Rajaraman R, Ravindran T R, Amarendra G and Sundar C S 2012 Probing the local structural changes across the amorphous to crystalline transition in iron phosphate glass: Positron annihilation and micro Raman studies *J. Non. Cryst. Solids* **358** 1014–8

Qian B, Liang X, Yang S, He S and Gao L 2012 Effects of lanthanum addition on the structure and properties of iron phosphate glasses *J. Mol. Struct.* **1027** 31–5

Rajkumar K and Aravindan S 2009 Microwave sintering of copper–graphite composites *J. Mater. Process. Technol.* **209** 5601–5

Rao K J, Vaidhyanathan B, Ganguli M and Ramakrishnan P A 1999 Synthesis of inorganic solids using microwaves *Chem. Mater.* **11** 882–95

Rappeneau J, Taupin J L and Grehier J 1966 Energy released at high temperature by irradiated graphite *Carbon N. Y.* **4** 115–24

Reynolds W N 1968 *Physical properties of graphite* (Elsevier Publishing Co. Ltd., New York)

Ristić M M and Milosević S D 2006 Frenkel's theory of Sintering *Sci. Sinter.* **38** 7–11

Rizzo S, Grasso S, Salvo M, Casalegno V, Reece M J and Ferraris M 2014 Joining of C/SiC composites by spark plasma sintering technique *J. Eur. Ceram. Soc.* **34** 903–13

Rublevskiy V P 2012 Commercial nuclear reactors and 14C *At. Energy* **113** 117–20

Rupesh Kumar A, Rao T G V M, Neeraja K, Rami Reddy M and Veeraiah N 2013 Gamma ray induced changes on vibrational spectroscopic properties of strontium alumino-borosilicate glasses *Vib. Spectrosc.* **69** 49–56

Saddeek Y B, Gaafar M S and Bashier S A 2010 Structural influence of PbO by means of FTIR and acoustics on calcium alumino-borosilicate glass system *J. Non. Cryst. Solids* **356** 1089–95

Saheb N, Iqbal Z, Khalil A, Hakeem A S, Al Aqeeli N, Laoui T, Al-Qutub A and Kirchner R 2012 Spark plasma sintering of metals and metal matrix nanocomposites: a review *J. Nanomater.* **2012** 1–13

Sahin F C, Kanbur H E and Apak B 2012 Preparation of AlON ceramics via reactive spark plasma sintering *J. Eur. Ceram. Soc.* **32** 925–9

Schofield J M 2011 *Vitrification of a chloride containing actinide waste surrogate* (The University of Sheffield)

Schofield J M, Bingham P A and Hand R J 2009 The immobilisation of a chloride containing actinide waste surrogate in calcium aluminosilicate glasses *Environ. Issues Waste Manag. Technol. Mater. Nucl. Ind. XII. Ceram. Trans.* **207** 69–80

Schroeder J, Wu W, Apkarian J L, Lee M, Hwa L-G and Moynihan C T 2004 Raman scattering and Boson peaks in glasses: temperature and pressure effects *J. Non. Cryst. Solids* **349** 88–97

Schweitzer D G and Singer R M 1965 Oxidation rates of alternately irradiated and annealed graphite *J. Nucl. Mater.* **16** 220–6

Seifert F A, Mysen B O and Virgo D 1982 Three-dimensional network structure of quenched melts (glass) in the systems SiO_2-$NaAlO_2$, SiO_2-$CaAl_2O_4$ and SiO_2-$MgAl_2O_4$. *Am. Mineral.* **67** 696–717

Sengupta P 2012 A review on immobilization of phosphate containing high level nuclear wastes within glass matrix - present status and future challenges *J. Hazard. Mater.* **235-236** 17–28

Serne R J, Lokken R O and Criscenti L J 1992 Characterization of grouted low-level waste to support performance assessment *Waste Manag.* **12** 271–87

Shelby J E 2005 *Introduction to glass science and technology* (The Royal Society of Chemistry, Cambridge)

Smith B 2011 *Fundamentals of fourier transform infrared spectroscopy* (CRC Press/Taylor and Francis, Boca Raton, FL)

Socrates G 2004 *Infrared and Raman characteristic group frequencies* (John Wiley and Sons., West Sussex)

Song S, Wen Z, Liu Y, Zhang Q, Wu X, Zhang J and Han J 2009 Influence of dopants on the crystallization of borosilicate glass *Ceram. Int.* **35** 3037–42

Sontakke A D, Biswas K and Annapurna K 2009 Concentration-dependent luminescence of Tb3+ ions in high calcium aluminosilicate glasses *J. Lumin.* **129** 1347–55

Środa M and Paluszkiewicz C 2008 The structural role of alkaline earth ions in oxyfluoride aluminosilicate glasses-Infrared spectroscopy study *Vib. Spectrosc.* **48** 246–50

Stacey W M 2007 *Nuclear reactor physics* (WILEY-VCH Verlag GmbH & Co. KGaA, Weinheim)

Stennett M C and Hyatt N C 2009 Microwave processing of glasses for waste immobilization *Scientific Basis for Nuclear Waste Management XXXII, MRS Proceedings* vol 1124 pp 147–52

Stennett M C, Pinnock I J and Hyatt N C 2011 Rapid synthesis of $Pb_5(VO_4)_3I$, for the immobilisation of iodine radioisotopes, by microwave dielectric heating *J. Nucl. Mater.* **414** 352–9

Suárez M, Fernández A and Menéndez J 2013 Challenges and opportunities for spark plasma sintering: a key technology for a new generation of materials *Sintering Applications* ed B Ertug

Tamayo A, Mazo M A, Rubio F and Rubio J 2014 Structure properties relationship in silicon oxycarbide glasses obtained by spark plasma sintering *Ceram. Int.* **40** 11351–8

Telling R H and Heggie M I 2007 Radiation defects in graphite *Philos. Mag.* **87** 4797–846

Thostenson E T and Chou T W 1999 Microwave processing: fundamentals and applications *Compos. Part A Appl. Sci. Manuf.* **30** 1055–71

Tokita M 1999 Mechanism of spark plasma sintering *Proceeding of NEDO International Symposium on Functionally Graded Materials* vol 21 p 22

Vidhyanathan B, Ganguli M and Rao K J 1994 A novel method of preparation of inorganic glasses by microwave irradiation *J. Solid State Chem.* **113** 448–50

Vogel N, Nomade S, Negash A and Renne P R 2006 Forensic $^{40}Ar/^{39}Ar$ dating: a provenance study of middle stone age obsidian artifacts from Ethiopia *J. Archaeol. Sci.* **33** 1749–65

Vulpius D, Baginski K, Fischer C and Thomauske B 2013 Location and chemical bond of radionuclides in neutron-irradiated nuclear graphite *J. Nucl. Mater.* **438** 163–77

Wang J-S, Jeng J-S and Ni C-T 2009 The study on the phosphate glass melted by microwave irradiation *J. Non. Cryst. Solids* **355** 780–4

Wang X and Dou W 2012 Preparation of graphite oxide (GO) and the thermal stability of silicone rubber/GO nanocomposites *Thermochim. Acta* **529** 25–8

Westrich H R, Stockman H W and Eichelberger J C 1988 Degassing of rhyolitic magma during ascent and emplacement *J. Geophys. Res.* **93** 6503

White I F, Smith G M, Sauders L J, Kaye C J, Martin T J, Clarke G H and Wakerley M W 1984 Assessment of Management Modes for Graphite from Reactor Decommissioning *Comm. Eur. Communities EUR 9232* 1–119

White W B and Minser D G 1984 Raman spectra and stuctural of natural glasses *J. Non. Cryst. Solids* **67** 45–59

Wickham A J, Neighbour G B and Dubourg M 1999 The uncertain future for nuclear graphite disposal: crisis or opportunity? *Proceedings of the Technical Committee Meeting on Nuclear Graphite Waste Management* (Manchester, UK) pp 1–16

Wilson P D 1996 *The nuclear fuel cycle: from ore to wastes* (Oxford University Press)

Windes W, Burchell T and Bratton R 2007 Graphite technology development plan *Idaho Natl. Lab. PLN-2497, Rev 0*

Winterstein-Beckmann A, Möncke D, Palles D, Kamitsos E I and Wondraczek L 2014 A Raman-spectroscopic study of indentation-induced structural changes in technical alkali-borosilicate glasses with varying silicate network connectivity *J. Non. Cryst. Solids* **405** 196–206

WNA 2015 Nuclear Power Reactors *World Nucl. Assoc.* Online: http://www.world-nuclear.org/info/Nuclear-Fuel-Cycle/Power-Reactors/Nuclear-Power-Reactors/

Xie G 2013 Spark plasma sintering: a useful technique to develop large-sized bulk metallic glasses *J. Powder Metall. Min.* **2** 2–4

Yang G, Möbus G and Hand R J 2006 Cerium and boron chemistry in doped borosilicate glasses examined by EELS *Micron* **37** 433–41

Yim M-S and Caron F 2006 Life cycle and management of carbon-14 from nuclear power generation *Prog. Nucl. Energy* **48** 2–36

Yu Y-H, Lin Y-Y, Lin C-H, Chan C-C and Huang Y-C 2014 High-performance polystyrene/graphene-based nanocomposites with excellent anti-corrosion properties *Polym. Chem.* **5** 535

Zhang C, Chen M, Xu X, Zhang L, Zhang L, Xia F, Li X, Liu Y, Hu W and Gao J 2014 Graphene oxide reduced and modified by environmentally friendly glycylglycine and its excellent catalytic performance *Nanotechnology* **25** 135707

Zhang J, Tu R and Goto T 2012 Fabrication of transparent SiO_2 glass by pressureless sintering and spark plasma sintering *Ceram. Int.* **38** 2673–8

Appendix A1: Density of Distilled Water at Various Temperatures

T/ºC	0.0	0.1	0.2	0.3	0.4	0.5	0.6	0.7	0.8	0.9
10.	0.99973	0.99972	0.99971	0.99970	0.99969	0.99968	0.99967	0.99966	0.99965	0.99964
11.	0.99963	0.99962	0.99961	0.99960	0.99959	0.99958	0.99957	0.99956	0.99955	0.99954
12.	0.99953	0.99951	0.99950	0.99949	0.99948	0.99947	0.99946	0.99944	0.99943	0.99942
13.	0.99941	0.99939	0.99938	0.99937	0.99935	0.99934	0.99933	0.99931	0.99930	0.99929
14.	0.99927	0.99926	0.99924	0.99923	0.99922	0.99920	0.99919	0.99917	0.99916	0.99914
15.	0.99913	0.99911	0.99910	0.99908	0.99907	0.99905	0.99904	0.99902	0.99900	0.99899
16.	0.99897	0.99896	0.99894	0.99892	0.99891	0.99889	0.99887	0.99885	0.99884	0.99882
17.	0.99880	0.99879	0.99877	0.99875	0.99873	0.99871	0.99870	0.99868	0.99866	0.99864
18.	0.99862	0.99860	0.99859	0.99857	0.99855	0.99853	0.99851	0.99849	0.99847	0.99845
19.	0.99843	0.99841	0.99839	0.99837	0.99835	0.99833	0.99831	0.99829	0.99827	0.99825
20.	0.99823	0.99821	0.99819	0.99817	0.99815	0.99813	0.99811	0.99808	0.99806	0.99804
21.	0.99802	0.99800	0.99798	0.99795	0.99793	0.99791	0.99789	0.99786	0.99784	0.99782
22.	0.99780	0.99777	0.99775	0.99773	0.99771	0.99768	0.99766	0.99764	0.99761	0.99759
23.	0.99756	0.99754	0.99752	0.99749	0.99747	0.99744	0.99742	0.99740	0.99737	0.99735
24.	0.99732	0.99730	0.99727	0.99725	0.99722	0.99720	0.99717	0.99715	0.99712	0.99710
25.	0.99707	0.99704	0.99702	0.99699	0.99697	0.99694	0.99691	0.99689	0.99686	0.99684
26.	0.99681	0.99678	0.99676	0.99673	0.99670	0.99668	0.99665	0.99662	0.99659	0.99657
27.	0.99654	0.99651	0.99648	0.99646	0.99643	0.99640	0.99637	0.99634	0.99632	0.99629
28.	0.99626	0.99623	0.99620	0.99617	0.99614	0.99612	0.99609	0.99606	0.99603	0.99600
29.	0.99597	0.99594	0.99591	0.99588	0.99585	0.99582	0.99579	0.99576	0.99573	0.99570
30.	0.99567	0.99564	0.99561	0.99558	0.99555	0.99552	0.99549	0.99546	0.99543	0.99540